

University of Reading

Novel Printed Resonant Structures for Multi-Modal Wireless Power Transfer within Smart Garments

Philip Kunovski

Biomedical Engineering

University of Reading

UK

Thesis submitted for the degree of Doctor of Philosophy

August 2020

Declaration

I confirm that this is my own work and the use of all material from other sources has been properly and fully acknowledged.

Philip Kunovski

Acknowledgements

I would like to express my sincere gratitude towards my supervisor Professor Simon Sherratt for his continuous support of my study, for his patience, motivation and knowledge. He helped me throughout the earliest exploratory stages of my research, all the way up to writing and submission of the thesis. I would have been surely lost without his guidance.

I further gratefully acknowledge the funding received, primarily from KYMIRA Ltd., who funded every aspect of the research and development; as well as from the University of Reading, whose Regional PhD Bursary contributed significantly towards tuition fees.

A warm thank you to all my peers for all their regular support, guidance and necessary distractions. A particular mention to Dr Russel Torah and Mahmoud Wagih from the University of Southampton for providing access to equipment and assisting in experiment set-up and recording. I would also like to acknowledge Tim Brownstone, founder and CEO of KYMIRA Ltd., for enabling me to pursue my research while also growing and running a successful business together.

I would especially like to give a heartfelt thank you to my wife, Monira, for the immense support received. Besides proof reading and helping me edit my thesis, she took great care of me and my health to ensure I could always be the best version of myself. Her patience, understanding and ability to sacrifice is like no other, and I am deeply grateful for her endless love and encouragement throughout my research.

Finally, a sincere thanks to my parents for their continuous support and encouragement in all my academic pursuits, and to my daughter, Mina, whose conception greatly motivated me to finally finish and submit this thesis.

Abstract

With the proliferation of wearable and garment-based electronics, there is growing need to develop suitable solutions to power these devices. Wireless power transfer is a prime candidate to achieve this as it does not require any physical wires or connections. However, research in this field has historically focused on creating solid and bulky coil resonators to facilitate wireless transfer of energy and these solutions do not translate well into textile applications.

The aim of this thesis was to demonstrate the technical and commercial viability of a novel textile printed resonator structure to enable wireless power transfer in smart garments. The solution needed to be light weight, easy and cost-effective to manufacture, and robust enough to withstand garment wash cycles all while maintaining the comfort and flexibility expected of everyday clothing. This research delved into how such textile resonators functioned and how they could be manufactured to achieve these requirements. Computer simulation tools employing finite element analysis were used to develop an accurate approach to modelling the proposed structures and refined models were constructed and tested in order to verify theoretical models. The results showed that the proposed approach was indeed viable for the target application. Furthermore, experiments demonstrated an incredibly versatile design approach, allowing for multiple resonant frequencies to exist within the same 2D structure predicated on the size, shape and number of geometric patterns in a design. Successfully demonstrating this novel approach has opened up a new avenue for wireless power transfer research, not only limited to textile surfaces and smart garments, but transferable to other applications due to its ease of construction and flexibility in operational parameter design.

Table of Contents

Acknowledgements	ii
Abstract	iii
List of Figures	vii
List of Tables	xix
List of Abbreviations	xx
Notations and Symbols	xxii
1 Introduction	1
1.1 Motivation	1
1.2 Commercial requirements	4
1.3 Methodology	5
1.4 Contributions	5
1.5 Organisation of Thesis	6
2 Literature Review	8
2.1 A Brief History of WPT	8
2.2 Fundamentals of WPT	9
2.2.1 Methods of WPT	9
2.2.2 Magnetic Induction vs. SCMR	11
2.2.3 Power Transfer Principles	16
2.2.4 Coupled Mode vs. Circuit Theory	19

2.2.5	S-Parameters and Impedance Matching	23
2.2.6	Frequency Splitting	25
2.3	Practical Considerations of Mid-Range WPT System	33
2.3.1	Compensation Topologies	34
2.3.2	Coil Design Principles	38
2.3.3	Metamaterials and WPT	46
2.3.4	System Architectures	52
2.4	Industry Standards and Safety	66
2.5	Concluding Remarks	75
3	The Resonator as a Textile	77
3.1	Application	77
3.2	A New Type of Resonator	79
4	Design and Development	84
4.1	Yarn-level Design	84
4.2	Surface-level Design	86
5	Discussion of Experimental Approach	93
5.1	Modelling Magnetic Fields	93
5.1.1	Interpreting Maxwell’s Equations	93
5.1.2	The Finite-Element Method	95
5.2	Simulation Tools and Verification	96
5.3	Modelling Insights for Solid Geometries	99
6	Design and Construction of a Textile-based WPT System	111
6.1	Simulation Results and Insights	111
6.1.1	Setting up the Simulation	111
6.1.2	Observations with Self-Driven Geometries	115
6.1.3	Observations under WPT Conditions	126
6.2	Notes on Manufacturing the Resonator Design	130
6.3	Designing a Suitable Transmitter and Test Rig	132
6.3.1	Class E Inverter Analysis	133

6.3.2	Class EF Inverter Analysis	136
6.3.3	Constant Current Class EF Analysis and Implementation	139
7	Printed Resonant Structure Experiments and Results	147
7.1	Experiment set-up	147
7.2	Observations of Singular Geometries	148
7.3	Observations of Coupled Resonator Structures	150
7.3.1	Implementation	154
8	Future Work	160
9	Conclusions	164
	References	166
	Appendices	182
A	Mathematical Derivations for Class E Inverter	182
B	Mathematical Derivations for Class EF Inverter	188
C	MATLAB code for Class E and Class EF Waveforms	196
D	Analytical derivations and MATLAB code for a varying load in a standard Class EF inverter	198
E	Mathematical Derivation and MATLAB code for a Constant Output Current Class EF Inverter	204
F	Schematic, Layout and Embedded Code for Class EF boards	211
G	Analysis and Supplementary Figures of a Constant Output Current Class EF Inverter Implementation	213

List of Figures

2.1	2-coil system with series-series capacitor compensation.	12
2.2	System able to cope with obstructions to line-of-sight [2].	13
2.3	Plot of power transfer efficiency η a) vs normalised distances d/r for different Q -factors [29] and b) vs Q -factors for different coupling coefficients κ [30].	15
2.4	Plot of Energy Efficiency and Output Power with respect to R_L/R_S [32].	17
2.5	Wireless domino-resonator system powering a 14 W fluorescent bulb [41].	19
2.6	a) Coupled WTP system with identical transmitter and receiver, and b) the equivalent impedance as seen from the Primary and Secondary circuits [46].	22
2.7	2-port network S-parameter representation of a WTP system [50].	23
2.8	Plot of S_{21} as a function of κ and operating frequency [14].	27
2.9	Plot of a) Efficiency vs Frequency, and b) Normalised Power vs Frequency [61].	27
2.10	Plots for power transfer efficiency comparing a fixed driving frequency vs an automatic frequency tuning system as a function of a) the distance between the transmitter and receiver system and b) the angle between the transmitter and receiver system where an angle of 0 degrees corresponds to the coils facing each other, while 90 degrees corresponds to the receiver perpendicular to the transmitter [14].	29
2.11	Plot of power transfer efficiency vs distance for: case 1) fixed frequency and adaptive impedance and case 2) adaptive frequency and fixed impedance [67].	30

2.12 a) Proposed receiver side switching convertor, and b) effective impedance seen on the transmitter side as a function of duty cycle [68].	30
2.13 Plots of S_{21} with respect to frequency and distance for different radii (r_x) and coil turns (n_x) of transmitter coils (1) and receiver coil (2) [65].	31
2.14 S_{21} as functions of frequency and coupling, (a) with one-turn coil, (b) eight-turn coil, (c) three-turn coil, and (d) across varying coil inductances in the basic four-coil WPT system with DS of 0.3 between the resonant coils [70].	32
2.15 Plots for Power transfer efficiency η vs frequency for different coil resistances and separation [72].	32
2.16 Plots for a) Normalised Power out and Efficiency vs Coupling and b) Normalised Power output vs Normalised frequency. In each Plot, A) is well below κ_c thus a low power output, B) is at κ_c thus achieving maximum theoretical power, C) is beyond κ_c where peak power decreases, D) has been defined as κ_b , where the frequency bifurcation is now pronounced, and E,F,G) are points where constant power and efficiency can be achieved [74].	33
2.17 Far-field emission gain characters showing (a) frequency and (b) angle [75].	33
2.18 Capacitor circuit topologies: (a) SS, (b) SP, (c) PS, (d) PP [48].	35
2.19 Circuit models for a) Combined SS and PP, b) SS only, c) PP only and d) uncompensated system [84].	38
2.20 a) Open-End and b) Short-End Model.	39
2.21 Circuit models for a) a typical inductive WPT system without resonance, b) a WPT system operating at resonance, and c) a WPT system employing intermediary Open-End coils, as well as d) the voltage gain vs frequency plot for the systems a), b), c) [86].	40
2.22 Open- and short-end a) cylindrical system [89] and b) flat spiral system [14]; c) square coil WPT system [90]; d) proposed spiral winding pattern in a single loop structure [34]; e) top view of flat square coil [91]; and f) a bowl-shaped spiral Tx coil with different sized flat spiral Rx coil [92] .	42

2.23	Plot for efficiency vs coil separation distance for different coil radii. . . .	43
2.24	Simulation results of a) ferrite core resonator, and b) its Magnetic field distribution [87].	44
2.25	Simulation of Magnetic field strength vs coil position for a) a traditional spiral coil structure, and b) proposed coil structure. The numbered positioned 1-5 give a measurement of distance from the coil, which is 0.5mm, 0.6mm, 0.7mm, 0.8mm, 0.9mm respectively [101].	45
2.26	Electromagnetic wave propagation from air into a medium with negative ϵ and μ illustrating (a) refraction in the opposite direction, (b) beam spreading translation, (c) beam refocusing, and (d) Plane-to-Point source intensity redistribution [108].	46
2.27	a) A near-infrared array energy harvester using copper split square rings and a copper micro-strip collector [115], b) a metamaterial formed by etched-copper SRRs on standard FR4 circuit board [120], c) an exploded view of a double slit ring metasurface incorporating a ground plane and energy harvesting feeds (cooper), separated by Rogers RT6006 (blue) and RT6002 (red) [116], and d) a metamaterial rectifying surface as part of a larger radio frequency energy harvesting metasurface formed of copper top pattern, ground plane and rectifier, separated by multiple layers of Rogers RO4450F bondplys [117].	48
2.28	a) Schematic of a cell and the effective permeability of that cell with different frequencies, b) the curves of the cell's effective permeability with varying frequency (solid line) as well as the equivalent-circuit RLC resonant frequency (dotted line) for reference [121].	49
2.29	WPT system to power a 40 W lightbulb (a) without the metamaterial slab, (b) with the 3D metamaterial slab, (c) with a planar metamaterial slab, and (d) the recorded transmission efficiency of each system respectively [125].	49

2.30	a) a hybrid metamaterial slab with different negative μ at the edges and zero μ at the centre (left), and b) a comparison of system performance without the metamaterial slab (top), with a traditional uniform μ metamaterial slab (middle), and the proposed hybrid μ metamaterial slab (bottom) [126].	50
2.31	Simulation shows a) the field strength for a single dipole, b) how the field could be radially expanded by the use of the proposed shell, and c) how the field could be focused by another separated shell. Considering d) two dipoles, the simulation shows how the ratio of the inner and outer radii of the shell could be changed to e) confirm the field and f) expand the field in free space [128].	51
2.32	Simulation of WPT system a) using air only, b) using the metamaterial as theorised in [104], and c) using the Open-End self-resonant coil as in [130].	52
2.33	Comparison of system efficiencies of a 2- and 3-coil system under different loading conditions when the source resistance is a) 2 ohms and b) 50 ohms.	53
2.34	Comparison of the electromagnetic field strength of 2- and 3-coil systems during normal alignment (top) and during misalignment (bottom). . . .	54
2.35	a) System employing third intermediary coil for a standard 2-coil system and b) power transfer efficiency vs load resistance as reported in [136]. .	55
2.36	4-coil system representation showing the extra mutual coupling present between the individual coils [89]	56
2.37	Power transfer efficiency vs transmission distance comparison between equivalent 4-coil and 2-coil systems [140]	56
2.38	Conformal SCMR system whereby the transmitting (Tx) and receiving (Rx) coils are in the same place as the source and load coils [145]. . . .	57
2.39	Efficiency vs transmission distance for a conformal SCMR system. Plot compares the efficiency achieved through a fixed transmitting coil and varying driving coil turns. The (<i>cermaics</i>) and (<i>mica</i>) refer to the capacitor dielectric used [71]	58

2.40	Efficiency vs transmission area simulation for a 4-coil system using four flat transmitting resonators driven by a single loop source antenna [148].	59
2.41	a) 6-coil SCMR system diagram and b) simulated and measured power ratio vs operating frequency [150].	60
2.42	a) Proposed orthogonal multi-coil SCMR system and b) efficiency vs angular misalignment of the proposed system [155]	60
2.43	Efficiency vs transmission distance with various C_P and C_S configurations [156].	61
2.44	Efficiency vs phase angle between current and voltage waveforms in the transmitter and receiver respectively [158].	62
2.45	a) Proposed system diagram [164] and b) theoretical operation under principle of superposition of current waves [164].	63
2.46	a) Simulating schematic for the WPT system proposed in [172] incorporating the impedance converter network $N1$ and $N2$ and plots for b) system efficiency and c) transferred power vs load resistance [172]	66
2.47	a) Example of proposed system deployed on a motorway and b) diagram showing proposed system operation [173].	67
2.48	Plot of Efficiency vs Load current for both Qi and $Rezencc$ standards, either through direct power or Battery charge-cycle (BCC) [179]. The drop in efficiency observed between the direct power and BCC approach occurs as more energy is consumed simply to charge the battery beyond 90%. Thus, this energy does not reach the load circuitry, resulting in a loss of effective transmitter to receiver efficiency.	69
2.49	Plots of reference levels for exposure to time varying a) electric fields and b) magnetic fields [183]	70
2.50	Spatial plots showing dominant field component for a) Open-End and b) Short-End coils [186]. Positive ζ shows the electric field is dominant while a negative ζ shows that the magnetic field is dominant.	72
2.51	Plots of quality factor vs frequency for a) coil in muscle tissue and coil inside an airbox in muscle tissue, and b) comparison of quality factors with different airbox sizes [194]	74

2.52	Plots of efficiency vs a) transmission distance and b) angular misalignment angle for both simulated and measured effects of a wearable WPT system vs a free space WPT system [145]	75
3.1	Hypothetical environments where WPT could be employed: a) a military scenario to charge body worn soldier equipment [197]; b) a factory floor charging various equipment and individuals [198]; c) a remote health monitoring suite to charge an implanted device [199]; and d) an eventual home setting, to charge consumer electronics [200].	78
3.2	Different textile coil implementations, a) early implementation of a stitched on coil structure [201], b) sewn-on insulated conductor using copper fibres, c) printed coil using silver-polymer ink on a printed interface layer, d) square coil using Light Stitches conductive thread and e) circular coil using PTFE standard wire [202].	80
3.3	Stacked C-shaped conductor layers and ring-shaped dielectric layers and their equivalent RLC resonant circuit [205].	82
4.1	a) Cross-section of cylindrical resonant yarn, with overlapping conductive elements (18a), separated by a dielectric insulating layer (18d), wrapped around a polymer yarn (17); b) and isotropic and top view of a flat-substrate (17b), with insulated and overlapping conductive elements (18b and 18c) applied on one substrate face; and c) a cross-section of cylindrical resonant yarn as in a), however employing a material-loaded polymer (24), comprising in this case of ferrite particles (24a).	85
4.2	(a) Standard helical coil and (b) a surface pattern of a repeated geometries made up of layers of printed conductive and dielectric elements	87
4.3	Drawings of the three resonator element designs, namely a) C-type, b) O-type and c) W-type.	87
4.4	Example resonator structure models, named accordingly. Note, solid lines indicate foreground elements and dashed lines indicate background elements.	88

4.5	Arrow plots for the surface current density for a 40 mm element diameter O(6×6) resonator design at the first six resonant modes.	89
4.6	3D magnetic field line plots for a 40 mm element diameter O(6×6) resonator design at the first two resonant modes.	90
4.7	Example transverse modes from waveguide theory to compare to current loops illustrated in Figure 4.5.	90
4.8	Spectra plots of $\Re(Z_{in})$ showing the SR modes and dominant frequency mode for a selection of self-driven models.	92
5.1	An example coil used for verification testing with a simple helical morphology	97
5.2	Plots for a simple coil, modelled as a 2D axi-symmetric geometry, with a current flowing from top to bottom showing a) the electric field (in Volts) and b) the magnetic field generated (in Tesla).	98
5.3	3D plots for various coil arrangements showing: a) top view of a driven coil (left), an intermediate coil (middle) and single loop-load coil (right) separated by 30 cm with the associated magnetic fields overlaid; b) top view of a driven coil (left), an intermediate coil (middle) and single-loop load coil (right) separated by 15 cm overlaying the average power flow; c) isometric view of a driven coil (left) and load coil (right) both straddling a soft ferrite cylinder with associated magnetic field overlaid; and d) a 1D plot of the real part of a single coil impedance, through which the unloaded Q -factor can be calculated.	100
5.4	Various coil models for 2-, 3- and 4-coil simulations, including (a, f) helical and (b, c) spiral coils; segmentation coils (d) with ferrite and (e) without ferrite; and (f) a helical coil with dielectric between the loops. .	101

5.5	Three models (one per row), showing the 3D model of an identical coil set up with (a) no ferrite, (d) a ferrite enclosing sphere (<i>part hidden of clarity</i>), and (g) ferrite backplates; along with their respective plots for the magnetic flux density logarithmically scaled and colour matched between images (b), (e) and (h); and streamline plots of the magnetic field along the same view, colour matched between images (c), (f), and (i).	104
5.6	S_{21} vs frequency plots for (a) 5-section and (b) 10-section stacked segmented coil with source and load ports between the first and the last layers; S_{21} vs frequency plots for a 10-section stacked segmented coil with the load port (c) 6 stacks and (d) 8 stacks down from the source port.	106
5.7	3D models where transmission gain is just over 60% (left) with associated gain contour plots vs separation distance and frequency (right): (a, b) 3-coil helical, (c, d) 4-coil helical, (e, f) 4-coil spiral with parallel driving/load coils and (g,h) 4-coil spiral with coplanar loop and resonant coils WPT systems.	107
5.8	Gain contour plots across separation distance and frequency for a 4-coil spiral with coplanar resonant coils of 10 cm diameter and loop coils of (a) 8 cm, (b) 5.4 cm, (c) 4 cm (<i>note the change in contour scale</i>) and (d) 3 cm (<i>note the change in contour scale</i>) diameters; and DS line plots for (e) S_{21} vs frequency and (f) transmission link efficiency vs frequency for a 4-coil spiral with coplanar resonant coils of 10 cm diameter and loop coils of 4 diameter.	109
6.1	C(8×1) models used to test a number of different port connection configurations. Models a) and b) use parallel connected ports on the first and forth coil position respectively, whereas models c), d) and f) use series connected ports as gap feeds.	112

6.2	a), b), c) $\Re(Z_{in})$ and d), e) $ I_x $ vs frequency plots for C(8×1) models used to test a number of different port connection configurations, whereby in d) the colours refer to the following port in d) pink: 1 and 8, yellow: 2 and 7, black: 3 and 6, Blue, 4 and 5; and in e) blue: 1 and 8, red: 2 and 7, purple: 3 and 6, yellow: 4 and 5.	113
6.3	Arrow plots of the Poynting vector a) front on view, b) top view and a c) magnetic field line plot for a C(2×2) model.	116
6.4	Plot of Q -factor vs number of elements for the first SR mode in C- (<i>black</i>), O- (<i>blue</i>) and W- (<i>red</i>) type.	118
6.5	$\Re(Z_{in})$ and $\Im(Z_{in})$ plots for models as indicated, showing the characteristic dominant mode and SR modes.	119
6.6	$Re(Z)$ vs frequency plots showing the SR Modes for the indicated models.120	
6.7	Frequency vs increasing elements for C- (<i>blue</i>), O- (<i>black</i>) and W- (<i>red</i>) type models following the best fit curve.	120
6.8	a) Dominant mode frequency and b) SR Mode frequency vs increasing element density for C-type models following the best fit curve.	122
6.9	Illustration of stacked structure showing individual sections separated by a dielectric layer	123
6.10	Plot for number of sections vs frequency for C(6×6) (<i>blue</i>), C(4×4) (<i>red</i>) and W(3×2) (<i>black</i>) following a best fit curve of the form $Ax^b + C$	123
6.12	Plot of Q -factor vs number of elements for the different thicknesses of the examined C-type elements. These were 12 (<i>black</i>), 24 (<i>blue</i>), 48 (<i>green</i>), 72 (<i>red</i>) and 96 (<i>cyan</i>) microns.	125
6.11	Plot of \sqrt{t} vs f for variations in C(2×2) (<i>blue</i>), C(4×4) (<i>green</i>), C(6×6) (<i>red</i>), C(8×8) (<i>black</i>) models.	125
6.13	4-coil WPT set up with a) single loop drive and load coils, and b) duplicate resonant drive and load structures.	129
6.14	An example planar resonator with three stacked arrays of electrically conductive elements separated from one another by layers of dielectric material.	130

6.15	Several examples of constructed resonator patterns built up onto a heat-transfer vinyl.	132
6.16	a) Manual heat press used to apply a temperature of 160°C at roughly 6 Bar for 12 seconds, b) patterns printed onto a black polyester fabric, and c) demonstration of a resonant structure’s textile like property. . . .	133
6.17	A typical Class E inverter circuit	134
6.18	Waveform plots for $V_D(\omega t)$, $I_D(\omega t)$, $I_{C_1}(\omega t)$ and $I_o(\omega t)$ normalised with respect to I_i and V_i	136
6.19	A Class EF inverter circuit	137
6.20	Waveform plots for $V_D(\omega t)$, $I_D(\omega t)$, $I_{C_2}(\omega t)$ and $I_o(\omega t)$ normalised with respect to I_i and V_i , with $k = 0.867$, $D = 0.375$ and $q1 = 2$	139
6.21	Waveform plots for $V_D(\omega t)$, $I_D(\omega t)$, $I_{C_2}(\omega t)$ and $I_o(\omega t)$ normalised with respect to I_i and V_i , for $k = 0.867$, $D = 0.375$ and $q1 = 2$, as R_L changes from $0.75 * R_L$ (Blue) to R_L (Black) to $0.75 * R_L$ (Orange).	140
6.22	Waveform plots for $V_D(\omega t)$, $X_c I_D(\omega t)$, and $X_c I_o(\omega t)$ normalised with respect to V_i , for $k = 1.3296$, $D = 0.3$ and $q1 = 1.67$, as ρ changes from 1.5 (Blue) to 3 (Black) to 5 (Orange).	142
6.23	(a) Transmitter prototype, including DC power source and oscilloscope, and (b) top view of the signal generator (left), Class EF board (middle) and test transmitting coil L_3 (right).	144
6.24	(a) Transmitting and receiving coils brought close to demonstrate tight coupling and associated (b) oscilloscope traces: voltage across MOSFET V_D (50V/div - red); voltage across $1 \Omega R_L$ (1V/div - magenta); current through $1 \Omega R_L$ (1A/div - green); and (c) thermal captures of the board after 1 hour operation with surface temperature reading of the MOSFET (left) and L_1 (right).	145
6.25	(a) 3D render and (b) photo of a fabricated Class EF board.	146
7.1	a) A Rohde & Schwarz ZVB4 2-port VNA used throughout experiments, and b) schematic for driving a pair of transmission lines in differential mode [230].	148

7.2	Plots of $\Re(Z_{in})$: differential measured (blue) vs differential simulation (black). Note, simulated spectrum in (b) was calculated using the newly calculated relative permeability ϵ of 2.73.	149
7.3	Plots of $\Re(Z_{in})$: non-differential measured (green) vs differential measured (blue) vs differential simulation (black).	151
7.4	a) L-matching circuit schematic and b) example of two constructed SMA probe attachments.	151
7.5	Plots of $ S_{11} $ (green) and $ S_{21} $ (blue) for a selection of coupled SR modes.	153
7.6	Thermal image capturing resistive heating across a WPT system, and demonstrating the vast majority of the power remaining within feed cable. Note, the colour spectral range was around 10-20°C with areas at the top of the range in red (28.5 C), and areas at the bottom range in blue (21.0 C).	155
7.7	Example test implementations, showing the fabric printed resonators, transmitting power to a 50 Ω load, plotting the received current and voltage on an oscilloscope.	156
7.8	Thermal images capturing resistive heating from resonant structures, showing a) temperature increase after 300 seconds of operation on a W(3×2) design, b) distribution of current in a O(4×4) design, and confirmation of different current loops that form on a W(3×2) design at c) 148 MHz, and d) 256 MHz. Note, the colour spectral range shows areas at the top of the range in red (28.5 C), and areas at the bottom range in blue (21.0 C).	158
A.1	A Class E inverter circuit	182
B.1	A Class EF inverter circuit	188
F.1	(a) Schematic of the Class EF Inverter and receiving side circuitry, (b) Board layout, and (c) Etched layout on a single layer Aluminium Board	211
F.2	(a) Schematic of the Class EF Inverter and receiving side circuitry, (b) Board layout highlighting the Top Layer, and (c) Board layout highlighting the Bottom Layer.	212

G.1	Oscilloscope traces at no load R_L for (a) the drive signal from Arduino at 1 Mhz f_s and 30% D (5V/div); (b) the voltage across the MOSFET V_D (50V/div - red) and the input current I_i (0.2V/div - green); (c) a close-up of the voltage across the MOSFET V_D (50V/div - red) and the Output current I_o (1A/div - green); and (d) thermal images of Class EF circuit board after 30 minutes operation without the cooling fan (left) and with the cooling fan (right).	214
G.2	Oscilloscope traces of the the voltage across the MOSFET V_D (50V/div) as a resonant receiver approaches the transmitting coil L_3 from (a) 6cm through to (d) a few mm.	215
G.3	Oscilloscope traces of the voltage across the MOSFET V_D (50V/div - red); voltage across the load R_L (1V/div - magenta) and current through the load R_L (1A/div - green) when the Load on the receiver is (a) 8.2Ω (b) 1Ω (c) 0.1Ω , separated by the same distance away from the transmitting coil L_3	215
G.4	Bench top images of the WPT system, illustrating power transfer through a high-power LED when (a) no power is transmitted, (b) some power is transmitted to dim the LED and (c) sufficient power is transferred to fully switch on the LED.	216

List of Tables

2.1	Comparing the four main compensation topologies across key WPT requirements	38
2.2	RF Exposure limits set for general public (100 kHz - 10 MHz)	71
2.3	Comparison of different WPT systems for output power of 467mW [193]	73
5.1	Properties observed with changing dielectric constant and distance with respect to the coil	102
5.2	Properties observed with changing scale	110
6.1	Properties observed with increasing number of elements	118
6.2	Properties observed with increasing number elements density	121
6.3	Properties observed with increasing number of sections	122
6.4	Properties observed with increasing layer thickness	124
6.5	Wireless Transfer Efficiencies for select models	127
6.6	Component Values of a 1 MHz Constant Current Class EF Inverter . . .	143
7.1	Component values calculated for desired matching networks	152
7.2	Measured S-parameters and calculated power transfer efficiency η for coupled modes	152
7.3	P_o from measured V_{rms} , I_{rms} and ϕ at a separation DS	157

List of Abbreviations

Abbrev.	Meaning
A4WP	Alliance for Wireless Power
AC	Alternating Current
BC	Boundary Condition
CMT	Coupled Mode Theory
CT	Circuit Theory
DC	Direct current
DS	Distance-to-Size Ratio
EM	Electromagnetic
EMF	Electromagnetic Field
EMI	Electromagnetic Interference
ESR	Equivalent Series Resistance
E-Textile	Electronic Textile
FCC	Federal Communications Commission
FEM	Finite-Element Method
FGMRES	Flexible Generalized Minimal Residual
IBC	Impedance Boundary Condition
ICES	IEEE International Committee on Electromagnetic Safety
ICNIRP	International Commission on Non-Ionizing Radiation Protection
MEE	Maximum Energy Efficiency
MFS	Magnetic Field Shaping

Abbrev.	Meaning
MIT	Massachusetts Institute of Technology
MoM	Method of Moments
MOSFET	Metal Oxide Semiconductor Field Effect Transistor
MPT	Maximum Power Transfer
PCT	Patent Cooperation Treaty
PEC-BC	Perfect Electric Conductor Boundary Condition
PMA	Power Matters Alliance
PP	Parallel-Parallel
PS	Parallel-Series
PTFE	Polytetrafluoroethylene
RAM	Random Access Memory
RFID	Radio-Frequency Identification
SAR	Specific Absorption Rate
SCMR	Strongly Coupled Magnetic Resonance
SP	Series-Parallel
S- Parameter	Scattering Parameter
SPS	Series-Parallel-Series
SR	Semi-resonance/resonant
SRR	Split Ring Resonators
SS	Series-Series
TBC	Transition Boundary Condition
VNA	Vector Network Analyser
WPC	Wireless Power Consortium
WPT	Wireless Power Transfer
ZCS	Zero-Current Switching
ZVDS	Zero-Voltage Derivative Switching
ZVS	Zero-Voltage Switching

Notations and Symbols

Symbol	Meaning
C_x	Capacitance of component x
L_x	Inductance of component x
X_x	Reactance of component x
R_x	Resistance of component x
Z_x	Impedance of component x
V_x	Voltage across component x
I_x	Current through component x
P_x	Power in component x
$\Re(x)$	Real component of x
$\Im(x)$	Imaginary component of x
r	radius
d	separation distance
\mathbf{B}	Magnetic Flux Density Vector
\mathbf{A}	Magnetic Vector Potential
\mathbf{H}	Magnetic Field Strength Vector
K	Coupling factor (Coupled Mode Theory)
κ	Coupling factor (Circuit Theory)
K_c/κ_c	Critical Coupling Point
$M_{x1,x2}$	Mutual coupling between components $x1$ and $x2$

Symbol	Meaning
Γ	Decay (Coupled Mode Theory) or Loss (Circuit Theory)
Q	Quality Factor (Circuit Theory)
Q_L	Loaded Quality Factor
Q_U	Unloaded Quality Factor
η	Transmission Efficiency
η_{max}	Maximum Transmission Efficiency
f	Frequency
ω	Angular Frequency
ω_0	Fundamental Resonant Frequency
λ	Wavelength
D	Duty Cycle
S_{21}	Forward Gain in S-parameters
S_{11}	Reflection Coefficient in S-parameters
μ	Permeability
$\mu(\omega)$	Frequency dependant Permeability
ϵ	Permittivity
$\epsilon(\omega)$	Frequency dependant Permittivity
σ	Conductivity

Chapter 1

Introduction

Electronic textiles, or *e-textiles* are anticipated to be the next paradigm in personal electronic devices. With that, new challenges in the design, manufacture, and integration of traditional technologies emerge. The electronics industry is quickly adapting to these new requirements, fully aware of the enormous commercial potential that lies before them.

KYMIRA Ltd., a smart garment company and relatively new player in this field, is currently developing the manufacturing methods to produce such e-textile solutions at commercial scale. They are the corporate sponsors of this thesis, whereby a new type of textile-printed electromagnetic resonator structure is proposed seeking to challenge the traditional idea of coil resonators for wireless power transfer (WPT).

The viability of such an approach is explored in this thesis from a technical, commercial, and end-user perspective within e-textile charging applications comparing the proposed system's performance and operation to existing and pervading resonator designs.

1.1 Motivation

Traditional methods of printed circuit board production are starting to give way to novel additive manufacturing techniques, using silver inks and conductive adhesives rather than etched copper tracks and solder. Box-shaped, rigid and bulky electronic devices are being replaced by conformal, flexible, and miniature systems. Moreover, the use of

long cables terminated with cumbersome connectors are being phased out from most consumer devices. These changes have been driven predominantly by the smartphone and tablet industries, offering ever more portability and user-friendliness in a more concise, sustainable, and cost-effective manner [1]. These new innovations have allowed the concept of body worn electronics, and particularly smart garments, to enter into the realm of possibility for product designers. Already there are commercial products entering the market with some form of biomonitoring, as such Hexoskin, Catapult, Athos, Firstbeat, and Xsens. This enables some form of rudimentary analysis, mostly targeting the sports or wellness markets. Although these are exciting developments, they are only the earliest examples of what may come in the next few years.

The apparel industry servicing professional sports, healthcare telemonitoring, security, and defence, as well as personal protective equipment, will experience drastic changes with the advent of cost-effective e-textile solutions. Within this new wave of innovation and product development, practical challenges have started to emerge, particularly in the powering and recharging of future devices. Well-established electrochemical batteries found in most of today's laptops, smartphones and more recently, vehicles, are excellent high-energy-density storage devices, but could inevitably prove unsuitable for fully integrated e-textiles. Besides inherent degradation with increasing charging cycles, the need to either detach from clothing or face the challenges of washability quickly discourages their use for any competitive product.

While capacitive yarns and printed flexible batteries are active areas of research promising increasingly better energy storage densities, they are still far from being able to even match electrochemical batteries in terms of energy storage density. On the other hand, coupling these technologies with some form of seamless power generation and/or recharging does in fact make them a viable energy storage solution, and herein lies the key motivation for this thesis.

WPT and in particular the application of near-field magnetic induction is a reliable method of delivering a substantial amount of power without the need to physically tether devices to power sources. Some would argue that charging pads and surfaces, while convenient, still impose strict limits on portability; however, a growing field of research, focusing on mid-range power transfer through Strongly Coupled Magnetic

Resonance (SCMR) [2], has demonstrated that even across several meters significant power transmission can be achieved safely and conveniently. Moreover, recent advancements in semiconductor technologies have enabled energy efficient switching necessary to achieve the frequencies used in power transmission. With the growing need for such a solution, mid-range WPT is poised to become a new standard in charging portable systems from smartphones and smart garments to flying drones and electric vehicles.

Since its popularisation by MIT researchers in 2007 [2], SCMR as a means of delivering useful power at a distance has received much attention. It has quickly become a broad topic, rooted in the general physics of electromagnetic fields, but focused predominantly on electronic system design principles and different coil architectures in order to achieve the precise conditions necessary for practical SCMR. While the fundamentals for this type of mid-range power transfer have become well-established, there are still open questions surrounding practical implementation.

Many key works have successfully demonstrated aspects of this technology's capability, but they have cautiously achieved this with devices of an impractical size for human wearable applications. Moreover, many recent works have focused too heavily on achieving quite generic marginal gains in both transmission power and distance, often at the cost of practicality of implementation in real-world scenarios (for example, see work by Melki and Moslem in section 2.3.2 on differences between pairs of coil radii).

As it is often the case, the application dictates the approach required, and so far, there has been little work around this method of power delivery within e-textiles. Although there have been efforts whereby wire or conductive yarn has been stitched into rudimentary coil shapes directly onto a textile surface to showcase possibilities (as explored in section 3.2), one can hardly call this a deep exploration into textile-based resonant structures.

Given the increase in smart garment products entering the market, the real and practical implementation of mid-range power transfer mitigated via e-textiles must now be considered, and this context helps set this work apart from many others. In fact, this thesis boldly diverges from the classical coil architectures typified by wireless

power research in favour of something more akin to metamaterials; a loosely related but distinct field of research in its own right. Taking inspiration from both areas of knowledge has enabled a new way of thinking about electronic resonators, with the aim of demonstrating a more versatile design approach tailored to the target application which can match and at times even surpass the performance of conventional solutions.

1.2 Commercial requirements

The proposed technical approach has been selected with professional sports and healthcare end-user requirements in mind, particularly,

- creating an inexpensive and discrete charging solution, minimising system maintenance;
- minimising adoption to a new technology, ensuring ease-of-use across many types of users;
- allowing for standard washability and product longevity, ensuring ease-of-deployment.

Achieving the above goals thus increases the chances of product success as users are much quicker to accept and adopt the solution.

Furthermore, enabling a solution that is easy to manufacture and does not require new or specialist equipment, opens up broader opportunities for cost savings, thus increasing potential profit margins for the supplier. The proposed resonator structure explored in this thesis takes into account the aforementioned factors with the aim of delivering a solution that,

- maximises wireless power delivery at variable distances, allowing a degree of user freedom;
- provides a discrete, 2D solution that exists only on the surface of the garment, without restricting fabric properties (i.e bendability, flexibility, washability, etc.);
- uses low quantities of material, thus is relatively inexpensive, as well as an ubiquitous production method employed in standard garment graphics printing

industries.

1.3 Methodology

Having proposed a new approach to electronic resonators, the aim of this thesis is to assess the real-world viability of this approach within a textile for the capture and transmission of WPT. Therefore, the main research activities undertaken were:

- Examining the frequency behaviour of different metamaterial inspired geometries to determine design strategies and effective ways to achieve a desired performance outcome.
- Implementing CAD optimised designs using up-to-date additive manufacturing techniques in order to realise the solution in a commercially relevant process and product.
- Exploring efficient power amplifier transmitter design with low switching losses to test the solution, as well as showcase recent advancements with the proposed design.

In order to perform the above tasks in a timely and cost-effective manner, physics simulation software was employed in the design stages of the resonator, followed by physical testing using screen printed techniques to compare results. The transmitter was designed using known amplifier principles, following an established circuit design approach, mathematical modelling with software, and eventual construction and benchtop functional testing.

1.4 Contributions

The main contributions of this work are as follows:

- A novel electromagnetic resonator structure comprised of segmented and overlapping elements, offering design and performance flexibility over standard resonator geometries.

- A yarn level design of the proposed resonator structure for wireless power and data transfer¹.
- A surface level design of the proposed resonator structure (or *planar* resonator) for wireless power and data transfer².
- A detailed examination and modelling of the multi-modal behaviour of these proposed planar resonator structures, aimed at WPT.
- A method of manufacturing the proposed planar structure for commercial production.
- An examination of a highly efficient transmitter design for the electronic resonator.

It is well worth noting that while the focus of this work has been towards applications involving garments, the principle behind these structures is transferable to any thin and/or flexible material surface or substrate including general textiles, such as upholstery, carpeting, and curtains, as well as building infrastructure, including walls, ceilings and flooring – thereby demonstrating the potential applicability of this work beyond its initial ideation.

1.5 Organisation of Thesis

This report is organised as follows: Chapter 2 discusses WPT, tracing its roots with a brief history of electromagnetism through to an examination of the fundamental principles and practical considerations of the state of the art. It covers different design approaches, popular system architectures and prominent works, concluding with some notes on industry standards and safety considerations. Chapter 3 is an introduction to the proposed novel resonator design, briefly touching on the expected application requirements. Chapter 4 delves into specific details with regards to the yarn-level and surface-level embodiments proposed for the new resonator concept unique to this work. Chapter 5 examines and validates the experimental approach

¹UK Patent GB2562548 (Status: Granted), PCT Application No. WO2019058123A1

²UK Patent GB1914854.3 (Status: Pending).

undertaken, as well as verifies the simulation tools employed using known models. Chapter 6 reports and discusses the behaviours and characteristics developed through simulations of the various resonator geometries in addition to detailing the selected manufacturing technique, before concluding on the development of the test rig for physical experiments. Chapter 7 reports on the physical testing and insights garnered, comparing the simulated and experimental results. Chapter 8 presents the scope for future research and finally, chapter 9 summarises the work presented in this thesis. The appendices thereafter give additional details on the transmitter side electronics development with related code for software modelling and signal generation.

Chapter 2

Literature Review

2.1 A Brief History of WPT

Since methods for WPT centre on electricity and magnetism, it is pertinent to begin any background discussion at the point where the unique relationship between these two phenomena was first observed.

In 1820, Hans Christian Ørsted [3] noticed that a compass needle was deflected when an electric current flowed in a nearby cable, thus confirming that electric currents create magnetic fields. He later published his findings [4] which showed that the magnetic field produced forms a circular pattern around a charge-carrying wire. This profound discovery inspired André-Marie Ampère to develop a mathematical model to understand this relationship [5]. During the next few years, Ampère's experiments demonstrated several important phenomena and led to his famous force law and circuital law. Through his works and publications, Ampère became a prominent figure in the establishment of this new science called electrodynamics, coined in his 1827 memoirs.

During a similar period, Michael Faraday [6] was also exploring electromagnetic properties of materials and discovered electromagnetism in 1831. With his experiments he demonstrated that an electromotive force could be induced in a conductor by a time-varying magnetic field. This phenomenon was modelled mathematically by James Clerk Maxwell [7], and in 1862, Maxwell incorporated Faraday and Ampère's works to formulate the classical theory of electromagnetic radiation [8]. This was the most

important achievement in the field so far. His equations elegantly unified the concepts of electricity, magnetism and light into one mathematical model. The conclusions drawn from his equations had profound implications throughout many emerging fields at the time, but of particular importance for WPT, his equations predicted the existence of electromagnetic waves forming from oscillating electric and magnetic fields. The theory also predicted that these electromagnetic waves could propagate with a speed approximating the then-known speed of light. This led Maxwell in 1865 to propose that light itself was indeed an electromagnetic wave [9].

Heinrich Rudolf Hertz [10] later confirmed the existence of electromagnetic radiation as predicted by Maxwell. He did this in 1888 by experimentally producing and receiving radio waves, to transmit electricity over a tiny air gap. In 1891, Nikola Tesla [11] conducted the first experiments exploring WPT, and over the next 10 years focused on developing ways to send power across great distances using microwave technology.

Though there were many pioneers during the early 20th century, it was Tesla himself who made the most profound impact to the field of WPT with his many notable experiments [12]. The rest of the 20th century saw tremendous technological achievements, many of which were underpinned by the knowledge and understanding that came from these early discoveries. The technology back then had advanced based on the needs at the time, and recently, due to the increased use of portable electronic devices, a new need for mid-range WPT has emerged.

2.2 Fundamentals of WPT

In order to effectively tackle the challenges of the future, there is a need to understand the physical laws that govern WPT. This section presents these principles in relation to current literature and establishes the rationale behind this thesis.

2.2.1 Methods of WPT

WPT can be generally classified as far-field or near-field transmission based on the dominant mode of energy transfer.

In far-field or *radiative* transmission, energy propagates outward from an electrical

source in the form of electromagnetic waves. Typical systems normally operate at microwave frequencies and could have transfer distances spanning many kilometres, given a direct line-of-sight between the transmitter and receiver. These systems have long been used for communications and broadcast applications; however, they suffer from poor transmission efficiency as power density decreases with distance r by a factor of $1/r$, as r tends towards infinity [13]. The transmission efficiency can be increased significantly if the system is made more directional [14], usually achieved by focusing the propagating waves into narrower beams. In fact, the use of focused microwave beams to effectively transfer energy between two distant points was proposed as early as 1964 by Brown [15]. During this period, the idea of microwave beaming sparked tremendous interest in the Solar-Power Satellite concept, proposing the capture of solar energy from satellites in orbit, which could effectively beam energy back to earth to be converted and used for electrical power. Today, research into this idea is still ongoing due to the clear benefits it could bring to humanity's growing energy needs. However, there are still enormous technical challenges to be overcome before this becomes a reality.

For consumer devices, the use of millimetre beaming (such as with *mmWave 5G wireless* [16]) for WPT poses a whole set of challenges: besides the obvious safety issues, in real-world scenarios devices would likely move unpredictably and, at times, be totally obscured from view of any transmitter. Transmission systems would therefore need to employ complex tracking systems which would only increase system costs without significantly improving reliability of supply.

In near-field transmission, energy does not primarily propagate in the form of electromagnetic waves; rather, it is spatially concentrated in the vicinity of the source (i.e. smaller than one wavelength), forming an *evanescent* field [17]. This field is the medium for energy transfer, which occurs through an electric and/or magnetic field produced at a source *coupling* to some nearby receiver. Within half a wavelength, this is mainly *non-radiative* transmission as energy is constantly being exchanged between the field and the source as charges oscillate [18]. Thus, unlike in far-field transmission, very little energy is actually radiated to the surroundings in the absence of a receiving conductor [2]. This makes the near-field more suitable for device applications whose receiver's position and presence in the vicinity of transmission may be unpredictable.

The transmission efficiency could theoretically be very high for this method of energy transfer when the distance r is only a few millimetres, but will tend to reduce drastically with increasing r as the power density within half a wavelength will drop off by a factor of $1/r^3$ [19] and by a factor of $1/r^2$ when the distance is greater than one wavelength [20].

The main challenges discussed in the literature are normally centred around ways to increase this transmission efficiency as well as effective transmission distance, both of which are crucial if any wireless power system is to be adopted as a viable commercial technology [21]. Other system considerations will become apparent over the course of this chapter; however, it is worth noting that the near-field method of using time-varying magnetic fields in order to transmit power is the focus of this work.

For a long time this method did not attract much attention due to the inherent weaknesses of magnetic induction for larger transmission distances. In 2007, this changed dramatically when Kurs *et al.* [22] re-introduced the potential use of this method through SCMR. There is some debate on whether this approach was truly novel: Tesla made use of magnetic resonance in many experiments dating as early as 1893 and the importance of High- Q coils for magnetic resonance was known as early as 1955 [23]. What is certain, however, is that this work radically changed the research focus for mid-range WPT. It is therefore appropriate to briefly identify the differences between the classical magnetic induction method and SCMR.

2.2.2 Magnetic Induction vs. SCMR

Consider the set up in Figure 2.1, where two identical coils are positioned a distance d away from one another. Each coil has an inductance $L_{1,2}$ and is connected to a series capacitor with capacitance $C_{1,2}$. $R_{1,2}$ represents the ohmic resistance in the real coils, R_S represents the internal resistance of a source V_S and R_L represents a simple load.

If one were to drive the primary coil with an oscillating current, this would give rise to an oscillating magnetic field \mathbf{B} , whose strength at every position r could be determined by applying Biot-Savart's Law as presented in equation (2.2.1),

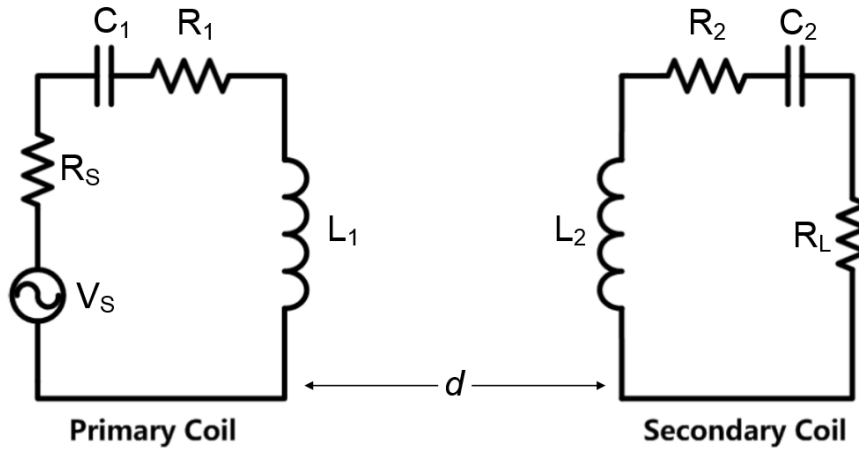


Figure 2.1: 2-coil system with series-series capacitor compensation.

$$\mathbf{B} = \frac{\mu_0}{4\pi} \oint \frac{\mathbf{I}d\mathbf{l} \times \mathbf{r}}{|\mathbf{r}|^3} \quad (2.2.1)$$

where μ_0 is the permeability of free space and $\mathbf{I}d\mathbf{l}$ is the current distribution in the primary coil. If the secondary coil is brought sufficiently close to the primary coil, then the oscillating magnetic field in the primary coil would induce an electromotive force in the secondary coil according to Faraday's Law, thus energy transfer would occur wirelessly.

In a typical non-resonant set-up, any practical energy transfer between these two coils could only take place at a very close range (several millimetres up to a few centimetres) and would likely make use of ferromagnetic cores. As with typical transformer set-ups, these cores would help confine and concentrate the magnetic fields produced in order to increase the efficiency and rate of energy transfer. These merits would decrease dramatically if coils are instead separated by air (due to its poor magnetic permeability) or with increasing physical separation d .

To counteract this weakness, Tesla introduced magnetic resonance and famously applied it to several of his experiments [23]. In a 1893 lecture [24], Tesla discussed the importance of creating the conditions for resonance in AC circuits by tuning the self-inductance of a coil with a series connected capacitor so that these reactive components would cancel each other out at a particular resonant frequency. The principle behind this thinking was to reduce the impedance in the coils, thus minimising significant losses

overall. Many of today’s technologies apply this principle still, however, operating at resonance alone does not ensure the high efficiencies nor high power transfer rates desired for practical mid-range WPT.

Kurs argued that operating in the *Strongly Coupled* region, for which resonance is a precondition, is what makes SCMR suitable for mid-range WPT and distinguishes it from short-range magnetic induction [2]. This region is a parameter space whereby resonant objects couple more strongly to one another, facilitating high power transfer rates [22]. By operating in this region, it is postulated that the WPT system becomes more independent to changes in relative coil orientations and alignment; that there is significantly reduced interference with non-resonating extraneous objects such as wood, metals or any other electronics; and furthermore, that there would be a very low coupling with the human body, thereby making these systems safer for future commercial use. Kurs had further shown that this method of WPT would be able to cope better with obstructions to line-of-sight, as shown in Figure 2.2.

In many works, coupled mode theory (CMT) is used to analyse the WPT system, and it has been identified that the condition for strong coupling is met when

$$\frac{K}{\sqrt{\Gamma_t \Gamma_r}} \gg 1 \quad (2.2.2)$$

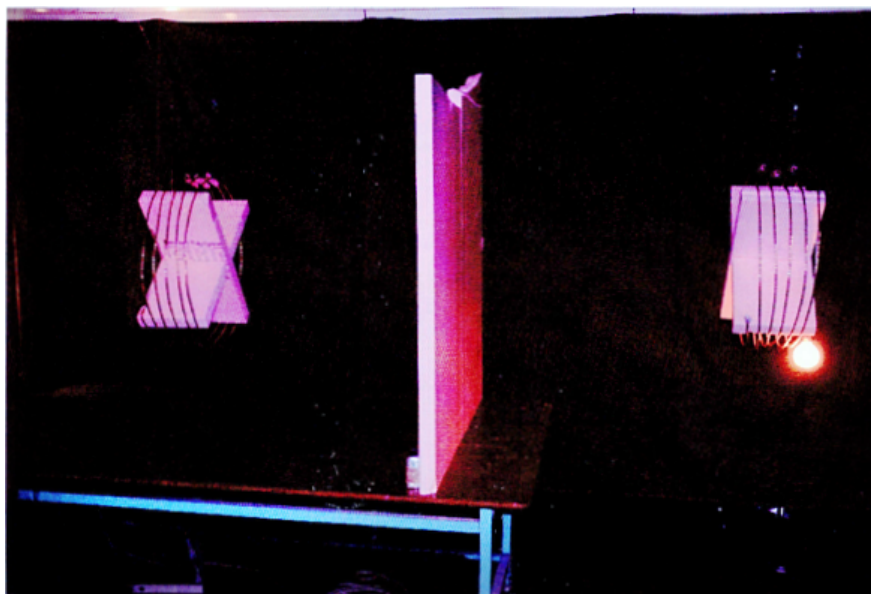


Figure 2.2: System able to cope with obstructions to line-of-sight [2].

where K is the coupling coefficient and $\Gamma_{t,r}$ are the intrinsic decay rates of the transmitting and receiving coils respectively. These decay rates encapsulate all losses suffered by the coils from absorption, radiation and heat dissipation [25]. What this ratio illustrates is that by minimising the energy loss per cycle in relation to the coupling coefficient, more energy can be transferred between the coils.

While CMT is suitable for describing the propagation of energy, it is not so familiar to electronic engineers [26]. It has been demonstrated by subsequent works that any SCMR WPT system can equally be represented by lumped values of R , L , C , and standard formulations from circuit theory (CT). The differences and similarities between the two are expanded further in Section 2.2.4, but for the remainder of this discussion the more intuitive CT will be used.

In CT, the expression in (2.2.2) is equivalent to

$$\kappa\sqrt{Q_t Q_r} \gg 1 \quad (2.2.3)$$

where κ is the coupling coefficient and $Q_{t,r}$ are the quality(Q)-factors of the transmitter and receiver coils respectively. The Q -factor is an important metric frequently used in microwave engineering as an indication of how much energy loss a device suffers per cycle as given by

$$Q = \omega \frac{\textit{Energy Stored}}{\textit{Energy Dissipated}} \quad (2.2.4)$$

Furthermore, it gives an indication of the system's bandwidth or the effective range of frequencies over which an external signal can be received. In typical RFID applications, the Q -factor is normally limited to around 10-20 in order to allow a broad enough channel to support high communication data transfer rates [27]. However, to realise the conditions of strong, or in other words, efficient coupling within mid-range WPT systems, coils would require a much higher Q -factor (typically in the 100s or 1000s) [21]. This is demonstrated by equation (2.2.5) where the maximum efficiency of a system η_{max} is given in terms of κ and the coil Q -factors.

$$\eta_{max} = \frac{\kappa^2 Q_t Q_r}{\left(1 + \sqrt{1 + \kappa^2 Q_t Q_r}\right)^2} \quad (2.2.5)$$

High Q -factors essentially counteract the sharp decline in the coupling co-efficient at increased distances, thereby maintaining a strong coupling between coils over a greater range [28]. Figure 2.3 aptly illustrates how power transfer efficiency dramatically changes with relative distance, coupling, and Q -factor.

Considering the system presented in Figure 2.1, the series RLC coils would have a Q -factor defined by

$$Q = \frac{1}{R} \sqrt{\frac{L}{C}} \quad (2.2.6)$$

At resonance, the reactances will equal one another, whereby

$$\omega L = \frac{1}{\omega C} \quad (2.2.7)$$

hence, the resonant frequency ω_0 is

$$\omega_0 = \frac{1}{\sqrt{LC}} \quad (2.2.8)$$

Substituting equation (2.2.8) into (2.2.6), the Q -factor becomes

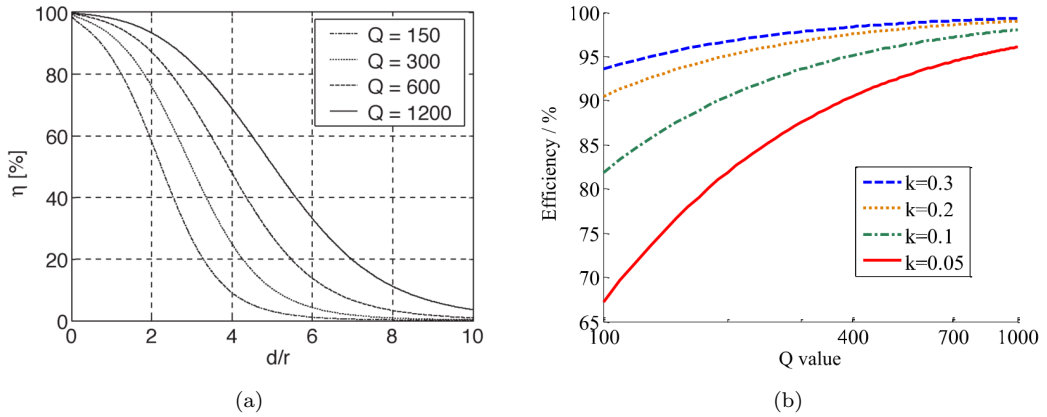


Figure 2.3: Plot of power transfer efficiency η a) vs normalised distances d/r for different Q -factors [29] and b) vs Q -factors for different coupling coefficients κ [30].

$$Q = \frac{\omega_0 L}{R} \quad (2.2.9)$$

It is apparent that to create high- Q coils, the resistance R and the inductance L must be decreased and increased respectively. This is practically achieved by a combination of different coil materials, thicker wires, increased coil windings, and a larger coil loop area. Clearly, these parameters will be highly constrained by the application and thus not always adaptable. Therefore, creating coils with higher resonant frequencies is the most suitable option, and this explains why typical operating frequencies for SCMR WPT systems are in the megahertz range (MHz).

Operating in the Strongly Coupled region by using high- Q coils is not without its challenges, and much of the literature over the last decade has attempted to address these challenges by analysing and constructing different system architectures, circuit topologies, coil designs and control systems in order to push the limits of what can be achieved in terms of transfer distance, power and efficiency. How these challenges arise will be explored in the following sections.

2.2.3 Power Transfer Principles

One of the first decisions to be taken in the design of WPT system is whether to aim for maximum possible power to the receiving load or to maintain maximum link efficiency. In this section, the principles of maximum power transfer (MPT) and maximum energy efficiency (MEE) will be briefly explored.

Maximum Power Transfer

MPT follows the concept of impedance matching in power electronics, whereby a source impedance is *matched* to a connected load impedance in order to facilitate maximum power transfer between the source and load. An analysis that elaborates on the mechanism of power propagation in this fashion can be found under *Circuit Theory* in Section 2.2.4.

Assuming a WPT with complex impedances, if the source impedance is $R_S + jX_S$ and the load impedance is $R_L + jX_L$, then maximum power will be delivered to the

load if $R_S = R_L$ and $X_S = -X_L$ [31]. This is another way of saying that the source and load impedances must be complex conjugates of one another in order to minimise reflections and maximise power transfer. At resonance, the reactances will cancel out and the power transfer efficiency η_τ will depend on just R_S and R_L ,

$$\eta_\tau = \frac{\text{Output Power}}{\text{Total Power}} = \frac{i^2 R_L}{i^2 R_S + i^2 R_L} = \frac{R_L}{R_S + R_L} \quad (2.2.10)$$

From equation (2.2.10) one can see the main limitation of the MPT principle: the maximum efficiency at $R_S = R_L$ has a theoretical limit of 50%. Plotting *Output Power* and η_τ against R_L/R_S , as shown in Figure 2.4, clearly illustrates this point.

Maximum Energy Efficiency

Unlike MPT, the MEE principle examines general design considerations to transmit power at the highest possible efficiency. The most common design choice is to select a power source with as low an impedance as possible in order to reduce the energy dissipation in R_S and transfer more energy overall to the load R_L .

Other significant system losses are attributed to the skin effect and the proximity effect [33]. The skin effect is a phenomenon whereby charge carriers in a conductor tend

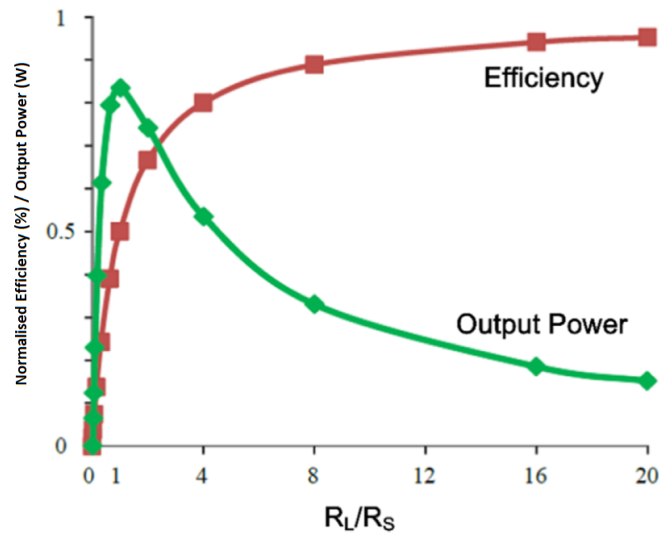


Figure 2.4: Plot of Energy Efficiency and Output Power with respect to R_L/R_S [32].

to concentrate towards the outer surface of the conductor as frequency increases. This variation in the current distribution effectively increases the ohmic losses in conductors at higher frequencies [34]. The proximity effect will occur most commonly in tight coil windings whereby alternating current flowing in one wire will induce eddy currents in adjacent wires (and vice versa) changing the current distribution of the overall current flow. As with the skin effect, this causes the effective resistance in the coil to increase [35]. It is difficult to calculate this overall resistance increase caused by these effects, although it is well-known (and often cited in the literature) that using Litz wire instead of solid conductors can significantly reduce these effects. It is worth noting, however, that using copper Litz wire alone would only increase the effective resistance caused by the proximity effect [36, 37]. Instead, the use of various layers of magnetoplated Litz wire has been proposed; the principle being that an alternating magnetic flux would flow more easily through these magnetic thin films, thereby increasing inductance and reducing the proximity effect induced resistance. In doing so, efficiency improvements of around 6% over copper Litz wire for a 1 W transmission at 13.56 MHz have been reported [37]. Nevertheless, reducing the operating frequency of the system may also be desirable for MEE, as not only does this naturally reduce skin and proximity effects, but it also minimises switching losses from voltage regulators and power amplifiers, commonly present in WPT system realisations [38].

Systems designed under the MEE principle would ultimately deliver lower system power transmission; however, it would be theoretically possible to achieve system efficiencies much greater than 50% [39]. The main restriction with these systems is that they require much closer transmission distances for successful operation [40]. One way researchers have attempted to counter this is by using high-Q coils in order to increase the coupling coefficient and extend transmission distances [23], or by using relay coils as illustrated in Figure 2.5 [41].

Both MEE and MPT aptly demonstrate the usual dilemma researchers and engineers are faced with when initially constructing a WPT system: that of concentrating efforts towards maximising power or transmission efficiency. As with most systems, it will depend heavily on the application: in high-energy applications, such as in Electric Vehicle charging [42], improved efficiency will most certainly be

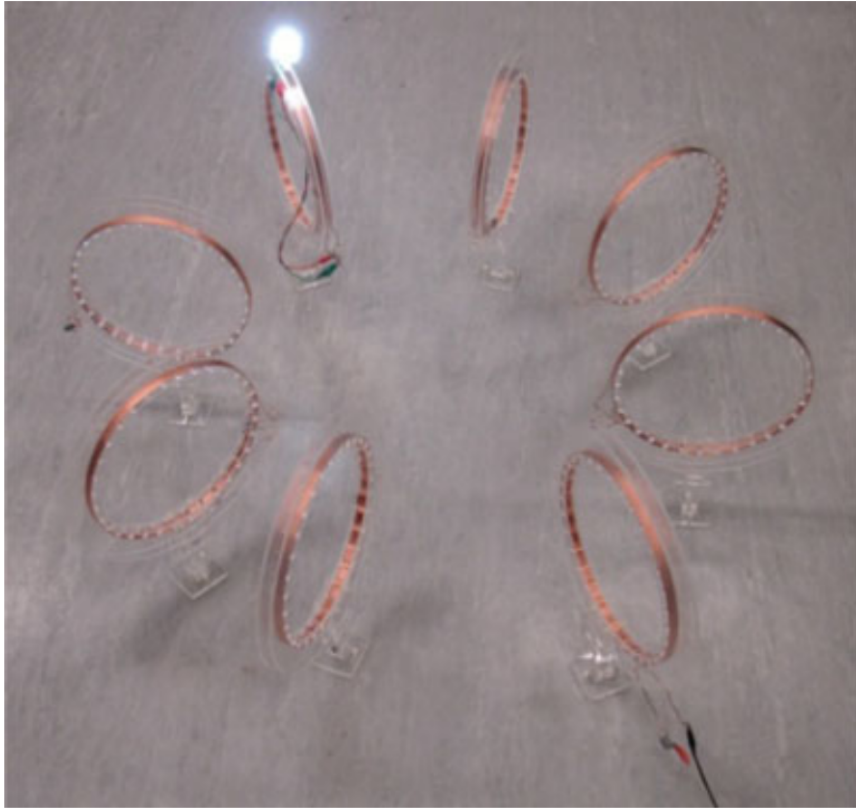


Figure 2.5: Wireless domino-resonator system powering a 14 W fluorescent bulb [41].

favoured over energy transmission rates. However, in low-energy wearable applications, maximising power is required over transmission efficiency, as the energy lost would be inconsequential compared to the consequences of device off-time. Realistically, a compromise between the two principles will almost certainly be selected which will be dictated by the application's specific needs.

2.2.4 Coupled Mode vs. Circuit Theory

Researchers in the field of SCMR will normally analyse their systems using either CMT or CT, therefore it is worth understanding these different approaches.

Coupled Mode Theory

CMT was originally formulated in the 1950s and was primarily concerned with electromagnetic mode propagation in microwave transmission lines [43]. The theory was applied to SCMR by Kurs [2] and Karalis *et al.* [44]. In essence, the theory modelled how energy could be efficiently passed between a pair of coupled systems,

and in its simplest form, is described by the following equations [45]

$$\frac{da_1}{dt} = j\omega_1 a_1 + jK_{12} a_2 \quad (2.2.11)$$

$$\frac{da_2}{dt} = j\omega_2 a_2 + jK_{21} a_1 \quad (2.2.12)$$

where $a_{1,2}$ are the mode amplitudes, $\omega_{1,2}$ are the natural resonant frequencies and K_{12} and K_{21} are the coupling coefficients between the two systems. In a lossless system set into oscillation, energy would be exchanged between these two systems in time t . The energy at any point is given by $|a_{1,2}|^2$. Considering a real WTP system using two identical resonators with equal coupling coefficients, the equations now become

$$\frac{da_t}{dt} = j(\omega_o - \Gamma_t) a_t + jK a_r + V e^{j\omega t} \quad (2.2.13)$$

$$\frac{da_r}{dt} = j(\omega_o - \Gamma_r - \Gamma_L) a_r + jK a_t \quad (2.2.14)$$

where $\Gamma_{t,r}$ represent the intrinsic decay rates for the transmitter and receiver respectively, ω_o is the resonant frequency of the WTP system, $V e^{j\omega t}$ is the driving voltage signal in the transmitter and Γ_L represents the additional energy decay from a load in the secondary.

The intrinsic decay rates are largely due to ohmic losses in the wires and coils of the circuit. A small portion of Γ is also caused by electromagnetic radiation, however this is often ignored during analysis. Expressions for the transfer efficiency η and the transferred power to the load P_L are given by

$$\eta = \frac{\Gamma_L |a_r|^2}{\Gamma_t |a_t|^2 + (\Gamma_r + \Gamma_L) |a_r|^2} \quad (2.2.15)$$

$$P_L = 2\Gamma_L |a_r|^2 \quad (2.2.16)$$

It is often the case that one wants to determine what values of Γ_L or coupling K would maximise η and P_L . This is done by substituting the values for $|a_{t,r}|^2$ from the equations (2.2.13) and (2.2.14) into equations (2.2.15) and (2.2.16), calculating the derivative with respect to Γ_L and K , and setting this to zero. This gives

$$\Gamma_{L\eta_{max}} = \Gamma_r \sqrt{1 + \frac{K^2}{\Gamma_t \Gamma_r}} \quad (2.2.17)$$

$$\Gamma_{LP_{Lmax}} = \frac{K^2 + \Gamma_t \Gamma_r}{\Gamma_t} \quad (2.2.18)$$

$$K_{P_{Lmax}} = \sqrt{\Gamma_t \Gamma_r + \Gamma_t \Gamma_L} \quad (2.2.19)$$

However,

$$\frac{d\eta}{dK} = \frac{2\Gamma_L \Gamma_t K}{(K^2 + \Gamma_t \Gamma_r + \Gamma_L \Gamma_t)^2} \neq 0 \quad (2.2.20)$$

as the intrinsic decay rate cannot be zero, implying that there is no optimum K that maximises η . Note, these expressions are valid for a system that is being driven at resonance.

Circuit Theory

It is often more intuitive to use Circuit Theory (CT) based on the models for mutual inductance between coils. Consider a 2-coil arrangement where each coil is compensated by a series capacitor as shown in Figure 2.6a.

R_S , R_1 , R_2 and R_L represent the internal resistance of the source V_S , resistances of the primary and secondary coils and the load; C_1 and C_2 represent the compensated capacitors connected in series with L_1 and L_2 which are the inductances of the primary and secondary coils, respectively. When an oscillatory magnetic field arises in the primary coil, a portion of the energy from the field will couple with, and hence, transfer to the secondary coil with the mutual coupling between these coils being represented by M . This *extraction* of energy from the primary circuit can be viewed as an extra impedance Z_{sref} in series with the primary coil, as shown in Figure 2.6b, and is dependent on the impedance characteristics Z_2 of the secondary circuit. Likewise, the transferred power can be viewed as a new source V_{pref} in series with the primary side reflected impedance Z_1 and the Secondary coil.

As in the previous instance, it is often desired to find the values of load resistance R_L and coupling M that will either maximise the power or transfer efficiency of the system and these are given by equations (2.2.21) to (2.2.23) [46],

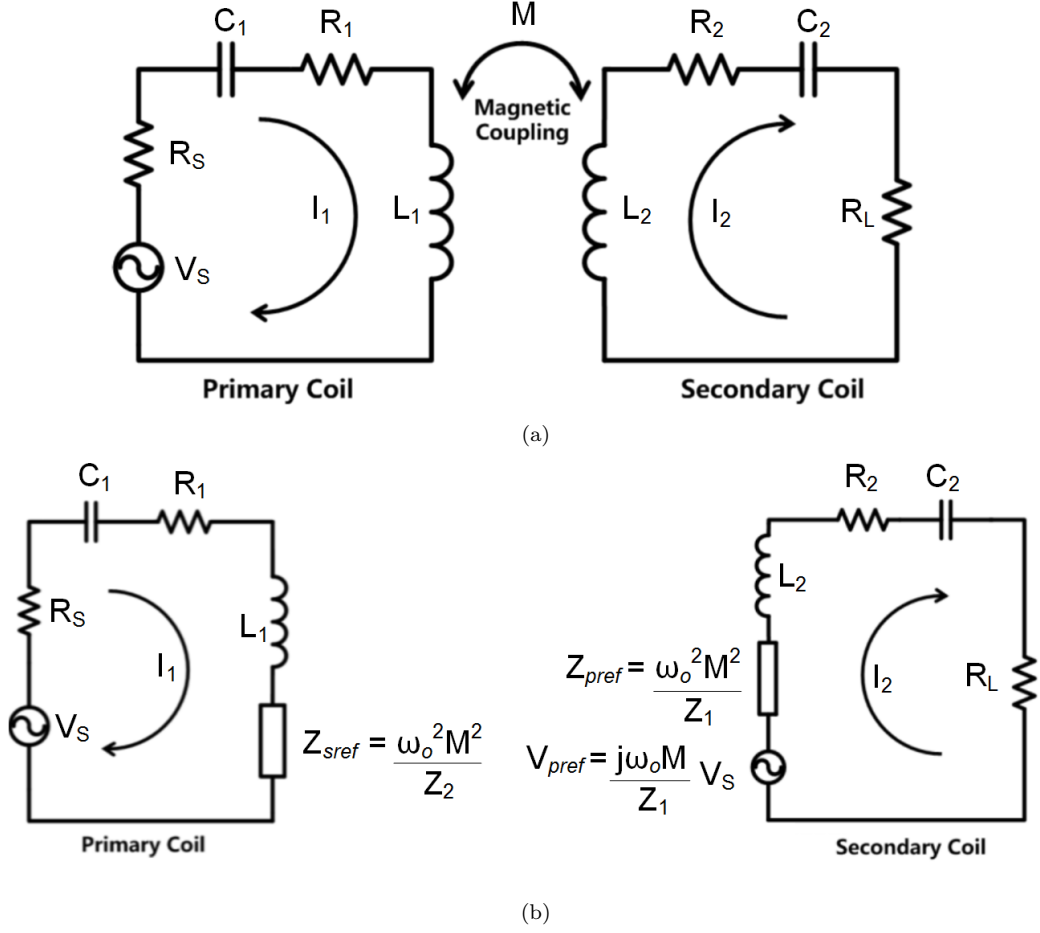


Figure 2.6: a) Coupled WTP system with identical transmitter and receiver, and b) the equivalent impedance as seen from the Primary and Secondary circuits [46].

$$R_{L\eta_{max}} = \sqrt{\frac{\omega_0^2 M^2 R_2^2}{R_1 + R_S} + R_2^2} \quad (2.2.21)$$

$$R_{LP_{L_{max}}} = \frac{\omega_0^2 M^2}{R_1 + R_S} + R_2^2 \quad (2.2.22)$$

$$M_{P_{L_{max}}} = \frac{\sqrt{(R_2 + R_L)(R_1 + R_S)}}{\omega_0} \quad (2.2.23)$$

Note that as in the previous analysis, there is no value for M that maximises η . Hence, from equations (2.2.17) to (2.2.19) and (2.2.21) to (2.2.23), one can clearly see the similarities between CMT and CT. The following relationships should also be noted in order to conveniently switch between the two methods,

$$\Gamma_L = \frac{R_L}{2L_2}, \quad \Gamma_2 = \frac{R_2}{2L_2}, \quad \Gamma_1 = \frac{R_1}{2L_1}, \quad K = \frac{\omega_0}{2} \kappa = \frac{\omega_0 M}{2\sqrt{L_1 L_2}} \quad (2.2.24)$$

The analysis and subsequent conclusion presented in this section recurs throughout the literature. Of note, Kiani *et al.* [47] presented a very detailed and noteworthy mathematical proof of this relationship. Their work explained that the two approaches are equivalent particularly for near-field non-radiating conditions for short and mid-range transmission distances, and that beyond these conditions, CT should be used to further the analysis. They further concluded that CMT is only accurate for coils with both small coupling coefficients and large Q -factors.

2.2.5 S-Parameters and Impedance Matching

When developing a WPT system, it is important to be able to predict the system's behaviour and measure the power gain on the receiver side. At increasing frequencies, it becomes more difficult to accurately measure voltage and current using probes due primarily to the probe's own impedance [48]. Furthermore, it is difficult to create short and open circuits for AC signals over a wide bandwidth as there is an inherent risk of damaging active components [49]. Instead, many researchers incorporate scattering(S)-parameter analysis: these S-parameters are defined in terms of incident and reflected travelling waves and accurately quantify how energy propagates through the system without the need to analyse the system structure. Consider a 2-port WPT system which can be represented by Figure 2.7.

a_1 and a_2 are incident waves, and b_1 and b_2 are reflected waves on ports 1 and 2 respectively. The S-parameters represent the ratio of power gain from one port to another and are represented by equation (2.2.25).

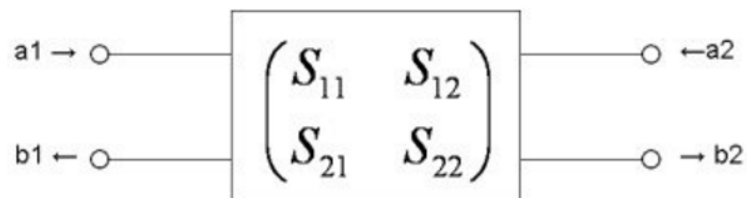


Figure 2.7: 2-port network S-parameter representation of a WTP system [50].

$$\begin{pmatrix} b_1 \\ b_2 \end{pmatrix} = \begin{pmatrix} S_{11} & S_{12} \\ S_{21} & S_{22} \end{pmatrix} \begin{pmatrix} a_1 \\ a_2 \end{pmatrix} \quad (2.2.25)$$

In practice, a Network Analyser can be used to measure the corresponding S-parameters of any system and, more specifically, a Vector Network Analyser is often employed as to preserve both phase and magnitude data [51].

It is often the case in many low-power WTP systems that MPT is desired, and hence impedance matching is used as described in section 2.2.3. In order to fully understand how energy propagates from the source to the load, it is necessary that the entire system is analysed. This not only makes the analysis more accurate but also allows for targeted optimisation during system design. While S-parameters have been demonstrated to be useful when performing an impedance matching analysis, their employment has often not been used to obtain the full picture. Most prior art tends to isolate the impedance matching and corresponding analysis to just the transmitter and receiving coils, and while it is clear that this common practice simplifies the solution, it does mean that results, and hence, conclusions drawn about the system's performance can be misleading. For example, in the well-known MIT experiments of 2007, the authors reported a transfer efficiency of 45% for a system that powered a 60 W bulb at a distance of two metres. While this seems very promising due to the increased transfer range, the whole system transmission efficiency was only about 15% at this distance, implying around 400 W was actually needed at the input to power the light-bulb [2]. Note that low system efficiency is the primary reason why many SCMR WPT systems based on the MPT principle are seldom employed in high-power applications such as electric vehicle charging [28].

When performing S-parameter analysis over a wide band of frequencies, the condition of impedance matching is met by maximising the forward gain S_{21} (which is often referred to as the transmission coefficient [32]). Given by equation 2.2.26, this parameter is defined as the ratio of the forward wave b_2 to the reflected wave a_1 when an input signal is present at Port 1.

$$S_{21} = \frac{b_2}{a_1} \quad (2.2.26)$$

Note that the power transfer efficiency η_r in terms of S-parameters is given by [52]

$$\eta_r = \frac{|S_{21}|^2}{1 - |S_{11}|^2} \quad (2.2.27)$$

where $|S_{21}|^2$ represents the power delivered to the load and $|S_{11}|^2$ represents the portion of power reflected from the source, hence one minus this value gives the power injected from the source.

It is apparent that, in practice, impedance matching poses a serious challenge to any dynamic WPT system. Consider the fact that the impedance seen on the reflected side will necessarily be dependent on the coupling between the coils, and thus would change significantly with changes in the relative position of the coils. The effects of lateral and angular coil misalignments are further studied in section 2.3.4. Consider also that the presence of a variable impedance seen on either side of transmission will ultimately change the resonant frequency ω_0 . This is, in fact, a common characteristic of the strongly coupled or overcoupled region, whereby the resonant frequency will tend to split into two different frequencies located either side of ω_0 after a threshold value of the coupling coefficient κ has been surpassed. This divergence from ω_0 and its effects are further studied in the following section.

2.2.6 Frequency Splitting

Since MPT is often desired for many SCMR WPT systems [53], the impedance matching approach will be undertaken as examined previously. The parameter S_{21} will therefore need to be maximised in order to meet this condition. When the coils are separated by a fair distance and are in an undercoupled or *loosely* coupled state, the frequency that maximises S_{21} will correspond to the resonant frequency of the system ω_0 . This is true until the coils are moved closer together so that their coupling coefficient reaches a threshold value commonly referred to as the *critical* coupling point κ_c . Beyond this threshold, the system is in an overcoupled or strongly coupled state and the frequency that maximises S_{21} will begin to split into, typically, two frequencies either side of ω_0 .

This phenomenon is aptly named *Frequency Splitting* (or *Frequency Bifurcation* in the case of two-peak splitting), and being a staple of strongly coupled WPT, it is necessary to focus some attention towards its causes and effect on practical implementation.

Many works [54, 55, 56, 57, 58] have examined this phenomenon for a number of different coil architectures, and there are a number of perspectives and analogies from which to draw on an explain for its cause. Ultimately, the effect is dictated by the inductive coupling between the various system coils: when this coupling coefficient changes, the series equivalent impedance seen on the transmitting coil will change, shifting the amplitude-frequency and impedance-frequency angle for the system input impedance Z_{in} [59]. Changing the coupling coefficient κ , normally achieved by changing the transmitting and receiving coils separation distance, may create new and often multiple frequencies where maximum power transfer from source to load will occur. The divergence of these frequencies from ω_0 will typically increase with an increase in the value of coupling κ . Figure 2.8 illustrates the effect on S_{21} as a function of coupling and frequency. It shows that in the overcoupled region (marked by a red dashed box), maximum power transfer efficiency can occur irrespective of coil separation in this range if the appropriate operating frequency is selected. With reference to CMT as presented in section 2.2.4, Niu *et al.* [60] show that the critical coupling K_c can be expressed as

$$K_c = \sqrt{0.5\Gamma_t^2 + 0.5(\Gamma_r + \Gamma_L)^2} \quad (2.2.28)$$

In the case of bifurcation, it has been further demonstrated that the frequencies in the overcoupled region that maximise S_{21} can be computed via equation (2.2.29) [60]. The CT counterpart to equation (2.2.29) can also be found using the relationships presented in section 2.2.4.

$$\omega = \omega_o \pm \sqrt{K^2 - 0.5\Gamma_t^2 - 0.5(\Gamma_r + \Gamma_L)^2} \quad (2.2.29)$$

Note that this frequency splitting phenomenon does not occur for a system's energy efficiency characteristics, as analysed under the MEE principle [61]. Instead, the

frequency that maximises energy efficiency will always correspond to the resonant frequency of the system. Figure 2.9 illustrates this point for a 2-coil WPT system in an overcoupled state with ω_0 equal to 10 MHz.

The lower frequency peak is sometimes referred to as the lower or *odd* mode and the higher frequency peak as the upper or *even* mode [62]. The current in the transmitter and receiver coils will be in-phase at the odd mode and anti-phase (i.e. 180°) at the even mode. Typically, operating at the odd frequency mode will achieve a slightly higher power transfer efficiency compared to the even mode, since this reduced operating frequency will decrease both skin and proximity effects [63].

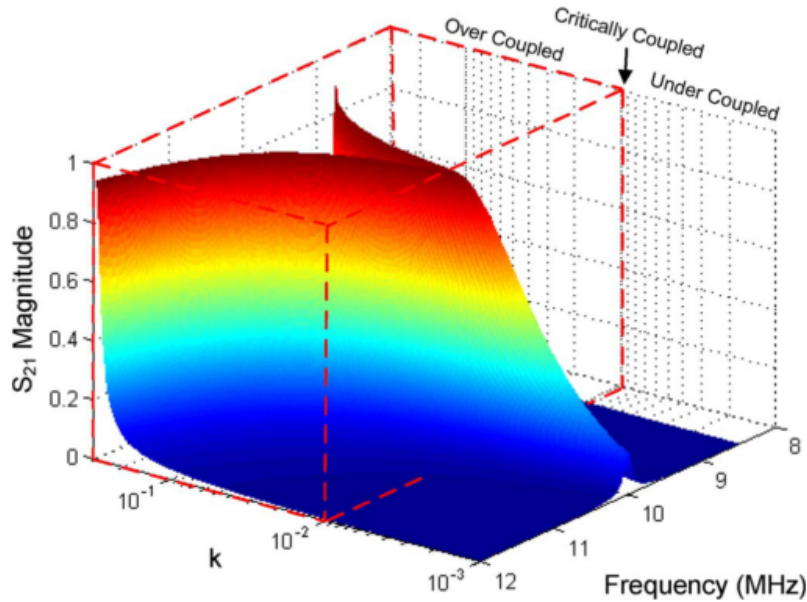


Figure 2.8: Plot of S_{21} as a function of κ and operating frequency [14].

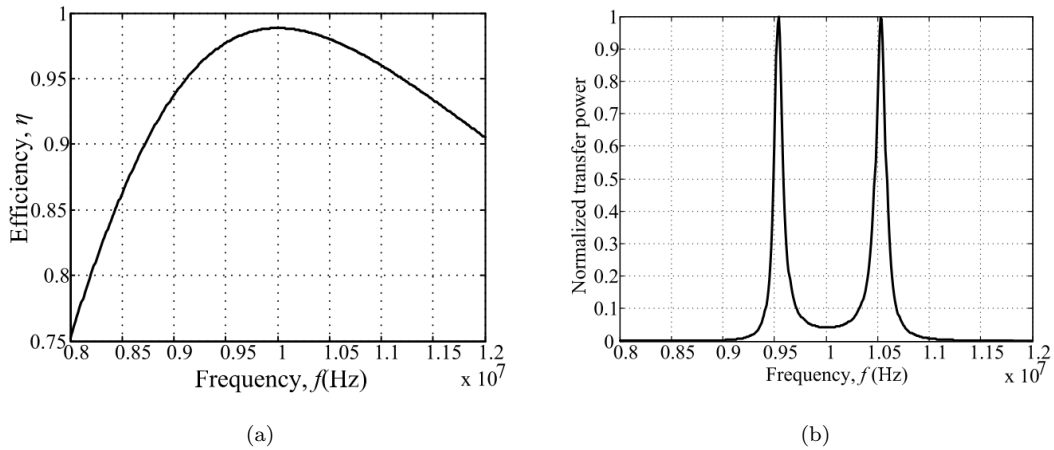


Figure 2.9: Plot of a) Efficiency vs Frequency, and b) Normalised Power vs Frequency [61].

Thus far, it has been assumed that the coils involved in the transmission were exactly identical, however in real-world applications the transmitting and receiving coils would likely be structurally different, both in terms of size, shape and number of turns. For asymmetrical coils, the frequency splitting pattern would no longer be uniform with the divergence of modes being more pronounced depending on the individual coil characteristics [64, 65]. Moreover, these differences will also produce different values for S_{21} at the critical coupling point in particular as well as between the mode peaks themselves [14].

The scope of this section's discussion has been limited to a simple 2-coil architecture (i.e. comprising a single pair of transmitting and receiving coils), however, frequency splitting in the overcoupled region also exists in multi-coil systems; whether they be multi-transmitter, multi-receiver coils, or a combination of both [46]. This leads to some interesting behaviours that could be exploited; however, analysing and implementing multi-coil systems becomes increasingly difficult and there is no established design scheme that can be applied to all situations [66]. Instead, the WPT engineer would need to work to the requirements of the specific application and determine ways to either track, control, or suppress the effects of frequency splitting.

Many solutions in the literature have been proposed that track and model the frequency splitting as the coils move relative to each other in an overcoupled state. Sample *et al.* [14] presented a control system that automatically adapted the system's operating frequency. Figure 2.10 illustrates how the system was able to maintain a high power transfer efficiency for both lateral and angular displacements.

Likewise, Park *et al.* [67] presented how such a frequency-tuning method might compare to one that instead adapts the transmitter circuit impedance. Park *et al.* rightly pointed out the difficulties of implementing such an impedance tuning scheme in any real-world application as it would involve varying the coil separation for a multicoil transmitter. Nevertheless, their proposed scheme would deliver superior power transfer efficiency over frequency tuning alone, as illustrated by Figure 2.11.

Taking this idea further, Ahn *et al.* [68] presented a different impedance tuning method by adapting the load impedance on the receiver side. This was achieved by creating a switching converter between the receiver coil and the load which altered the

effective impedance seen at the transmitter side. The converter, as presented in Figure 2.12, also has the added benefit of performing voltage regulation for the load, arguably simplifying the circuit design.

The major downside between these and other similar solutions is that they all require some form of control processing as well as feedback to overcome the effects of frequency splitting. While this may not complicate the design of systems already employing communication between the transmitter and receiver, it does mean that applications may end up expending valuable power simply to maintain a power delivery control mechanism.

Other works have instead explored ways to eliminate the frequency splitting phenomenon altogether. Lv *et al.* [69] and Lyu *et al.* [65] examined frequency splitting suppression while maintaining the same effective transmission distance and efficiency by changing the relative geometries of the coils involved [69]. The explanation given was that by altering the reactive properties of the coils separately the coupling could become more uniform over a range of distances as illustrated in Figure 2.13. Note, as this was for 2-coil architecture the authors were limited in the changes they could make to the system's single coupling link.

On the other hand, Hwang *et al.* [70] demonstrated how changing the κ between each link in a 4-coil architecture could produce quite different transmission

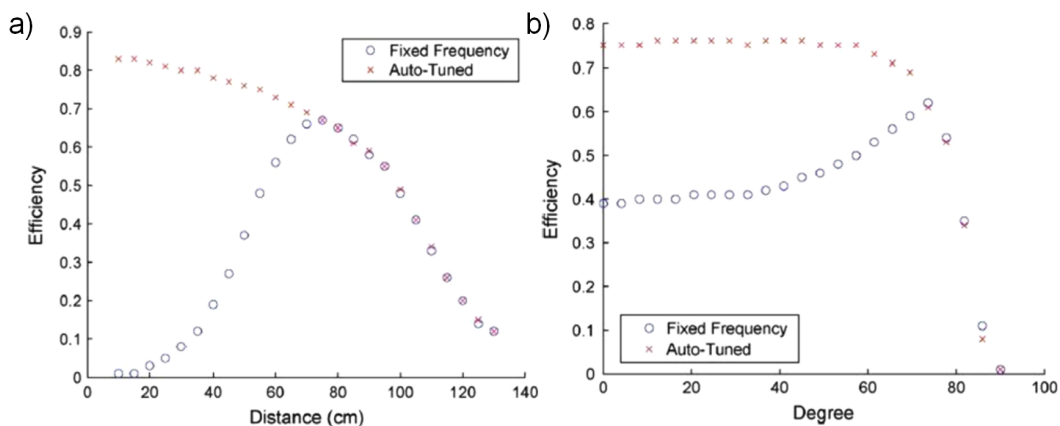


Figure 2.10: Plots for power transfer efficiency comparing a fixed driving frequency vs an automatic frequency tuning system as a function of a) the distance between the transmitter and receiver system and b) the angle between the transmitter and receiver system where an angle of 0 degrees corresponds to the coils facing each other, while 90 degrees corresponds to the receiver perpendicular to the transmitter [14].

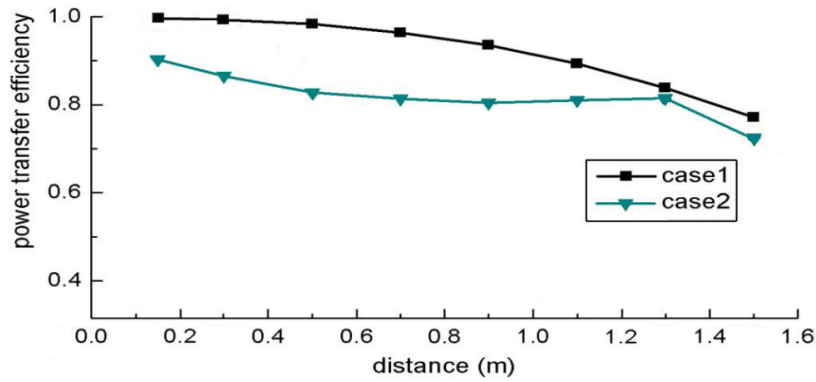


Figure 2.11: Plot of power transfer efficiency vs distance for: case 1) fixed frequency and adaptive impedance and case 2) adaptive frequency and fixed impedance [67].

characteristics. To do this, they only changed the number of turns of the source and load coils relative to the resonant coils. Normally, these coils are single loop coils in order to maintain a high efficiency over a larger coil separation [71]. However, in their experiments they demonstrated how varying the number of turns could create not only the classic bifurcation seen with 2-coil systems, but also other peaks and even a near-flat response along a varying coil separation. This is illustrated by the gain plots in Figure 2.14.

While these design strategies seem promising, this might lead to a reduction of mutual coupling, leading to a reduction in the power transfer capability. It should therefore be noted that this practice could likely only be employed where large enough coils are used in order to achieve the desired separation for WPT without needing to

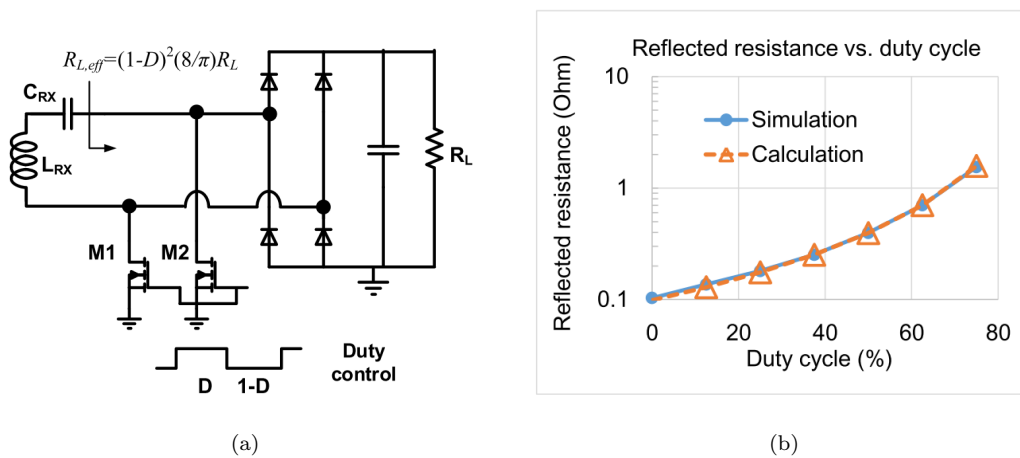


Figure 2.12: a) Proposed receiver side switching convertor, and b) effective impedance seen on the transmitter side as a function of duty cycle [68].

use strong coupling.

Zhang *et al.* [59] analytically demonstrated that by reducing the source resistance R_S , the frequency splitting phenomenon becomes much less pronounced. At the same time, by decreasing the Q -factor of the coils by, say, increasing their resistance, one could also suppress the effects of frequency splitting as shown in Figure 2.15. It should be noted, however, that reducing the Q -factor too much would lead to the system no longer being in an overcoupled state, and less power would be transferred to the receiver as shown by the right-hand plots of Figure 2.15.

Researchers have also attempted to build a more general model of frequency splitting in order to achieve a desired response [73]. For example, Mastri *et al.* [74] presented a model for a coupling-independent WPT by focusing on how to achieve a constant power output at a constant efficiency throughout the overcoupled region. It was shown that, by operating the system at pre-defined frequencies slightly off of the upper or lower modes one could reproduce the load impedance on the transmitter side independently of any variations in the coupling κ above the critical coupling point κ_c . While this would mean that the system may not operate at maximum power, it does ensure the system has a much more stable and predictable power output when in an overcoupled state. Figure 2.16 illustrates how this system could achieve constant power at a constant efficiency, however it should be noted that, in practice, some form of rudimentary

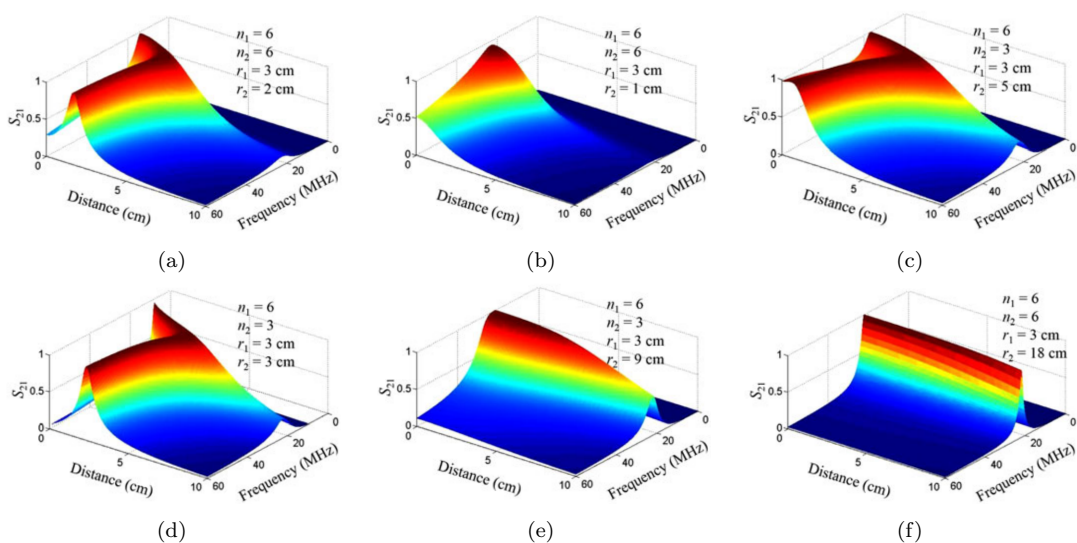


Figure 2.13: Plots of S_{21} with respect to frequency and distance for different radii (r_x) and coil turns (n_x) of transmitter coils (1) and receiver coil (2) [65].

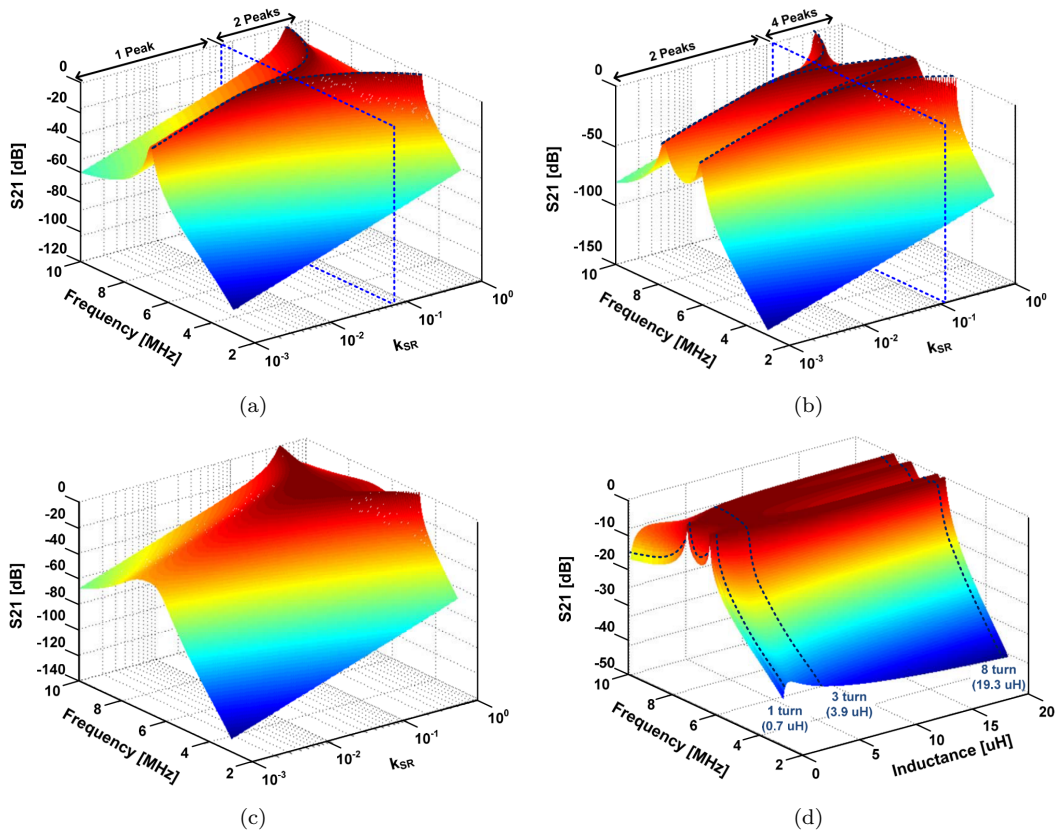


Figure 2.14: S_{21} as functions of frequency and coupling, (a) with one-turn coil, (b) eight-turn coil, (c) three-turn coil, and (d) across varying coil inductances in the basic four-coil WPT system with DS of 0.3 between the resonant coils [70].

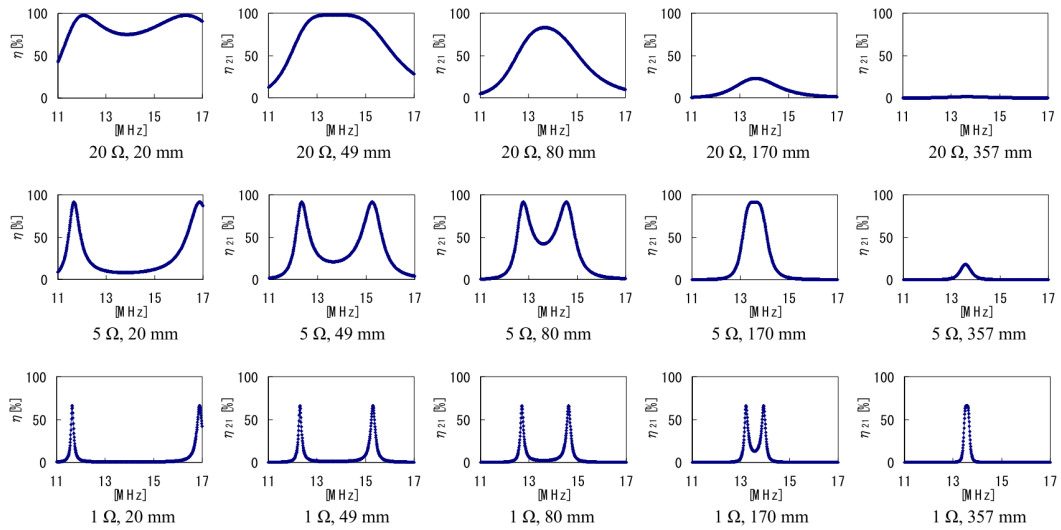


Figure 2.15: Plots for Power transfer efficiency η vs frequency for different coil resistances and separation [72].

frequency tracking would still be required, albeit for a much smaller range.

Finally, it has been shown that from a safety and power transmission efficiency

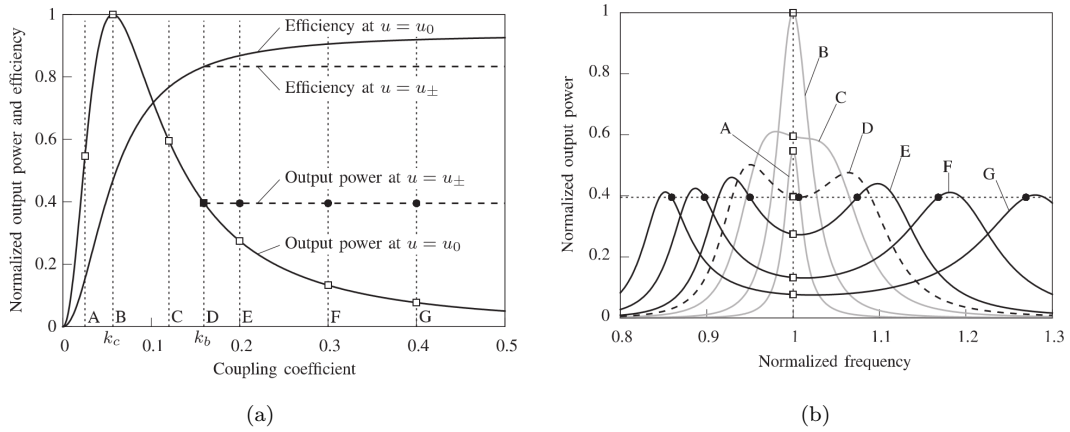


Figure 2.16: Plots for a) Normalised Power out and Efficiency vs Coupling and b) Normalised Power output vs Normalised frequency. In each Plot, A) is well below κ_c thus a low power output, B) is at κ_c thus achieving maximum theoretical power, C) is beyond κ_c where peak power decreases, D) has been defined as κ_b , where the frequency bifurcation is now pronounced, and E,F,G) are points where constant power and efficiency can be achieved [74].

point of view, if frequency bifurcation were to occur it would be more suitable to drive the system at the higher frequency known commonly as the *even mode*, as this would reduce the far-field emission as shown in Figure 2.17. This is due to the fact that, at the even mode, the current in the transmitting and receiving coils have opposite directions, hence the resultant emission from both coils is cancelled [75].

2.3 Practical Considerations of Mid-Range WPT System

Over the last decade a plethora of different WPT system design principles and architectures have emerged, each dedicated to solving a particular set of generic issues or

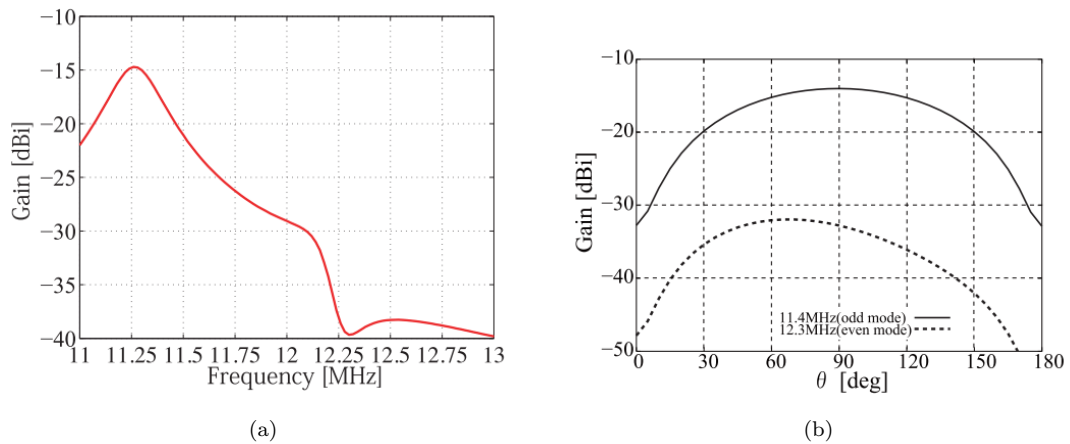


Figure 2.17: Far-field emission gain characters showing (a) frequency and (b) angle [75].

constructed to overcome some weakness or shortfall in conventional system design. This section will explore different circuit topologies, coil designs and the most notable system architectures in order to understand the advantages, disadvantages and compromises in different designs as well as the the rationale behind their implementation.

2.3.1 Compensation Topologies

It is well known from magnetic induction that loosely coupled coils create a significant leakage inductance on either side of the coil circuitry which, acting as an extra inductive impedance, causes system losses [76]. It is therefore a common practice to compensate for this by connecting a capacitor in each transmitting and receiving coil circuit in a WPT system. From this perspective, the primary winding's compensation capacitor C_1 is selected to create a zero-phase-angle between the voltage and current in the transmitter at a particular coupling κ and load R_L , and the secondary compensation capacitor C_2 is selected to tune the receiver to the resonant frequency ω_0 determined by the transmitter's circuit impedance characteristics, in order to achieve high transfer efficiency [48]. For a 2-coil WPT system, there are four basic compensation topologies: Series-Series (SS), Series-Parallel (SP), Parallel-Series (PS) and Parallel-Parallel (PP), and these are illustrated in Figure 2.18.

The topology as well as the capacitor values selected will have a significant effect on the WPT performance, thus the choice becomes a crucial aspect in the design of any WPT system. Li *et al.* [30] derived equations for C_1 as a function of the other WPT system characteristics, and these are presented in equations (2.3.1) to (2.3.4),

$$C_{1,SS} = \frac{C_2 L_2}{L_1} \quad (2.3.1)$$

$$C_{1,SP} = \frac{C_2 L_2}{L_1} \left(\frac{1}{1 - \kappa^2} \right) \quad (2.3.2)$$

$$C_{1,PS} = \frac{C_2 L_2}{L_1} \left(\frac{R_L^2}{\omega_0^2 L_2^2 \kappa^4 + R_L^2} \right) \quad (2.3.3)$$

$$C_{1,PP} = \frac{C_2 L_2}{L_1} \left(\frac{R_L^2 (1 - \kappa^2)}{[\omega_0^2 L_2^2 \kappa^4 + R_L^2 (1 - \kappa^2)]^2} \right) \quad (2.3.4)$$

where L_1 and L_2 are the transmitter and receiver coil inductances respectively. It can be seen that SS is the only topology that is independent to variations in both the coupling κ and load R_L of the system. Its simplicity and ease of implementation is also the reason why the SS topology is the most common choice encountered in the literature: for example, Kim *et al.* [53] had asserted that not only were they able to simplify the selection of C_1 with the SS topology, but they were also able to use first-order current-driven rectifiers as opposed to second-order voltage-driven rectifiers on the receiver side. This reduces overall complexity, switching losses and circuit volume when built.

It should be noted, however, that the other topologies offer certain advantages over the simple SS topology and these are worth examining further. Several works [77, 78] have pointed out that a parallel compensated secondary leads to a reduced dependence on the load value as a current source would now be seen at the receiver side of transmission instead of a voltage source (as one would expect with a series compensated secondary). This, they argued, would therefore be better suited for battery charging applications. Similar conclusions can be drawn for multi-receiver WPT systems as demonstrated by Kim *et al.* [79]: they showed that a PS topology with multiple receivers would be more sensitive to variations in the individual loads whilst

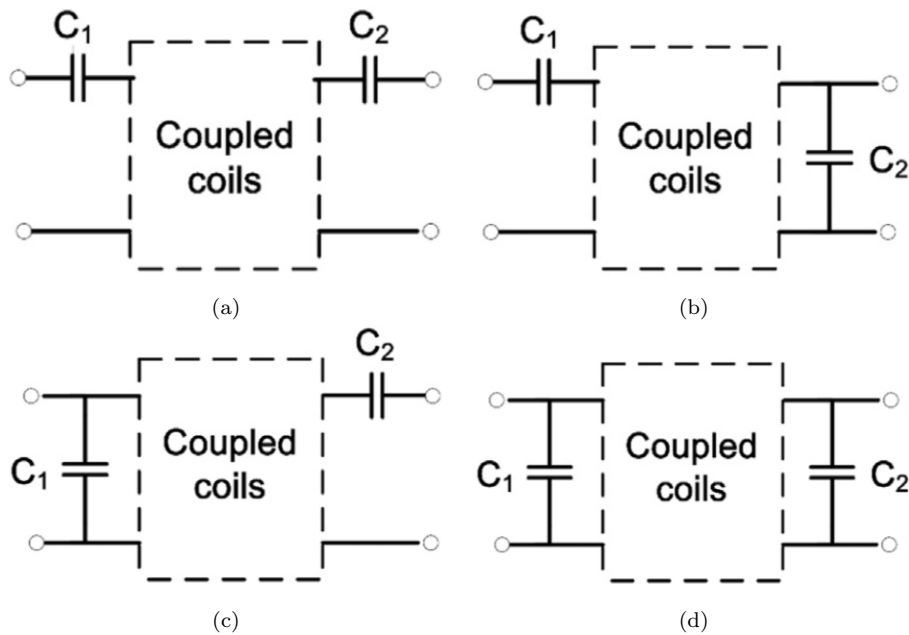


Figure 2.18: Capacitor circuit topologies: (a) SS, (b) SP, (c) PS, (d) PP [48].

SP would instead be more sensitive to the mutual coupling between the transmission links.

Note that when selecting a parallel compensation on the secondary, the WPT engineer would now need to compensate for a reflected reactance X_{pref} from the primary circuit. This would not be present when a series compensation is used on the receiver side, thus making the parallel compensation design choice more complex. Wang *et al.* presented a thorough analysis of topology selection for WPT systems and stated that the reflected reactance for a primary compensated secondary can be determined by equation (2.3.5) [80]. It was also concluded that, in practice, C_1 would likely be designed to a fixed value according to the minimum power requirements as it would be impractical to vary C_1 with changing system parameters to achieve optimum performance.

$$X_{pref} = -j\frac{\omega_0 M^2}{L_1} \quad \text{or} \quad X_{pref} = -j\omega_0 \kappa^2 L_2 \quad (2.3.5)$$

Lu *et al.* [28] argued that while SS would be preferred for systems with high efficiency, PP would actually be more suitable for systems with relatively low efficiency. This, they argued, would achieve a higher effective coil induction, thus improving coupling. Sangswang *et al.* [42] drew attention to the output power variation problems seen in high operating frequency SS topologies when the load is small. It was further shown that by removing the secondary capacitor and adapting the primary compensator capacitors one could significantly increase the power transfer capability for systems with small load resistance R_L .

Normally, the coil parameters are already known and one would then need to determine the terminating impedances to optimise the design. Instead, Monti *et al.* [81] discussed the inverse problem and presented a formulation to determine the best coil parameters for each of the four topologies in order to select the best topology for a given load. Sallan *et al.* [82] stated that, on the contrary, there is no one topology based on system parameters alone and instead present an optimal design process in order to determine which topology would be most suitable given the application. Some

noteworthy conclusions were: SS and SP topologies are more suitable for high power applications while PS and PP allow larger transmission distances for the same operating frequency; series circuits work for higher voltages whereas parallel designs would be better suited for higher currents.

Several works have also explored ways of combining topologies in order to achieve improved performance over the basic ones presented: Villa *et al.* [83] presented an interesting analysis showing how each topology might perform during coil misalignment. It was concluded that during misalignment or in the absence of a secondary winding, SS and SP topologies could cause a potentially hazardous increase in current in the primary windings. By contrast, PS and PP reduce current in these situations and hence are arguably safer to use in high power applications. This occurs due to the decrease in transmitter impedances in SS and SP (Z_{1_SS} and Z_{1_SP}) and the increase of transmitter impedances in PS and PP (Z_{1_PS} and Z_{1_PP}). Equations (2.3.6) to (2.3.9) demonstrate this relationship at resonance with respect to M for each topology.

$$Z_{1_SS} = R_1 + \frac{\omega_0^2 M^2}{R_2 + R_L} \quad (2.3.6)$$

$$Z_{1_SP} = R_1 + \frac{\omega_0^2 M^2}{R_2 + j\omega_0 L_2 + \frac{R_L}{1+j\omega_0 C_2 R_L}} \quad (2.3.7)$$

$$Z_{1_PS} = \frac{1}{R_1 + j\omega_0(L_1 + C_1) + \frac{\omega_0^2 M^2}{R_2 + R_L}} \quad (2.3.8)$$

$$Z_{1_PP} = \frac{1}{j\omega_0 C_1 + \frac{1}{R_1 + j\omega_0 L_1 + \frac{1}{R_L + (R_2 + j\omega_0 L_2)(1 + j\omega_0 C_2 R_L)}}} \quad (2.3.9)$$

They proposed a series-parallel-series topology (SPS) and concluded that this would offer a good power transfer rate even at a relatively high misalignment. Chen *et al.* [84] built on this idea and presented a system that combined both series and parallel topologies within the same coil circuit. The proposed system is shown in Figure 2.19a and it was claimed that the system was able to achieve an increased transfer distance or transfer efficiency when compared to the equivalent series, parallel or uncompensated topologies presented in Figure 2.19b-d. In this way, the system was also more adaptable to different WPT applications by being able to easily balance efficiency and transfer

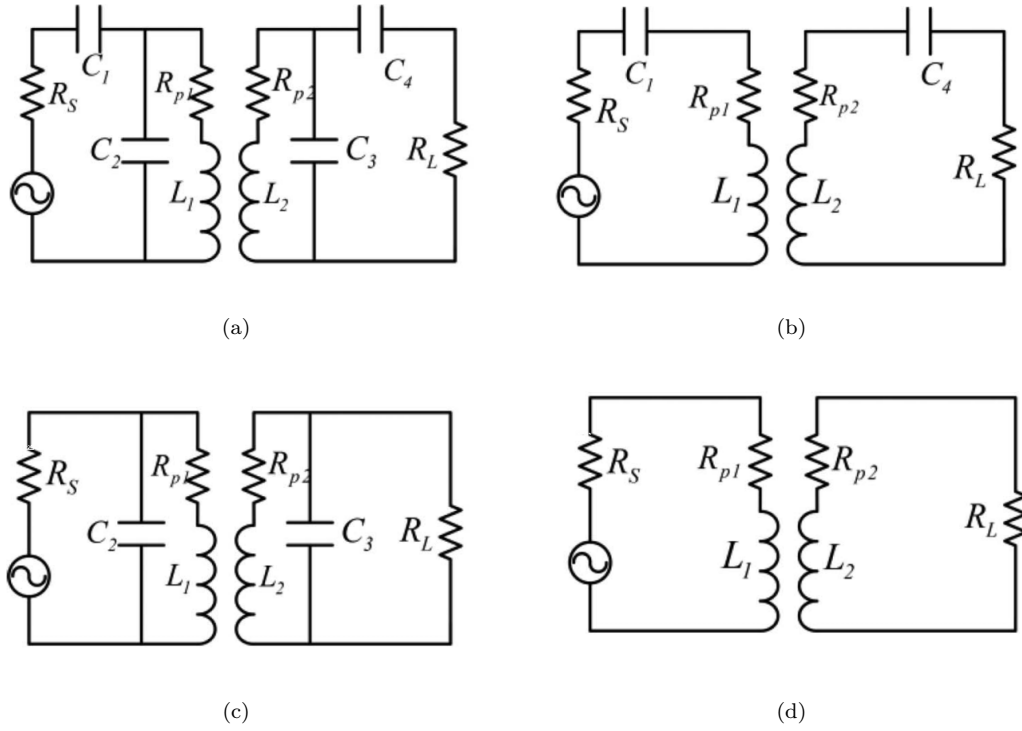


Figure 2.19: Circuit models for a) Combined SS and PP, b) SS only, c) PP only and d) uncompensated system [84].

range through the optimal selection of C_1 , C_2 , C_3 and C_4 .

As shown, all four topologies have their virtues and drawbacks, and choosing which one to employ will heavily depend on the type of WPT application. Table 2.1 gives a succinct summary of the key points to note when comparing and choosing topologies.

Table 2.1: Comparing the four main compensation topologies across key WPT requirements

Topology	Simplicity	Adoption to load changes	Multiple receivers	Larger trans. distances	High power apps	Misalignment tolerance
SS	++	+++	++	-	-	-
SP	+	-	--	--	-	-
PS	-	--	+	+	++	+
PP	--	---	+	+	++	+

2.3.2 Coil Design Principles

Coils, resonators, couplers, antennas: all these refer to elements that create the wireless link that facilitates the transfer of energy in any WPT system. Their design,

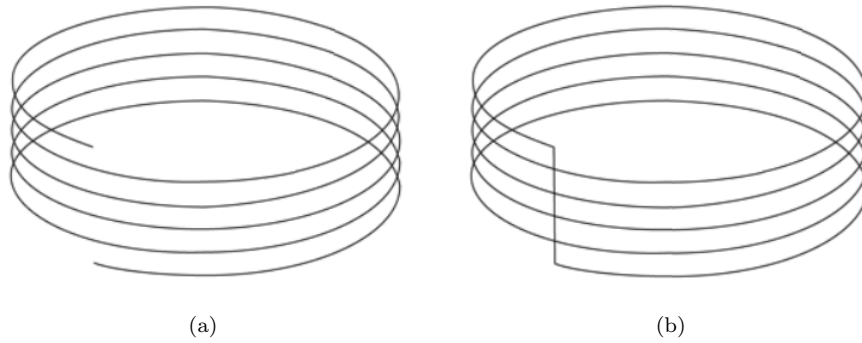


Figure 2.20: a) Open-End and b) Short-End Model.

construction and optimisation are hot topics across multiple fields, all in an effort to achieve greater power transmission and efficiency at ever increasing distances. With reference to the current state-of-the-art, some of the most important principles in the design of these transmitting and receiving elements will be explored in this chapter.

When discussing WPT using inductive coils, there are 2 main types presented in the literature which, for convenience, will be referred to as *Open-End* and *Short-End* coils as presented in Figure 2.20.

Open-End, as the name suggests, are coils which do not form a closed circuit and are typically not compensated by a parallel or series connected capacitor. To achieve resonance, these coils are instead operated at a frequency dictated by their self-inductance along with their own parasitic capacitance. This self-capacitance is normally attributed to capacitances that exist between adjacent coil turns [33]. These would often be tiny for typical coil sizes; hence, systems employing Open-End coils would need to be operated at megahertz frequencies in order to achieve *self-resonance* of the coils. Conversely, Short-End coils form closed circuits and would likely use compensating capacitors in order to achieve resonance at lower frequencies. As one might expect, Open-End coils can only act as intermediary transmitting or receiving coils as they could not directly connect to either a source or load. Instead, a Short-End coil connected to a source (often referred to as a *driving coil*) would transmit energy to an Open-End coil at its resonant frequency. This energy could then be transmitted from the Open-End coil to the load via another Short-End coil (aptly referred to as the *load coil*).

Though this might appear to increase system complexity, there is a clear rationale

behind the use of Open-End coils in WPT systems in order to achieve very high coupling. The Q -factor for an isolated RLC resonator was already defined in equation (2.2.9), however, this is only the unloaded Q -factor or simply Q_U . When the resonator is connected to a source or load circuitry, the actual Q -factor for the system will decrease according to these new resistive components. This total system Q -factor is known as the loaded Q -factor or simply Q_L , and in practice, should not exceed $\frac{1}{5}$ th of Q_U [85]. Beyond this threshold, circuit losses within the WPT system would become exponentially more excessive as represented by equation (2.3.10).

$$\text{Circuit Losses} = 20 \log \left(1 - \frac{Q_L}{Q_U} \right) \quad (2.3.10)$$

This phenomenon would clearly impose a limit for the Q -factors in any WPT system, limiting the effective range for SCMR. However, by using intermediary Open-End coils, inductively coupled to a source or load circuit, the transmitting and receiving Q -factors could now be dictated by the Q_U of the isolated coils themselves, hence high- Q SCMR WPT could take place. Cannon *et al.* [86] compared the Q -factors of resonant and non-resonant WPT systems to demonstrate how using a system of Open-End and Short-End can lead to a much better system performance compared to traditional Short-End systems. Figure 2.21 illustrates the performance of three different systems.

It should be noted that self-resonant Open-End coils are quite susceptible to changes in temperature, humidity, and even the presence of users nearby [87]. This could make a long-term stable implementation of such a system difficult as the resonant frequency could shift away from the operating frequency with different surrounding conditions. Moreover, these coils tend to produce a much greater electric field in the vicinity of the coils, which would limit the amount of power that could be safely transmitted for wearable technologies under the *International Commission on Non-Ionizing Radiation Protection* (ICNIRP) guidelines [88]. These implications along with a further elaboration on safety concerns for WPT systems can be found in section 2.4.

Once the type of coils to use are decided upon, WPT engineers would next need to consider the physical structure of the coils to achieve the desired effect. Figure 2.22

illustrates some well-known and noteworthy structures that have been encountered in the literature. Each of these different structures and their combinations would create noticeable changes in coil performance for various applications; however, it is important to note that a significant enhancement in transfer efficiency will always arise simply by making the coils bigger. In fact, many works have deliberately used relatively large coils in order to demonstrate how transmission at a distance could be plausible.

Melki and Moslem [93] made a point of how significant this difference in coil size can be for the same resonant operating frequency as presented in Figure 2.23.

Typically, resonators and their performance would be analysed from their magnetic and electric field characteristics using the Finite-Element Method (FEM) or, the more seldom used Method of Moments (MoM). The most common software packages employed for this task are ANSYS Maxwell [94] and COMSOL Multiphysics [95]. Essentially, the software package will solve Maxwell's equations for electromagnetism in a meshed 2D or 3D space in order to visualise the magnetic interactions, gain a sense of how a proposed system might perform and where there might be room for improvement. While simulations are useful, it is important to also understand how coils interact with the surroundings when implemented. For example, Park *et al.* [67] presented a simulation of a relatively high efficiency WPT system. However, when constructed, the

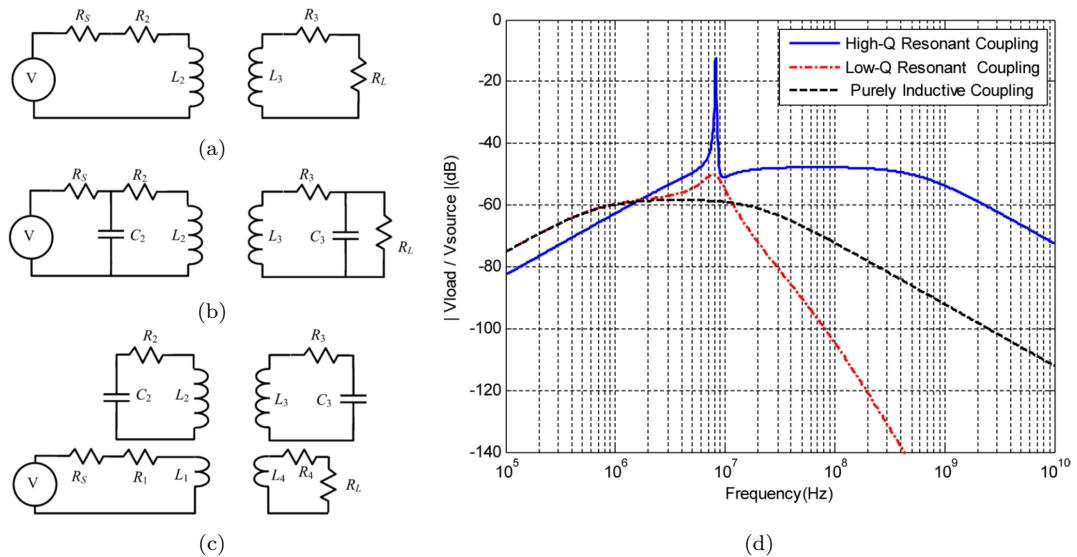


Figure 2.21: Circuit models for a) a typical inductive WPT system without resonance, b) a WPT system operating at resonance, and c) a WPT system employing intermediary Open-End coils, as well as d) the voltage gain vs frequency plot for the systems a), b), c) [86].

efficiency dropped as much as 30% simply due to the presence of a plastic dielectric support structure for the coils in the experiment. This aptly demonstrates how essential it can be to consider the entire structure of the system and not just the WPT coils in isolation.

Besides shaping and up-sizing coils, many researchers have also proposed enhancing performance by adding ferromagnetic or paramagnetic materials. Changbyung *et al.* used a shaped ferrite core to enhance the overall transmission characteristics of a WPT at frequencies as low as 20 kHz [87]. Figure 2.24 demonstrates the system's function

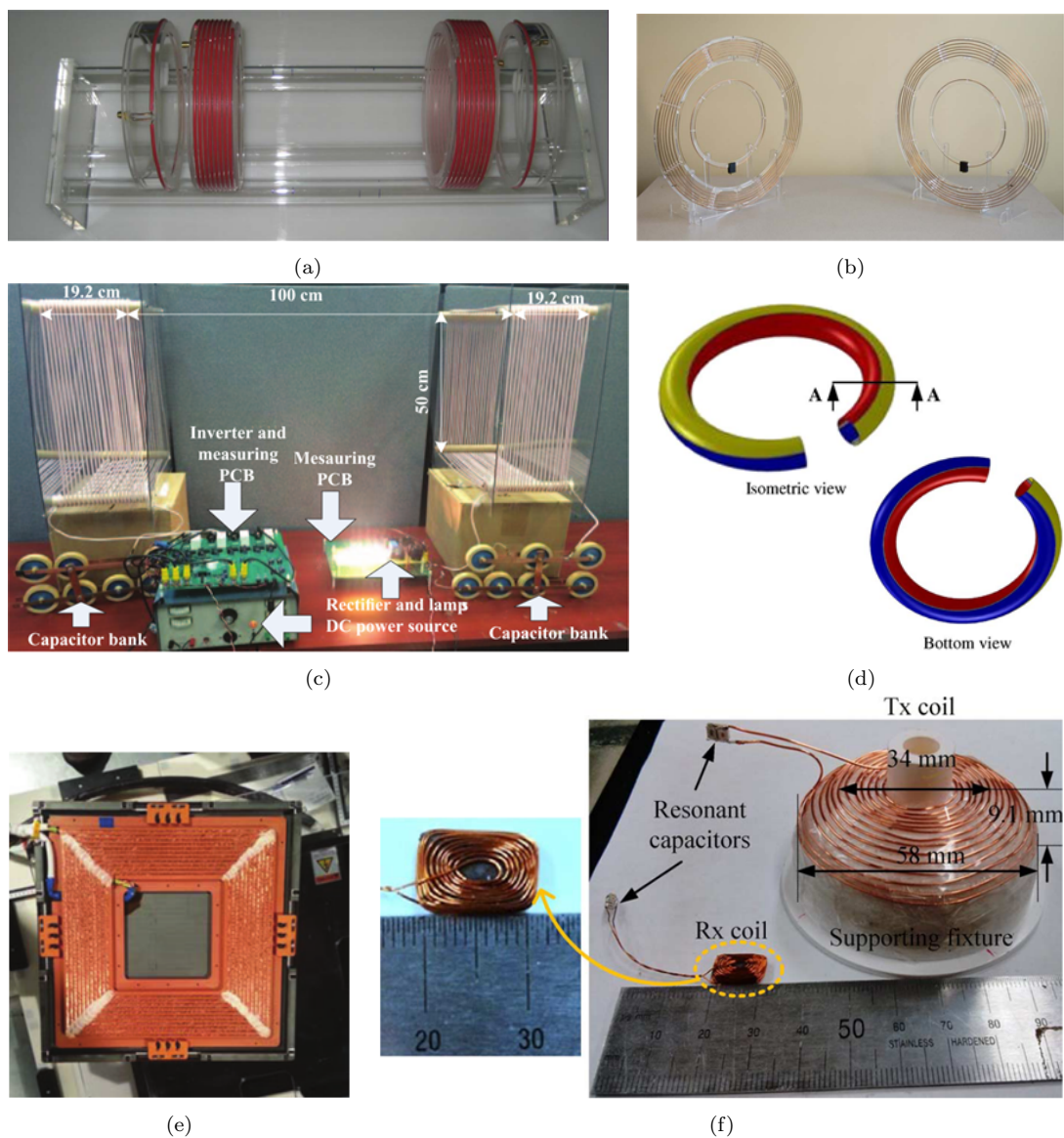


Figure 2.22: Open- and short-end a) cylindrical system [89] and b) flat spiral system [14]; c) square coil WPT system [90]; d) proposed spiral winding pattern in a single loop structure [34]; e) top view of flat square coil [91]; and f) a bowl-shaped spiral Tx coil with different sized flat spiral Rx coil [92]

and the magnetic field strength distribution over the resonator geometry.

Ding and Wang [96] applied a manganese-zinc core to a cylindrical coil WPT system. It was shown that using this soft ferrite core could increase power transfer efficiency by an additional 40%. Ahn *et al.* [97] also used ferrite, but instead focused on its capability to shield users from flux leakage when a WPT system is incorporated into furniture. This was demonstrated by using a multi-coil transmitter with a ferrite E-core. Knaisch *et al.* [98] combined both ferrite and aluminium structures in order to obtain an enhancement of the coupling factor for an electric vehicle WPT system, but more importantly, to shield from flux linkage to the vehicle body itself. By doing this, they argued, one could maintain a reasonably high power transfer link, while at the same time conforming to the safety standards set by the ICNIRP. Huang *et al.* [99] also studied the effects of ferrite and aluminium, however, the work compared the effects of a laminated and non-laminated aluminium mobile phone casing structure on transmission efficiency. Unsurprisingly, they observed substantial losses due to eddy currents but also noted how the addition of these cases shifted the peak power transmission frequency of the system by varying degrees. While these additions could greatly enhance system performance, the individual material properties (and their losses) will need to be accurately accounted for which might overcomplicate the analysis, leading to greater computer simulation

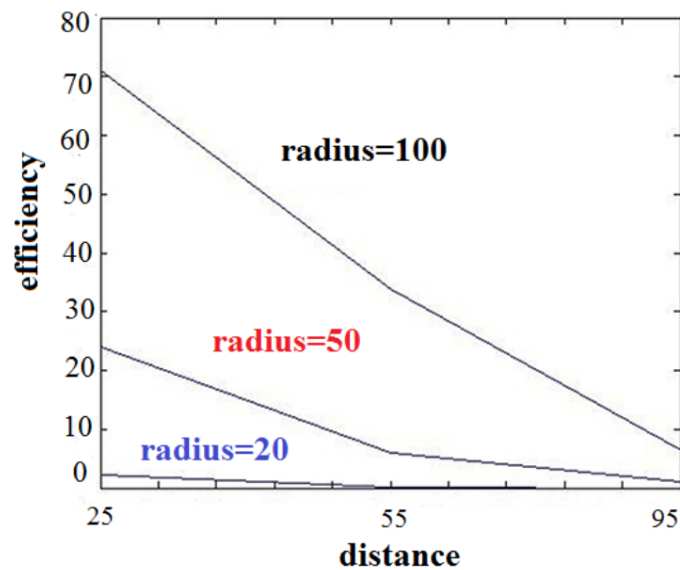


Figure 2.23: Plot for efficiency vs coil separation distance for different coil radii.

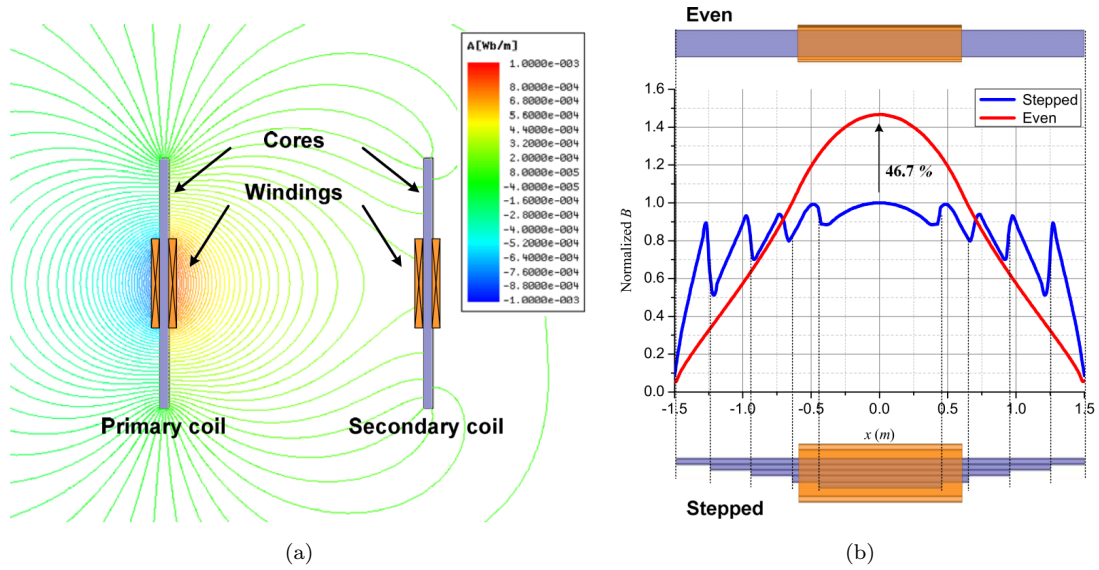


Figure 2.24: Simulation results of a) ferrite core resonator, and b) its Magnetic field distribution [87].

time and optimisation iterations. As a final example, Sohn *et al.* [100] compared the shielding effects of ferrite and copper plates for various transmitting coil architectures, in order to limit magnetic field exposure in a particular direction. It was demonstrated how copper is a better shield, but would reduce total magnetic field strength over the entire transmitting range. On the other hand, ferrite could enhance the field strength in the desired forward direction, but would only marginally shield it in the other direction.

One might have noticed that some of these enhancements are in effect a way of *shaping* the magnetic field in order to direct energy propagation. Other works have focused more specifically on the shaping aspect of field enhancement in order to achieve better WPT system performance through increased coil coupling and a decrease in flux leakage. Ye *et al.* [101] proposed a coil structure that more evenly distributes the magnetic field along the entire coil area, arguably improving WPT performance. They showed that their design could achieve a much more uniform coupling vs. the traditional spiral coil, but in doing so, sacrificed peak magnetic field strength as shown in Figure 2.25.

Besides changing the coil turns pattern, another way to re-distribute the magnetic field is by using multiple coils. Lim *et al.* [102] analysed the magnetic field distribution for two perpendicularly positioned square loop antennas. They showed that by alternating the current phase between the coils, they were able to create a

constructive and destructive interference pattern to effectively direct the magnetic field in varying lateral directions around the two antennas. They refer to this technique as *beamforming* due to its semblance with the classical phase-shift approach used in RF transmission. However, it is the author’s opinion that beamforming is not a suitable term as it incorrectly alludes to a radiative propagation of energy, which is not the case in magnetic coupling systems. This misnomer has been encountered in other instances, and it is suggested that *Magnetic Field Shaping* (MFS) would be a more appropriate term to use as it represents the actual process taking place. From experiments, Lim *et al.* [102] showed a 20% improvement in transmission efficiency for WPT as opposed to a single antenna approach. Yang *et al.* [103] also demonstrated a MFS technique using multiple transmitter coils, however the focus was on the tuning controller rather than the coils themselves. This work analytically demonstrated how to minimise power draw from all the transmitter coils and showed that the optimal current in the case of identical transmitter coils was proportional to the mutual inductance between the transmitting and receiving coils.

An interesting trend in MFS techniques is the design and use of *metamaterials*. These are repeated structures that manipulate, confine and focus the magnetic field path, similar in principle to how optical lenses effect light [104]. Metamaterials effectively mimic a permeability μ that might not exist in ordinary materials, such as a zero or negative μ [105], and their use within WPT has grown in recent years. They have been an inspiration in the design of this work’s unique resonant structures. A more thorough review of the science and use in previous works is presented in the next section.

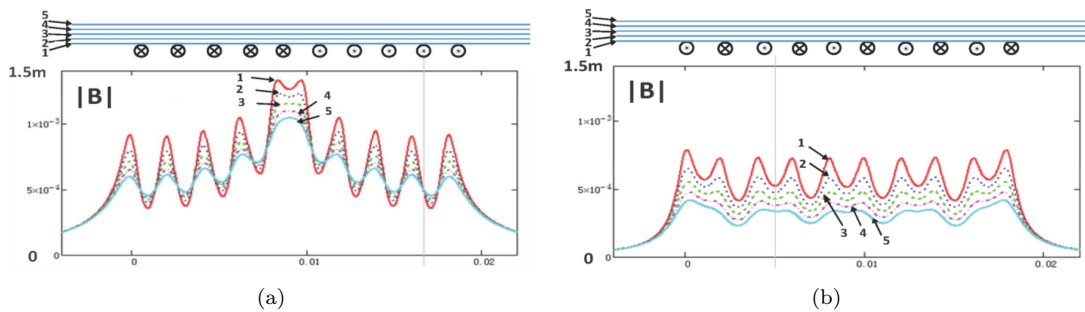


Figure 2.25: Simulation of Magnetic field strength vs coil position for a) a traditional spiral coil structure, and b) proposed coil structure. The numbered positioned 1-5 give a measurement of distance from the coil, which is 0.5mm, 0.6mm, 0.7mm, 0.8mm, 0.9mm respectively [101].

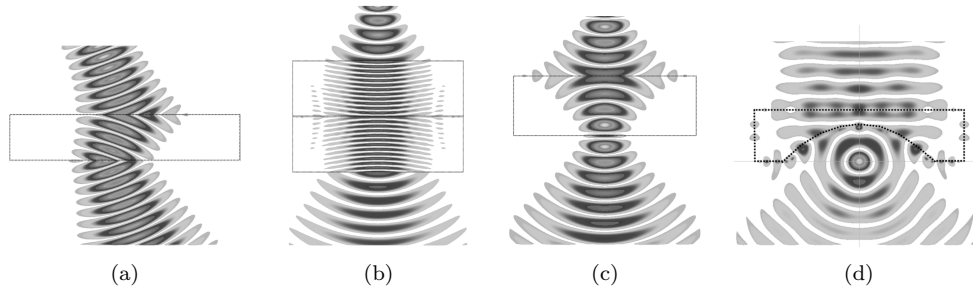


Figure 2.26: Electromagnetic wave propagation from air into a medium with negative ϵ and μ illustrating (a) refraction in the opposite direction, (b) beam spreading translation, (c) beam refocusing, and (d) Plane-to-Point source intensity redistribution [108].

2.3.3 Metamaterials and WPT

The study of metamaterials is an exciting field in physics that has recently attracted the attention of WPT researchers. The first real exploration of these artificial materials dates back to as early as 1898 when Bose [106] published work on the manipulation of electric waves with the use of artificial twisted structures. Different avenues of research carried on throughout the 20th Century and in 1968, Veselago [107] presented a theoretical study on plane-wave propagation using a hypothetical material where both the permittivity ϵ and permeability μ were negative. Such an improbable material would be able to change the behaviour of light and other electromagnetic waves interacting with it in a number of noteworthy ways (e.g. Doppler shift reversal; reversal of the direction of Cherenkov radiation, etc.). Figure 2.26 illustrates some examples of a wave transition through a series of simulated homogeneous metamaterials.

While an exciting proposition, it was not until 1999 when Smith *et al.* [109] and Smith *et al.* [110] experimentally demonstrated that an artificially constructed medium composed of periodic metallic wires and split rings could exhibit this type of behaviour over a narrow frequency band. Fundamentally, this was possible as the dimensions of a single element or *cell* in the periodic array were much smaller than the wavelength of the incident electromagnetic wave, thus the entire structure could be taken to be a homogeneous medium with an effective and frequency dependent $\epsilon(\omega)$ and $\mu(\omega)$ [111]. This discovery opened a whole new set possibilities for the field of metamaterials with several practical applications starting to emerge throughout the early 2000s, such as new imaging techniques and filters, sensors, electromagnetic cloaking, and radar absorbers.

The range of applications is potentially wide but fundamentally limited by fabrication technology [112]. Hence, much of today's research is concentrated on new fabrication techniques to manufacture metamaterials to scale for millimetre, terahertz, infrared, and even visible light parts of the spectrum.

The functionality of a metamaterial is typically limited to a narrow band of frequencies centred around the resonant frequency of the structure, hence, they are sometimes referred to as a frequency-selective surface or device. Within the periodic structure, each cell has its own reactive properties. When all cells are identical and sufficiently separated from one another in the array as to not couple significantly and affect their impedance [113], the resonant frequency of single cell dictates the resonant frequency of the whole periodic structure. The typical resonant behaviour observed is that the structure will either reflect or absorb energies at particular frequencies depending on the cell shape. At all other frequencies, the metamaterial structure would simply allow waves to pass through it unaffected. Note also that as more cells are incorporated into the overall surface the bandwidth of operation becomes narrower [114]. The most popular cell structures for energy absorption are typically composed of Split Ring Resonators (SRR) which are circular or square-shaped and made up of one or multiple broken concentric loops. Figure 2.27 shows a number of popular realisations found in the literature, and these are typically incorporated for radio frequency energy harvesting applications [115, 116, 117, 118, 119].

Copper tends to be the material of choice for conductive elements in the microwave region, however, gold and silver are being increasingly used [112] — silver in particular, due to its popularity in additive manufacturing as well as for its very low electrical resistance. It is also common to incorporate a ground plane for energy harvesting applications [117]. As with normal communication antennae, these help focus the propagating electromagnetic waves which are incident at wider angles.

Research on metamaterials for WPT was a relatively recent shift in focus and most likely spun-out organically from radio frequency energy harvesting research. The clever application of traditional metamaterials was thought to be the solution for many common issues of WPT. Firstly, by effectively increasing the amount of magnetic flux linkage, thereby increasing the coupling κ between coils; and secondly, by

allowing smaller Q -factors to be used and thus increasing system tolerance to change. Metamaterials were typically constructed to be just-off resonance of the WPT system's operating frequency in order to exploit a negative effective $\mu(\omega)$ medium in the power transfer path as presented in Figure 2.28.

As mentioned previously, the common interpretation in relevant literature is that the metamaterial behaves somewhat like a magnetic lens; manipulating, confining and focusing the magnetic field path similar to how optical lenses do for light [104]. A more apt interpretation is that metamaterials act to amplify the evanescent waves that would otherwise decay sharply in free space alone. Typically, researchers focus on achieving what is termed a *single-negative metamaterial*, in which only μ has a negative (or zero) real value [105]. It is important to note that this approach is only valid when applied

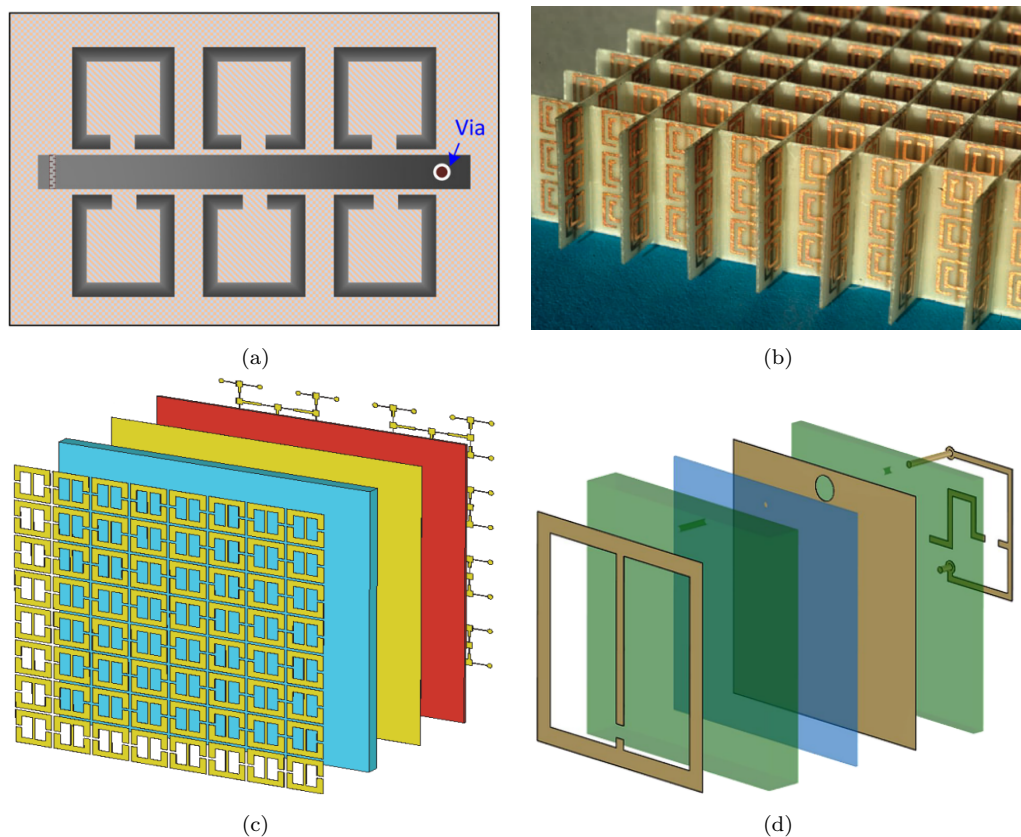


Figure 2.27: a) A near-infrared array energy harvester using copper split square rings and a copper micro-strip collector [115], b) a metamaterial formed by etched-copper SRRs on standard FR4 circuit board [120], c) an exploded view of a double slit ring metasurface incorporating a ground plane and energy harvesting feeds (copper), separated by Rogers RT6006 (blue) and RT6002 (red) [116], and d) a metamaterial rectifying surface as part of a larger radio frequency energy harvesting metasurface formed of copper top pattern, ground plane and rectifier, separated by multiple layers of Rogers RO4450F bondplys [117].

to the near-field region, where μ and ϵ are decoupled, and thus, independent from one another [122]. ϵ -negative media do in fact exist in nature, such as with silver or gold for visible and infrared light [123], however, naturally occurring μ -negative materials remain elusive.

Wang [124], whose earliest work (ca. 2010) illustrated the potential efficacy of metamaterials applied to near-field WPT, is a key contributor to the field and helped in seeding this new area of research. A review paper by Wang *et al.* [125] presented different metamaterial solutions using repeated coil patterns in order to improve transfer efficiency. Figure 2.29 demonstrates one of Wang *et al.*'s popular solutions for a 4-coil system powering a 40 W lightbulb which uses a single or multilayer planar coil pattern to increase transferred power. How this compares to open-ended repeater coils is further explored by Chalbalko *et al.* below.

Instead of a uniform coil pattern, Cho *et al.* [126] presented a unique hybrid coil metamaterial slab as illustrated in Figure 2.30. This created a negative μ at the edges of the slab and a zero μ in the centre, allowing for a much greater concentration of flux

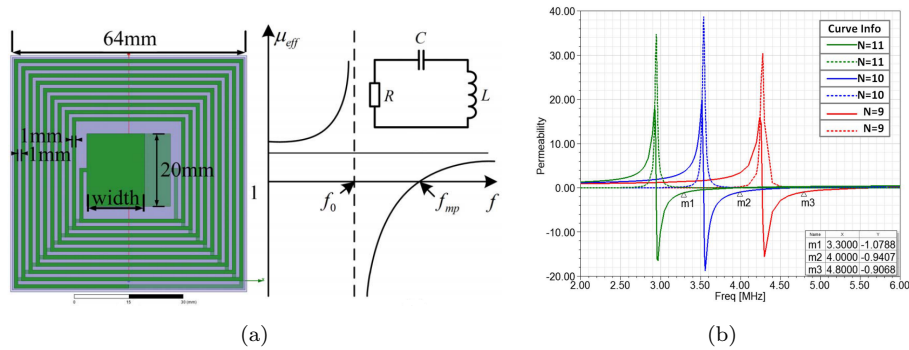


Figure 2.28: a) Schematic of a cell and the effective permeability of that cell with different frequencies, b) the curves of the cell's effective permeability with varying frequency (solid line) as well as the equivalent-circuit RLC resonant frequency (dotted line) for reference [121].

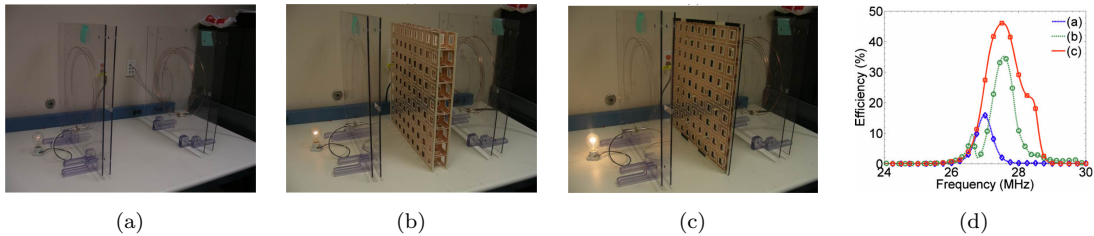


Figure 2.29: WPT system to power a 40 W lightbulb (a) without the metamaterial slab, (b) with the 3D metamaterial slab, (c) with a planar metamaterial slab, and (d) the recorded transmission efficiency of each system respectively [125].

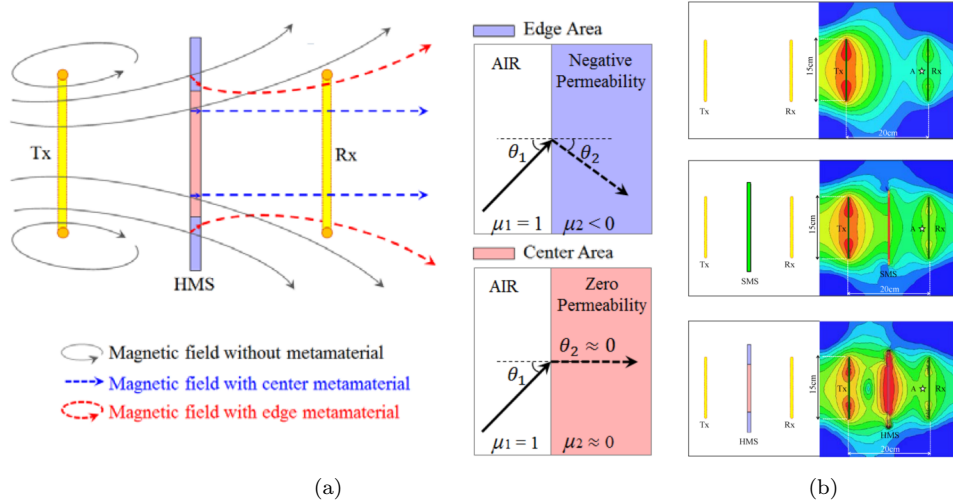


Figure 2.30: a) a hybrid metamaterial slab with different negative μ at the edges and zero μ at the centre (left), and b) a comparison of system performance without the metamaterial slab (top), with a traditional uniform μ metamaterial slab (middle), and the proposed hybrid μ metamaterial slab (bottom) [126].

to the receiver coil.

It is sometimes argued whether these types of implementations can be classed as true metamaterials as they exhibit a very similar structure and overall behaviour to coil relay architectures [114]. This argument has motivated other researchers to use a composition of different natural homogeneous materials instead to fundamentally achieve the same result. Some have even proposed the use of strongly diamagnetic materials as a way of uniquely confining magnetic fields or even to enhance their effective range: a superconductor inherently acts as a perfect diamagnetic and can be used to confine or concentrate the magnetic flux to increase the field strength [127]. Navau *et al.* [128] proposed a cylindrical metamaterial shell theoretically composed of ferromagnetic and superconductor alternating wedges in order to enhance magnetic coupling. Through an analysis, based on transformation optics, it was concluded that such a metamaterial shell around the transmitting side could drastically improve the effective range of transmission, while a shell on the receiving side could instead concentrate the magnetic field towards the centre of the shell, thereby improving the system's flux linkage. Figure 2.31 illustrates the proposed system's operation: the images on the left consider a single magnetic dipole, whereas the images on the right consider two dipoles.

Diaz-Rubio *et al.* [129] presented a similar system to Navau *et al.*, however,

they used Radial Photonic Crystal shells operating as a quadrupole instead of superconductors to achieve a similar effect. The only other encounter in the literature of a quadrupole WPT system was given by Pavel *et al.* [52]. Here, high refractive index dielectric spherical resonators instead of the more familiar Open-End coils were used, which could be operated in either dipole or quadrupole mode at select frequencies in the hundreds of megahertz range.

Very little work has been presented regarding how metamaterials compare to simple coil relays. Chalbalko *et al.* [130] addressed this issue in particular and presented a direct comparison between a theorised *perfect* metamaterial structure with negative μ and what was essentially an Open-End self-resonant coil, both of which positioned mid-way between the transmitting and receiving resonators. Simulations by Huang *et al.* [104] as presented in Figure 2.32, suggest that using an Open-End self-resonant coil of comparable size is actually a much better solution than the theorised metamaterial, thereby offering an opposing viewpoint that metamaterials necessarily deliver a significant improvement over multi-resonator system architectures.

Furthermore, in most cases encountered, the implementation of a metamaterial has impractically increased the size of the transmitting and receiving elements [131]. In

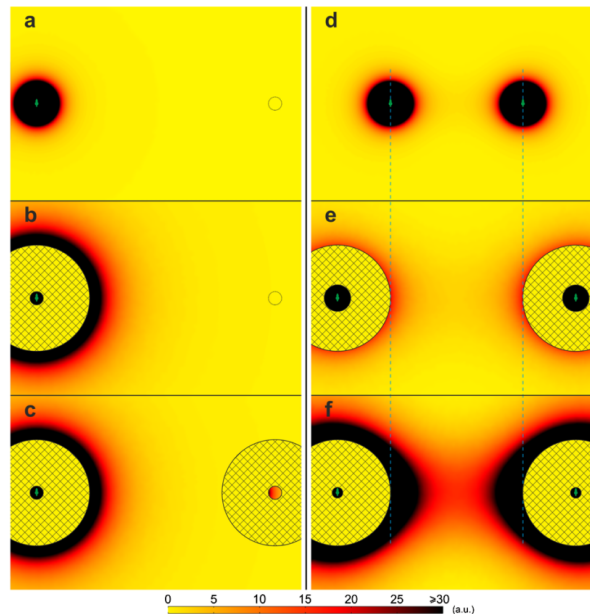


Figure 2.31: Simulation shows a) the field strength for a single dipole, b) how the field could be radially expanded by the use of the proposed shell, and c) how the field could be focused by another separated shell. Considering d) two dipoles, the simulation shows how the ratio of the inner and outer radii of the shell could be changed to e) confirm the field and f) expand the field in free space [128].

other instances, their very presence between transmitting and receiving couplers might seem to contradict the point of having a *wireless* transmission solution altogether [132]. Finally, their fabrication complexity and associated costs has historically inhibited research progress and commercial investment, especially since key target markets for practical applications are still in their infancy. Whatever the architecture or nomenclature, the key concept of creating a significantly different physical structure that can enhance WPT coupling has inspired this work. The advantages and novelty of an approach using multiple miniaturised coil structures outweigh the current downsides, which might be more easily overcome with the proper choice of application and a creative approach.

2.3.4 System Architectures

Having discussed the operation of the WPT coils themselves, it is pertinent to explore some of the most noteworthy holistic system architectures that have been developed. This section will examine different coil arrangements as well as the electronics and control systems employed to manage dynamically changing parameters during normal real-world operation.

Coil Arrangements

Throughout this chapter, reference has been made to the use of multi-coil systems. To clarify, the most common arrangements encountered in the literature can be categorised as either 2-, 3- or 4-coil WPT systems. 2-coil inductive systems are the simplest and

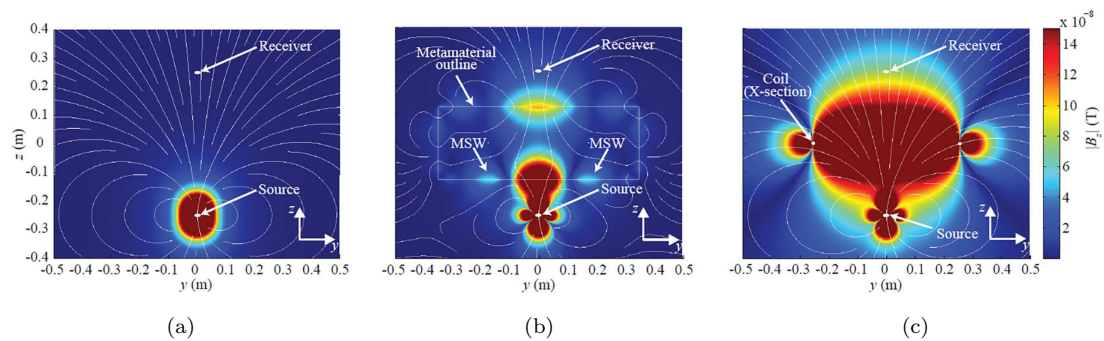


Figure 2.32: Simulation of WPT system a) using air only, b) using the metamaterial as theorised in [104], and c) using the Open-End self-resonant coil as in [130].

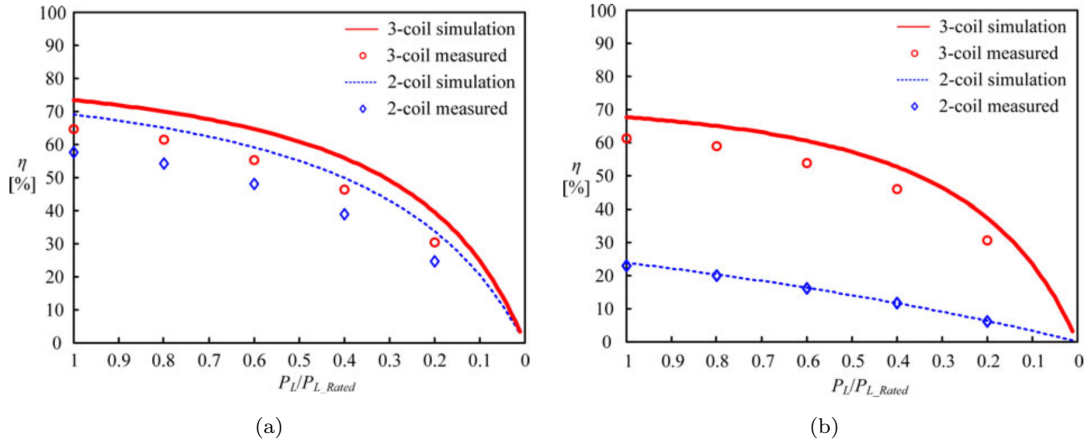


Figure 2.33: Comparison of system efficiencies of a 2- and 3-coil system under different loading conditions when the source resistance is a) 2 ohms and b) 50 ohms.

most dated arrangements; hence, they are often used as the benchmark against which 3- and 4-coil arrangements are compared.

Kiani *et al.* [133] presented an early comparison of these coil arrangements in terms of total power transfer and transfer efficiency. It was shown that 4-coil systems tend to be the most efficient but suffer from the least power transfer capability. By contrast, 2-coil systems tend to deliver the most power but exhibit the least transfer efficiency of all the arrangements over a set transfer range. A good compromise between both power and transfer efficiency seems to be provided by 3-coil systems (i.e. comprising an open-ended repeater coil sandwiched between a single pair of transmitting and receiving coils). Zhong *et al.* [134] attributed this increase of power transfer efficiency from multi-coil systems to the low resistivity of Open End coils. As previously discussed, these coils do not directly connect to the source or load circuits; hence, it was argued that these intermediary coils shift the current stress away from the lossy source circuits in the driving coil thereby enhancing the overall magnetic coupling to the receiver. Figure 2.33 illustrates this point clearly by comparing the efficiencies of 2- and 3-coil systems with changing source resistance.

Besides an increase in efficiency and robustness, a 3-coil system also reduces the electromagnetic field (EMF) strength in the vicinity of the coils during misalignment. This is an important factor to consider as misalignment or non-coupling of coils is inevitable in real-world applications and could create instances where the field strengths surpass what is permissible for human safety levels. Zhang *et al.* [135] demonstrated the

EMF for 2- and 3-coil systems: their simulation results, illustrated in Figure 2.34, show how the EMF for both systems are comparable when the coils are aligned. However, during misalignment, the EMF of the 2-coil system is significantly increased.

A 3-coil system also provides a more uniform efficiency across different load resistances when compared to a 2-coil system, however, in practice, voltage drops in power electronics and the non-linearity of circuits disrupts this uniformity [135].

Many of the advantages of a 3-coil system persist even when the coils are perpendicular to one another as reported by Ye *et al.* [136]. The work compared a standard 2-coil inductive system operating at 85 kHz with the same system employing a flat third coil in-between the two coils as shown in Figure 2.35. It was reported how employing this third coil translated into a potential size reduction of up to 66% of the transmitting and receiving coils to achieve the same power transmission efficiency at a set distance. They also argued that using a flat horizontal coil is a much more effective use of space, however, one would need to consider the material cost increase of their arrangement as opposed to other more compact solutions.

While 3-coils offer a good compromise, most works have tended to focus on maximising power transfer efficiency instead, hence the 4-coil system would likely be selected and indeed has been the most studied system architecture over the last decade. This coil arrangement is not a new idea: one of the earlier references of its use comes from a 1998 patent on WPT [137]. As illustrated in Figure 2.36, 4-coil systems

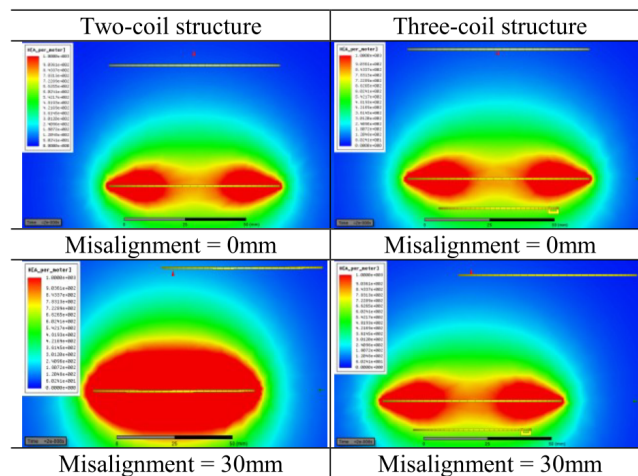


Figure 2.34: Comparison of the electromagnetic field strength of 2- and 3-coil systems during normal alignment (top) and during misalignment (bottom).

provide two extra mutual coupling coefficients, which provides extra freedom in coil position configurations in order to further extend transmission distances. It has been demonstrated that by varying the separation distances between each of these coils one could maximise either power transfer efficiency or transmission range [138, 139]. It was further shown that there are ideal separation distances between the coils depending on the desired performance, and that it is not simply a case of bringing the coils closer together, as doing so would significantly shift the resonant frequency of the system due to overcoupling, as examined in section 2.2.6.

According to Chen *et al.* [89] and with reference to Figure 2.36, the condition for maximum power in a 4-coil system can be expressed as

$$\frac{\kappa_{PS}\kappa_{RD}}{\kappa_{SR}} = 1 \quad (2.3.11)$$

meaning that even at long transmission distances where κ_{SR} could be very small, by improving the coupling between the source and transmitting coil, and the receiving and load coil, one could still theoretically achieve maximum power transfer efficiency.

Although 4-coil systems have been stated to be the weakest in terms of power transfer capabilities [133], they could easily provide sufficient power for most of the envisioned human wearable applications. In fact, at this relatively low power, achieving

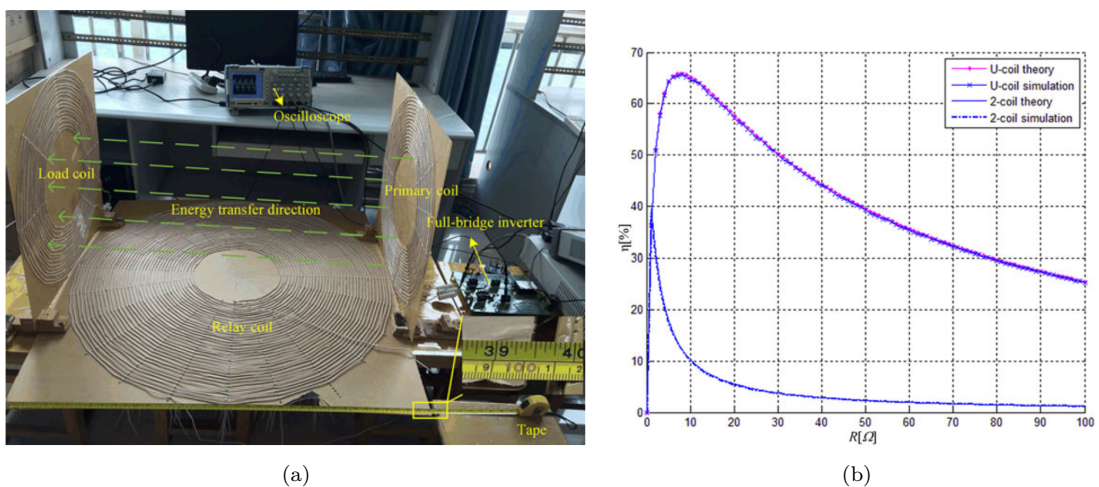


Figure 2.35: a) System employing third intermediary coil for a standard 2-coil system and b) power transfer efficiency vs load resistance as reported in [136].

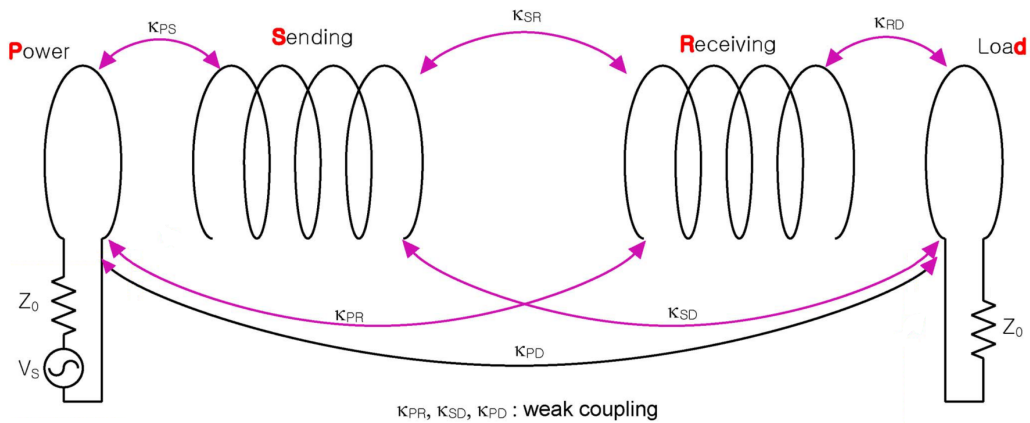


Figure 2.36: 4-coil system representation showing the extra mutual coupling present between the individual coils [89]

high power transfer is a priority, and 4-coil systems are exceedingly good at maintaining this over transmission distances well beyond the effective transmitting coil dimension [32]. Dang *et al.* [140] modelled the performance of a 4-coil system and compared it with the classic 2-coil system confirming that, for parameter equivalent systems, a 4-coil arrangement is able to maintain a sufficiently high power transfer efficiency over a much longer range than the 2-coil system as presented in Figure 2.37. Additionally, 4-coil systems have a much higher misalignment tolerance than any other arrangement examined so far.

It is worth pointing out that 4-coil systems employ impedance matching and hence can only ever have a maximum system efficiency of 50%. This has often been stated as the main drawback with 4-coil implementations for mid-range WPT [32]. For this study,

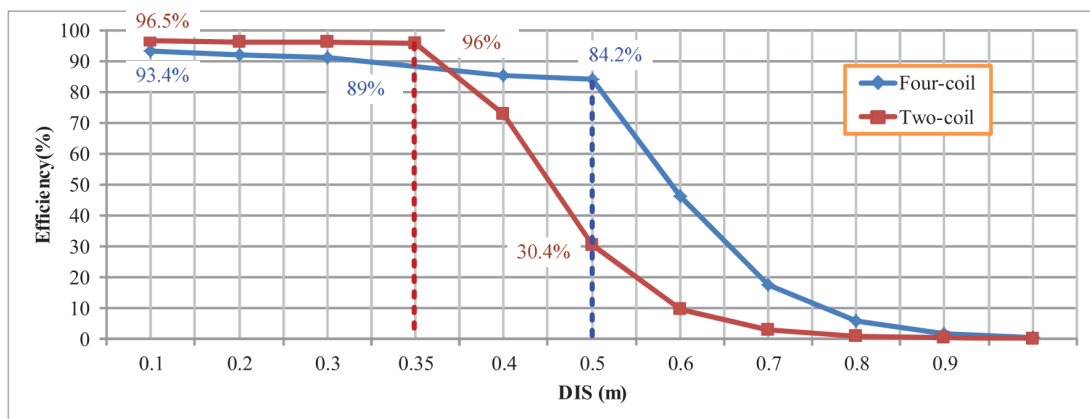


Figure 2.37: Power transfer efficiency vs transmission distance comparison between equivalent 4-coil and 2-coil systems [140]

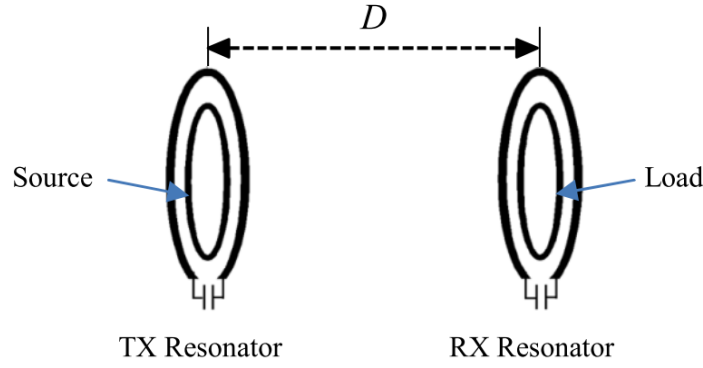


Figure 2.38: Conformal SCMR system whereby the transmitting (Tx) and receiving (Rx) coils are in the same place as the source and load coils [145].

however, the use of low-power applications as well as the need for large transmission distances makes the 4-coil system (or at least the principle behind 4-coil transmission) an attractive solution over the other coil arrangements discussed.

A primary challenge with 4-coil systems is the greater spatial requirement as intermediary coils tend to be designed as helical resonators [48]. Many works have explored ways to minimise the space requirements, often at the expense of coupling [141, 142, 143, 144]. The most popular solution encountered is to create conformal coils as illustrated in Figure 2.38. This structure could reduce the volume considerably, making the 4-coil system more suitable for mobile devices and wearable applications [145] and even implantable devices [146, 147].

However, an issue that arises with this sort of structure is that the coils in either the transmitting or receiving pairs could become too close to one another. This has the effect of reducing the operating Q -factor of the system as if both coils were loaded to the source. This arises from the significantly increased mutual coupling between κ_{PS} and κ_{RD} [71]. In order to overcome this, the inductance ratio of the coils, according to equation (2.3.12) below, must be as high as possible to reduce the loading of the resonator and thus increase the operational Q -factor as illustrated in Figure 2.39.

$$Ind_{ratio} = \frac{L_P}{L_S} \quad \text{and} \quad \frac{L_R}{L_D} \quad (2.3.12)$$

Incidentally, this is often why the driving and load coils are single-loop antennas,

while the transmitting and receiving resonators are often constructed as multi-loop helical coils. It can be further observed that the dielectric of the capacitor has a very strong impact on the internal resistance of the circuits, therefore it is important to select low loss and low ESR capacitors to improve system efficiency as transmission distances increase [71].

Another noteworthy 4-coil structure has been presented by Jolani *et al.* [148]. A flat array of transmitter resonators driven by a single large loop source coil was proposed in order to increase the effective area of the transmission side while at the same time maintaining a relatively uniform transmission efficiency over the whole transmission area as shown in Figure 2.40. In essence, this could be viewed as a field-shaping technique but applied to an entire architecture. Their solution was in response to the problem of lateral misalignment issues that are common for dynamic WPT systems.

The argument for using multi-coil arrangements does not necessary end with 4-coil systems. In fact, many works suggest using many intermediary coils in order to further extend transmission distance [149]. Liu and Wang [150] presented a strongly coupled system using 4 resonators instead of just 2. Though more complex than the usual 4-coil arrangement, they argued that this 6-coil system achieved a much larger operational frequency range where high power efficiency transfer could occur. Note the presence of

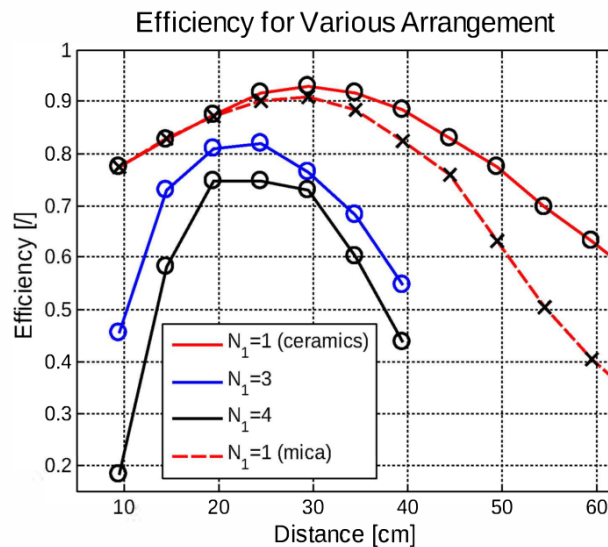


Figure 2.39: Efficiency vs transmission distance for a conformal SCMR system. Plot compares the efficiency achieved through a fixed transmitting coil and varying driving coil turns. The (*ceramics*) and (*mica*) refer to the capacitor dielectric used [71]

three frequency peaks in the strongly coupled region instead of the usual two as shown in Figure 2.41.

The most cited multi-coil system in the literature is by Zhong *et al.* [41] which used an aptly named domino relay arrangement of many Open-End coils achieving high power transfer efficiencies at several watts over a few metres transmission distances. Subsequent works have also explored the possibility of turning each relay coil in the domino chain into its own separate load or transmitter device. In one system [151], each relay device could extract a portion of the transferred power and then re-transmit any unused power to the next device along the chain. Though incredibly complex to achieve at this stage, in a real-world dynamic system this would be a highly effective method of ensuring that multiple unpredictable devices in an enclosed area can be powered with minimum overall losses.

As has been stated throughout this discussion, one of the biggest issues with WPT systems is coil alignment. Normally, published works quote the efficiency, power and/or transmission distance given the optimum alignment; however, this would rarely be the case in practice. Both lateral and angular misalignment between transmitting and receiving coils would often occur, and while some coil designs, topologies and arrangements are more efficient than others at compensating for these misalignments,

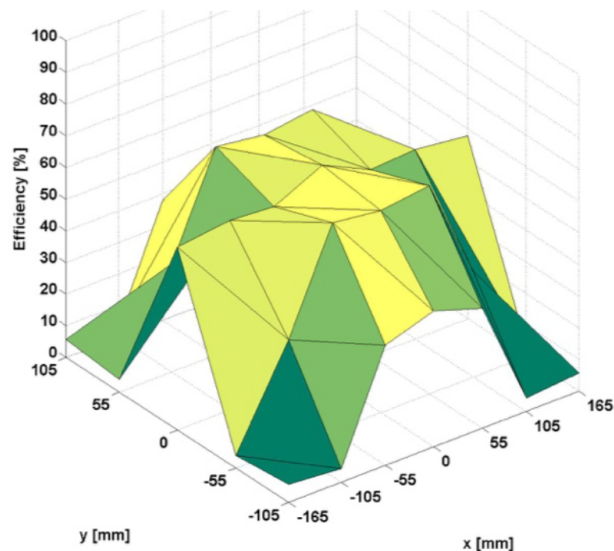


Figure 2.40: Efficiency vs transmission area simulation for a 4-coil system using four flat transmitting resonators driven by a single loop source antenna [148].

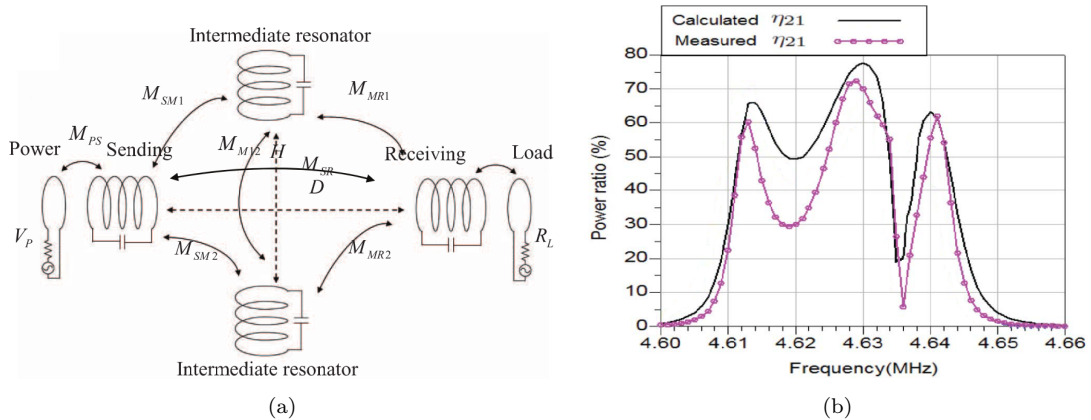


Figure 2.41: a) 6-coil SCMR system diagram and b) simulated and measured power ratio vs operating frequency [150].

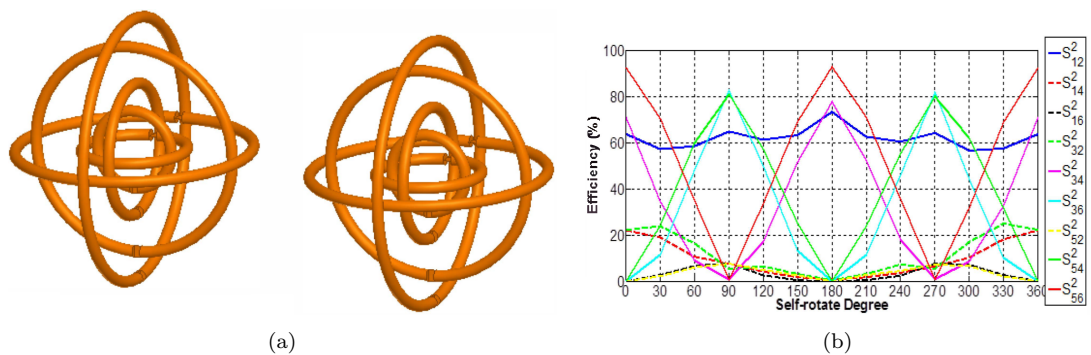


Figure 2.42: a) Proposed orthogonal multi-coil SCMR system and b) efficiency vs angular misalignment of the proposed system [155]

the overall effect of misalignment will always be non-trivial [21]. Some works have addressed this issue by designing orthogonal transmission and receiving multi-coils [152, 153, 154]. The only noteworthy improvement in recent years is from Daerhan *et al.* [155] which presented a multi-coil orthogonal transmitting side, but incorporating the 4-coil principle for high transfer efficiency. The proposed system used conformal loop coils to maintain a relatively uniform efficiency characteristic over the entire range of angular alignment as shown in Figure 2.42. It is clear that such omni-directional WPT systems would require larger volumes for the transmitting and receiving coils and hence, are not currently suitable for smaller WPT applications.

Control Systems

When considering the practical implementation of WPT systems, it is likely that a control system will need to be employed in order to maintain desired performance.

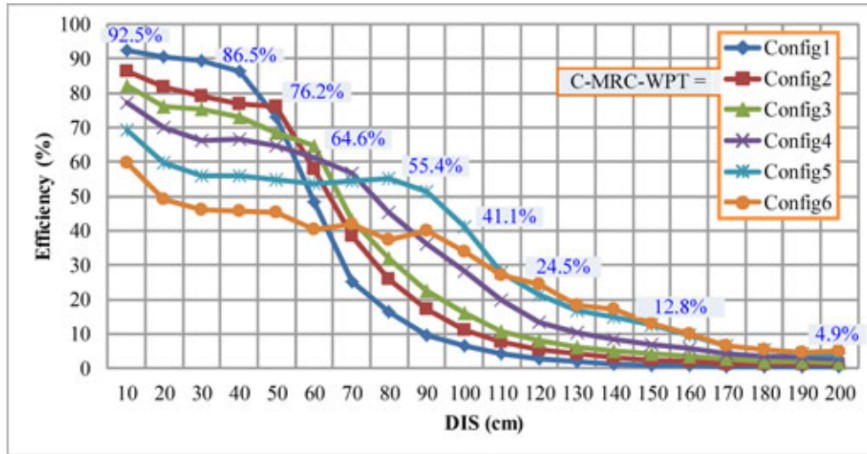


Figure 2.43: Efficiency vs transmission distance with various C_P and C_S configurations [156].

For example, in the aforementioned orthogonal multi-coil systems, a control system may take the form of a current phase controller in order to create an interference pattern to enhance the magnetic field in particular directions [153]. In a standard 4-coil implementation using an SPS topology, Dang *et al.* [156] used a switch controller to extend transmitting distances via capacitive tuning. Essentially, by digitally varying the capacitive values of C_P and C_S on the transmitting side they could maintain a high transmission efficiency over the entire transmission range as shown in Figure 2.43. A similar method of operation was also reported by Mao *et al.* [157], whereby the system varied the resonant frequencies of both the transmitter and receiver via digital capacitive switching in order to maintain a fixed operating frequency.

Aside from the control methods mentioned above, all other control strategies for SCMR tend to involve tuning the operating frequency of the system. Changes in the surrounding temperature and humidity, the presence of highly permeable materials, or even the human body itself could inadvertently shift the resonant frequency enough to significantly alter a system's performance. This sensitivity is due to a combination of the self-resonant nature and the narrow operational bandwidth attributed to high- Q coils in typical SCMR. A mismatch between the operating and resonant frequencies of as little as 1.5% could see power transfer efficiencies drop by a staggering 60% [139]. Zhao *et al.* [158] presented a simple way to accurately infer this frequency mismatch according to the phase difference between the transmitter and the voltage of the receiver. The greater this phase difference, the larger the frequency mismatched,

and hence the more severe the drop in system transfer efficiency, as shown in Figure 2.44.

Clearly, accurate frequency tracking is key, and this will need to be achieved through a feedback controller. The method of communication between WPT devices is another important aspect in research and would normally be facilitated through a dedicated short range radio frequency transmitter link as part of the system architecture or even, in some rare cases, through the transmitting and receiving coils themselves [159]. Note that in the latter case careful consideration is required as there would naturally be a trade-off between data transfer rates and power efficiency due to the use of high Q coils which, as already mentioned, are characterised by their extremely narrow operational frequency band [160].

Often in the literature, different control strategies are primarily explored for multi-transmitting or multi-receiving WPT systems. As one can envisage, future WPT systems might need to power multiple devices using a single transmitter. Alternatively, multiple devices in motion may need to be able to co-ordinate power transfer between multiple transmitter nodes [161]. It is rare to encounter multi-transmitter systems concurrently powering a single receiver, possibly due to their limited use in applications, but also due to the inherent difficulty in achieving maximum power transfer efficiency. Ku and Kong [162] presented an analysis for such a system and showed that only by varying both the signal amplitude and phase between all transmitters with respect

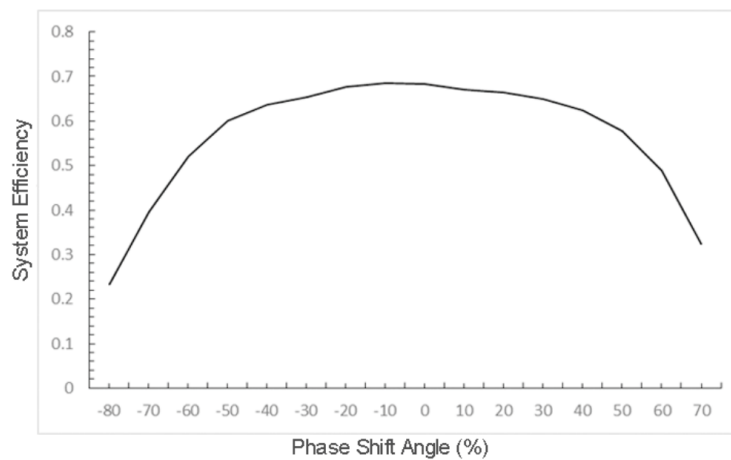


Figure 2.44: Efficiency vs phase angle between current and voltage waveforms in the transmitter and receiver respectively [158].

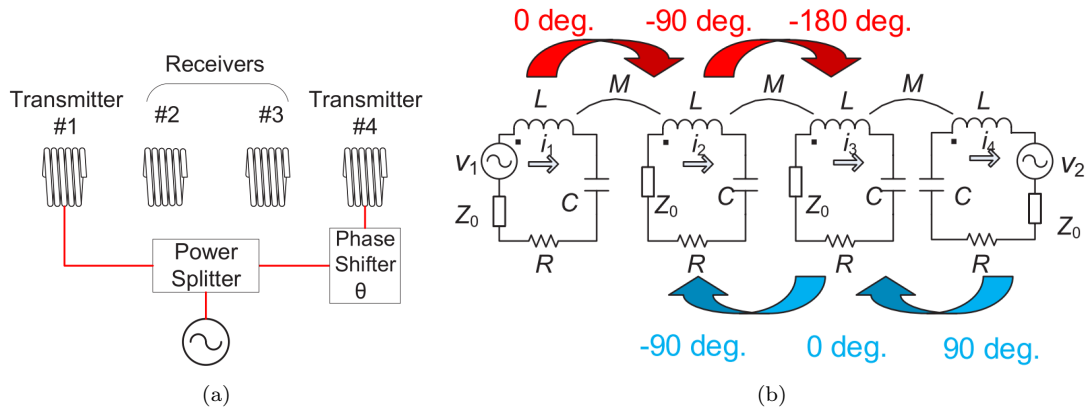


Figure 2.45: a) Proposed system diagram [164] and b) theoretical operation under principle of superposition of current waves [164].

to receiver-relative position and alignment can maximum power transfer efficiency be achieved. Clearly, a very complex control system would be required in practice.

In the case of multi-receiver systems, the main challenge is related to power capacity: as multiple receivers simultaneously draw power from the transmitter's near-field, the power delivered to each receiver will naturally be heavily reduced depending on the number of receivers as well as their relative positions. A relatively simple implementation to address this issue was presented by Moghadam *et al.* [163]. A *point-to-multipoint* system which employed a dynamic time-sharing algorithm was proposed which actively switched the receivers' power capture circuits on and off, depending on the total number of receivers and their proximity to the transmitter. Unfortunately, continuously switching these types of circuits at potentially high rates is not ideal. Instead, Yoshida *et al.* [164] presented a continuous targeted power delivery approach using multiple transmitters. By altering the current phase in each transmitter, different receivers in a chain could receive different power levels through constructive or destructive current superposition as illustrated in Figure 2.45. However, despite this clever approach, there is only a niche set of applications where this could feasibly be implemented. Moreover, it is not the most effective means of targeted transmission as, from experiments, the untargeted receiver was still able to capture around 10% of the total power intended for the targeted receiver.

A better targeted multi-receiver system was presented by Kim *et al.* [165]. The proposed system was able to tune the operational frequency of the transmitter to only

match the resonant frequency of a single receiver at any one time. By using high enough Q -coils, the resonant frequencies of distinct receivers could be made very close to one another, however, the authors purposely maintained a resonant frequency separation of 2.5 MHz between receivers in order to minimise the risk of overlap due to frequency shifts caused by changes in the surrounding conditions. With this method, they were able to limit *leakage* to untargeted receivers to less than 0.6%. Though impressive, note that there would be a very small number of receivers that this system could feasibility operate with due to legally-set bandwidth limitations [48].

As a final note on control systems, maximum power transfer or maximum system efficiency can be highly dependent on the load resistance. This has been shown in numerous works throughout the literature and is often considered during normal system design. However, many works on multi-receiver systems rarely consider the case when coupling between the receivers themselves occurs, and in fact, this may drastically change the optimum load condition. As rigorously demonstrated by Monti *et al.* [166], not accounting for this additional coupling in multi-receiver systems could have serious consequences for system performance. In their work, they presented a means to adapt their system, possibly by digitally introducing new reactances into the receiver side circuitry in order to counteract this unwanted coupling and maintain the desired system performance.

Power Management

So far, different coil systems and the associated control strategies employed to maintain the optimum power transfer link between them have been discussed. However, these are but one part of an entire power management system composed of power electronics, microcontrollers, convertors, rectifiers and impedance matching networks. Altogether they make up the real WPT system, hence these components need to be understood and their non-ideal characteristics accounted for in order to assess and make accurate predictions on system performance [167].

Often, an AC transmitting signal with a set of desired characteristic will be produced by a microcontroller. This signal alone would constitute no power and therefore, a power amplifier would need to be used, usually supplied by a DC source which in

itself might have been supplied through AC power lines. This conversion and power regulation is somewhat mirrored on the receiver side also, as ultimately electrical loads would need a stable DC supply at a fixed voltage. Commercially there are many solutions that aid in performing these conversions, but of particular interest for researchers in WPT is the choice and design of the amplifier, as this is where a vast majority of power loss would occur due to high frequency MOSFET switching losses [168]. Class D and E amplifiers are commonly encountered in the literature, and while they do not offer the best signal fidelity compared to Class A through C amplifiers, they certainly make up for this with their high efficiencies (in practice 80-90%) [169].

In 2009, Low *et al.* [142] presented a very thorough practical comparison between Class D and E amplifiers for WPT systems and ultimately concluded that, despite its lesser popularity at the time, Class E would be the preferred choice of amplifier. Interestingly, variations of the Class E design have since become the most popular choice used by WPT researchers, and these have appeared in several works either as the focal point in the study [170] or merely as the choice amplifier during system implementation and testing [171]. The main argument for Class E implementation is that it is both simpler and more efficient [142]: Class D would normally require a supply voltage 1.687 times that of an equivalent Class E design, as well as requiring a pair of out-of-phase gate drives as opposed to just one. Finally, Class D would need to be more carefully designed to maintain an accurate frequency tuning as coil separation varies.

Assuming a Class E design, minimum power dissipation would occur by ensuring a zero voltage exists across the MOSFET during switching, as well as a zero current during the closing phase of the switch. In doing so the optimum condition is achieved and the amplifier maintains the expected high transfer efficiencies. However, in practice maintaining this zero-voltage condition is not always easy due to changes in the reflected load impedance seen on the primary, due to coupling variations between the transmitting and receiving coils. Wang *et al.* [172] examined this issue for a practical WPT system and proposed the addition of a double-end impedance converter network as shown in Figure 2.46. This solution incorporated a low ESR capacitor and inductor circuit in order to maintain a uniform efficiency over a large range of effective load values.

For this work, an approach based on the Class E amplifier has been chosen. The design, realisation and testing is detailed in chapter 6.

2.4 Industry Standards and Safety

While there have been several practical examples of systems employing WPT (e.g. RFID or electric toothbrush charging), a huge commercial opportunity has recently arisen, partly due to the ever-increasing popularity of portable smart devices. In fact, outside of academia, many industries have been working on commercial solutions by filing patents, incorporating companies, and exercising their influence to push for new proprietary standards to be adopted. Besides consumer technologies, there is a use for this technology in future smart-city infrastructure: for example, the UK government had initially considered trails for electric vehicle charging technologies to be deployed on motorways and major A roads [173]. The need for such a system, as shown in

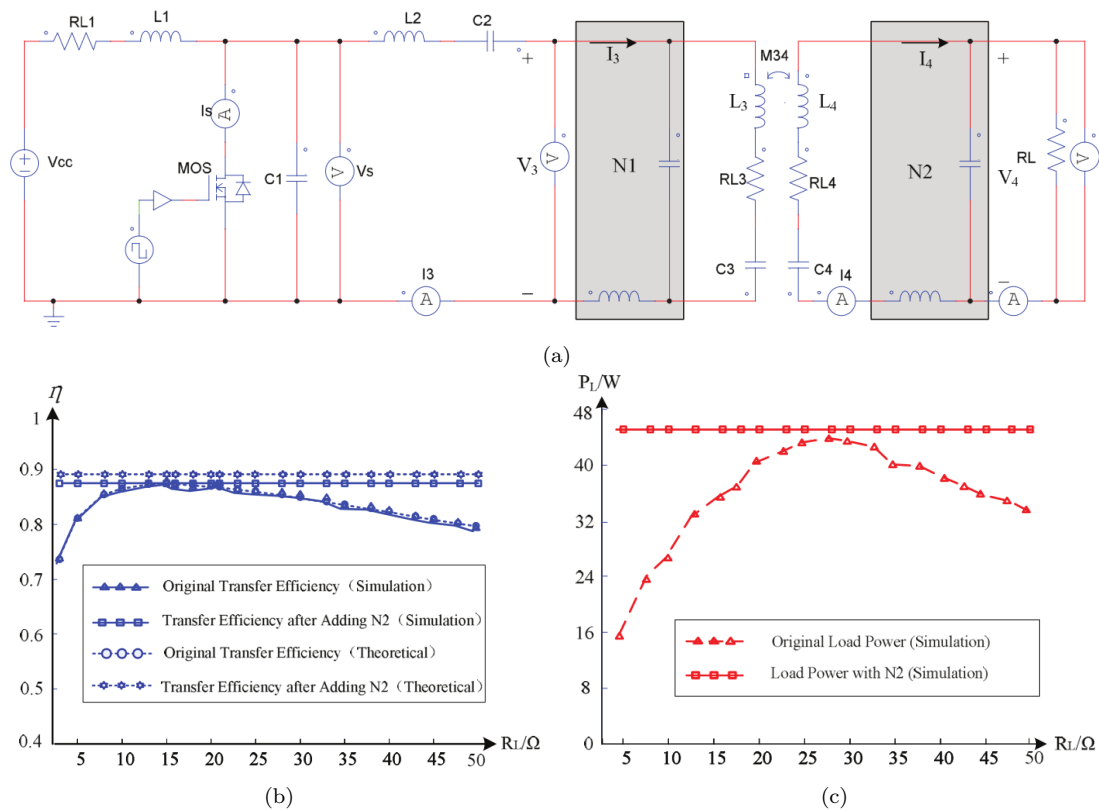


Figure 2.46: a) Simulating schematic for the WPT system proposed in [172] incorporating the impedance converter network $N1$ and $N2$ and plots for b) system efficiency and c) transferred power vs load resistance [172]

Figure 2.47, has emerged due to an increase in electric vehicle popularity as well as global initiatives to reduce fossil fuel reliance and air pollution. This specific trial is still pending deployment, however, it demonstrates the breath of scope of WPT.

The earliest forerunners for commercial WPT took the form of start-up companies: notably, a spin out from the University of Florida called WiPower was created in 2004 in order to develop and commercialise academic research for WPT systems. Their technology used a simple system that could dynamically adjust power supplied to a receiver without the need for a control system. Similarly, the famous 2007 research conducted at MIT culminated in the incorporation of WiTricity [174], likewise formed in order to capitalise on the emerging market opportunity presented by WPT.

Shortly after, the Wireless Power Consortium (WPC) was formed in December 2008 and was the first real attempt to create and promote a new interface standard for all new commercial products. Their interface, named Qi , defined protocols for charging portable devices up to a maximum of either 5 W or 120 W, depending on the class, up to a distance of 40 mm using charging platforms incorporating more traditional resonant inductive coupling at frequencies between 80 and 300 kHz [157]. Currently, the consortium has over 220 member companies and including the likes of Nokia, HTC, LG, Huawei, and Apple [175].

In response to Qi , several other companies joined forces in 2012 to form a new consortium and launch their own competing WPT standard [176]. This consortium was called the Alliance for Wireless Power (A4WP) and originally included WiPower (which had been acquired by Qualcomm in 2010), WiTricity and Samsung along with

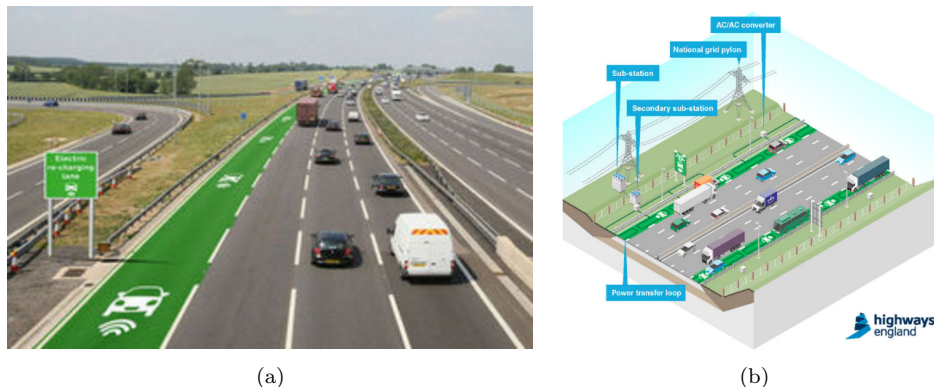


Figure 2.47: a) Example of proposed system deployed on a motorway and b) diagram showing proposed system operation [173].

some other major component manufacturers. A4WP later expanded its membership to include Intel in 2013. Their initial interface standard was named *Rezence* and used magnetic resonance at 6.78 MHz (± 15 kHz) to transmit a maximum of 50 W for up to eight devices at distances of up to 50 mm. The standard also included a 2.4 GHz communication channel as part of the control protocol in order to identify valid loads and protect against non-compliant devices. Around the same time the Power Matters Alliance (PMA) was formed, likewise to advance standards and protocols for WPT. It included AT&T, Duracell, the Federal Communications Commission (FCC), and Starbucks. In June 2015, A4WP and PMA merged into one entity called The AirFuel Alliance, which arguably became the new de facto industry organisation driving wireless charging adoption, using their unified *Airfuel* interface standard. Today, many products use both standards; however, *Airfuel* seems to be the preferred option over *Qi* as more popular devices are becoming certified almost exclusively under this standard. Some certified products include nearly all newer Samsung Galaxy smartphones and tablets, some Nokia models, LG and iPhone models, and some newer Dell Monitor ranges [177]. This increased popularity seems to have arisen from *Airfuel*'s superior charging tolerances for both angular and lateral misalignments, giving users a much broader spatial freedom [178]. Currently, the standards examined, though impressive, do not represent the best solutions with the majority of reported end-to-end efficiencies still well under 60% for various loads as shown in Figure 2.48.

Nevertheless, analysts predict that this emerging market alone will triple its current value by the end of 2020, growing to between \$12-15 billion [180, 181, 28] with WPT being deployed across multiple sectors including Consumer Electronics, Transport, Sports, Fashion, Healthcare, Medical, and Military.

When designing commercial systems as well as the standards that govern them, human and animal safety are of the utmost importance. Exposure to electric, magnetic and electromagnetic fields is of serious concern and many countries either enforce statutory limitations via independent bodies (such as the FCC), or merely incorporate recommendations from internationally recognised bodies as a matter of government policy. The main bodies cited are the ICNIRP and the IEEE International Committee on Electromagnetic Safety (ICES); both of which regularly review and

publish guidelines based on evolving scientific evidence [182].

For low power near-field WPT, one would expect the energy in the form of electromagnetic waves to be well under the limitations set by both ICNIRP and ICES [91], hence, this will be omitted from further discussion. When the SCMR scheme by Karalis *et al.* [44] was presented in 2007, the researchers had asserted that their proposed system would be inherently safe. They argued that, as humans are non-magnetic, users would be practically unaffected by the magnetic fields formed, making a somewhat naïve comparison to the large fields created in MRI machines regularly used during health screenings. Subsequent works have correctly pointed out that, in fact, it is electric currents induced in the body by time-varying magnetic fields that is the main cause of concern, not exposure to the magnetic field itself. A review paper by Hui *et al.* [32] pointed to multiple sources that demonstrated how the electric and magnetic fields created by the 4-coil system by the MIT team at instances had surpassed the limits on exposure set by both the ICNIRP and ICES. Through modelling, it can be

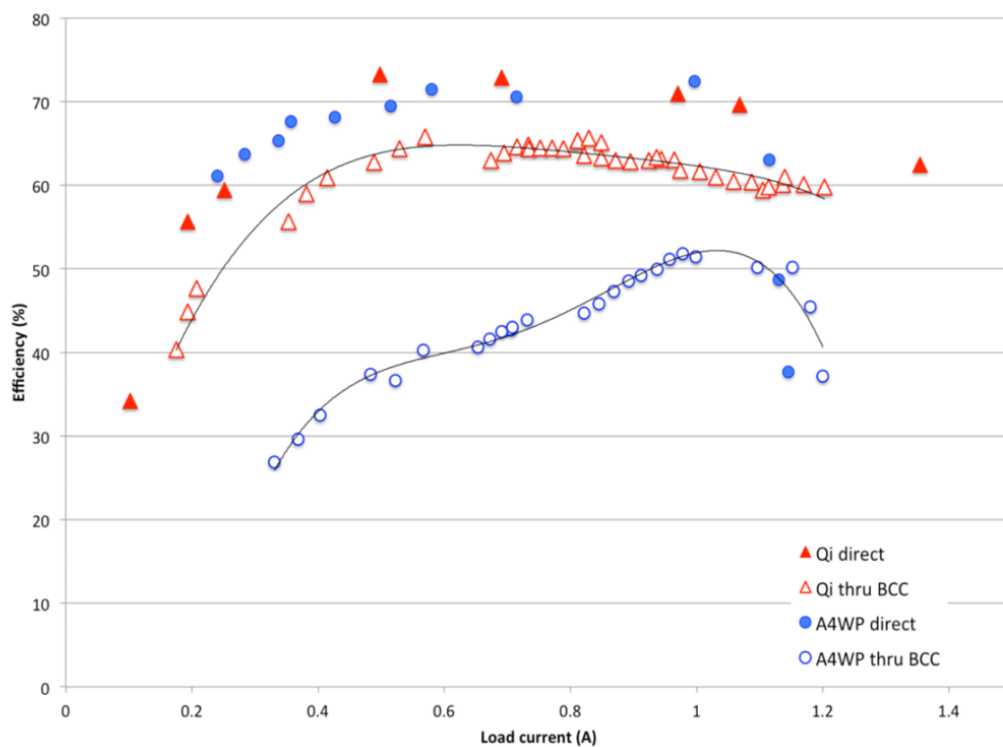


Figure 2.48: Plot of Efficiency vs Load current for both Qi and *Resence* standards, either through direct power or Battery charge-cycle (BCC) [179]. The drop in efficiency observed between the direct power and BCC approach occurs as more energy is consumed simply to charge the battery beyond 90%. Thus, this energy does not reach the load circuitry, resulting in a loss of effective transmitter to receiver efficiency.

determined that the received transmission power under the MIT design would need to be limited to around 45 W, in order to comply with regulation, assuming no shielding or flux confinement methods are employed.

Clearly, both the strengths of electric and magnetic fields as well as their rate of change must be considered in order to safely design near-field WPT systems. This health concern primarily arises due to adverse effects associated with nerve and muscle stimulation, as well as tissue heating. The severity of these effects is highly dependent on frequency, and in general, electro-stimulation effects dominate under 100 kHz whereas tissue heating effects would likely dominate above 100 kHz [32].

Nerve stimulation for both the central and peripheral nervous system is deeply discussed in ICNIRP's 1998 [183] and 2010 standards [88] which give figures for the maximum permissible internal electric field and current density induced by time-varying magnetic fields. It has often been stated that measuring these induced effects is quite difficult in practice and would require either sophisticated measurement techniques with living subjects or very accurate body models to simulate the exposure under various conditions. Both the ICNIRP and the ICES have therefore set their own reference field strengths for WPT systems at various frequencies in order to create a convenient set of conservative upper limits for any system designed, ensuring current safety requirements are met. These figures, however, stem from limited studies and thus are subject to change as more evidence continues to emerge. The current levels and their variance with frequency are illustrated in Figure 2.49.

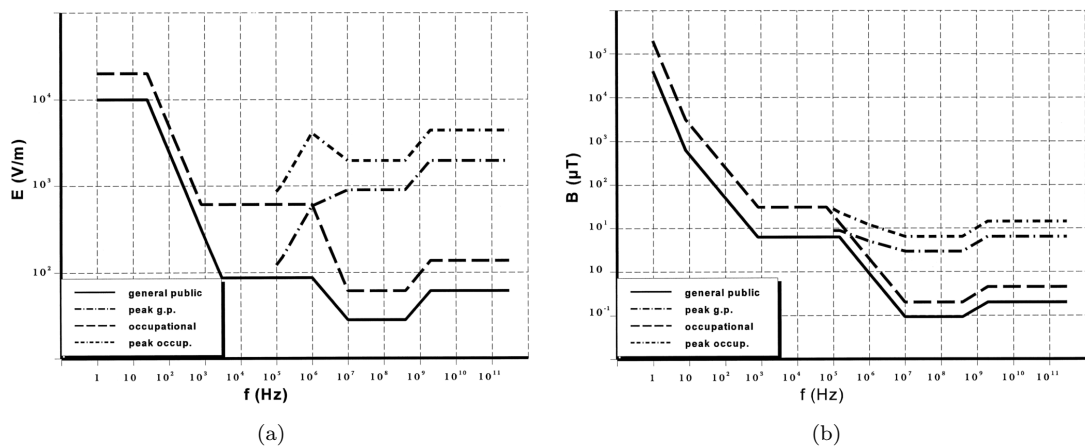


Figure 2.49: Plots of reference levels for exposure to time varying a) electric fields and b) magnetic fields [183]

In the case of tissue heating, both the ICNIRP and ICES recommend figures using specific absorption rate (SAR), which is a measure of the amount of energy absorbed by various parts of the body. SAR values directly translate into a rise of temperature for specific tissues and, as a general rule of thumb, have been set in order to limit the temperature rise of any part of the body to 1-2°C [184]. Note that there is still much debate on the commercial SAR limits set, with some claiming they are still too high, while others asserting that at current levels, even the most sensitive human organs and tissue would not be adversely affected [185]. The current permissible SAR levels for different parts of the body are presented in Table 2.2.

Table 2.2: RF Exposure limits set for general public (100 kHz - 10 MHz)

	SAR[W/kg] Whole Body Average	SAR[W/kg] Head/Trunk - determined over the mass of 1 gram	SAR[W/kg] Limbs - determined over the mass of 1 gram	Induced E (2mm ³ -avg) [V/m] CNS [†] & PNS [‡]	Induced J (1cm ² -avg) [mA/m ²] Head/Trunk
ICNIRP 1998	0.08	2	4	-	f*/500
ICNIRP 2010	0.08	2	4	1.35x10 ⁻⁴ f*	-
FCC	0.08	1.6	4	-	-

[†] Central Nervous System. [‡] Peripheral Nervous System. *Signal frequency.

Many works have pointed out that WPT systems employing SCMR typically have very low losses due to the use of high- Q coils, which arguably help limit the amount of human exposure. However, in many works, SCMR is normally achieved using Open-End coils which, as discussed in section 2.3.2, resonate based on the self-inductance and parasitic capacitance of the coils themselves. This means that energy emitted from these coils will be conveyed by both electric and magnetic fields. This is in contrast to Short-End coils, where the electric field would become concentrated in the connected lumped capacitor, and instead the energy is practically conveyed by the magnetic field alone. This is an important observation since the safety threshold for energy conveyance is much higher for magnetic fields, given that the human body is not directly affected by them. Hirayama *et al.* [186] compared the difference between these two coil types both in terms of CT and CMT. As illustrated in Figure 2.50, for equivalent coils, self-inductance is four times larger for Short-End coils as opposed to the Open-End

coils. Moreover, the electric field coupling is twice as large for the Open-End versus the Short-End coil type.

It is obvious that Short-end coils suffer from less electric field *leakage* and arguably would constitute a safer method for WPT as the human body in general has much greater permittivity ϵ than a vacuum, while at the same time having a relatively low permeability μ [187]. However, note that the self-inductance is also significantly increased in Short-end coils and this should be properly accounted for in terms of the ICNIRP reference levels, as this would require lowering the transmission power in order to reduce the induced electric field inside the body [186]. A more detailed study should be conducted which takes into account both the benefits and the shortcomings from the lower electric field and greater magnetic field for Short-End coils versus Open-End coils, in order to better determine how they compare in terms of safety.

Several works have addressed the issues of exposure, primarily through modelling of the field strengths around transmitting elements and comparing these values to the limits set by the ICNIRP and ICES [53]. On the other hand, some works have opted to use anatomical whole-body models in order to simulate the direct effect on the human body. Several databases have been cited and are available to researchers: of note are the Virtual Family Project [188] and the IT'IS biological database for thermal and electromagnetic parameters [189] as well as propriety research group voxel models

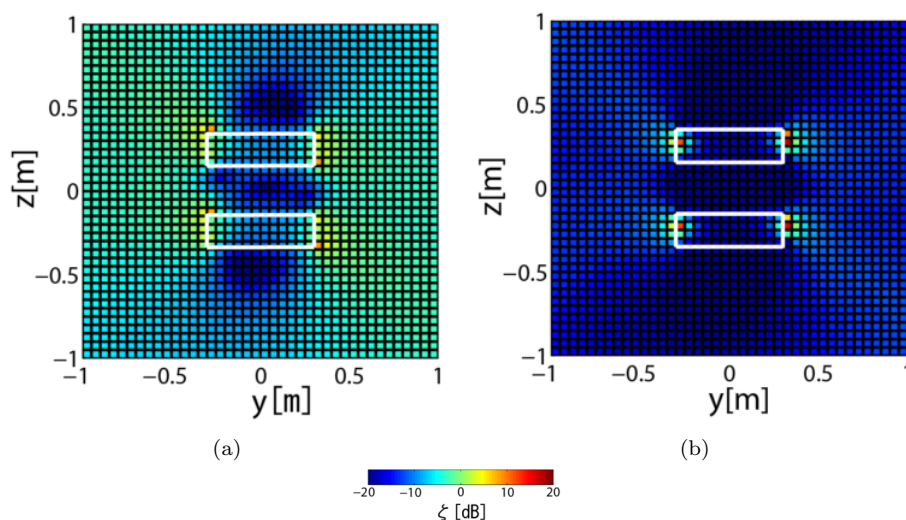


Figure 2.50: Spatial plots showing dominant field component for a) Open-End and b) Short-End coils [186]. Positive ζ shows the electric field is dominant while a negative ζ shows that the magnetic field is dominant.

[190, 191]. Often, these body models are used to simulate the exposure under different expected real-world scenarios, normally in the case where the most sensitive body parts are in closest proximity with the transmitting elements for an extended period of time [192]. In the case of a wearable application incorporating a WPT system, most works will incorporate conformal coil structures for SCMR due to the inherently flat design. Moreover, Hu and Georgakopoulos [193] argued that using conformal coils for wearable or implantable solutions would lead to a reduction in SAR as well as to a noted improvement in transfer efficiency. Table 2.3 compares the conformal coil system to other types of coupling methods for frequencies of 226 MHz at an implant deep of 30 mm.

Table 2.3: Comparison of different WPT systems for output power of 467mW [193]

Coupling Type	Field Parameters and Efficiency			
	Input Power [W]	Max H-field [A/m]	Max SAR [W/kg]	Efficiency (%)
Resonant Coupling	93	35	25	0.5
SCMR	1.3	5	1	35
CSCMR*	1	0.31	0.67	46.7

* *Coplanar SCMR.*

Hu *et al.* [194] modelled the performance of a conformal coil WPT system while in direct skin contact or while superficially implanted within the human body. Hu *et al.* modelled human skin, fat, muscle, bone, and heart tissue based on their known electrical and magnetic properties, and demonstrated that in either case, one would expect to see a significant decrease in the receiving coil's Q -factor, thus reducing system transfer efficiency. This decrease seemed to occur primarily due to the presence of either muscle and heart tissue, as both possess a relatively large magnetic permeability μ . To counteract this, Hu *et al.* demonstrated that by enclosing the receiving coil in an air-filled container, one would maintain a desired high Q -factor as shown in Figure 2.51. They simulated how even at a thickness of 1.5 mm, the Q -factor would remain high, suggesting that it is physical contact with the human body itself that seems to

cause this Q -factor reduction. While the results are intriguing, the authors gave little explanation for these simulated effects.

Finally, Gonzalez *et al.* [145] examined wearable conformal coil WPT systems in terms of their transfer efficiencies. As expected, even when employing SCMR, the human body reduced the overall efficiency of the system, even when only in close proximity to the transmitting or receiving elements. A discrepancy of as much as 20% can be observed in their work between the simulated and measured human body tests due to inherent limitations of anatomical models. Figure 2.52 illustrates this as well as the significant drop in maximum transfer power between the free space transmission and human body transmission experiments.

It has become increasingly important to understand the effects of electric and magnetic fields on the human body. It is especially important to not only consider the immediate effects as discussed here, but also the long-term consequences that might arise, even with energy levels below the currently set limits. Some of today's smartphones have more than ten antennas for data transmission alone [178], and as more and more devices become part of the continually expanding *Internet of thing*, the concern for user safety will likely increase [195]. Moreover, with higher-power commercial WPT solutions starting to enter markets, it has become even more vital to understand the biological effects of exposure. While both the ICNIRP and ICES have thus far reported that there are no permanent long term effects arising from exposure at current levels [196], investigations are ongoing and researchers in the field of WPT must endeavour to develop better solutions which minimise stray fields, thus improving transfer efficiencies and increasing practical transmission distances.

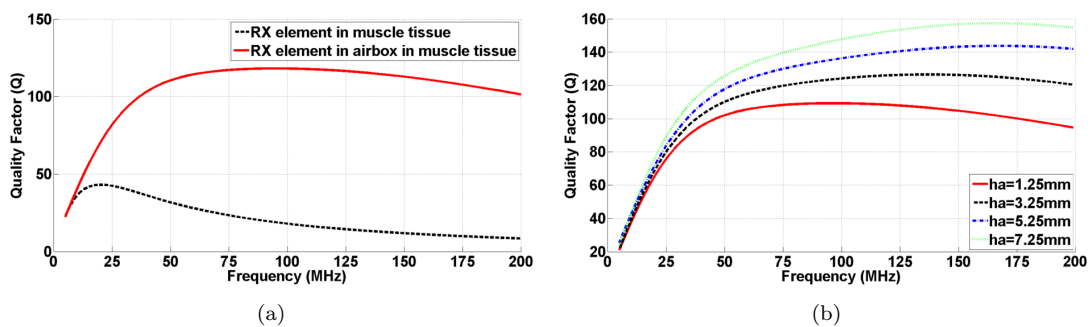


Figure 2.51: Plots of quality factor vs frequency for a) coil in muscle tissue and coil inside an airbox in muscle tissue, and b) comparison of quality factors with different airbox sizes [194]

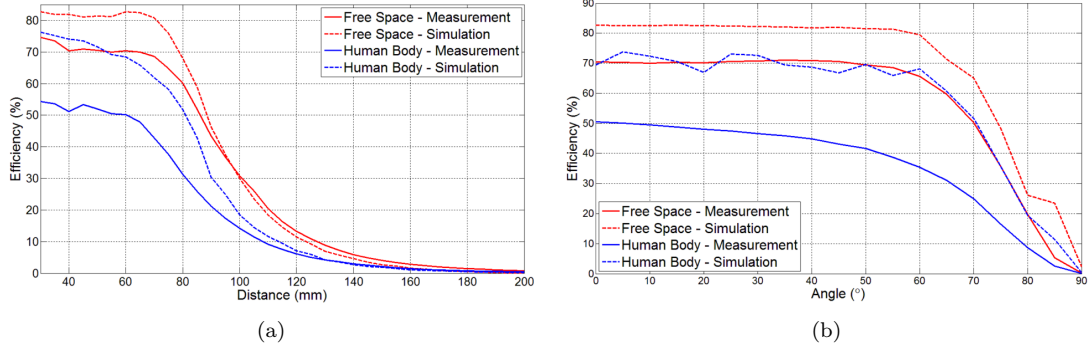


Figure 2.52: Plots of efficiency vs a) transmission distance and b) angular misalignment angle for both simulated and measured effects of a wearable WPT system vs a free space WPT system [145]

2.5 Concluding Remarks

This literature review chapter has presented a wide overview of the different challenges associated with the construction of a WPT system. The fundamental science of magneto-inductive energy transfer was explored which led into a discussion on various mid-range WPT system constructions. Some of these systems were generic, aiming to optimise a particular operational parameter (such as power transfer efficiency and/or operating distance), while others were designed with a specific application in mind. Some features of WPT were intentionally highlighted or examined in more detail throughout, as they represented genuine considerations during the construction of this work, and thus the necessary background information needed to be presented in order to appreciate certain design choices.

To the uninitiated the construction of a mid-range WPT system can seem like a daunting task with what sometimes appear as arbitrary design choices potentially having a profound impact on the final system performance. The field is well studied and at this point any significant improvement to any system's overall performance can only emerge by tailoring the design principles to a well-defined applications. As with most practical electronic engineering challenges, there will be some set of defined operational boundaries and often this will represent a stark compromise between design flexibility and a narrow, but optimised, performance.

For this thesis, it was paramount to report on the variety of different approaches undertaken in previous works. Besides dictating the available avenues for innovation,

this exercise greatly assisted in the ideation of the proposed system, ultimately leading to an innovative resonator concept tailored for body worn WPT applications.

Chapter 3

The Resonator as a Textile

Having explored various underlying principles of WPT, this chapter brings together the key arguments for the work presented in this thesis.

3.1 Application

Consider a body-worn biosensing application primarily used indoors and needing regular charging. In such instances, it is anticipated that the number of receiver units that could wirelessly capture energy for these sensors would be both unprecedented and unpredictable: no such wireless charging infrastructure has ever been attempted on a large scale, and likewise, the movements of individuals throughout the environment may be quite irregular. Scenarios where biosensing applications monitoring individuals would be employed include the following: industrial or construction sites and any hazardous environment where health and safety would be paramount; and equally, hospitals, sports training grounds, and military encampments – essentially, any environment where the use of portable battery-powered devices, while tremendously beneficial in principle, has historically proven impractical due to the constant need for charging. As such environments place a high demand on time efficiency, safety and productivity, wireless charging technology that reduces the burden on personnel while at the same time allowing for important monitoring to take place presents an ideal solution. It is envisioned that body-worn sensors can thus be intermittently charged as individuals traverse a particular area in a building or on-site. In order to maintain

human safety, while at the same time ensuring efficient power delivery at reasonable source-load separation distances, WPT via evanescent magnetic fields would be the most suitable choice.

One could imagine that the power transmitter electronics and associated magnetic field coupler geometries may form part of the building or site infrastructure: either located inside or on the surface of walls, door frames, furniture and fixtures. Figure 3.1 illustrates such hypothetical scenarios. This implementation places relatively trivial constraints on the transmitter-side electronics, other than being able to cope well in cases where no receiver is present. Chapter 6 explores this particular necessity further and derives a suitable design used during testing.

Instead, the design and implementation of a suitable receiver-side resonator pose the greatest challenge for a body-worn biosensing application: it needs to be practically sized, safe to use and comfortable to wear without inhibiting the user from their

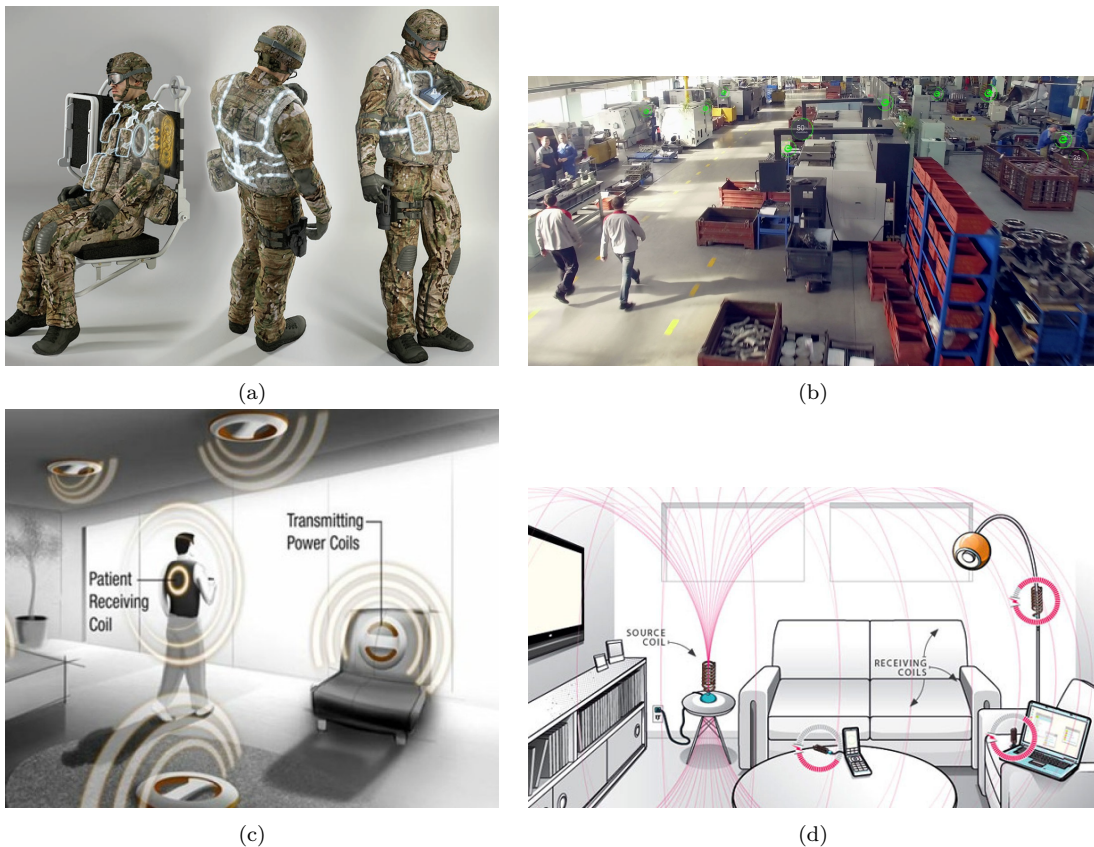


Figure 3.1: Hypothetical environments where WPT could be employed: a) a military scenario to charge body worn soldier equipment [197]; b) a factory floor charging various equipment and individuals [198]; c) a remote health monitoring suite to charge an implanted device [199]; and d) an eventual home setting, to charge consumer electronics [200].

anticipated day-to-day activities. Current solutions suffer greatly from very low transfer efficiencies and practical operation distances. The main critique of many current works is that they focus too heavily on the individual sensor nodes gathering power rather than on the whole body worn system. No matter how many marginal gains one can make through coupler geometry optimisation and topology, material selection and higher frequency operation, the impact of these gains is often minuscule for practical implementation. Ultimately, the limiting factor will more often than not, come down to coupler geometry: to capture significantly more power, one requires bigger, more effective couplers providing a large area for magnetic flux linkage.

Instead of creating individually isolated receivers per sensor node, one large receiver could capture the vast majority of transmitted power which could then be distributed to each sensor node (either directly or via tight wireless coupling). Arguably this has loosely been attempted through the application of intermediary couplers or relays, however, these have been presented as cumbersome helical or spiral metal structures that are impractically sized, rigid and susceptible to coupler misalignment: far from suitable for the proposed application.

3.2 A New Type of Resonator

Given the growing commercial interest in wearable electronics over the last few years, and the clear advantages of adopting near-field or evanescent wireless charging (i.e. user friendliness, hassle-free charging, water- and dust-proofing), it is surprising that not more academic research has focused on solving associated challenges of implementation. Fortunately the trend is changing, and researchers have began exploring the practical implementation of garment-based wireless power solutions. Zhu *et al.* [201] looked at stitching conductive wire in the form of coils into fabric and evaluating their performance. Key applications include charging body-worn electronics as users sat in armchairs, whereby the textile coils could be stitched straight into the upholstery. Grabham *et al.* [202] further evaluated different techniques for manufacturing coils for textile applications. They demonstrated a number of fabrication techniques, illustrated in Figure 3.2 and concluded that track resistance would play a major role in the

overall system performance. Moreover, the system would need to be comfortable and breathable as it would likely be against human skin. The researchers point to PTFE or silk-coated thin Litz wire sewn onto the fabric in the shape of a coil – as a suitable compromise between electrical performance, comfort and practical realisation.

While a promising solution in the short-term, there are still a number of unanswered questions and important challenges to overcome that might not make this approach the best suited for an eventual consumer product. Firstly, while Litz wire helps to reduce losses associated with skin and proximity effects, it can be notoriously expensive, especially for wire diameters significantly smaller than the typical skin depth associated with MHz operation. Connection between Litz wire and other elements of the system could also be problematic due to the large number of strands. Furthermore, by using the self-capacitance of these coils alone, there is little control on the coil-resonant frequency, and hence the system operating parameters are dictated by the geometry of the stitched coil on the receiver end, which is undesirable. From a design perspective, the surface area of the garment incorporating standard coil shapes is also well under-utilised.

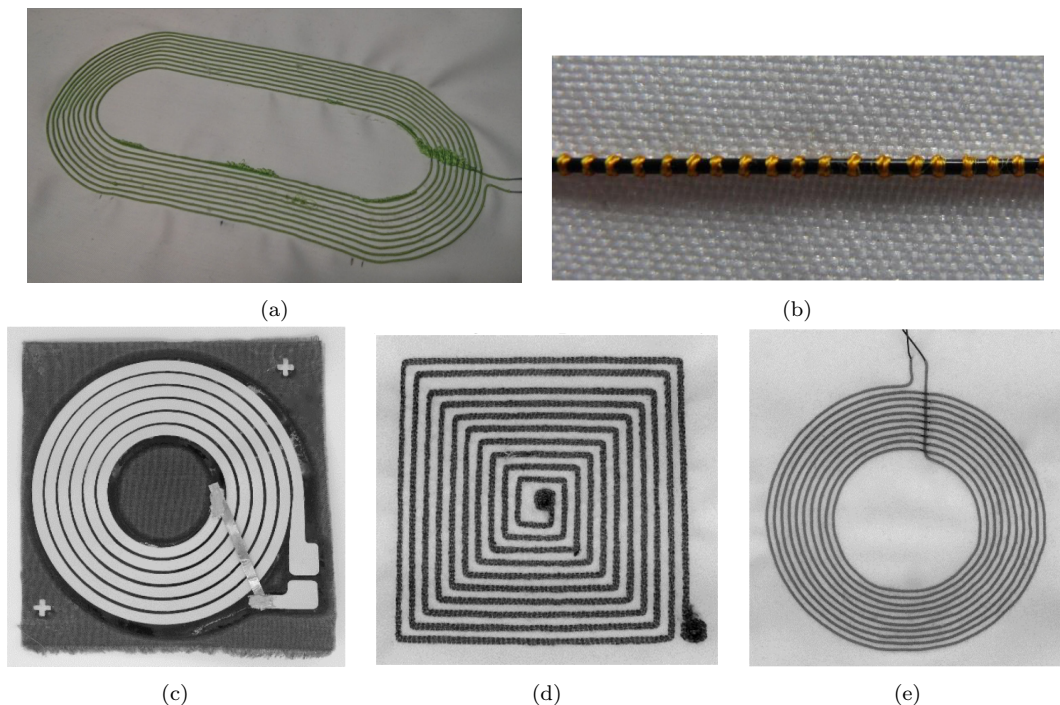


Figure 3.2: Different textile coil implementations, a) early implementation of a stitched on coil structure [201], b) sewn-on insulated conductor using copper fibres, c) printed coil using silver-polymer ink on a printed interface layer, d) square coil using Light Stitches conductive thread and e) circular coil using PTFE standard wire [202].

With the rise of additive manufacturing, mineral-loaded polymers, and conductive and dielectric ink printing there is a plethora of new approaches that could be applied here to create couplers with non-standard geometries, superior performance and textile-like properties.

A key inspiration for the design approach undertaken in this work stems from the field of metamaterials. Typically, a periodic or repeated pattern of metallic elements is arranged to create an effective surface designed to absorb or reflect particular frequencies of incident electromagnetic waves or changing electric and magnetic fields. In previous WPT research, their main use had been limited to aiding in field manipulation and shaping by effectively concentrating magnetic flux on the path between transmitter and receiver. Instead, this work explores the possibility of designing a similarly structured *metasurface* to primarily absorb the available energy provided by the oscillating magnetic field. Furthermore, this work employs screen-printing industrial techniques to print conductive as well as dielectric materials onto a suitably flexible substrate. Not only does this significantly reduce the overall coupler size but it also creates a simpler, potentially less expensive, solution when compared to using equally thin Litz wire. Furthermore, it enables a design that is more commercially viable for mass-scale manufacture via roll-to-roll fabrication techniques. Compared to solid wire or subtractively etched layers, printed solutions using silver inks have historically suffered from much higher electrical resistances (typically an order of magnitude increase) which is the key contributor to loss of performance within a WPT system [203]. It is worth noting, however, that this trend is rapidly changing within the industry and, with ever-improving electrical performances being demonstrated by print and material manufacturers, this proposed approach was deemed worth exploration within this thesis.

A distinct avenue of research into the use of layered inexpensive thin-film conductive and dielectric materials has already been explored for coil design as well as WPT applications. Sullivan and Beghou [204] introduced a novel structure in 2013 based on thin-film layering to achieve a high- Q self-resonant coil. They stacked alternating film layers of C-shaped conductive split rings and dielectric rings to form a cylindrical coil. They determined that for a given normalised volume of coil, their proposed system

achieved an order of magnitude reduction in typical coil losses (resistive losses, induced eddy currents, dielectric dissipation, etc). This helped them achieve a very high- Q in the order of 1,000+ without the need for an unloaded 4-coil architecture. An exploded view of these stacks as well as the equivalent circuit design is given by Figure 3.3.

As already examined, the Q -factor is a key system parameter that many works seek to maximise: A larger Q compensates for the significantly reduced coupling factor k between transmitting and receiving elements typified by mid-range WPT. These parameters are related to the power transfer efficiency η by

$$\eta = \frac{k^2 Q_t Q_r}{(1 + \sqrt{1 + k^2 Q_t Q_r})^2}$$

Sullivan and Beghou’s research inspired subsequent works which presented similar constructions boasting more detailed formulaic descriptions and a reduction in size [205], improvements to the choice of substrate, and fabrication approach [206] as well as refinements to the ferrite core geometry surrounding the stacks [207, 208].

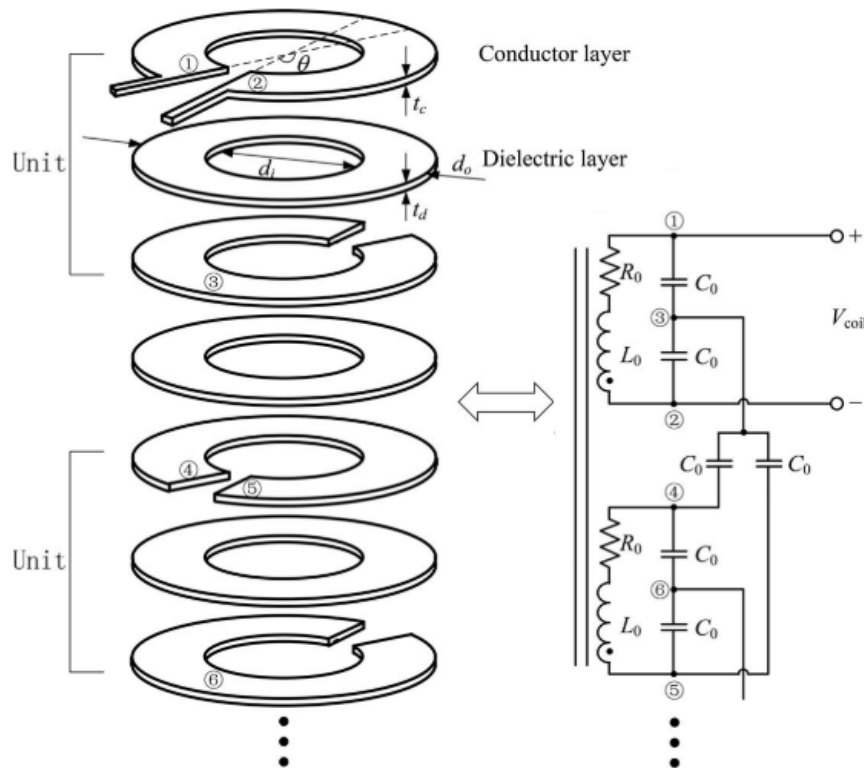


Figure 3.3: Stacked C-shaped conductor layers and ring-shaped dielectric layers and their equivalent RLC resonant circuit [205].

Previous work helped verify that an approach based on thin overlapped layers of alternating conductive and dielectric material could in fact improve system efficiency at greater transmission distances. Likewise, prior art on metamaterials, has demonstrated the usefulness of minute periodic electromagnetic elements both from an electrical performance point-of-view, and also from an application design perspective.

Chapter 4

Design and Development

4.1 Yarn-level Design

Based on the arguments presented in chapter 3, a resonator yarn capable of inductively capturing energy was initially designed. The goal was to incorporate inductive and capacitive elements in such a fashion as to structurally mimic a typical yarn used within fabric and garment construction. Doing so would not only allow resonator structures to be created, free from the physical constraints of a looping coil shape, but also enable their easy integration into a garment via standard manufacturing techniques. Full details of this proposed approach are found in the published UK granted patent¹, however the key points are summarised henceforth.

The resonator structure envisioned is illustrated in Figure 4.1, whereby resonator elements no greater than 2mm could be applied and spaced along an axis for a cylindrical yarn (as in Figure 4.1a) or printed on a flat yarn-like substrate (as in Figure 4.1b). Depending on the response required it is possible to vary the degree of overlap between elements, thereby increasing the resonator capacitance as well as load the polymer substrate in the case of a cylindrical yarn with ferrite particles (as in Figure 4.1d), to increase the effective inductance.

Each element in isolation would only be able to provide a small inductance and/or capacitance (in the order of a few nH and pF, respectively), however, by repeating this pattern and maintaining a relatively tight coupling between elements along a yarn, the

¹UK Patent GB2562548 (Status: Granted), PCT Application No. WO2019058123A1

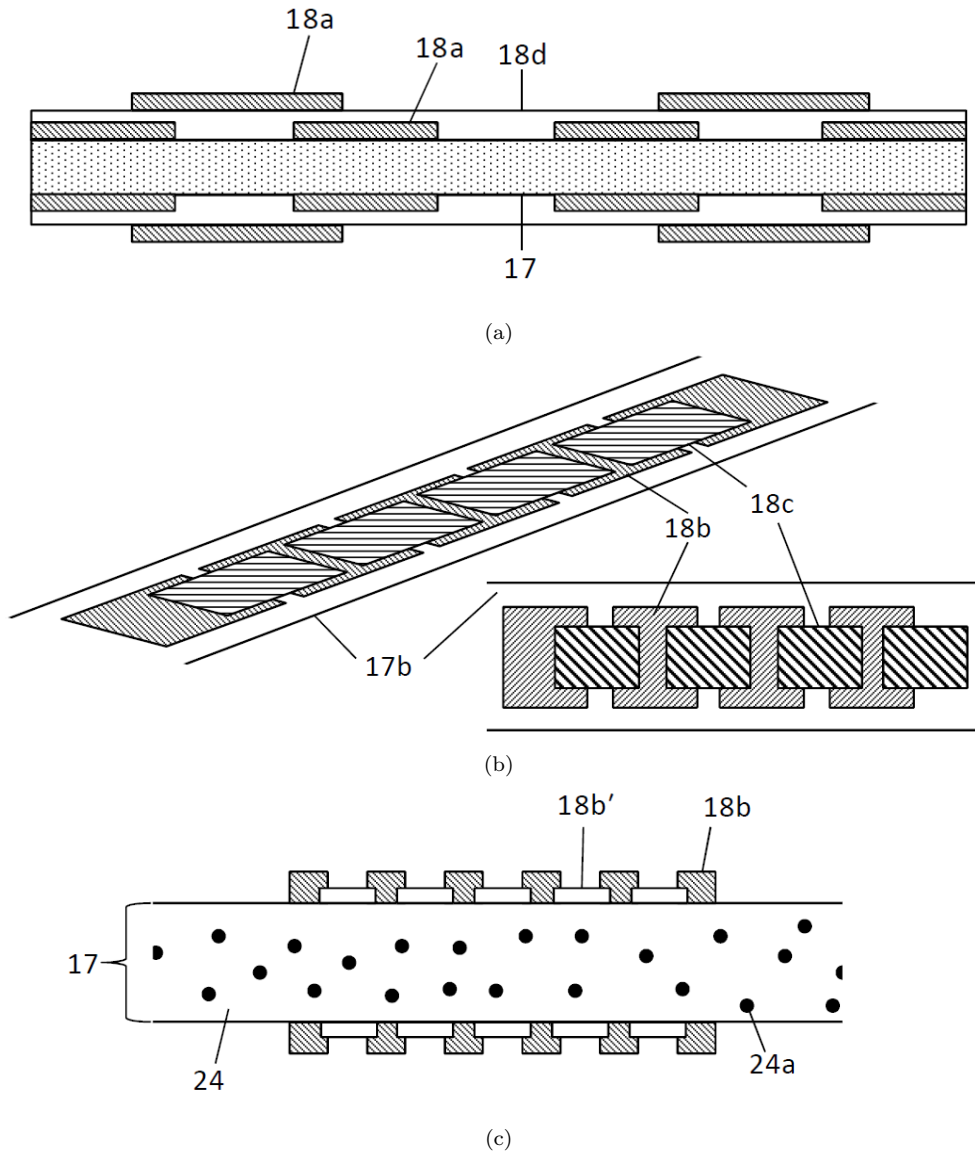


Figure 4.1: a) Cross-section of cylindrical resonant yarn, with overlapping conductive elements (18a), separated by a dielectric insulating layer (18d), wrapped around a polymer yarn (17); b) and isotropic and top view of a flat-substrate (17b), with insulated and overlapping conductive elements (18b and 18c) applied on one substrate face; and c) a cross-section of cylindrical resonant yarn as in a), however employing a material-loaded polymer (24), comprising in this case of ferrite particles (24a).

effective electrical parameters for the entire structure would grow substantially to allow for WPT in the MHz region. The proposed structure also allows for a highly flexible design: for example, there could be multiple types of resonator elements along the structure to allow for a particular multi-modal frequency response or even field shaping behaviour to arise once the final garment is constructed from the yarn. Furthermore, the resonant structure may act to shield or even enhance transmission of electromagnetic

fields in and around the wearer beyond just the application of WPT: for example, and considering a military application, perhaps to amplify typical data transmission systems in remote environments, thus increasing communication range, or to protect worn or implantable electronics from damaging electro-magnetic pulses.

The remainder of the patent details particular considerations when constructing such yarns as well as fabrics or membranes composed of the same principle resonator architecture. It further proposes a means of extracting captured energy from the resonant structure either via inductive coupling with smaller, nearby collector coils as well as an embedded vari-cap network built into the structure.

This *Resonant Yarn* concept, while intriguing was abandoned after initial simulation as it was deemed too complex and expensive a development activity to further within the scope of this thesis. Instead, a similar, yet much more simplified construction is presented in the following section, which nevertheless forms a solid foundation for any future work into yarn-level resonators to build upon.

4.2 Surface-level Design

A textile surface-level, metamaterial-inspired resonator structure is proposed with its efficacy for body worn applications demonstrated throughout the rest of this thesis. The fundamental principle, as with the yarn-level design, was that by creating repeated geometries using a combination of conductive and dielectric layers, the intrepid designer could create a structure that, in principle, behaved as Figure 4.2a, but was physically constructed as 4.2b.

Besides ease of manufacture (as further discussed in section 6.2), the key difference between the yarn- and surface-level designs was that the yarn-level only considers resonator element patterns in 1-dimension (i.e. along the surface of the yarn), while the surface-level enables 2D as well as 3D patterns (via stacked layers) to arise, giving even greater flexibility in adapting and tuning the frequency response. Full details and some different embodiments of this proposed approach may be found in the published UK patent application², however the key features of operation are discussed henceforth.

²UK Patent GB1914854.3 (Status: Pending)

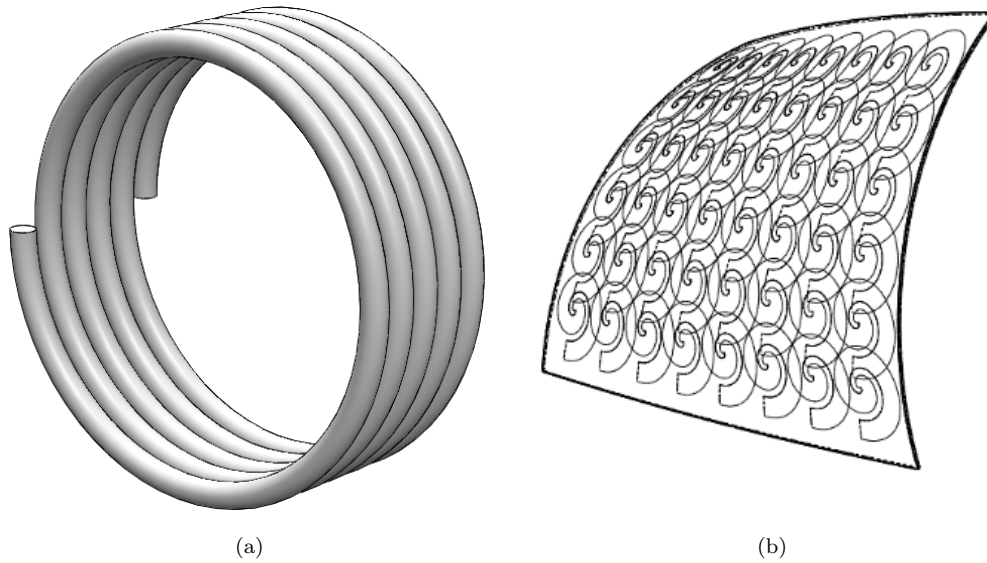


Figure 4.2: (a) Standard helical coil and (b) a surface pattern of a repeated geometrics made up of layers of printed conductive and dielectric elements

The focus of experiments in this thesis centred around three key element designs, which are herein referred to as C-type, O-type and W-type. Figure 4.3 illustrates the design of each of these element designs.

C-type resonators were fashioned after the work by Sullivan and Beghou and was chosen as a suitable asymmetric design to test. O-type is close to a C-type, however allowing for a highly symmetrical layout to compare the C-type against. Finally, the W-type is essentially a C-type but with a sinusoidal pattern around the C shape. This was another asymmetric design, but one that would have a significantly larger inductance to compare the other two designs against.

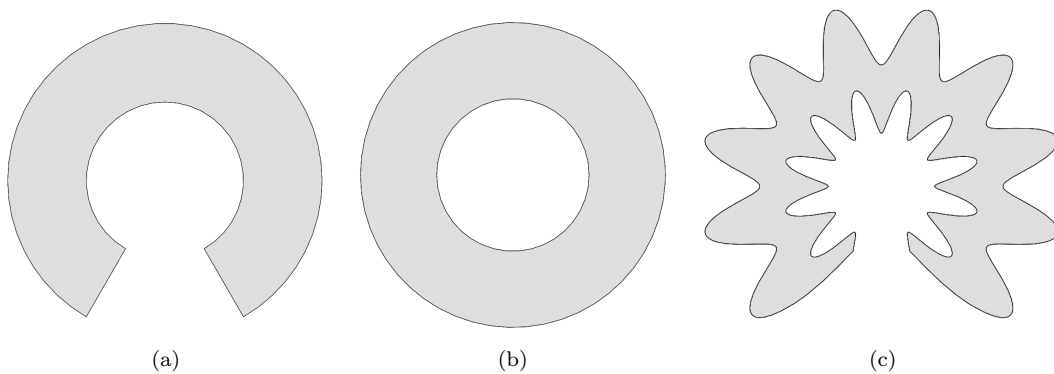


Figure 4.3: Drawings of the three resonator element designs, namely a) C-type, b) O-type and c) W-type.

Multiple identical elements were laid out in a pattern whose number of rows and columns will henceforth be referred to within the name of the design: so, a resonator surface made up of C-type elements with three rows and two columns, would be referred to as a C(3×2). Figure 4.4 gives a few resonator design examples for reference.

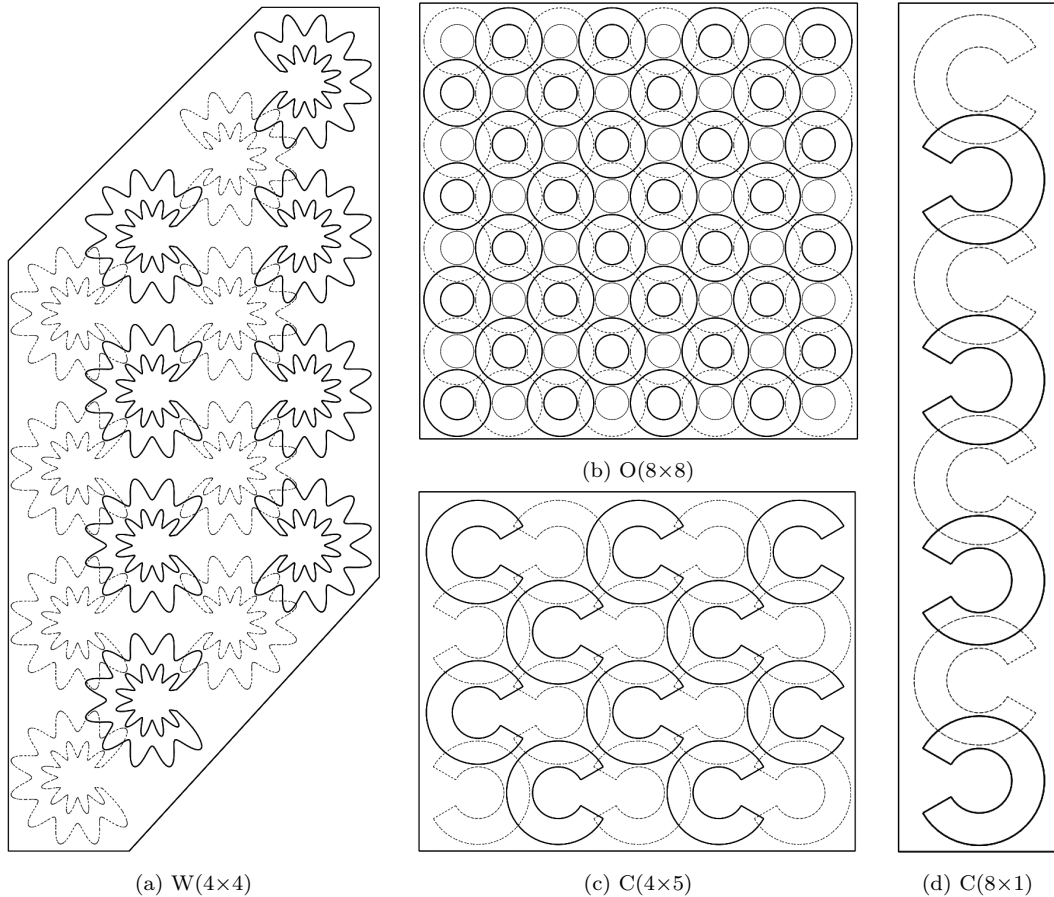


Figure 4.4: Example resonator structure models, named accordingly. Note, solid lines indicate foreground elements and dashed lines indicate background elements.

Note, W-type resonators do not follow the same pattern as the C- and O- types presented here, as the particular iteration shown enabled a better spectral performance over the originally conceived layout.

When current flows at different frequencies through this resonator structure, current loops form across different areas due to the capacitances created at the conductive element overlaps as well as the inherent electrical inductance defined by the resonator element geometry. Figure 4.5 illustrates the surface current density represented as an arrow plot at distinct frequencies for O(6×6). Figure 4.6 illustrates the magnetic field generated by these current loops, limiting the plots to Figure 4.5a and Figure 4.5b.

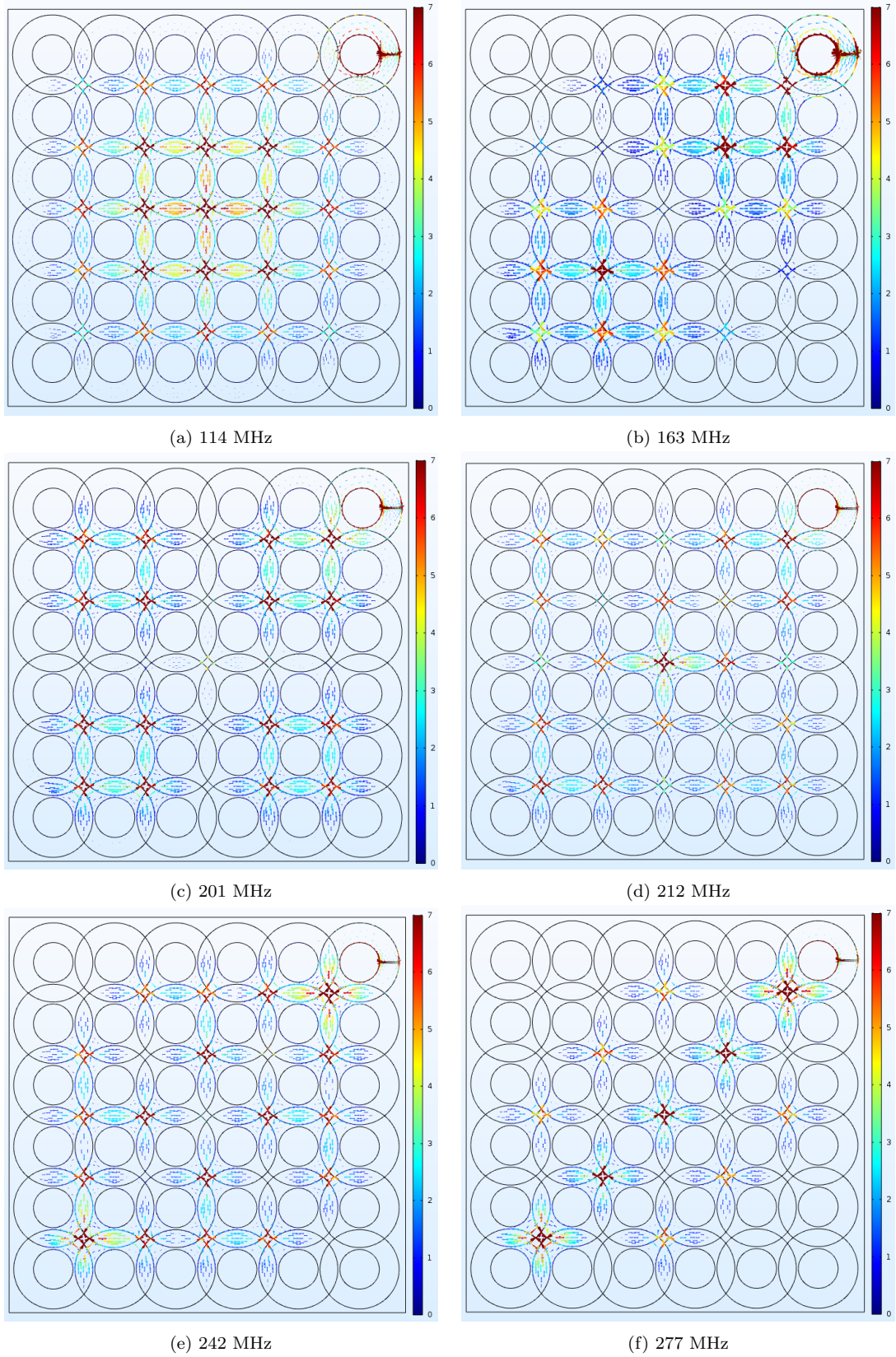


Figure 4.5: Arrow plots for the surface current density for a 40 mm element diameter $O(6 \times 6)$ resonator design at the first six resonant modes.

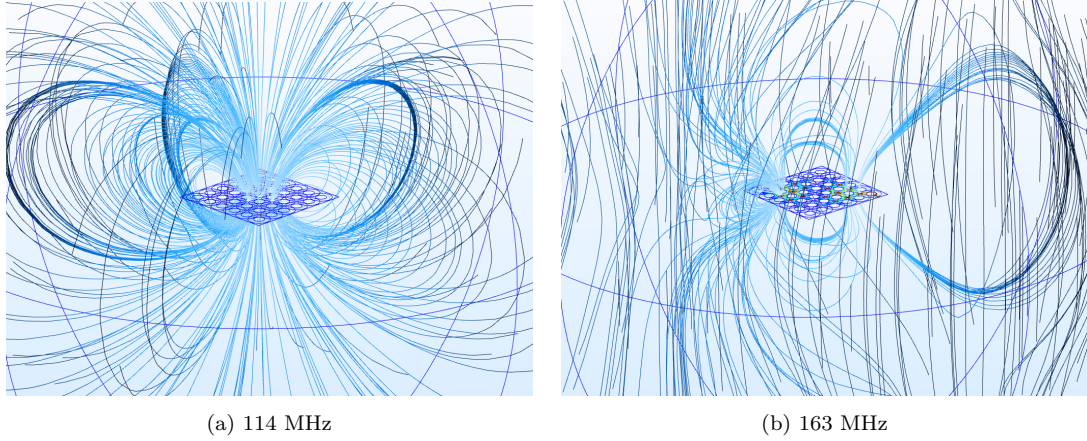


Figure 4.6: 3D magnetic field line plots for a 40 mm element diameter $O(6 \times 6)$ resonator design at the first two resonant modes.

The number of different current loops observed in the pattern seemed very much determined by the level of geometric symmetry in the repeated elements, and it has been observed that the larger and more asymmetric the pattern created by the conductive elements, the more distinct loops will form. Interestingly, these loops and the subsequent magnetic fields created resemble the classic transverse mode patterns found in waveguide theory, as illustrated in Figure 4.7. The relative shape and magnitude of these current loop patterns will also be highly dependent on the pattern of choice.

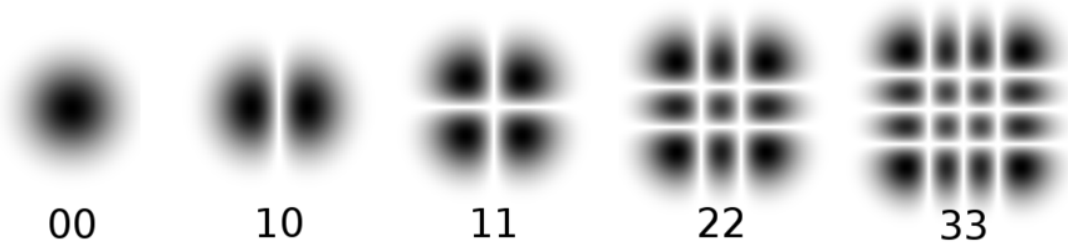


Figure 4.7: Example transverse modes from waveguide theory to compare to current loops illustrated in Figure 4.5.

Examining the spectral behaviour as seen from the driving port of the system, it was apparent that some resonant behaviour was taking place at these loop frequencies. The presence of loops is represented by distinct amplitude peaks or *modes* when examining spectral plots. During simulation, it was interesting to observe the many spectra generated by driving various different sized patterns and conductive elements. As

indicated previously, the geometry as well as the number of the selected conductive element design present in the structure had a very clear effect on the number and shape of the modes. Furthermore, not every mode that arose strictly behaved as a resonant mode in the classical sense: the frequency of electrical resonance in a simple circuit geometry is typically defined at the point when the frequency of a driving signal is such that it cancels the reactances within that circuit geometry. Practically speaking, this is often identified as the point in an impedance plot where the imaginary part of the input impedance $\Im(Z_{in})$ crosses the zero-line. However, in more complex geometries, such as the ones being explored here, a more nuanced approach to resonance may be required: one that gives rise to a proprietary concept herein referred to as *semi-resonance*. Semi-resonance (SR) describes multiple distinct frequencies along a spectrum where useful signal amplification could take place; however, it allows for the flexibility that these distinct frequencies do not necessarily take place across a zero-crossing on an $\Im(Z_{in})$ plot, but rather represent a local and rapid shift in the reactance of the circuit. Modes that arise at these points may be thought of as limited in their degree of resonant amplification due to residual reactances; however, there are ways to effectively account of this either through auxiliary matching networks or by changing the resonant structure design itself to reduce these residual reactances closer to the zero-line. Figure 4.8 illustrates a number of spectra generated by a selection of self-driven resonant structures. Note, while several high-amplitude, low- Q dominant modes have been observed with increasing frequency, the results reported herein were limited to examining the first of these encountered.

Aside from the clearly identifiable dormant mode spanning the spectrum and SR modes springing up along the way, each of the different model geometries have given rise to strikingly unique frequency behaviours. As will be shown in chapter 6, this frequency behaviour is in fact quite predictable and follows a set of design rules and derived equations, all of which stem from the actual geometry and associated patterns within each resonant structure. Determining the specific geometry that will give rise to a desired frequency response hence becomes the key design activity for these structures.

This chapter has examined the proposed resonant structure in detail and demonstrated a superiority in terms of design versatility when compared to standard

resonators, such as coils or antennae. The intricate characteristic behaviour shown of these surface resonators is an emergent property due to the segmentation and patterning of conductive and dielectric elements. The next chapter discusses the approach in understanding and predicting this behaviour through the use of appropriate physics simulation software.

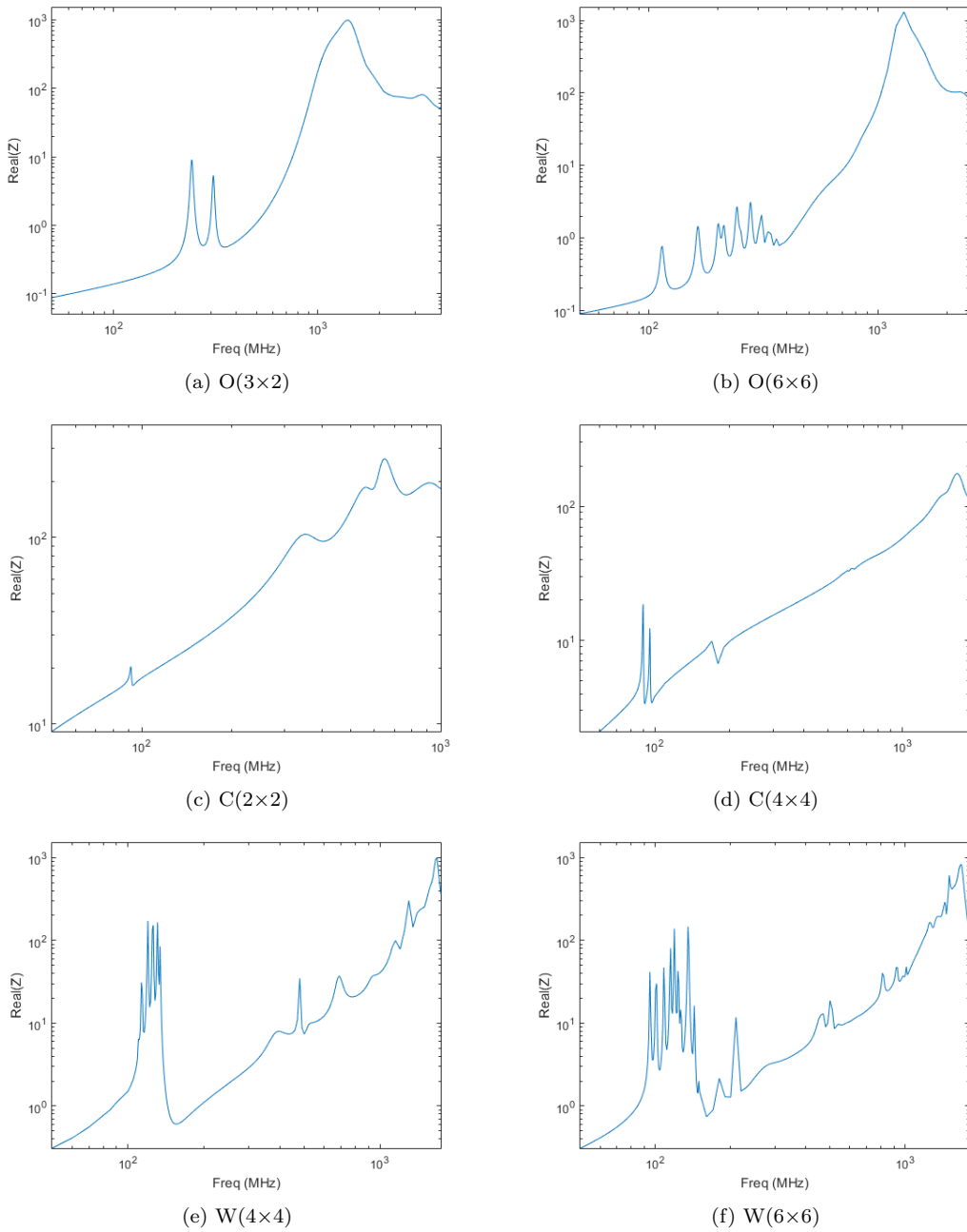


Figure 4.8: Spectra plots of $\Re(Z_{in})$ showing the SR modes and dominant frequency mode for a selection of self-driven models.

Chapter 5

Discussion of Experimental Approach

The proposed textile resonator concept was designed and studied using finite-element analysis in order to determine behaviour and functionality of multiple embodiments without the time and cost associated with physical construction. This chapter explores this FEM approach in more detail and reports on the verification procedure undertaken to provide confidence in the simulation tool and its outputs.

5.1 Modelling Magnetic Fields

Whether it is changing coil or coupler dimensions, creating an arrayed or relay resonator structure, or simply introducing homogeneous μ -materials that effect overall transfer efficiency: fundamentally, this all becomes an exercise of understanding and manipulating an electrically-induced magnetic field and its loop path, to better link a higher concentration of magnetic flux that induces a current within a receiving structure. Therefore, a brief examination into magnetic field calculations and modelling techniques is required.

5.1.1 Interpreting Maxwell's Equations

Classical electromagnetism is elegantly described by Maxwell's equations. Named after James Clerk Maxwell, these partial differential equations give real solutions for electric

and magnetic fields in 3D space, generated by time-varying charges, currents, as well as changes in the generated fields themselves. Depending on the nature of the problem to be solved, different forms of these equations, along with initial and material boundary conditions, are applied. While this might sound trivial, a deep understanding is actually required to appreciate the subtle nuances that can emerge and the approach to be taken for particular problems. Even within published research, there is some confusion and this primarily comes about because of the fuzzy nature of the near- and far-field boundary in electromagnetic fields and propagation. Before Maxwell, Faraday and others formulated laws based on magnetostatics and near-field induction. However, beyond magnetostatics, the original electromagnetic laws were inconsistent when it came to wave propagation, and it was Maxwell himself who resolved this inconsistency, leading to his namesake equations used today. Nevertheless, assuming a magnetostatic model can sometimes be very useful as it simplifies the mathematical problem. This approach in modelling is commonly referred to as the *quasi-static approximation* and when applied, accordingly generates a suitably accurate solution under the assumption that variations in time are small and that geometries modelled are considerably smaller than the wavelengths of the employed signals [209]. The downside and over-emphasis of this approach in the literature, however, masks the fundamental principle that it is just an approximation and will rarely provide a good solution for a complex and dynamic system. Part of the problem could stem from the choice in terminology and different perspectives that can be applied to any particular problem.

To avoid any confusion henceforth, the distinction between a discrete near- and far-field are to be replaced by a blanket concept of electric and magnetic field oscillation whose Poynting vector gives the direction of energy flow. This perspective offers a more palpable interpretation of how generated fields interact and exchange energy, and is inherently more flexible when geometries do not neatly conform to the simple interpretation of a *coil* or an *antenna*. Furthermore, instead of different equations for the near- and far-field, all regions between the surface of the source and infinity can be solved using one wave equation. In the case of WPT where the magnetic field is the main component for energy exchange, the following equation is hence solved over a range of frequencies ω .

$$\nabla \times (\nabla \times \mathbf{H}) + (j\omega\sigma\mu - \omega^2\epsilon\mu)\mathbf{H} = 0 \quad (5.1.1)$$

This chosen approach is valid as it still ultimately upholds the established distinction between a conceptual near-field region where emitted energy is mainly reabsorbed, and a far-field region where energy radiates out; however, it is not tied down with approximations and fuzzy boundaries. One can observe clearly how close to a particular source geometry, the Poynting vector becomes purely imaginary with a zero real part, hence, there is no net energy flow. Moving away in the direction of propagation, this vector changes and instead becomes purely real, implying that energy is flowing outwardly. Visualising and interpreting this shift in average energy flow for any particular source geometry gives a researcher a much deeper insight than can be expected from some estimated distances related to the wavelength of propagation alone.

5.1.2 The Finite-Element Method

Solving Maxwell's equations analytically for real geometries is, at best, impractical, therefore an approximation of these equations is constructed and normally based on discretisation. Doing so allows physical laws to be numerically solved with sufficient accuracy to reflect real-world phenomena.

The finite-element method (FEM), first recognised for its usefulness in the 1940s, has been well-developed over many decades to become one of the most powerful computational methods for solving real-world physics problems. Naturally, the sheer size and complexity of today's problems requires powerful and complex tools to solve, however, the thinking behind FEM is rather straight forward: One defines a physical geometry, setting its various boundaries, sources and sinks; one breaks-up or *discretises* the overall geometry into tiny components; then solves the physics equations within each element, using solutions already solved from adjacent elements to refine the solution; and finally, one performs some post-processing to extract the information required and to visualise the solution. Defining the problem in terms of number of dimensions, choice of element size and shape, as well as the choice of solver employed becomes an interesting challenge. More often than not it is highly dependent not only on the type

of physics problem to be solved but also the computational resources available.

Ultimately, this choice becomes a compromise between the time taken to solve the problem, the amount of physical memory required, and the accuracy of the final solution. Nevertheless, there are many obvious benefits to modelling and computationally simulating the behaviour of complex systems before actually constructing them in the real world.

For electrodynamic systems, FEM is very useful, primarily as it gives the ability to visualise the electric and magnetic fields generated by complex geometries as well as quickly calculate induced currents, energy distributions, energy flow, and thermal losses. It is also very convenient as it enables quick calculation of electrical properties, such as inductances, capacitances, mutual coupling, Q -factors, S -parameters, etc for any defined geometry and material selection. Rapid iterative development is hence achieved, and optimising any given solution becomes a matter of automating computation to either maximise or minimise a particular, often geometric, property.

5.2 Simulation Tools and Verification

The performance of the proposed coupler would be heavily dictated in the first instance by the geometry and relative positions of the different conductive and dielectric layers, and it was important to be able to rapidly and intelligently optimise a set design. It was further desirable to be able to visualise fields generated and observe changes with differing geometries, hence, computer-aided modelling and simulation tools were used in this work.

A combination of SolidWorks and COMSOL Multiphysics commercial software suites were used to model the system, rather than spend time writing new code to ultimately perform similar tasks. SolidWorks is a CAD tool that was used to construct the different 3D geometries, and COMSOL is a FEM suite that was used to simulate the relevant physics for the given geometry. While recognised for its usefulness and accuracy within industrial applications, it was still necessary to verify that COMSOL was in fact the right tool to use here and also that the modelling and simulation procedure undertaken was appropriate, and would lead to useful results and insights in

line with what would be obtained from real-world observation and experiment.

There were several physics modules that could have been used, and while some might seem similar from the outset, selecting the best module and study type for the tasks at hand was not a trivial task. Moreover, setting up the simulation correctly and the rationale behind the choices made for geometry simplification, meshing parameters, choice of solver, and study tool could in itself constitute an entire chapter of its own. Much of these aspects will not be delved into here, and it is assumed that the reader already possesses a working knowledge of FEM simulation tools, such as COMSOL, necessary to appreciate the choices made and intricacies involved.

In order to verify a chosen approach at every instance, simple helical or spiral coil geometries with parameters that could be easily calculated with standard equations were digitally constructed. Figure 5.1 shows one of these coils along with its geometric properties.

Given these simple coil properties and standard shapes, very good approximations for inductances L and capacitances C (and hence, derivative properties such as self-resonant frequency ω_o), could be calculated using standard and well-known methodologies.

To compare these numerical values to the calculations made from simulated fields, coils were modelled as Axi-Symmetric 2D geometries in order to simplify the initial calculations. Using the *Magnetic and Electric Fields Interface* which solved Maxwell's equations for a stationary problem, the magnetic vector potential \mathbf{A} as well as the

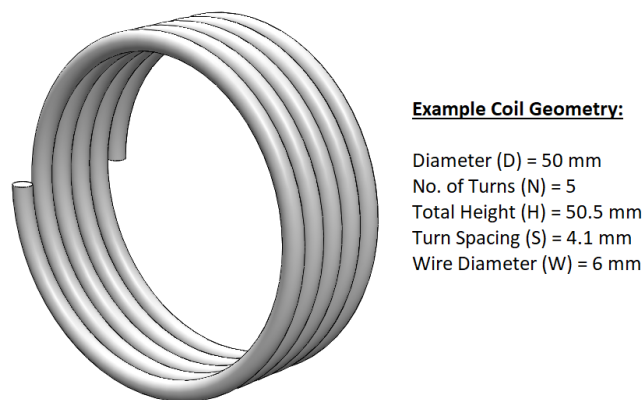


Figure 5.1: An example coil used for verification testing with a simple helical morphology

electric potential V were calculated. The corresponding electric and magnetic fields generated were as expected, and Figure 5.2 shows the plots for the coil in Figure 5.1. Finally, the model's electrical properties could be calculated, and these were found to align well with those calculated analytically. Note, the same verification procedure was undertaken with the coils modelled as 3D geometries, albeit they needed much more time to compute. In every instance, the different model domain sizes, as well as mesh element sizes and types, were explored in order to observe how results varied. Further details for such a procedure can be found in chapter 6.

While this interface proved to be useful in calculating single coil electrical properties (including the expected skin and proximity effects at different driving frequencies), it would have been insufficient at accurately modelling the dynamics of a wireless power transfer system. Instead, the *Electromagnetic Waves Interface* was used as it solved the time-evolving wave equation for the electric, and by extension, magnetic fields. In the previous chapter, it was briefly explained why this problem definition was valid when

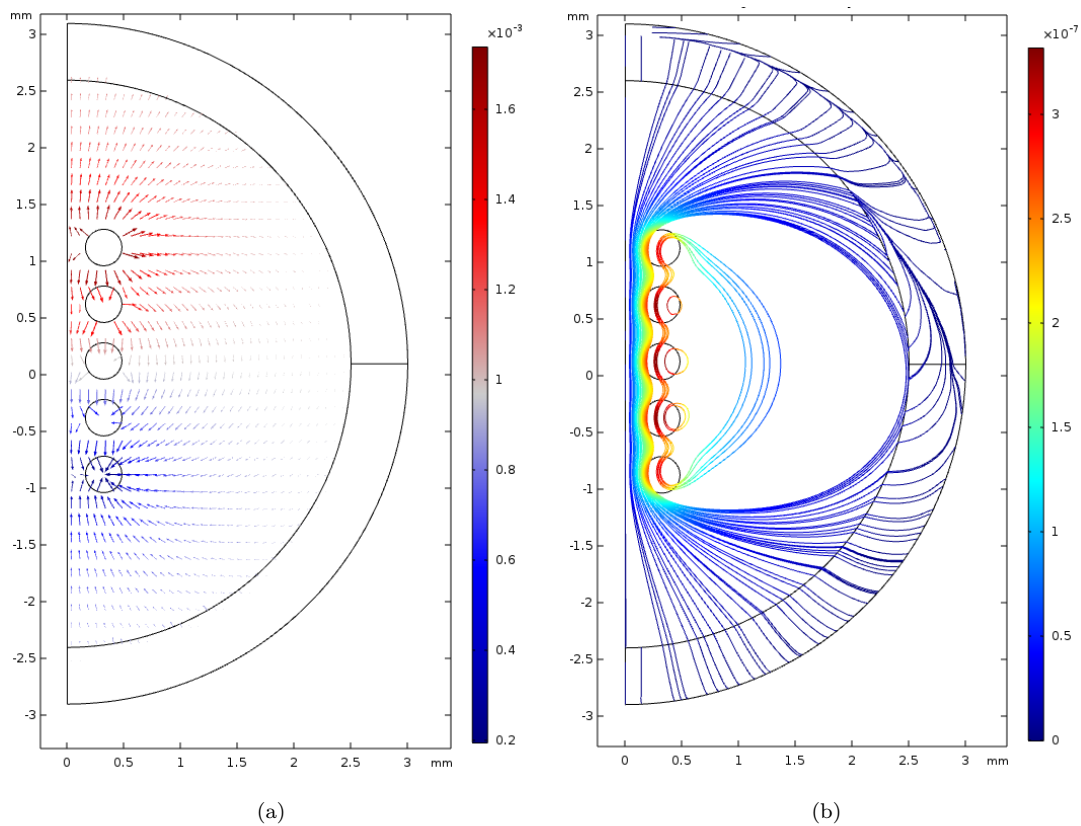


Figure 5.2: Plots for a simple coil, modelled as a 2D axis-symmetric geometry, with a current flowing from top to bottom showing a) the electric field (in Volts) and b) the magnetic field generated (in Tesla).

applied to near-field or evanescent-field coupling. To verify this hypothesis, a simple 3D coil geometry was simulated and the value of the Poynting vector at various points in the surrounding domain space was examined. It was found that close to the coil, the Poynting vector was purely or strongly imaginary in the direction of expected energy propagation. In the graphical model, this could be illustrated by arrows corresponding to the instantaneous Poynting vector which, in this case, were normal to the direction of radiative propagation. However, as one moved further away from the coil, the real part of the Poynting vector would start to increase and the arrow would begin to align more to the direction of radiative propagation with the turning point occurring at different points depending on the driving frequency. A quick domain volume integration also confirmed that the average power flow for a domain smaller than roughly one quarter of the wavelength was substantially zero. In the real world, one might have expected some greater amount of radiative power flow even at this proximity, but given that coils by their very nature make terrible antennae, the result was still considered valid to the limit that COMSOL could resolve the values for the Poynting vector. The electric and magnetic fields generated were observed under various conditions (such as changing loop separation or loop size) and were found to be as expected.

This selected interface also served to find the Q -factor of the modelled coil and system S-parameters, which was useful in measuring power transfer efficiency and, if needed, effective permeability μ_{eff} [210, 211]. When modelling several coil geometries and ferrite materials in the same model, induced currents J_i , average power transfer P_{avg} and coupling κ between coils was also determined. Figure 5.3 illustrates some of the visual outputs from the graphical interface.

5.3 Modelling Insights for Solid Geometries

Once the simulation procedure had been established, a number of WPT set-ups were modelled based on some key prior works in the literature. This was done primarily to validate the approach undertaken against model's whose solutions where either known or easily verifiable. Furthermore, it served to establish an expectation of system behaviour and performance under varying parameters and gave a baseline from which to

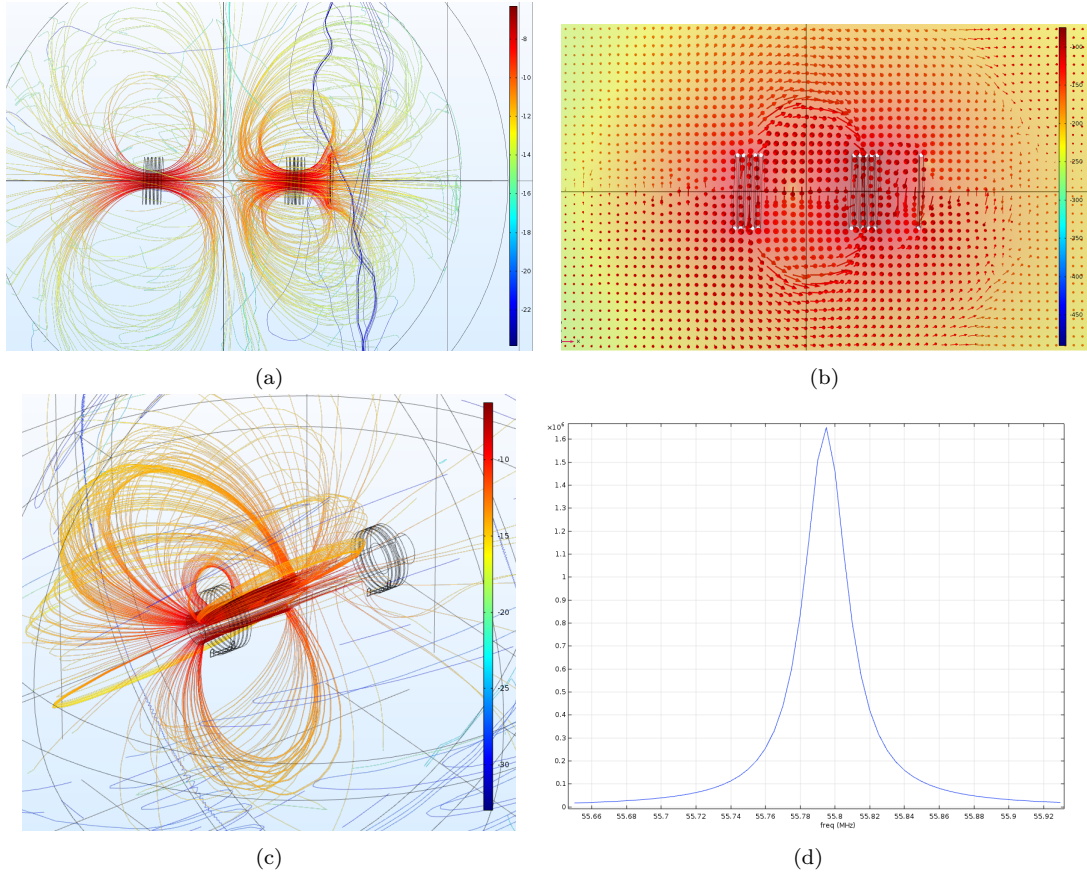


Figure 5.3: 3D plots for various coil arrangements showing: a) top view of a driven coil (left), an intermediate coil (middle) and single loop-load coil (right) separated by 30 cm with the associated magnetic fields overlaid; b) top view of a driven coil (left), an intermediate coil (middle) and single-loop load coil (right) separated by 15 cm overlaying the average power flow; c) isometric view of a driven coil (left) and load coil (right) both straddling a soft ferrite cylinder with associated magnetic field overlaid; and d) a 1D plot of the real part of a single coil impedance, through which the unloaded Q -factor can be calculated.

compare the results of this thesis. Besides energy transmission, the effects of dielectrics, ferrite materials and layered structures were examined. In recreating these works, several insights emerged, which had not necessarily been previously highlighted. 2-, 3- and 4-coil arrangements were explored, and these are shown in Figure 5.4.

Through these simulations, it was desirable to examine how one could improve overall transmission gain and efficiency, while at the same time minimising the dimensions of the geometries involved and minimising the system resonant frequency. These goals are somewhat conflicting and would naturally have required a compromise, however, it was interesting to observe the degree to which certain adjustments changed these systems' operation. The insights generated through these preliminary experiments would go on to predominantly inform the design of the transmitting coil,

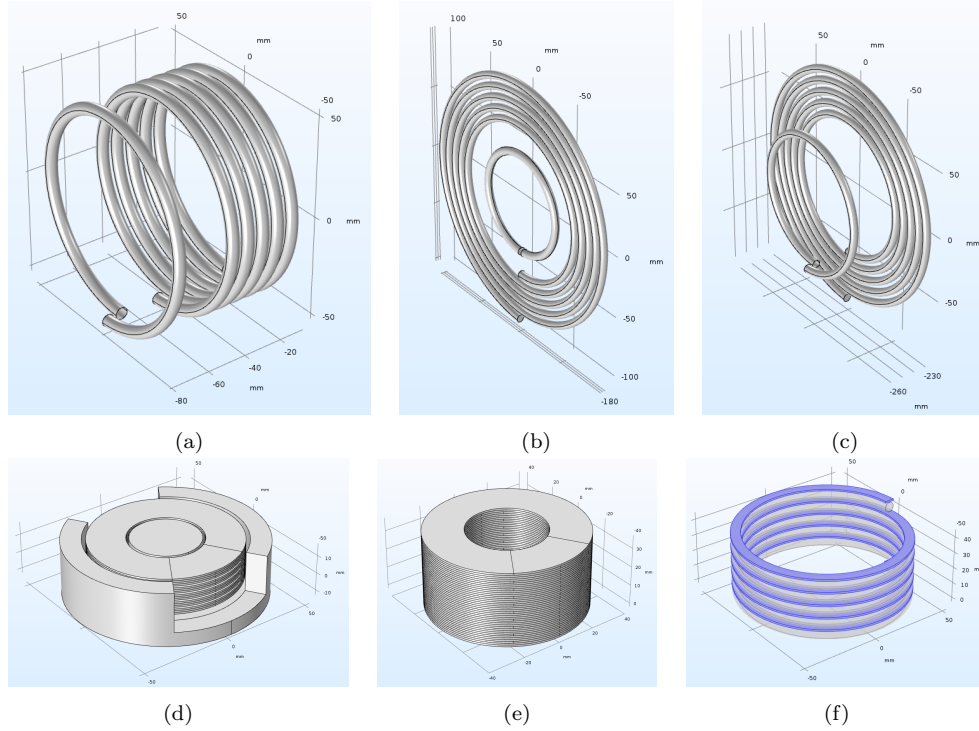


Figure 5.4: Various coil models for 2-, 3- and 4-coil simulations, including (a, f) helical and (b, c) spiral coils; segmentation coils (d) with ferrite and (e) without ferrite; and (f) a helical coil with dielectric between the loops.

but also various aspects of the proposed system as a whole.

Note that, throughout these simulations an *Impedance Boundary* condition, which assumed currents flowing only at the surfaces of conductors, was applied to the coil domain geometries as the skin depth for the materials modelled was much greater than the dimensions involved. Further note that, according to standard practice, the model was enclosed in a sphere with a *Perfectly Matched Layer* domain condition at the outermost layer in order to simulate a mathematically infinite surrounding air domain. It was observed that when following this procedure the physical model size of the surrounding air domain could marginally shift the resonant frequency of the systems. Compounding this with either imperfect meshing or even poorly selected solver conditions could generate varying results between successive simulations with deviations in excess of 10%. Careful consideration is therefore needed when constructing the model, and multiple simulations with changing conditions, meshes, and domain sizes are recommended in order to average and converge the results to a more accurate representation of real-world behaviour.

Dielectrics simulated included poly 4-vinylphenol and polyethylene terephthalate, both commonly used in many products. These had a typical relative permittivity ϵ or *dielectric constant* of between 3 and 10, depending on composition, which mirrored well the constants of most commercially available dielectric pastes. The inclusion of a dielectric material, say, between the coil loops as illustrated in Figure 5.4f, would help lower the resonant frequency without changing the overall volume of the helical coil. This occurs as the self-capacitance of the coil would increase. However, it was found that the placement of the material relative to the coil contributed more significantly than the dielectric constant itself. When the material was loosely positioned between loops with a proximity of within 10% of the coil wire diameter, the resonant frequency would only change by approximately 8% when even employing a material with a dielectric constant of 1000. However, when making contact with the loops, effectively moulded around the contour of the coil wire, the resonant frequency would be reduced by over 50%, even when using a material with a dielectric constant of just 3.

Table 5.1: Properties observed with changing dielectric constant and distance with respect to the coil

Example Material	Dielectric Constant	Distance away from coil as a % of coil radius	Change in resonant frequency
Polyethylene terephthalate	3	8.9	-7.6%
Strontium titanate	300	8.9	-7.7%
Barium titanate	1000	8.9	-7.9%
Polyethylene terephthalate	3	4.1	-8.7%
Polyethylene terephthalate	3	2.5	-17.0%
Polyethylene terephthalate	3	0.0	-52.3%
Dimethyl oxalate	8	5.0	-9.1%
Dimethyl oxalate	8	0.0	-61.3%
Poly 4-vinylphenol	9	0.0	-82.4%

The use of ferrite structures in or around the coil models also gave interesting results. Previous works had typically explored incorporating ferromagnetic materials in order to enhance transmission. Liou *et al.* [212] had compared a 4-coil system against a 2-coil system with and without a ferrite film, illustrating that a 2-coil system with ferrite could approximate the same performance to the 4-coil system albeit for a relatively small (i.e. less than one coil diameter) separation distance. It is generally agreed that

including ferrite along the central axis of coils provides the most potential for increasing the coupling factor [213]. Other works have looked at ferrite in combination with other materials in order to shield from the induced magnetic fields: Tang *et al.* [214] applied a thin copper film to ferrite back plates in a 2-coil WPT system, demonstrating that this minor addition increased what the authors called the *shielding effectiveness* by several orders of magnitude compared to plane ferrite. Likewise, Knaisch *et al.* [98] included aluminium plates in order to shield a car body in an e-vehicle inductive charging system. In most cases, using ferrite for shielding would normally mean sacrificing transmission link efficiency and power capability; the extent of which would be down to the geometric design of the ferrite shield.

In a series of simulations, the properties of a commercially available polymer-loaded ferrite film with a permeability μ of 125 were modelled for different ferrite structures. Note that in COMSOL there are a number of different ways to model ferromagnetic materials depending on how closely one wants to represent magnetic losses and hysteresis. Real materials generally have a frequency-dependent response to externally applied fields, and this dependence reflects the fact that a material's polarization or magnetisation does not change instantaneously. For this part of the study, it was assumed that relatively weak magnetic fields were being used with soft iron materials that did not store energy from the field as the current changed direction. Thus, a simple *relative permeability* constitutive relation was applied. Depending on how well real-world experiments compared, it may have been necessary to also consider *magnetic losses* and/or *B-H Curve* constitutive relations during simulation, however, since this was not the main focus of the study, it had been thus far omitted.

In near proximity to the coil (i.e. 50% of the coil diameter away), the ferrite's magnetic energy storage capacity was able to reduce the resonant frequency by 1-3%. Bringing the material to 20% of the coil diameter, the coil resonant frequency could drop as much as 30%. In both cases, especially in a strongly coupled WPT system, this would need to be accounted for in the design of the transmitting and receiving coils, least their self-resonant frequencies no longer match, dramatically affecting link efficiency. Figure 5.5 illustrates a number of mirrored coils and ferrite structures in a WPT link.

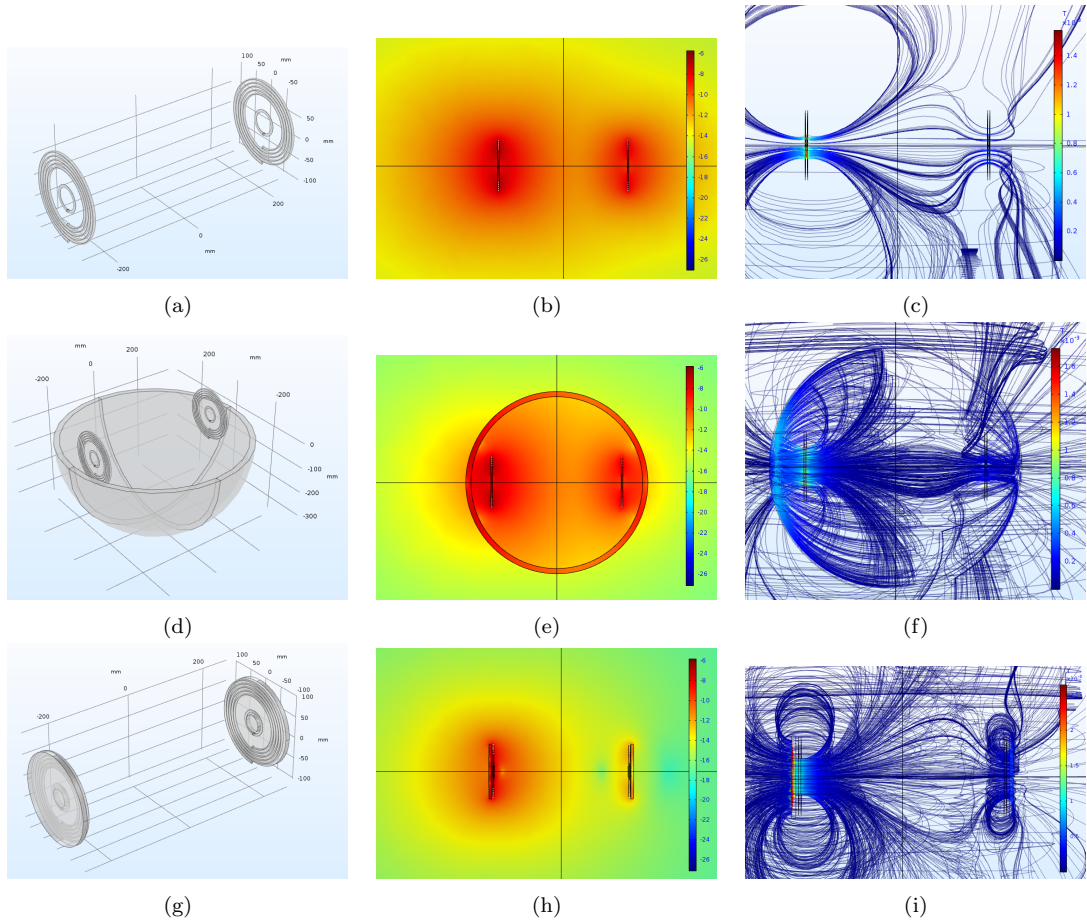


Figure 5.5: Three models (one per row), showing the 3D model of an identical coil set up with (a) no ferrite, (d) a ferrite enclosing sphere (*part hidden of clarity*), and (g) ferrite backplates; along with their respective plots for the magnetic flux density logarithmically scaled and colour matched between images (b), (e) and (h); and streamline plots of the magnetic field along the same view, colour matched between images (c), (f), and (i).

Each WPT system had a coil separation of 50 cm, or roughly 2.5 times the maximum coil diameter. This relationship between separation distance and coil size ratio will be henceforth referred to as the distance-to-size ratio or DS , and arguably provides a more suitable measure of coil transmission range than absolute distance. The top row in Figure 5.5 shows the situation where there is no ferrite present: in this scenario the gain on the receiving coil was measured as 51%. The middle row shows the situation where the coils are enclosed by a ferrite sphere, only improving the transmission gain by around 5%, but more importantly providing significant flux shielding, reducing leakage by around -12 dB immediately behind the ferrite sphere. The bottom row, representing the situation where ferrite backplates are used with each coil, proved to be the best at flux shielding, reducing leakage by around -18 dB at the equivalent distance behind

the prior example's receiver coil. However, its inclusion dropped the transmission gain between the coils to only 30%. These results exemplify that the proper use of ferrite-like materials for either shielding or enhancement is not always straight forward and this aligns well to several conclusions drawn from prior works [213, 215, 216].

Works related to layered segmented coils were further examined as these represented the closest structures to what has been proposed through this work, and thus an excellent opportunity to gather useful insights. Sullivan and Beghou's 2013 novel layered coil introduced previously was of particular interest. Multiple alternating layers of conductive and dielectric thin films were used to construct a cylinder with an effective overall self-inductance and self-capacitance. The structure had a number of benefits over conventional coils that helped reduce losses: distributed capacitances helped to equally share the current load between the thin conductive layers, reducing losses via heating; conductive foil thicknesses were an order of magnitude smaller than easily obtained Litz strand diameters, meaning that they were better at mitigating skin and proximity effects at megahertz frequency ranges; inductive coupling between sections meant that there are no terminations in the main resonant-current path, further minimising losses; and finally, their construction did not suffer from plate losses associated with conventional capacitors, as these were integrated into the structure itself. These results were encouraging for the proposed work as minimising system losses would be key to success; not as much for the sake of increasing the Q -factor, but more to allow induced currents to travel relatively long distances around a larger coil structure. During simulation, another interesting property for this coil emerged, which is not typically present in conventional coils: when sinking power from the layered structure, there seemed to emerge a number of peak frequencies or *modes* that facilitated the highest power transmission across the structure. The number of these modes seemed to depend on the number of coil sections present as defined by Sullivan and Beghou's work. Likewise, the relative amplitudes of these modes depended on where along the layered coil structure power was sunk. Figure 5.6 illustrates this point well, whereby the different plots are generated from driving the stacks across different sections in the layout, thereby changing the current propagation behaviour throughout the entire structure, giving rise to different modes. This effect could be

opportunistically exploited in future works as a means of transferring data efficiently across the garment coil structure at significantly higher frequencies.

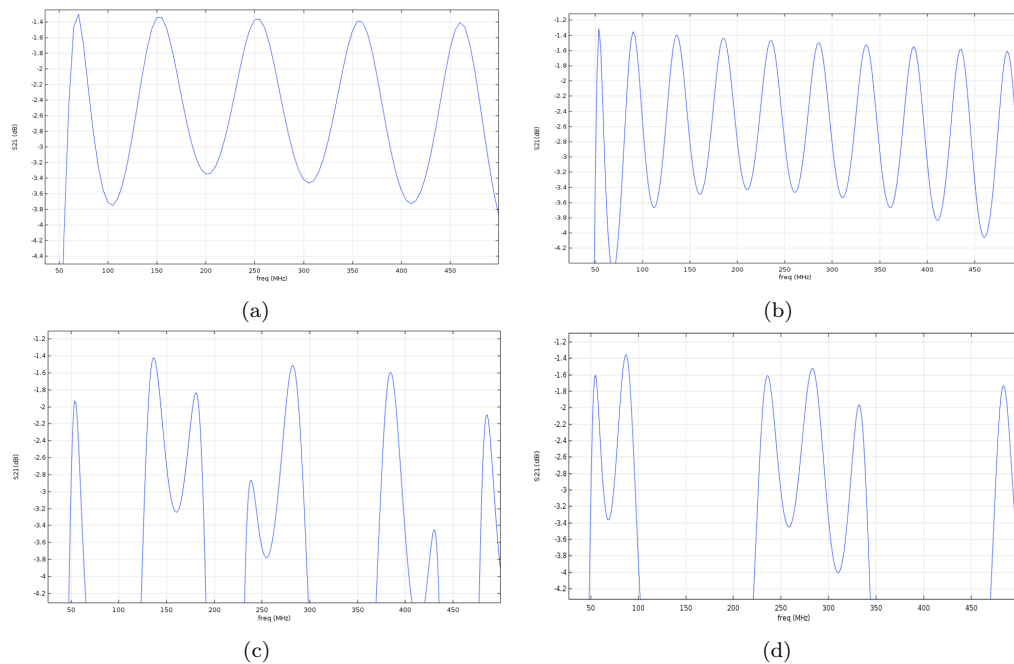
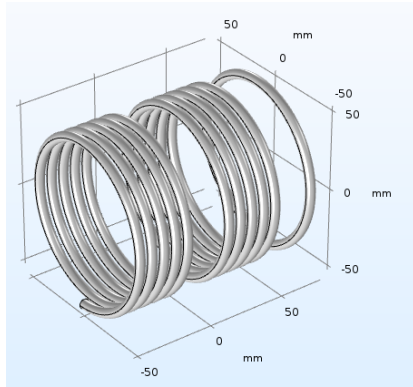


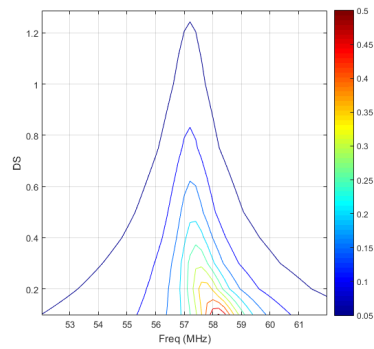
Figure 5.6: S_{21} vs frequency plots for (a) 5-section and (b) 10-section stacked segmented coil with source and load ports between the first and the last layers; S_{21} vs frequency plots for a 10-section stacked segmented coil with the load port (c) 6 stacks and (d) 8 stacks down from the source port.

Figure 5.7 illustrates a number of select system designs for comparison. The coil separation distance in each was always taken as the shortest distance between the resonant coils, and furthermore, a ratio between this separation distance and the maximum dimension of the coils was used rather than a pure distance measure.

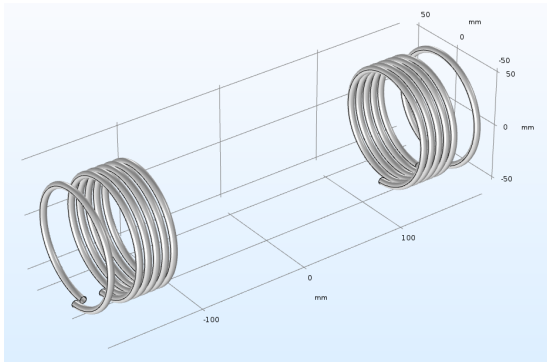
It became evident that a 3-coil system would not be suitable for the large separation distance, even when considering optimisation. The arrangement illustrated only achieved a gain of 50% at 0.2 DS. Instead, 4-coil designs would more likely need to be applied, and examining the plot for the classic helical design clearly illustrates that the gain remains above 50% even at a distance of 2.6 times the maximum coil dimension. Frequency bifurcation was also noted to take place below 1.5 DS. While a positive start, helical resonant coils would be too cumbersome to handle and would take up far too much volume for the desired application. Flat spiral coils were further examined, in particular, those with coplanar and non-coplanar driving and load coils. For simplicity, single loop coils were used; however, as previously indicated, there is an optimisation



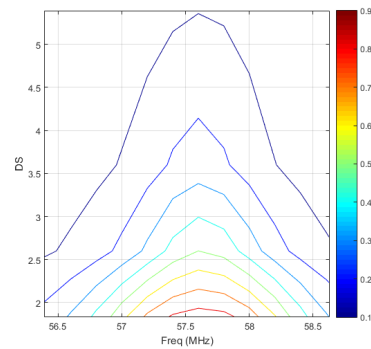
(a)



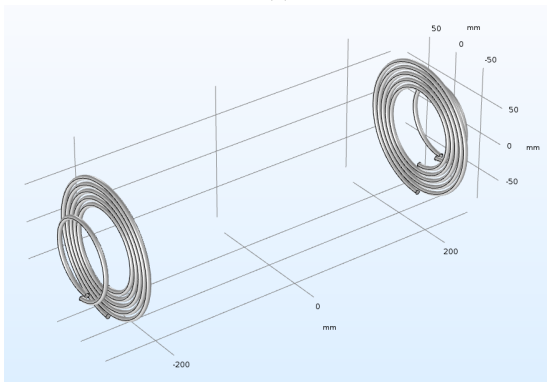
(b)



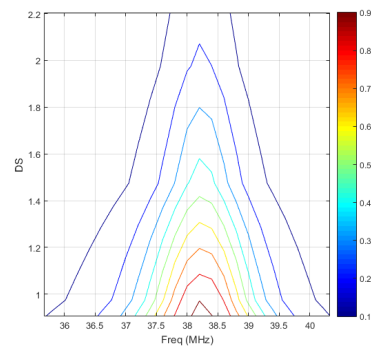
(c)



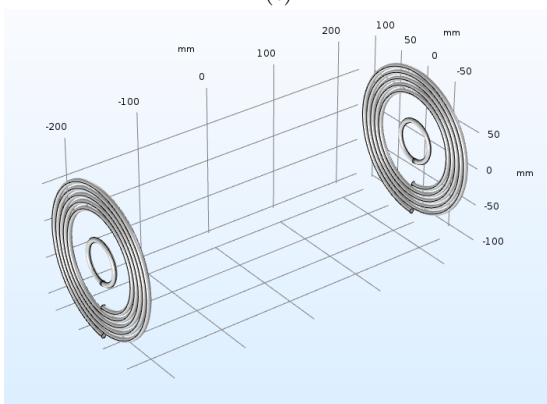
(d)



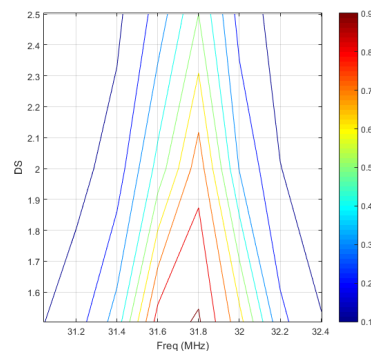
(e)



(f)



(g)



(h)

Figure 5.7: 3D models where transmission gain is just over 60% (left) with associated gain contour plots vs separation distance and frequency (right): (a, b) 3-coil helical, (c, d) 4-coil helical, (e, f) 4-coil spiral with parallel driving/load coils and (g,h) 4-coil spiral with coplanar loop and resonant coils WPT systems.

exercise that could be undertaken to change the transmission characteristic even further. Coplanar set-ups had outperformed non-coplanar set-ups by some margin, not only in terms of transmission characteristics, but also based on ease of implementation. Further simulations were undertaken to observe the effect of progressively growing and shrinking the size of the driving and load loop coils relative to the resonant spiral coil. The results are illustrated in Figure 5.8.

By varying the driving and load coil diameters relative to the resonant spirals, it was found that the separation distance which represented 60% gain could be extended to 3 times the coil diameter. Note that doing so would also extend the point by which frequency splitting would begin, thus a trade off between maximum effective transmission distance and minimum transmission distance can be considered, assuming no form of compensation for the drop in power capability at the resonant frequency takes place.

Compensation methods could include some consideration to coil geometry as previously discussed, but also an ability on the transmitter-side to change the operating frequency, similar in principle to maximum power point tracking. While relatively straightforward, the implementation of such a control system does increase system complexity and overall implementation cost and might not represent the most energy effective solution once in-use.

Finally, the effects of the overall system size was also observed, in order to monitor the power gain and efficiency previously recorded and how it changed with scale. A coplanar set-up was linearly scaled in size and it was observed that the effective transfer DS decreased with increasing scale. This could reasonably be attributed to the effective decrease in the coils' Q -factor with the decreasing resonant frequency.

The results were plotted in Table 5.2 and demonstrate that there is indeed a diminishing and possibly negative return in scaling the coil beyond a certain point, however within a practical size range for the proposed application, designing a bigger coil will always translate into an extension of the effective power transmission distance.

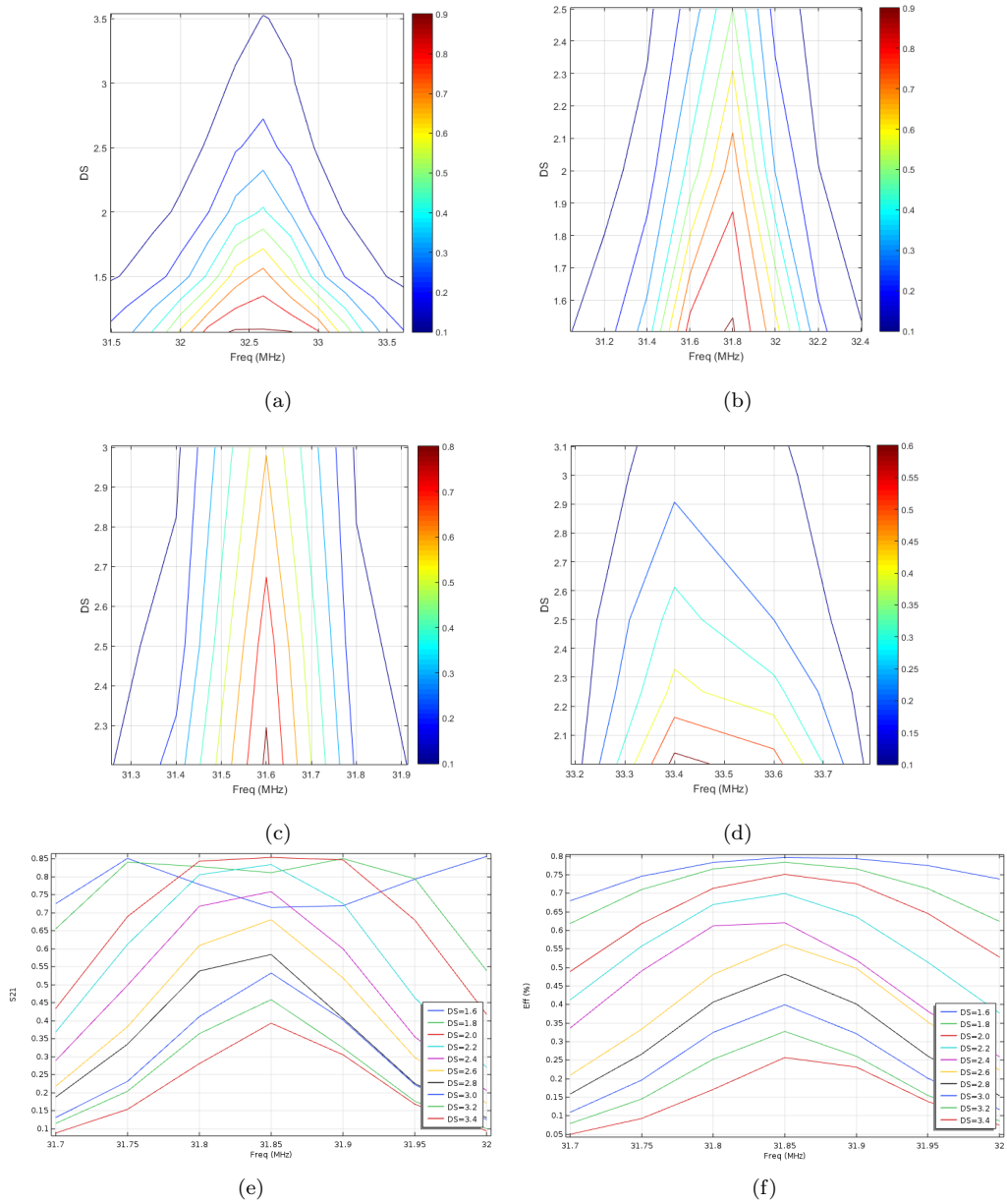


Figure 5.8: Gain contour plots across separation distance and frequency for a 4-coil spiral with coplanar resonant coils of 10 cm diameter and loop coils of (a) 8 cm, (b) 5.4 cm, (c) 4 cm (*note the change in contour scale*) and (d) 3 cm (*note the change in contour scale*) diameters; and DS line plots for (e) S_{21} vs frequency and (f) transmission link efficiency vs frequency for a 4-coil spiral with coplanar resonant coils of 10 cm diameter and loop coils of 4 diameter.

Concluding remarks

This chapter detailed the approach undertaken to simulate a WPT system. Models with known or easily verifiable solutions were simulated to further verify the simulation tool being used and also to gain a first hand appreciation of how these standard coil designs operated under varying system parameters. The physics interface employed was indeed

Table 5.2: Properties observed with changing scale

Scaling Factor	Coil diameter (cm)	DS at 60% Gain	Resonant Frequency (MHz)	Separation Distance (cm)
0.5	10	3.0	64.2	30
1	20	2.5	31.8	44
2	40	2.3	15.9	80
4	80	1.9	7.9	152
8	160	1.2	4.0	192

appropriate for both near-field and far-field modelling and as long as mesh element sizes were much smaller than the wavelengths of driving signals ($>10\times$), there was an established confidence that the simulated outputs would accurately represent the real-world model implementation.

Chapter 6

Design and Construction of a Textile-based WPT System

The previous chapter explored some known coil designs employed within previous works. Building on this knowledge, the following chapter reports on the simulation results for the key resonator designs explored for this thesis. It primarily explores the frequency and field behaviour for different resonator embodiments for each design, both when self-driven and when resonators are incorporated into a WPT system.

The latter half of this chapter examines the manufacturing method employed in order to produce these textile resonators for real-world testing. Finally, a design of a high efficiency transmitter system for physical testing is presented in order to complete the proposed WPT system design for this thesis.

6.1 Simulation Results and Insights

6.1.1 Setting up the Simulation

Simulations were primarily set up as defined in chapter 5; however, it was important to re-examine the different driving port set-up options given the non-standard shape of these resonators, as well as the conductive element boundary condition (BC) choice given the high aspect ratio for the model dimensions involved.

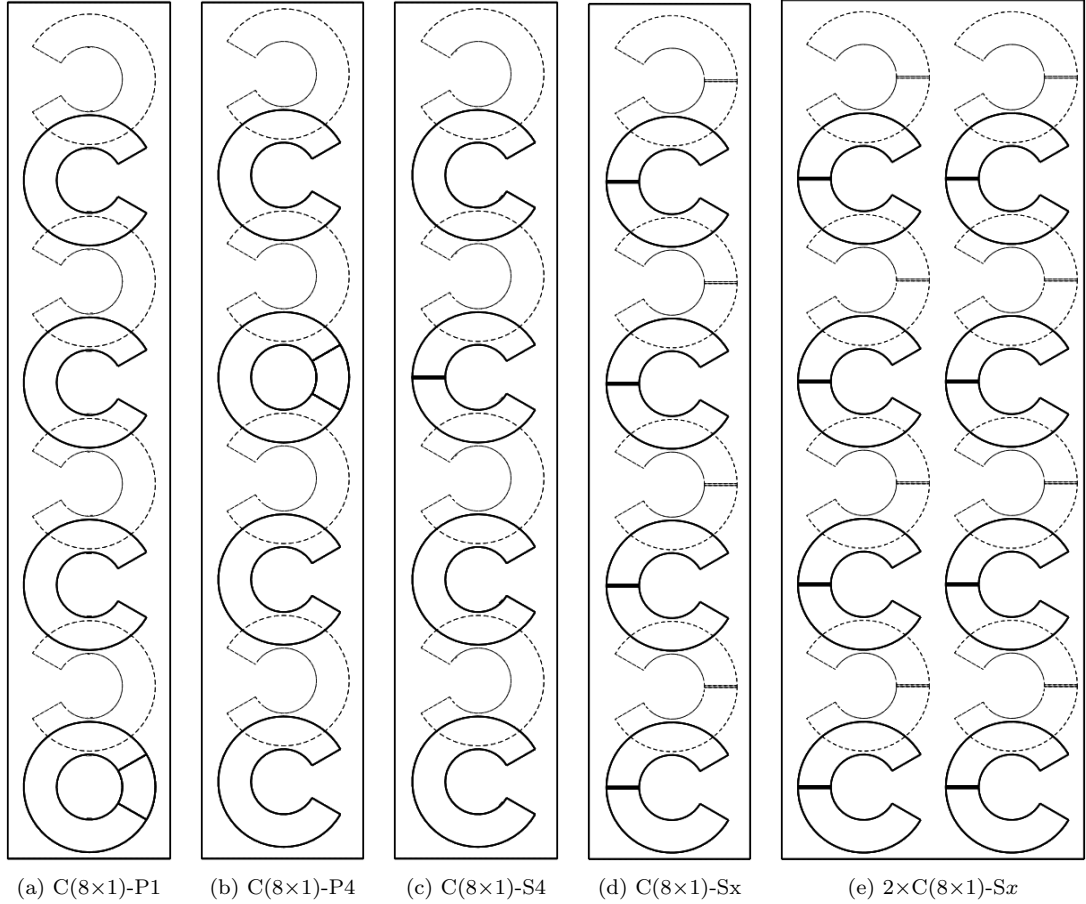


Figure 6.1: C(8×1) models used to test a number of different port connection configurations. Models a) and b) use parallel connected ports on the first and forth coil position respectively, whereas models c), d) and f) use series connected ports as gap feeds.

Driving Port Options

During initial simulations involving standard coil designs, connecting a driving port to the model was quite straight forward; however, with these resonator structures it was not immediately clear how best to introduce the required excitation. An initial C(8x1) design was simulated, using five different port options as illustrated and defined in Figure 6.1.

Note, selecting the optimal port impedance to perfectly match to the resonant structure is a different matter altogether, and while it would have little effect on the frequency values of the self-driven mode observed, it would greatly affect the power delivered to the structure and the eventual performance of a WPT system. At this stage of the design, minimal optimisation was undertaken and a characteristic impedance Z_{ref} of 50Ω and input voltage V_o of 1 V was set at the input port. Impedance matching

for WPT is further commented upon in section 6.1.3. With reference to Figure 6.2, a single mode frequency under scrutiny did not seem to change regardless of which port connection type was chosen; however, the spectrum of the real-part of the input impedance $\Re(Z_{in})$ did change shape. In designs C(8×1)-P4 and C(8×1)-P1, the mode manifested as a local maximum (albeit, with different magnitudes), whereas in C(8×1)-S4, the mode manifested as a local minimum. This is equivalent to an $\Re(Z_{in})$ response when a port is connected in parallel or series respectively. Furthermore, different ports were excited as in design C(8×1)-Sx, and the absolute current at each $|I_x|$ was observed. Again, the mode frequency did not change, only the magnitude of $|I_x|$ at each position. Finally, an additional but non-overlapping row was included in the C(8×1)-Sx model to demonstrate that, unless overlapped, additional resonator elements had little to no effect on the frequency mode.

Conclusions: This illustrates that regardless of the choice of port position and connection, the resonant modes could be clearly identified. It furthermore shows

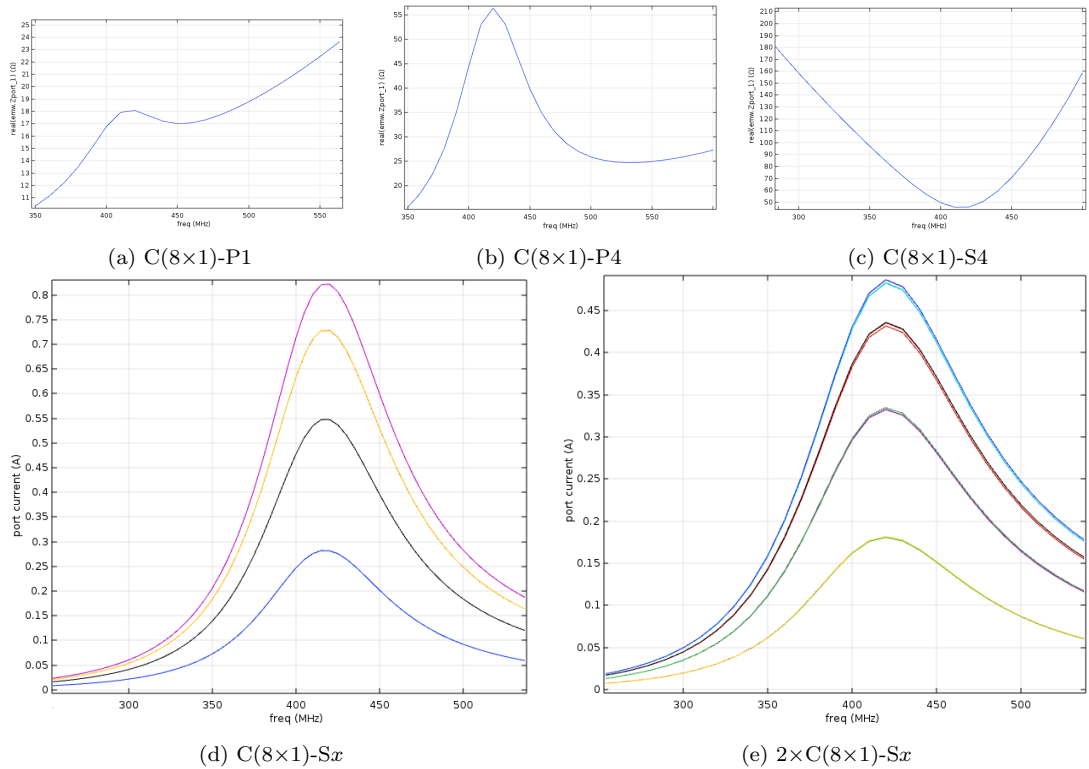


Figure 6.2: a), b), c) $\Re(Z_{in})$ and d), e) $|I_x|$ vs frequency plots for C(8×1) models used to test a number of different port connection configurations, whereby in d) the colours refer to the following port in d) pink: 1 and 8, yellow: 2 and 7, black: 3 and 6, Blue, 4 and 5; and in e) blue: 1 and 8, red: 2 and 7, purple: 3 and 6, yellow: 4 and 5.

that different resonant structures may be laid out very close to one another and not significantly affect the other's spectrum: this is useful across an entire surface if, say, multiple modes for power or data transfer are required by the application.

Conductive Layer BC

There are several ways to set up the conductive layer models all in an effort to reduce the computational complexity in simulation while maintaining or possibly even improving accuracy. In high frequency operation, BCs are usually selected for conductive geometries as, due to the skin effect, the majority of the electric currents will tend to distribute near the model's surface, meaning that there would be no need to mesh and model the physics for the vast majority of the conductive element's volume.

There are three main BC options for electromagnetic problems, and these are *Transition* (TBC), *Impedance* (IBC) and *Perfect Electric Conductor* (PEC-BC). IBC is the common choice for most problems; however, it will inherently treat any volume behind the boundary as infinitely large. While a valid assumption for most models, the thin layers involved required an additional examination using the TBC, which while more computationally taxing, would determine the impedance throughout the geometric thickness of the model.

When using either the IBC or TBC, the material properties defined in the model are taken into account. In this case, a silver ink with a known sheet resistivity R of ~ 10 m Ω per square at a thickness t of 25.4 μm was used. For COMSOL, it was necessary to convert this material value of R into conductivity σ ; hence

$$\begin{aligned}\sigma &= \frac{1}{Rt} \\ \sigma &= \frac{1}{10 \times 10^{-3} * 25.4 \times 10^{-6}} \\ \sigma &= 3.9 \times 10^6 S/m\end{aligned}\tag{6.1.1}$$

Note, solid silver typically has a material σ of 6.30×10^7 , so this ink is an order of magnitude more resistive. In order to appreciate the effect this would have on system performance, simulations using a PEC-BC were conducted. As the name implies,

this applied an idealised material to the conductive layers that was a perfect electric conductor (i.e. possessing a $\sigma = \infty S/m$).

Conclusions: After running the necessary simulations, there was negligible difference observed between the different BCs, as well as when comparing the results to a fully meshed conductive element domain; hence, the IBC was chosen and applied for the remainder of the simulations in this chapter. This helped reduce overall computational cost while maintaining integrity of the calculated results.

Confirmation of the Poynting Vector

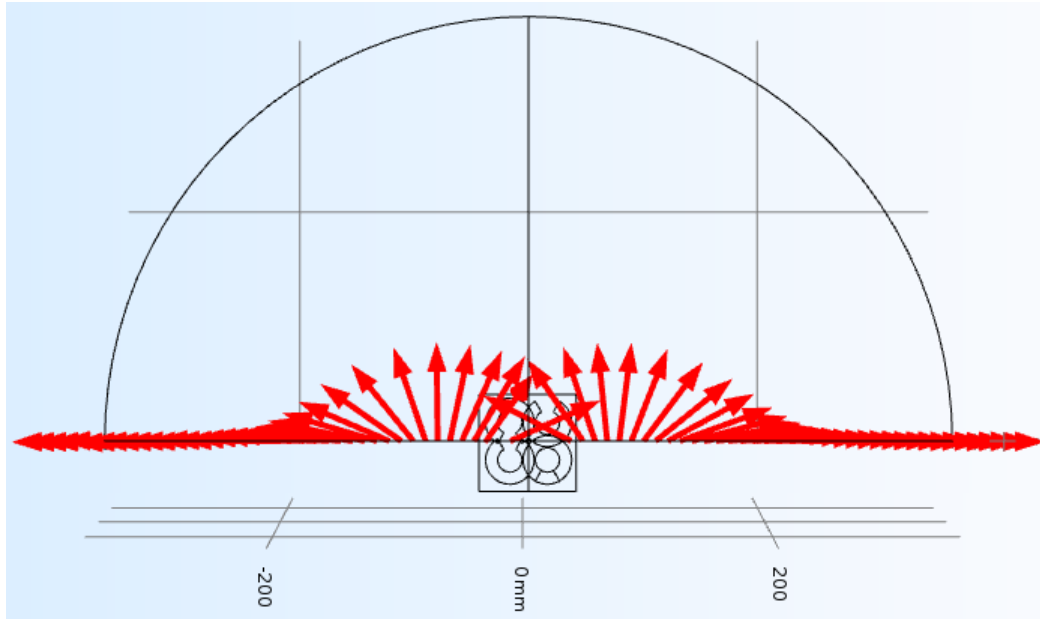
As previously explained in section 5.2, the angle given by a spatially defined Poynting vector could be used to confirm not only the direction of energy propagation within the model but also define the fuzzy boundaries of the near-field. It is generally accepted that the limit of the reactive near-field region of a typical antenna is a distance of $\lambda/2\pi$, where λ is the wavelength of the signal, determined by the frequency of that signal through the conductor. Hence, by looking at the Poynting vector of the model, one could confirm that a suitably sized near-field exists around the resonator.

Conclusions: Figure 6.3 illustrates the average power flow around an example C(2×2) model, with a mode frequency of 174 MHz. While the average power flow is not always uniform as one might expect from, say, a dipole antenna, overall the near-field produced was generally contained within the accepted $\sim 0.159\lambda$ radius (or in this case ~ 27 cm). Furthermore, when the magnetic field lines were plotted, the transition point between the near-field (closed loops) and far-field (lobbing outwardly) also confirmed this observation.

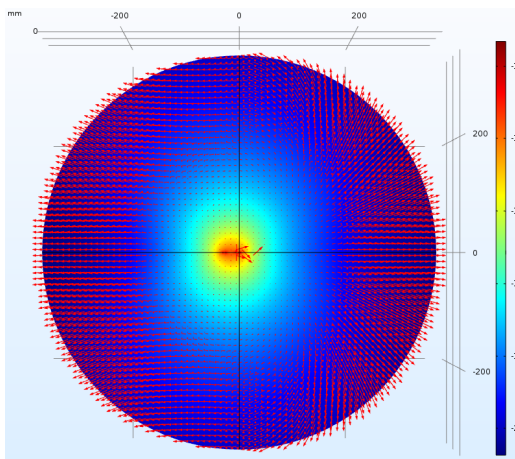
6.1.2 Observations with Self-Driven Geometries

Having set up the appropriate parameters for simulation, different C-type, O-type and W-type models were simulated and the results recorded. The vast majority of simulations employed a Flexible Generalized Minimal Residual (FGMRES) method iterative solver with an error tolerance of 0.1%. This was the recommended solver for these types of physics problems and worked exceedingly well throughout experiments.

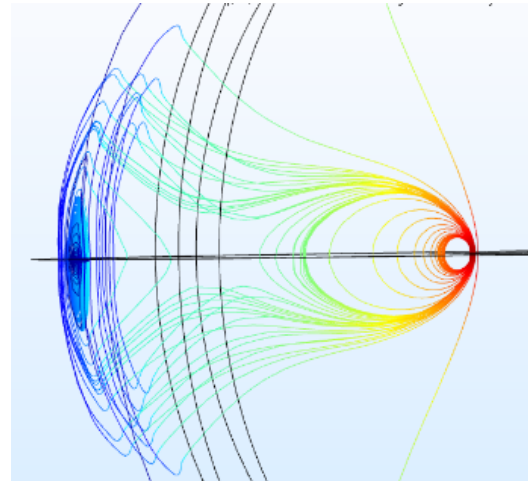
Note, the largest resonator models were limited to $x(8\times 8)$, as even with coarser



(a)



(b)



(c)

Figure 6.3: Arrow plots of the Poynting vector a) front on view, b) top view and a c) magnetic field line plot for a $C(2 \times 2)$ model.

meshed elements, anything larger tended to run out of computer memory during simulation instantiation. Even with a combined virtual and physical available RAM of nearly 64 GB, larger models were simply unable to assemble all the partial differential equations that required solving per mesh element. In the largest models, it became necessary to switch from an FGMRES to a GMRES solver in order to reduce RAM requirement at the cost of speed. For reference, the practical limitations of the solver given the hardware configuration were around 10 million degrees of freedom which equated to a limit of approximately 2 million mesh elements for these particular models.

Behaviour with Increasing Elements

The first set of experiments were concerned with the behaviour of different resonator structures as the number of elements in the patterned structure increased while maintaining the same absolute element size. Table 6.1 reports on each of the models simulated with a layer thickness of 24 μm and an individual element diameter of 40 μm (unless otherwise indicated).

In the case of C-type and W-type it appeared that regardless of the number of elements making up the structure, the dominant mode frequency remained more or less the same. It was also noted that changing the element size had the largest effect on this mode, suggesting that this was primarily dictated by the geometry of a single element. This observation is very similar to the behaviour of traditional metamaterials, whereby the resonant frequency is defined by a single element in the pattern and an increase in the number of identical adjacent elements served only to increase the Q -factor of the overall metamaterial. In contrast, this dominant mode frequency did undergo a distinct change with increasing elements in the case of the O-type, suggesting that increasing the area and possibly the symmetry of overlap between elements would enable some design flexibility for this low- Q dominant mode frequency. Furthermore, a notable change in different mode Q -factors was sometimes observed in the resonant structures examined; however, unlike in the case of metamaterials, it was not a straightforward increase and was even shown to decrease in certain instances. Figure 6.4 illustrates the trends observed in the Q -factor for the first SR mode for each of the designs observed.

The dominant mode in both the O-type and W-type was identified not only at the first significant peak in amplitude observed in the $\Re(Z_{in})$ plot, but also the point where a notable zero crossing occurred in the $\Im(Z_{in})$ plot. In the case for the C-type, the definition of this dominant mode had to be limited to a point of maximal amplification in $\Re(Z_{in})$ and an associated and characteristic drop in the phase in $\Im(Z_{in})$. These qualities are highlighted in Figure 6.5.

This observed behaviour in the dominant mode suggests that a highly symmetric geometric overlap between elements is required in order to significantly alter this mode away from the expected resonant frequency of a single element in the structure.

Table 6.1: Properties observed with increasing number of elements

Design	Structure Size (mm)	1 st SR Mode (MHz)	Dom. Mode (MHz)	No. of Modes under 300 MHz	Q of 1 st SR Mode	Q of Dom. Mode
C(1×2)	71×40	1,260	-	-	3.40	-
C(1×2(+1))*	71×71	231	-	1	178.10	-
C(2×2)	71×71	175	-	1	143.5	-
C(3×2)	102×71	93	-	1	142.61	-
C(3×3)	102×102	92	1,665	2	130.93	4.87
C(4×4)	133×133	87	1,660	4	118.67	5.02
C(6×6)	195×195	78	1,640	11	93.06	4.46
C(8×8)	257×257	69	1,635	15	42.50	5.67
O(2×2)	71×71	277	-	1	53.08	-
O(3×2)	102×71	242	1,400	2	46.10	5.49
O(4×4)	133×133	159	1,330	3	35.33	7.64
O(6×6)	195×195	114	1,075	6	30.81	7.17
O(8×8)	257×257	91	1,320	11	36.38	9.23
O(6×6) [†]	49×49	1,240	-	-	26.95	-
O(6×6) [‡]	390×390	40	640	6	9.14	8.89
W(2×2)	93×93	125	1,640	1	196.80	19.76
W(3×2)	116×76	117	1,650	2	183.28	25.67
W(4×4)	200×152	114	1,671	5	206.27	30.38
W(6×6)	310×267	95	1,672	9	209.23	20.50

*model with 3 elements in total: 2 in one row and 1 in another.

[†]model with element diameter of 10 mm.

[‡]model with element diameter of 80 mm.

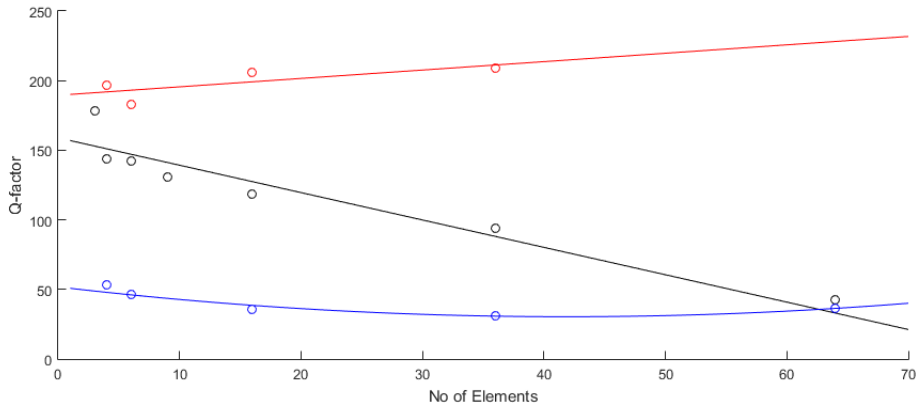
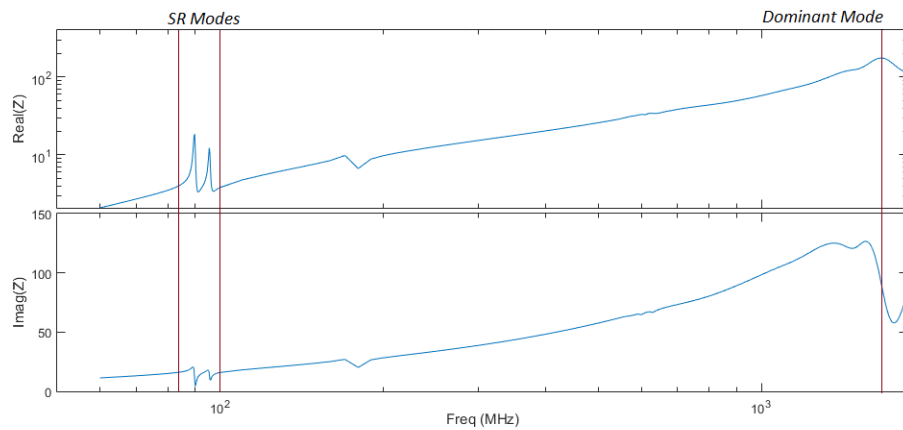


Figure 6.4: Plot of Q-factor vs number of elements for the first SR mode in C- (black), O- (blue) and W- (red) type.

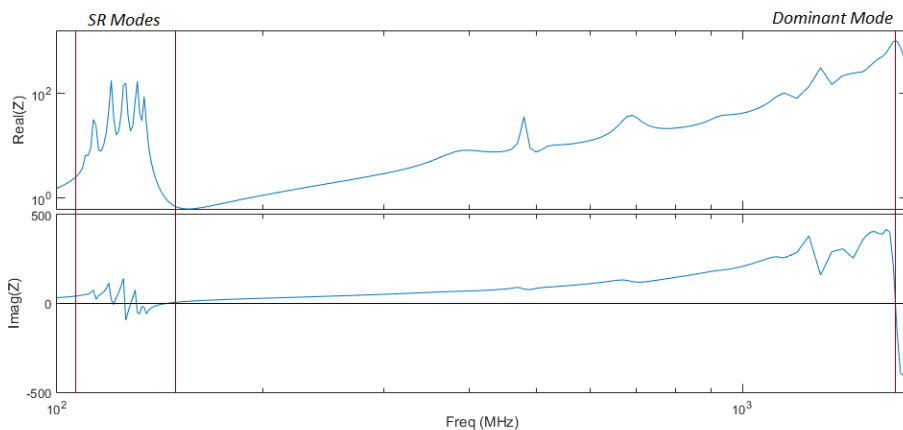
Likewise, it can be suggested that a larger inductance defined by the geometry of a single element helped to significantly increase its Q-factor. While not a striking observation in itself given the known relationship between these two quantities, a design change from

a simple unchanging boundary along a curved axis (as in the C-type) to a boundary defined by a loose sine function along the same sized and curved axis (as in the W-type), created an order of magnitude increase in the resonant structure Q -factor.

At the same time, changing the number elements in the structure had quite a different effect on lower frequency SR modes: increasing the number of elements not only decreased the frequency of these modes but also increased their number along the observed spectrum. This is thought that this arises as including more discrete elements along a dimension would allow further standing wave patterns to coalesce thereby increasing the number of discrete modes. The C- and W-type SR modes were quite asymmetric when compared to the O-type, both in terms of overall shape and amplitude. Figure 6.6 highlights these differences with a selection of $\Re(Z_{in})$ plots.



(a) C(4×4)



(b) W(4×4)

Figure 6.5: $\Re(Z_{in})$ and $\Im(Z_{in})$ plots for models as indicated, showing the characteristic dominant mode and SR modes.

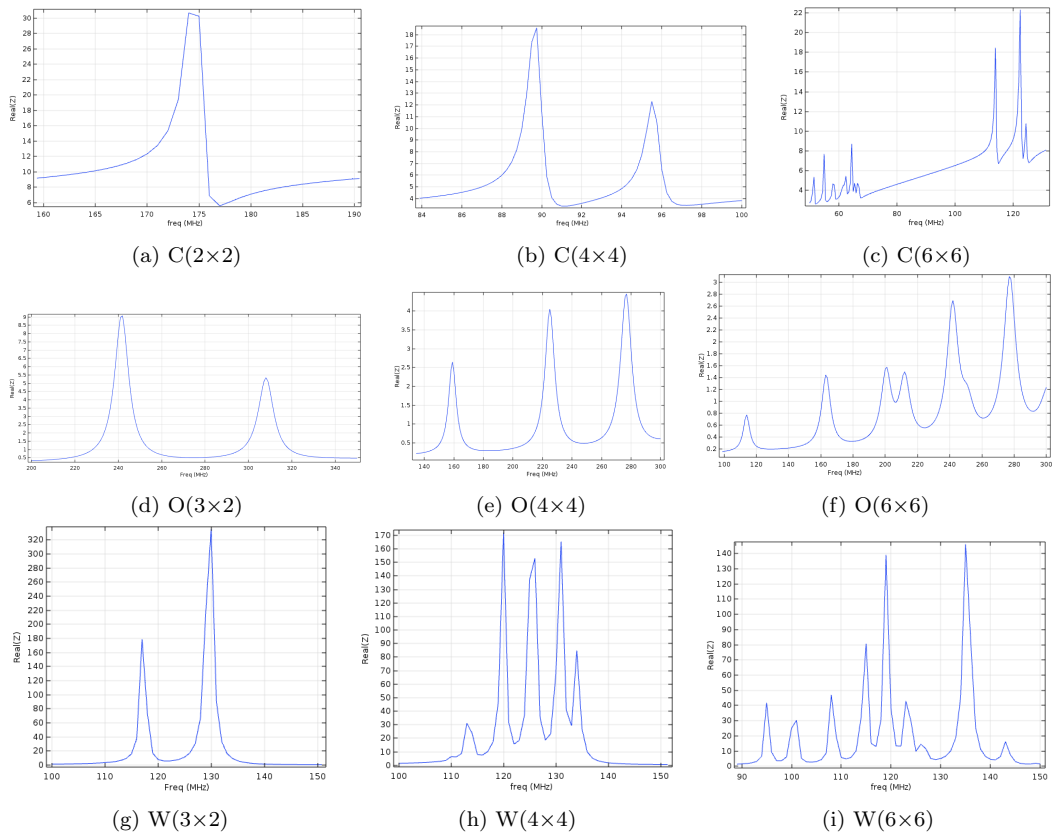


Figure 6.6: $Re(Z)$ vs frequency plots showing the SR Modes for the indicated models.

Furthermore, the decrease in frequency observed with increasing elements did follow a predictable relationship. In each case, a $Ax^b + C$ relationship was postulated as this gave the best fit for the recorded data points. The associated relationship and plots can be seen in Figure 6.7.

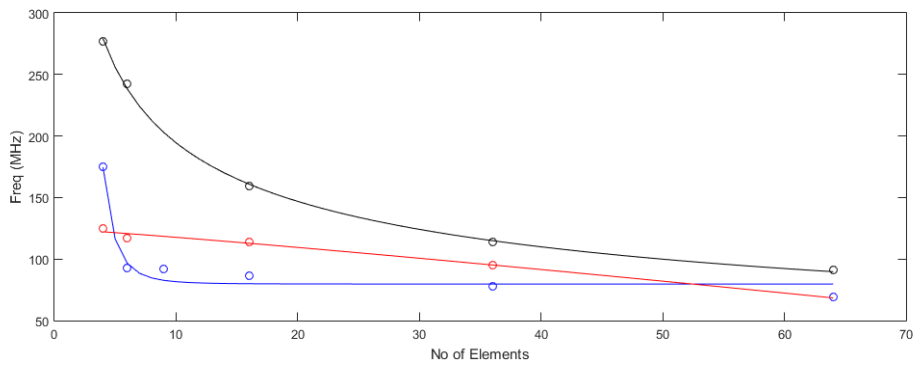


Figure 6.7: Frequency vs increasing elements for C- (blue), O- (black) and W- (red) type models following the best fit curve.

Behaviour with Increasing Element Density

The next set of simulations examined the behaviour of an increasing number of C-type elements within a set surface area. Table 6.2 reports on each of the models simulated with layer thicknesses of 24 μm .

Table 6.2: Properties observed with increasing number elements density

Design	Element Diameter (mm)	Structure Size (mm)	1 st SR Mode (MHz)	Dom. Mode (MHz)	No. of Modes under 300 MHz	Q of 1 st SR Mode	Q of Dom. Mode
C(2 \times 1)	144.79	257 \times 145	355	640	-	3.73	2.41
C(2 \times 2)	144.79	257 \times 257	92	650	1	25.48	5.91
C(3 \times 2)	100.78	257 \times 179	23	630	1	164.21	6.43
C(3 \times 3)	100.78	257 \times 257	23	700	1	183.86	5.00
C(4 \times 4)	77.29	257 \times 257	33	870	4	200.15	6.32
C(5 \times 4)	77.29	257 \times 208	43	1,020	4	237.11	3.25
C(5 \times 5)	62.68	257 \times 257	45	1,100	5	226.05	5.42
C(6 \times 6)	53.72	257 \times 257	52	1,240	10	103.57	5.56
C(8 \times 8)	40.00	257 \times 257	69	1,635	15	172.75	5.67

In the case of the dominant mode, this activity further served to illustrate the change in frequency with increasing element size when compared to simply increasing the number of elements present in the structure. In the case of the C-type, this followed a predictable behaviour as illustrated in Figure 6.8a.

In the case of the SR modes, it was desirable to examine this relationship for a fixed resonant structure area, whereby an increase in the number of elements translated to a decrease in their overall size. For a fixed area and element design, a local minimum frequency in the first mode was observed which began to increase again with ever increasing number of elements. This, as well as the relationship best fitting the observed behaviour, is illustrated by Figure 6.8b.

Behaviour with Increasing Layers

The next set of simulations examined the behaviour of increasing the number of sections for a selection of resonant structures. A section here is defined by a dielectric layer, sandwiched between companion conductive layer elements. Each additional section

was a copy of the previous one in the stack whereby each section was separated from another by a dielectric layer. This had the effect of creating the same overlap pattern along all directions in the resonant structure, as illustrated by Figure 6.9.

Table 6.3 reports on each of the models simulated with increasing sections at a layer thickness of $48\ \mu\text{m}$ and individual element size of $40\ \text{mm}$. Note, the increasing number of sections examined had negligible effect on the dominant mode frequency or shape, hence details of these were omitted from the table below.

Table 6.3: Properties observed with increasing number of sections

Design	Structure Size (mm)	1 st SR Mode (MHz)	No. of Modes under 300 MHz	Q of 1 st SR Mode
C(6×6×1)	195×195	109	10	156.67
C(6×6×2)	195×195	76	7	139.81
C(6×6×3)	195×195	63	7	127.43
C(6×6×4)	195×195	48	7	119.19
C(6×6×5)	195×195	43	7	115.21
C(4×4×1)	133×133	127	4	144.52
C(4×4×2)	133×133	81	4	144.29
C(4×4×3)	133×133	64	4	114.73
C(4×4×4)	133×133	55	4	108.43
C(4×4×5)	133×133	49	4	94.90
W(3×2×1)	116×76	165	1	195.71
W(3×2×2)	116×76	106	1	221.04
W(3×2×3)	116×76	85	1	218.69
W(3×2×4)	116×76	73	1	211.88
W(3×2×5)	116×76	65	1	210.97

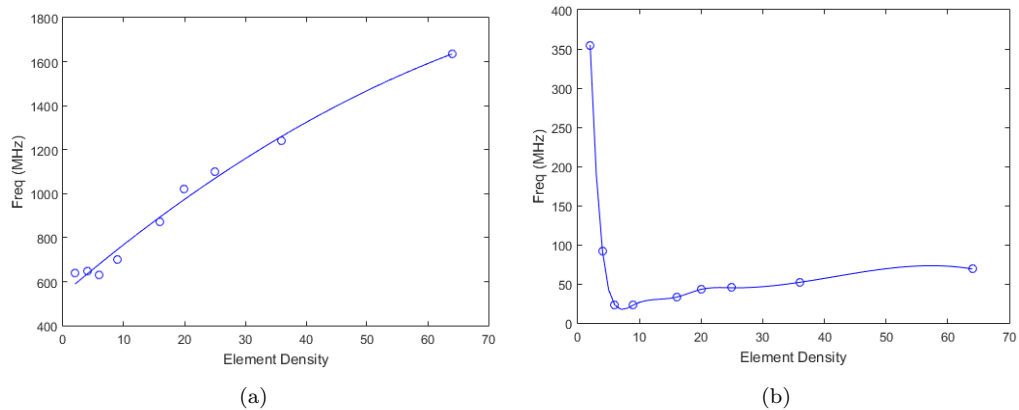


Figure 6.8: a) Dominant mode frequency and b) SR Mode frequency vs increasing element density for C-type models following the best fit curve.

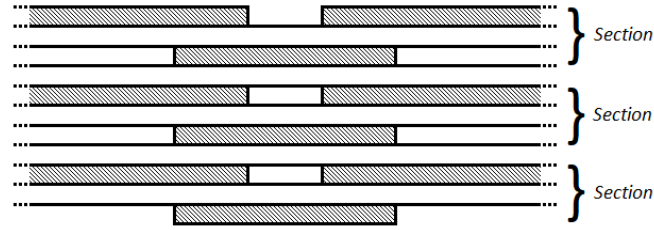


Figure 6.9: Illustration of stacked structure showing individual sections separated by a dielectric layer

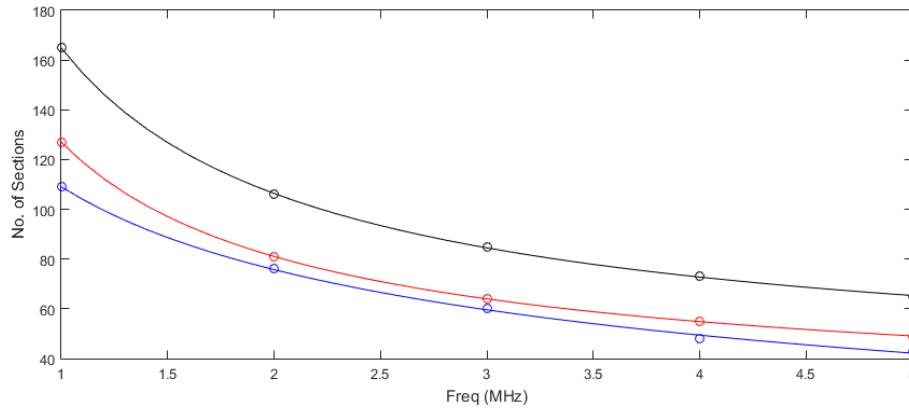


Figure 6.10: Plot for number of sections vs frequency for C(6×6) (blue), C(4×4) (red) and W(3×2) (black) following a best fit curve of the form $Ax^b + C$.

The overall shape, number and separation between modes did not appear to change whatsoever with increasing layers, however their frequency decreased with every additional section. The rate of this decrease was different for different element types and their respective relationships are illustrated in Figure 6.10. Note as well, the SR mode Q -factor also had a tendency to decrease with the addition of new sections; however, this was not always the case, as was observed with the W-type example given.

Behaviour with Increasing Layer Thickness

The next set of simulations examined the behaviour of increasing the layer thicknesses for a selection of C-type models. Table 6.4 reports on each of the models simulated with individual element sizes of 40 mm with increasing layer thicknesses. Note, the increasing layer thickness in the ranges examined had negligible effect on the dominant mode frequency or shape hence details of these modes were omitted from the table below.

While the table above presents the thicknesses modelled for all layers in the resonant structure, the change in behaviour observed can be exclusively linked to the dielectric

Table 6.4: Properties observed with increasing layer thickness

Design	Structure Size (mm)	Layer Thickness (μm)	1 st SR Mode (MHz)	No. of Modes under 300 MHz	Q of 1 st SR Mode
C(2×2)	71×71	12	123	1	147.28
C(4×4)	133×133	12	63	4	134.68
C(6×6)	195×195	12	55	10	96.49
C(8×8)	257×257	12	49	11	18.73
C(2×2)	71×71	24	175	1	143.5
C(4×4)	133×133	24	87	4	118.67
C(6×6)	195×195	24	78	10	93.06
C(8×8)	257×257	24	69	11	42.50
C(2×2)	71×71	48	243	1	173.93
C(4×4)	133×133	48	127	4	155.99
C(6×6)	195×195	48	109	10	83.78
C(8×8)	257×257	48	98	11	21.34
C(2×2)	71×71	72	289	1	145.08
C(4×4)	133×133	72	154	4	96.00
C(6×6)	195×195	72	132	10	44.1
C(8×8)	257×257	72	117	11	15.43
C(2×2)	71×71	96	332	-	141.23
C(4×4)	133×133	96	177	3	92.89
C(6×6)	195×195	96	152	9	26.22
C(8×8)	257×257	96	134	11	3.22

layer thickness. Given that the overlap area A and dielectric material properties (expressed by $\epsilon_0\epsilon_r$) define the capacitance C between the individual elements, it was expected that a decrease in the dielectric's thickness t would serve to increase the overall capacitance in the structure and hence decrease the frequencies observed. This relationship is expressed in 6.1.2.

$$\begin{aligned}
C &= \epsilon_0\epsilon_r \frac{A}{t} & f &= \frac{1}{2\pi\sqrt{LC}} \\
\therefore f &\propto \frac{1}{\sqrt{C}} & \therefore f &\propto \sqrt{t}
\end{aligned} \tag{6.1.2}$$

Figure 6.11 relates the square root of the thickness t to the decreasing frequency observed for each model type. It shows a constant plot gradient between them within an acceptable error tolerance, thus confirming the above relationship. Furthermore, the observation that the dominant mode frequency was not affected by the change in capacitance along the structure once again helped to solidify the previous assertion

that the dominant modes seem inherently linked to the individual element geometry, whereas the semi-resonant modes were independent of this constraint.

Finally, the Q -factor for the first SR mode was recorded during each experiment, and the trend for each thickness is given by Figure 6.12. All models show the expected decreasing trend in Q , although the rate of this decrease did vary with later thickness.

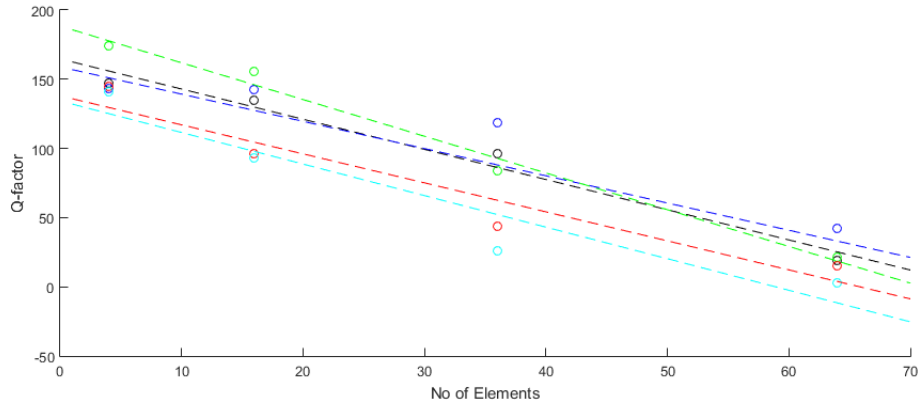


Figure 6.12: Plot of Q -factor vs number of elements for the different thicknesses of the examined C-type elements. These were 12 (black), 24 (blue), 48 (green), 72 (red) and 96 (cyan) microns.

Concluding remarks

In summary, these simulations showed that the SR modes and the dominant modes within a single structure are decoupled from one another, with the dominant mode being dictated by the properties of a single element within the structure and the shape and number of SR modes dictated by the global pattern and its properties. They

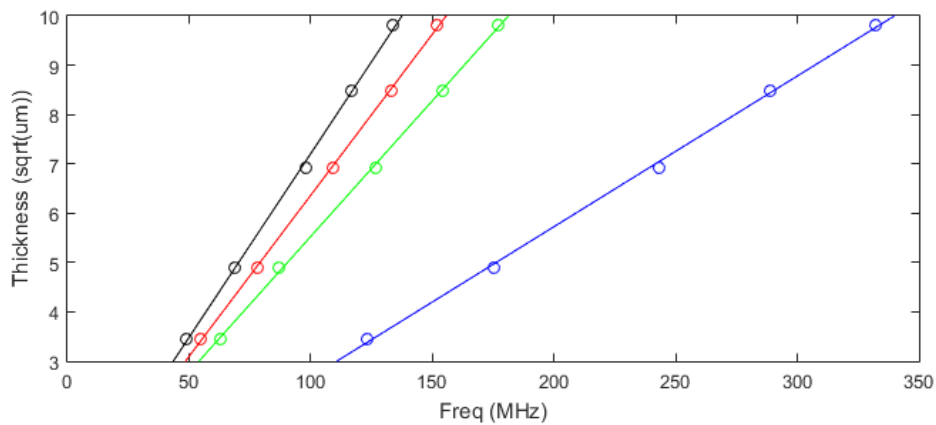


Figure 6.11: Plot of \sqrt{t} vs f for variations in C(2x2) (blue), C(4x4) (green), C(6x6) (red), C(8x8) (black) models.

also demonstrated how changing key geometric parameters (and to what degree) led to significant changes in the spectral behaviour. Where possible, predictable trends in the changes of the mode frequencies and their respective Q -factors with respect to physical geometry were noted. Characterising these behaviours thus enables the intrepid engineer to design resonant structures with whatever spectral pattern the application requires. While this analysis has been limited to just three core pattern designs, it aptly demonstrates how this novel approach to resonator design allows for a more dynamic spectral profile to emerge within a patterned, relatively simple structure.

6.1.3 Observations under WPT Conditions

With the individual resonator behaviours characterised, several choice resonator models were simulated as a WPT system. As with the previous simulations, an FGMRES iterative solver was used with an error tolerance of 0.1%. The WPT transmission link efficiency η was the key parameter under observation and could be evaluated a number of ways. The relationships in (6.1.3) are most often cited in the literature [217] and are employed according to the physical tools available to the researcher.

$$\eta = \frac{P_o}{P_i} = \frac{\kappa^2 Q_1 Q_2}{\left(1 + \sqrt{1 + \kappa^2 Q_2 Q_1}\right)^2} = \frac{|S_{21}|^2 (1 - |\Gamma_l|^2)}{|1 - S_{22} \Gamma_l|^2 (1 - |\Gamma_i|^2)} \quad (6.1.3)$$

Where P_o and P_i are the output and input power respectively, S_{xy} are the S-parameters given for a pair of input and output ports, Γ_l is the reflection coefficient at the load and Γ_i is the reflection coefficient at the input port. These are further given by

$$\Gamma_l = \frac{Z_l - Z_0}{Z_l + Z_0}$$

$$\Gamma_i = S_{11} + \frac{S_{12} S_{21} \Gamma_l}{1 - S_{22} \Gamma_l}$$

Besides attempting to maximise η , care was also taken to ensure that the maximum output power possible was achieved at every instance. Looking at the relationships above, there are some intuitive ways to approach this task: the with most effective means being to closely match the input and output port impedances with the coupled

resonant geometries in-between the ports at the operating frequency of interest. Within a simulation environment, the characteristic impedance Z_0 of these ports is set by the user and while some consideration is necessary to ensure that results generated were indeed valid, the ability to adjust the model's port features makes the problem of impedance matching relatively trivial. Note, the same cannot be said during physical implementation, and a brief examination of this is presented in section 6.3. Operating at the SR modes also helps ensure a larger Q in order to compensate for any decrease of κ with increasing separation distance, thereby enabling maximal gain. Finally, and as more of a practical recommendation, ensuring that the system could operate at a low Z_0 which translates into a low source and load resistance R . Following a combination of the above will help ensure maximum power delivery on the output.

Initially, a 2-coil type architecture was employed with identical resonators connected directly to input and output ports. The spectral behaviour observed when plotting the input impedance was mirrored when examining the S-parameters, in that the same number and position of SR modes was observed that facilitated enhanced energy transmission. These gave fair transmission efficiencies for the W-type but poor efficiencies for the O- and C- type, demonstrating the need for a larger inductance on the single coil elements. Table 6.5 reports on the maximal efficiencies for a selection of 2-coil models with layer thicknesses of $24\ \mu\text{m}$ and individual element diameters of 40 mm.

Table 6.5: Wireless Transfer Efficiencies for select models

Design	Structure Size (mm)	DS	SR Mode (MHz)	Q at select SR Mode	S_{21} at select SR Mode	S_{11} at select SR Mode	Power Transfer Efficiency η
W(4×4)	200×152	0.1	114	206.27	0.75	0.19	58.36%
W(4×4)	200×152	0.2	114	206.27	0.45	0.25	21.60%
W(6×6)	310×267	0.2	95	209.27	0.42	0.59	27.06%
O(4×4)	133×133	0.2	159	35.33	0.15	0.89	10.82%
O(6×6)	195×195	0.2	114	30.81	0.1	0.9	5.26%
C(4×4)	133×133	0.2	87	118.67	0.18	0.68	6.02%
C(6×6)	195×195	0.2	78	93.06	0.05	0.85	0.90%

The simulated efficiencies with respect to separation distance for the 2-coil W-

type resonator system was already in the same range as the classical 3-coil helical system, but with the added advantage of the individual resonator structure occupying negligible volume. Putting this into perspective, a single helical coil from the simulated 3-coil system presented in chapter 5 would need to occupy 1,345 times the volume than an equivalently scaled W-type resonator coil and would mostly be comprised of empty space. An equivalent helical 3-coil WPT system, not counting the space in-between the Tx and Rx side of the system, would need to occupy roughly 3,200 times the volume of an equivalently scaled W-type resonator WPT system. Comparing the volume requirements to an equivalent coplanar 3-coil WPT, similar to those presented in chapter 5, would depend on the chosen diameter of the wire material; however, the comparable volume would be a much more reasonable figure (in the range of 50 times the volume for a 3 mm thick coil wire). Nevertheless, a large portion of this volume would still be empty space given the nature of standard coils, thus the proposed resonator structure makes much better use of the available space.

Motivated by this comparison, the focus then shifted to examining the performance of a 4-coil type architecture which employed either a single loop drive and load coils, or duplicate resonant restructures acting as the drive and load coils, as illustrated in Figure 6.13.

It was observed that the introduction of the loop coils dramatically shifted the frequency response of the resonator structures, at several times even seeming to collapse the dynamic spectral behaviours observed into just a single SR mode for transmission. It is theorised that this may be caused by the loop coils' own resonant frequency coupling to the resonant structure and dominating the transmission mode. Furthermore, when compared to standard 4-coil transmission at 1 DS, the observed efficiency was very poor (in the order of 10%) across all the structures tested, implying that this set up was not suitable for mid-range WPT.

In order to counteract the effect of single loop driving and load coils, these were replaced by identical resonant structures. In these instances, the mirrored driving and receiving resonators merely caused a down shift in the spectral behaviour, but maintained the expected shape for a given design. The shift can be attributed to the close coupling of the respective resonator structures on the transmitting or receiving

ends, not unlike what can be observed in standard 4-coil transmission. Even after rigorous testing, the observed performance was still quite poor (in the order of 1-15%), across most of the structures tested.

Concluding remarks

In moving from a 2- to a 4-coil architecture, the usual intuitions derived from standard WPT geometries appear to break down, and thus a further examination into design principles for multi-coupler WPT systems using these proposed resonant structures would need to take place in order to optimise transmission efficiency with respect to separation distance while maintaining the enormous advantages garnered from this approach. This, however, is beyond the scope of this work and presents an interesting

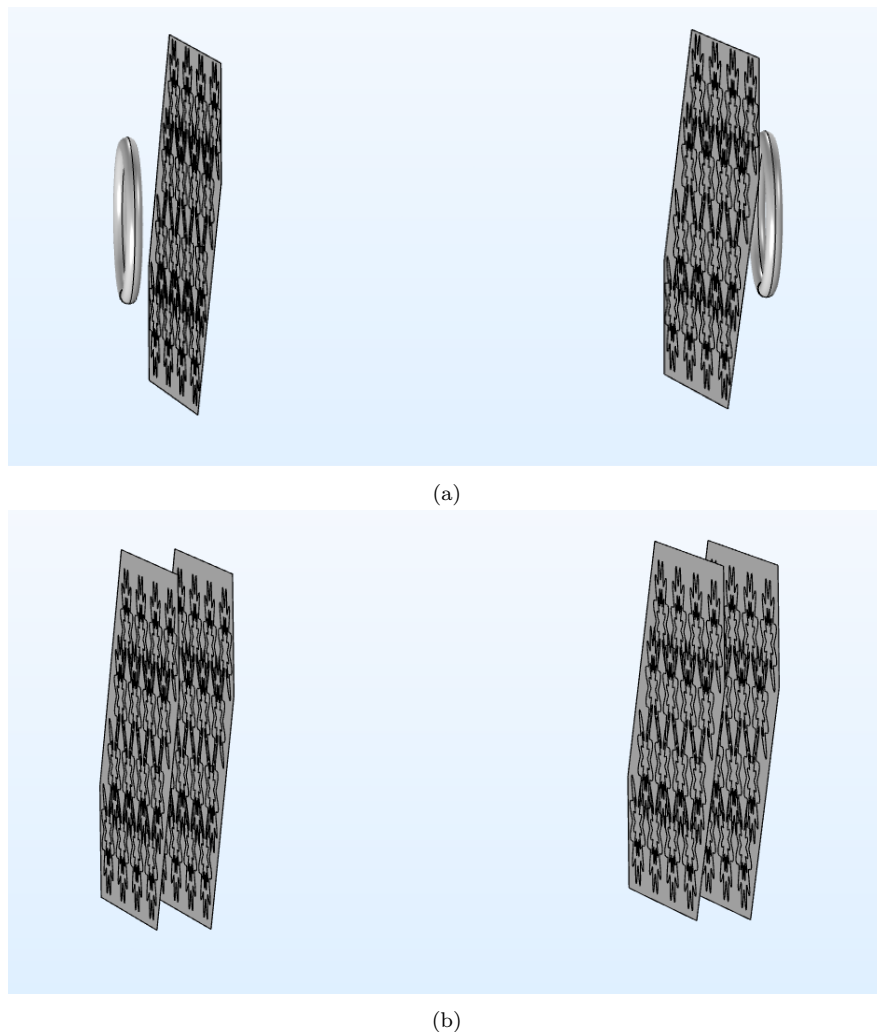


Figure 6.13: 4-coil WPT set up with a) single loop drive and load coils, and b) duplicate resonant drive and load structures.

avenue for future research.

6.2 Notes on Manufacturing the Resonator Design

Different methods of manufacturing the proposed textile resonator were briefly touched upon in chapter 4. Principally, these involved disposing a very thin layer of dielectric material between thin layers of electrically conductive elements, wherein each conductive element on one side of the separating dielectric overlaps with one or more of the conductive elements on the other side of the dielectric layer. Furthermore, the methods must be scalable so that any number of alternating layers of conductive and dielectric material could be applied as illustrated in Figure 6.14

Screen printing is a well-established manufacturing technique used to produce very thin, substantially planar layers of material. Printing is a simple, highly scalable approach for producing the planar resonators at a range of different sizes. In particular, the application of a planar resonator to a flexible textile material using printing allows the simple incorporation of WPT capabilities into wearable garments (for example, t-shirts, shirts, vests, shorts, trousers, jumpers, hoodies, sweatshirts, etc.).

A planar resonator comprising a flexible conductive material and/or a flexible dielectric material means that the planar resonator can conform to a wearer's physiology, once incorporated into the garment. Printing also allows planar resonators to be applied to a textile surface to either form at least part of a visually aesthetic design or pattern (for example, using opaque and/or coloured materials), or applied discreetly to a textile surface (for example, using substantially transparent materials).

Instead of directly printing onto a textile or finished garment, the various layers were first printed onto a suitable sheet of material and then heat transferred onto the garment. Besides allowing much more flexibility during the garment construction phase, this process lends itself to a much more efficient production line: a layer (between 5 μm

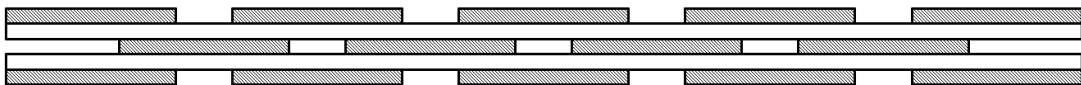


Figure 6.14: An example planar resonator with three stacked arrays of electrically conductive elements separated from one another by layers of dielectric material.

and 250 μm) could be printed and cured in a matter of minutes, and then cycled back for the same process to repeat for each subsequent layer required. The processes means that the different materials used only required curing at a temperature of 130°C for 2 minutes. Certainly, different material formulations may require different curing times and curing temperatures as well as different curing methods such as heat, pressure and UV irradiation.

The conductive material was a specific silver ink, formulated by one of KYMIRA's production partners. This ink had an impressive resistivity of approximately 7 $\text{m}\Omega$ per square at 25 μm which, for reference, is an order of magnitude more resistive than solid copper at the same thickness (i.e. 0.7 $\text{m}\Omega$ per square). Furthermore, it was able to stretch nearly as much as 50% its original length without suffering cracks; survive over 40 wash cycles with 1,000 hours in 85/85 tests; and was of a reasonable supply cost (<50p per gram), making it a commercially viable solution to use beyond the work presented in this thesis. The dielectric material had similar properties to the conductive material, save that it was an electrical insulator (with a dielectric constant of between 3 and 4) rather than conductor. The material was based on a standard polymer and could also serve as a waterproof or encapsulation layer over the whole pattern in order to protect the resonator from fluid ingress and associated damage (such as from sweat or washing detergents).

The largest production cost (in the order of several hundred pounds) was attributed to the mesh screen for printing. After this, however, the screen can be re-used for a number of years over thousands of prints, with each resonator pattern printed at a cost in the order of 10s of pence per sheet. Figure 6.15 shows several examples of constructed resonator patterns built up layer by layer onto a heat-transfer vinyl.

An industry-standard heat-activated fabric adhesive was applied to the pattern and activated using a temperature of 160°C for 12 seconds. To apply it to the fabric, a manual fabric heat press was used; a standard piece of equipment in the textile graphics printing industry. The heat-transfer sheet material was then peeled off, leaving the printed resonator structure affixed to the fabric as shown in Figure 6.16.



Figure 6.15: Several examples of constructed resonator patterns built up onto a heat-transfer vinyl.

6.3 Designing a Suitable Transmitter and Test Rig

One of the key challenges in a dynamic WPT system is designing circuitry that can not only provide enough power to a transmitted signal but is able to cope well with different coil positions – all while maintaining optimal performance and reduced electrical losses. Many approaches rely on control systems which, while effective, have several disadvantages stemming from their increased complexity. These systems tend to employ microcontrollers to sense transmitter circuit parameters or even to wirelessly receive feedback from the receiving unit, running algorithms to maintain high power or highly efficient transmission. They also tend to have a much higher component count, driving up the costs of manufacture and eventual deployment.

Better solutions have been presented in recent years and an approach based on a Class E inverter design had been chosen for this work. It is elegantly simple in its deployment, yet requires a very detailed understanding of amplifier design in order to

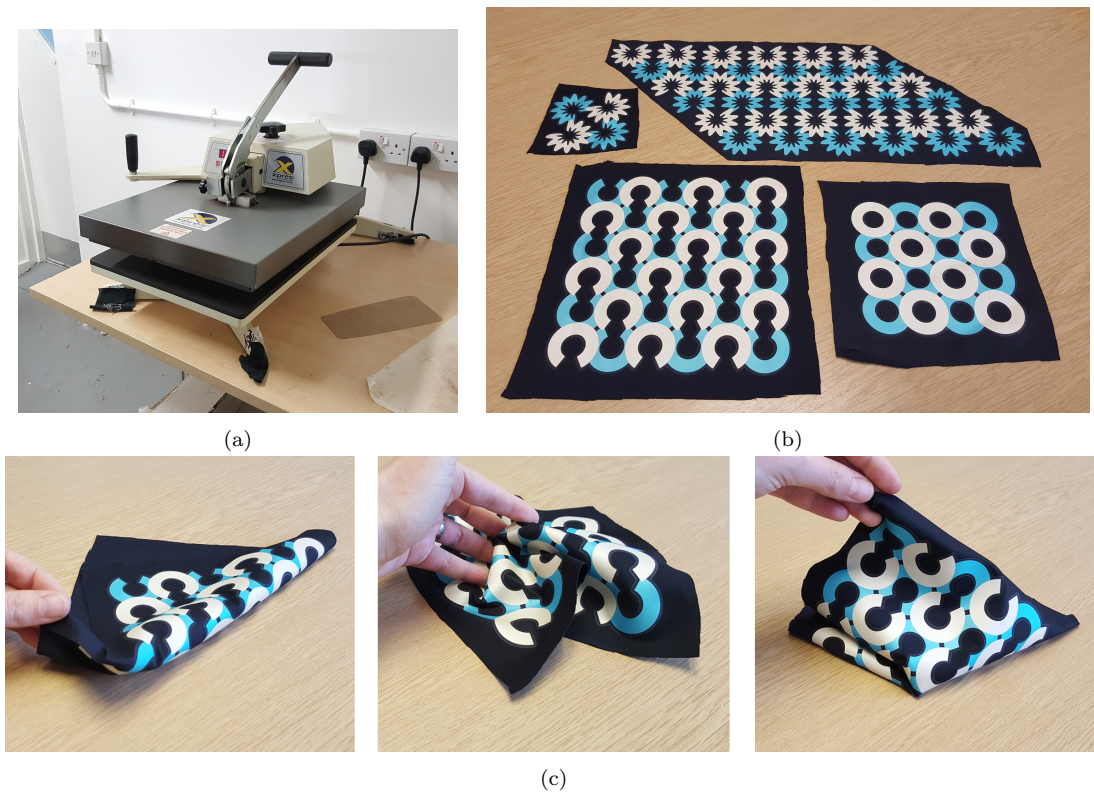


Figure 6.16: a) Manual heat press used to apply a temperature of 160°C at roughly 6 Bar for 12 seconds, b) patterns printed onto a black polyester fabric, and c) demonstration of a resonant structure’s textile like property.

derive and solve the necessary equations. In order to gain a suitable appreciation, this chapter explores its theoretical design and practical implementation for WPT.

6.3.1 Class E Inverter Analysis

The basic Class E inverter was first presented in 1975 by Sokal and Sokal [218]. Figure 6.17 illustrates the typical circuit design for a switching-mode Class E inverter. This type of inverter uses a MOSFET as a switch so that when the switch is closed, current flows into the switch and when the switch is open, current flows into the load. The main advantage of this class of inverter is that it can theoretically achieve 100% efficiency, as power dissipation in an ideal switch is zero and all the power is delivered to the matched load. In practice however, one typically achieves an $\sim 80\%$ efficiency due to non-ideal components, as well as power being lost in the harmonics of the switching frequency f_s .

The aim of this circuit is to create a sinusoidal current with frequency f_s from a

DC voltage source V_i . Applied to WPT, this current would drive the output resonant coil, defined here by L_2 and C_2 , and transfer power from the primary resonator to a nearby secondary circuit. This transfer of power to a secondary can be viewed as an additional impedance in series with the primary resonator which, assuming resonant power transfer, could be considered a simple resistant load R_L .

During the switching cycle, the MOSFET switch closes and pulls current out of the resonator L_2C_2 . When the switch is open, the resonator then pulls current from the capacitor C_1 in order to complete the cycle. Therefore, the output current alternates between the MOSFET and the parallel connected C_1 . In order to achieve high efficiency, one needs to minimise the power dissipation in the switch which would occur whenever a voltage across it exists and a current is able to flow at the same time. This is likely to occur during the opening and closing points of the switch, and hence Class E inverters are designed to operate at zero-voltage switching (ZVS) during a switch transition and zero-current switching (ZCS) when transitioning from an open to a closed state. ZVS is achieved by draining the capacitor C_1 before the switch transition and ZCS is achieved through a current phase shift caused by the inclusion of L_x .

Additionally, this configuration can achieve zero-voltage derivative switching (ZVDS) during an open-close transition, further reducing power losses in the switch. This practice is known as *soft* switching and is commonly employed to minimise EMI effects while still being able to use fast switching [219].

Combining ZVS, ZVDS and ZCS creates a practical high-power, high-efficient full soft-switching inverter capable of operating in the megahertz region. In the design

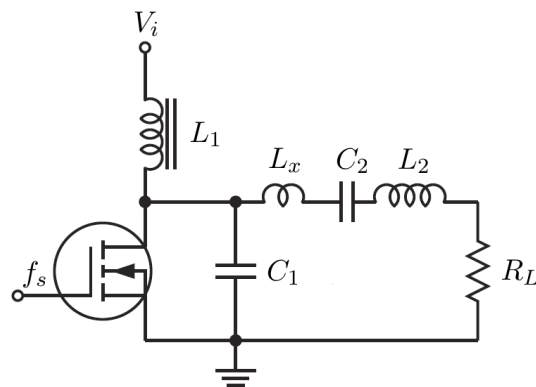


Figure 6.17: A typical Class E inverter circuit

process, the following assumptions are made:

- The choke L_1 is sufficiently high enough that the current following is DC.
- All components, including the switch, are ideal.
- The loaded quality factor Q_L of the output network is sufficiently high so that the output current can be assumed to be sinusoidal [220].
- The duty cycle of the switch is 50%.

A full derivation of the Class E design is presented in Appendix A. In summary, the characteristic current and voltage waveforms for a Class E are,

$$\frac{I_D(\omega t)}{I_i} = \begin{cases} 1 + \frac{\sqrt{\pi^2+4}}{2} \sin(\omega t + \phi) & \text{for } 0 \leq \omega t < \pi \\ 0 & \text{for } \pi \leq \omega t < 2\pi \end{cases}$$

$$\frac{I_{C_1}(\omega t)}{I_i} = \begin{cases} 0 & \text{for } 0 \leq \omega t < \pi \\ 1 + \frac{\sqrt{\pi^2+4}}{2} \sin(\omega t + \phi) & \text{for } \pi \leq \omega t < 2\pi \end{cases}$$

$$\frac{I_o(\omega t)}{I_i} = \frac{\sqrt{\pi^2+4}}{2} \sin(\omega t + \phi)$$

$$\frac{V_D(\omega t)}{V_i} = \begin{cases} 0 & \text{for } 0 \leq \omega t < \pi \\ \pi \left(\omega t - \frac{3\pi}{2} - \frac{\pi}{2} \cos \omega t - \sin \omega t \right) & \text{for } \pi \leq \omega t < 2\pi \end{cases}$$

where the switch current I_D , capacitor current I_{C_1} , output current I_o and switch voltage V_D are normalised with respect to the input current I_i and input voltage V_i over the period ωt . Plotting the above gives the following amplifier behaviour for an chosen optimum load.

To achieve this behaviour in practice, the component values of C_2 and L_2 are chosen such that at resonance (i.e. f_s) the voltage across them will be zero. Furthermore, the values of C_1 and L_x are calculated for a chosen optimum load R_L using the following

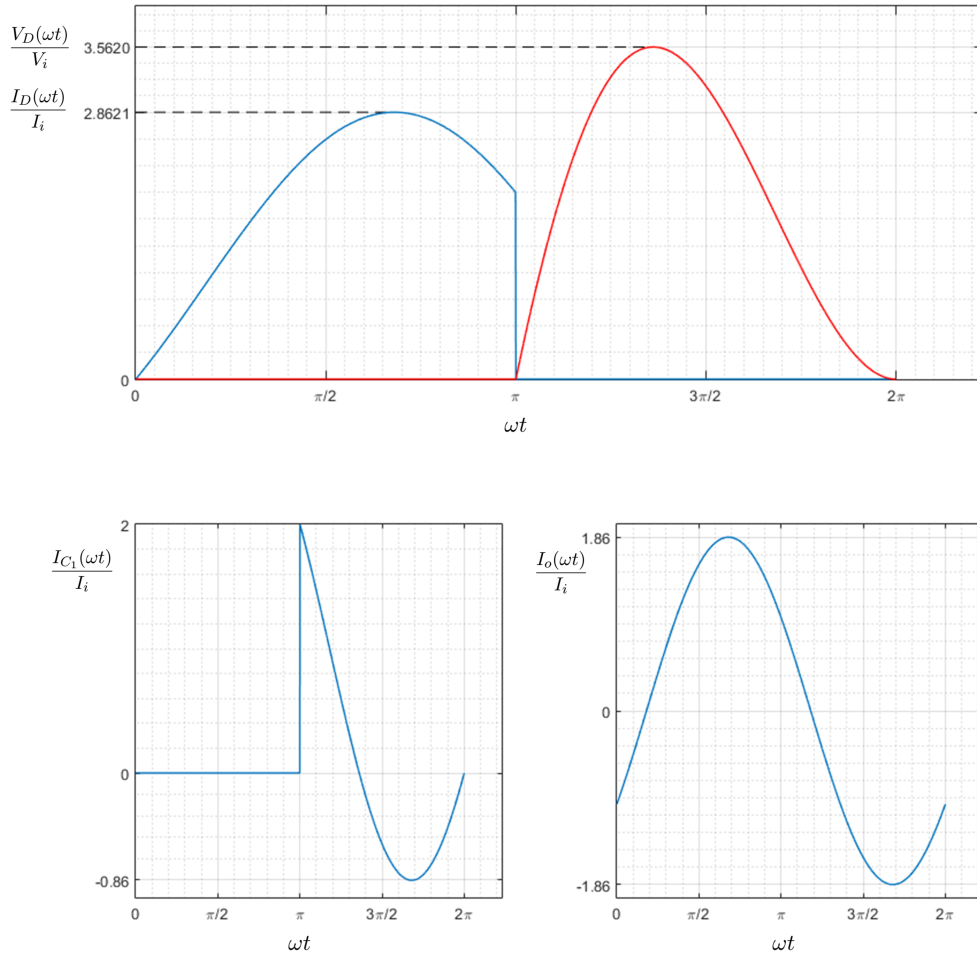


Figure 6.18: Waveform plots for $V_D(\omega t)$, $I_D(\omega t)$, $I_{C1}(\omega t)$ and $I_o(\omega t)$ normalised with respect to I_i and V_i

derived equations,

$$C_1 = \frac{8}{\pi(\pi^2 + 4)\omega R_L} \approx \frac{0.1836}{\omega R_L}$$

$$L_x = \frac{\pi^2 - 4}{2(\pi^2 + 4)\omega^2 C_1} \approx \frac{0.2116}{\omega^2 C_1}$$

6.3.2 Class EF Inverter Analysis

It can be seen from Fig. 6.18 that the peak voltage across and peak current through the switch are large multiples of V_i . While there are MOSFETs capable of operating at very high voltages and currents, if non-ideal switching were to occur due to either poor design or inherent variations in rated component values, this could mean significant power losses through a real switch due to its on-resistance. Practically, this power loss

would create excess heat and without appropriate cooling, this could create further drift away from the desired operation, ultimately causing a chain reaction which would likely damage components. A derivative of the Class E topology, often referred to in the literature as a Class EF inverter, was designed in order to reduce the voltage stress experienced by the switch, hence reducing real-world power losses [221] while at the same time reducing total harmonic distortion, thus improving EMI performance [222]. It achieves this through the insertion of an LC resonant circuit, normally tuned to a harmonic of the switch frequency f_s . Figure 6.19 illustrates this inverter topology.

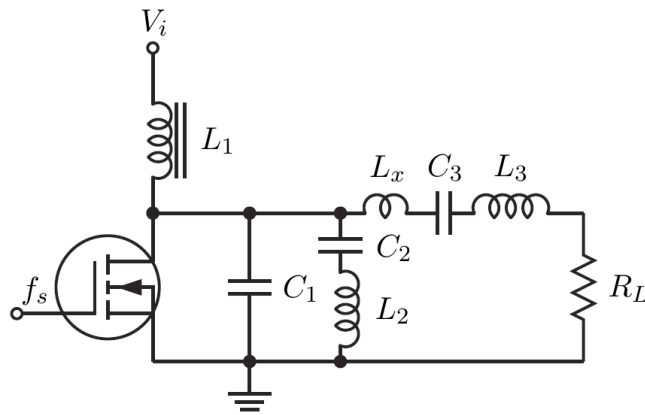


Figure 6.19: A Class EF inverter circuit

Both the Class E and general Class EF designs are highly dependant on the value of R_L , which for dynamic WPT systems would necessarily change according to the coupling κ between the transmitter and receiver. However, under a specific design condition, this load dependency for optimal performance can be eliminated up to a point thus effectively creating a near-constant current source through a range of R_L . Aldhaher *et al.* [223] termed this type of design a *Class EF load-independent inverter* and derived a parameter space where such operation would occur. In further works, they demonstrated inverter efficiencies of $\sim 85-95\%$ under high power operation and developed a design scheme which other engineers could follow for a desired amplifier design [224, 225]. A key distinction between their work and other similar works was in the system's ability to maintain efficient operation even when no output load was present, making it highly suitable for WPT applications where the presence and position of a receiving circuit is unpredictable.

The boundary conditions for the time domain analysis are the same as with the Class E, namely that ZVS, ZVDS and ZCS operation is desired. Likewise, the following assumptions are made:

- The choke L_1 is sufficiently high enough that the current following is DC current.
- All components, including the switch are ideal.
- The loaded Quality factor Q_L of the output network is sufficiently high so that the output current can be assumed to be sinusoidal [220].

The full derivation of the general Class EF design is presented in Appendix B. In summary, the key characteristic current and voltage waveforms for a Class EF inverter are,

$$\frac{I_D(\omega t)}{I_i} = \begin{cases} 1 - A_1 \cos(q_1 \omega t) - B_1 \sin(q_1 \omega t) - \rho(k+1) \sin(\omega t + \phi) & \text{for } 0 \leq \omega t < 2\pi D \\ 0 & \text{for } 2\pi D \leq \omega t < 2\pi \end{cases}$$

$$\frac{I_o(\omega t)}{I_i} = \rho(k+1) \sin(\omega t + \phi)$$

$$\frac{V_D(\omega t)}{V_i} = \begin{cases} 0 & \text{for } 0 \leq \omega t < 2\pi D \\ 2\pi \frac{\alpha}{\beta} & \text{for } 2\pi D \leq \omega t < 2\pi \end{cases}$$

where, as before, the switch current I_D , output current I_o and switch voltage V_D are normalised with respect to the input current I_i and input voltage V_i over the period ωt , defined by the duty cycle D ; and where

$$\alpha = \frac{k(\omega t - 2\pi D)}{k+1} + \rho(\cos(2\pi D + \phi) - \cos(\omega t + \phi)) \left(\frac{q_2^2}{q_2^2 - 1} - (k+1) \right) \\ + \frac{A_2}{q_2} (\sin(2\pi D q_2) - \sin(q_2 \omega t)) + \frac{B_2}{q_2} (\cos(q_2 \omega t) - \cos(2\pi D q_2))$$

$$\beta = \int_0^{2\pi} \alpha \, d\omega t$$

$$k = \frac{C_1}{C_2} \quad ; \quad q_1 = \frac{1}{\omega \sqrt{L_2 C_2}} \quad ; \quad q_2 = \sqrt{\frac{C_1 + C_2}{L_2 C_1 C_2}} \quad ; \quad \rho = \frac{C_2}{C_1 + C_2} \frac{I_m}{I_i}$$

and where

$$\frac{I_m}{I_i} = \frac{2\pi(1-D) + \frac{A_1}{q_1} \sin(2\pi D q_1) + \frac{2B_1}{q_1} \sin^2(\pi D q_1)}{\cos(2\pi D + \phi) - \cos \phi}$$

$$C_1 = \frac{\beta}{\pi \omega R_L} \left(\frac{\cos(2\pi D + \phi) - \cos \phi}{2\pi(1-D) + \frac{A_1}{q_1} \sin(2\pi D q_1) + \frac{2B_1}{q_1} \sin^2(\pi D q_1)} \right)^2$$

$$L_x = \frac{\int_{2\pi D}^{2\pi} \alpha \cos(\omega t + \phi) d\omega t}{\pi \omega^2 C_1} \frac{\cos(2\pi D + \phi) - \cos \phi}{2\pi(1-D) + \frac{A_1}{q_1} \sin(2\pi D q_1) + \frac{2B_1}{q_1} \sin^2(\pi D q_1)}$$

Finally, for a given k , q_1 and D , simultaneous equations can be solved numerically to give values for the constants A_1 , A_2 , B_1 , B_2 , ρ and ϕ . These equations along with the associated MATLAB code to generate the waveform plots in Figures 6.18 and 6.20 are found in Appendix C.

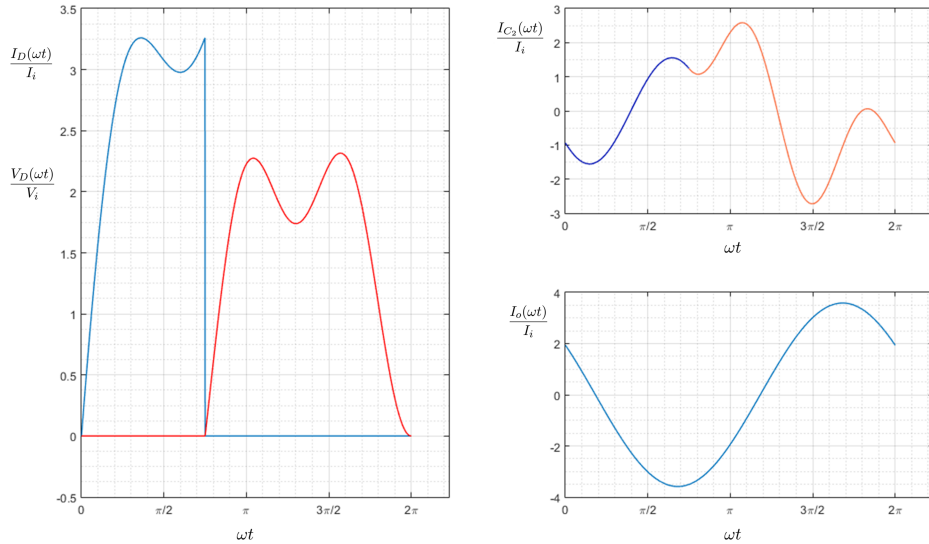


Figure 6.20: Waveform plots for $V_D(\omega t)$, $I_D(\omega t)$, $I_{C_2}(\omega t)$ and $I_o(\omega t)$ normalised with respect to I_i and V_i , with $k = 0.867$, $D = 0.375$ and $q_1 = 2$.

6.3.3 Constant Current Class EF Analysis and Implementation

So far, the component values for the presented inverters are designed to match a fixed value of load resistance R_L . As discussed, within WPT systems R_L will primarily depend on the reflected impedance of the secondary circuit, which itself is a function of mutual coupling. Hence, in a dynamic system, R_L will not be fixed, and so the traditional inverter's performance would degrade over time. If R_L becomes greater

than the design's optimum load resistance R_{Lopt} , the switch would turn on prematurely before the voltage across it has become zero. This leads to excess charge stored in the capacitor C_1 which would discharge into the MOSFET, causing a large current spike, leading to energy lost as heat in the MOSFET's on-resistance and potential component damage. The same will occur when R_L is less than R_{Lopt} , but since the potential across the MOSFET would be inverted, the MOSFET's body diode would begin to conduct allowing the current to flow through it instead of the MOSFET. Still, an undesired current spike would occur and overall efficiencies would degrade. Figure 6.21 illustrates the changes in voltage and current waveforms for a particular Class EF design as the value of R_L changes. Note, the analytical derivation for and the MATLAB code used to generate these plots can be found in Appendix D.

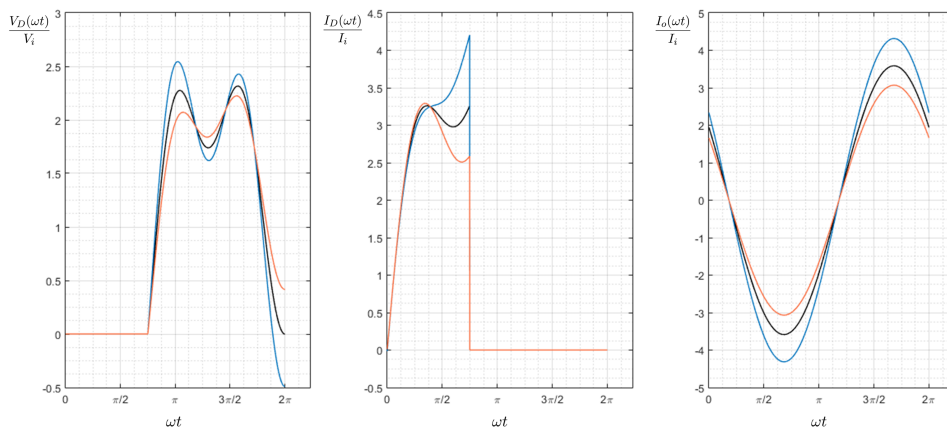


Figure 6.21: Waveform plots for $V_D(\omega t)$, $I_D(\omega t)$, $I_{C_2}(\omega t)$ and $I_o(\omega t)$ normalised with respect to I_i and V_i , for $k = 0.867$, $D = 0.375$ and $q_1 = 2$, as R_L changes from $0.75 R_L$ (Blue) to R_L (Black) to $1.25 R_L$ (Orange).

In the early 1990s, Zulinski *et al.* published a series of papers exploring the possibility of load-independent operation for a Class E inverter. Previously this had been achieved through an appropriate feedback control mechanism as conventional Class E inverters using constant-current-feed (via a theoretically infinite choke inductor L_1) could not inherently achieve load-independent operation. Instead, Zulinski and Grady [226] presented an analysis whereby the large valued L_1 was replaced by a finite DC feed inductance, whose reactance would influence the circuit in order to create the conditions for a load-independent output voltage and/or efficient operation. However, Zulinski *et al.* [227] pointed out the impracticality of such a configuration, as Class E

circuits using a finite DC feed inductance would be highly sensitive to other component value variations. This work concluded that there was presently no way to create a constant-current-feed Class E circuit that exhibited load-independence. This applied not only to constant output voltage operation, as was initially explored, but also to constant output power operation [228]. In 2015, a similar approach again using a finite DC feed inductance to achieve load-independence was presented by Roslaniec *et al.* [229]. In their analysis, the authors showed how using the principles of load-modulation, previously employed in outphasing inverter systems, could effectively create a constant output voltage at a fixed switching frequency over a range of load resistances; the caveats being that the load network impedance would need to remain substantially resistive as the output impedance changed and also that the value of the load must be maintained above a certain minimum value. This was necessary to ensure that the load current was in phase with the fundamental component of the drain voltage, maintaining ZVS and hence, efficient operation. Unfortunately, these conditions are not suitable for real WPT systems, where the load resistance R_L would more likely vary between 0Ω (i.e. with no receiver coupling) to some relatively small value of Ω .

It was clear from these earlier works that, in order to create the conditions for a constant current operation in the desired range of R_L , further reactive components would need to be included into the Class E configuration. It therefore follows that Class EF inverters and their derivatives presented a unique opportunity to not only reduce the spectral power and voltage stresses across the switch (as was the original intent), but also to create the conditions to achieve a constant current feed over a range of output loads. In 2016, Aldhafer *et al.* presented their load-independent Class EF Inverter which was able to maintain a near-constant output current and minimal reflection loss with R_L values ranging between 0 and 5Ω [223].

Mathematically, the key condition to derive for this type of operation was that of maintaining a constant or near-constant output current at ZVS over a defined range of R_L . Given this condition, a new set of simultaneous equations can be derived and solved for a desired set of current and voltage waveform characteristics. From here, the circuit component values that achieve this operation can be determined given a number of user defined parameters, a full analysis of which is found in Appendix E.

It soon becomes apparent that the parameter space that achieves constant output current operation is infinitely large, however, not all possibilities are practically achievable or even desired in real-world systems. Aldhafer *et al.* performed a follow-on analysis for a number of common operating conditions and introduced a handy set of predefined component relation tables which could be followed for a set number of designs [225]. The key insight from their work applied here is in the selection of the parameters k , $q1$ and ρ in order to achieve a relatively stable operation at high power capacity, while at the same time minimising the voltage and current peaks on the MOSFET's characteristic waveforms.

A set of operating conditions were then chosen and the characteristic waveforms shown in Figure 6.22 were calculated for the given design. Note, the change to current normalisation on y-axis in order to clearly illustrate the near-constant current operation achievable for any given range of load resistance. For this initial experiment the operating conditions were set to $f_s = 1$ MHz and $D = 30\%$ with $q1 = 1.5$, $k = 0.6722$, $\rho = 5$ and $R_{Lmax} = 5\Omega$. The components were subsequently determined from the equations derived in Appendix E which are given by Table 6.6.

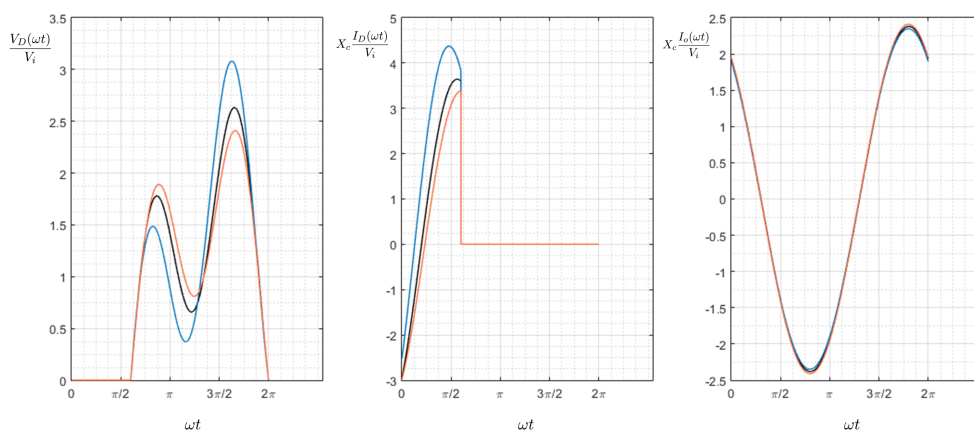


Figure 6.22: Waveform plots for $V_D(\omega t)$, $X_c I_D(\omega t)$, and $X_c I_o(\omega t)$ normalised with respect to V_i , for $k = 1.3296$, $D = 0.3$ and $q1 = 1.67$, as ρ changes from 1.5 (Blue) to 3 (Black) to 5 (Orange).

An initial set of prototype boards was designed and etched to test the practical performance as well as to compare their behaviour to the theoretical models. With a standard one-layer FR4 boards, thermal management became an issue, hence, aluminium based boards aided by a small PC fan were used to adequately sink any excess heat and allow the transmitter to operate for an extended period of time without

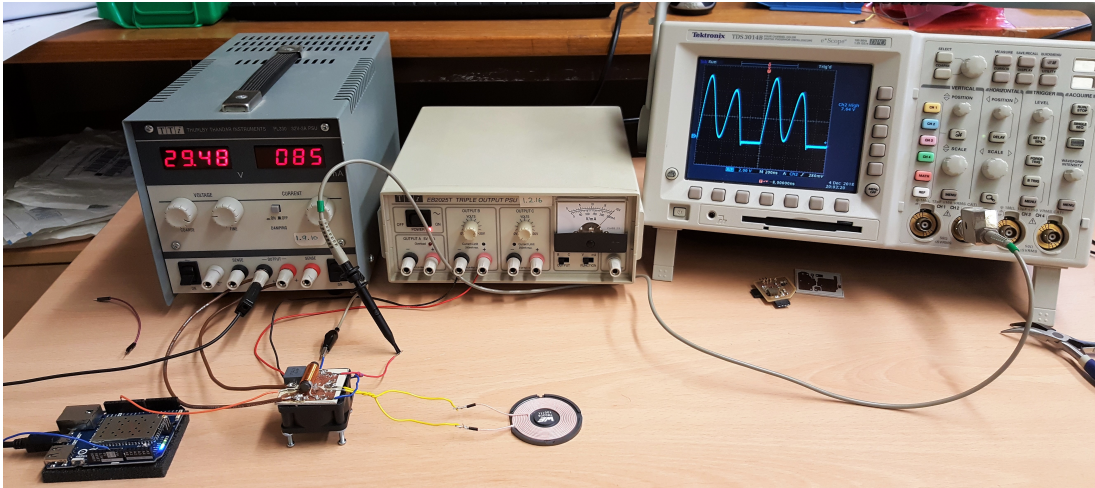
Table 6.6: Component Values of a 1 MHz Constant Current Class EF Inverter

Component	Value
C_1	$1.8423\text{nF} - C_{oo}^*$
C_2	1.2389nF
C_3	8.76nF
L_1	$40\mu\text{H}$
L_2	$9.087\mu\text{H}$
L_3	$6.3\mu\text{H}$

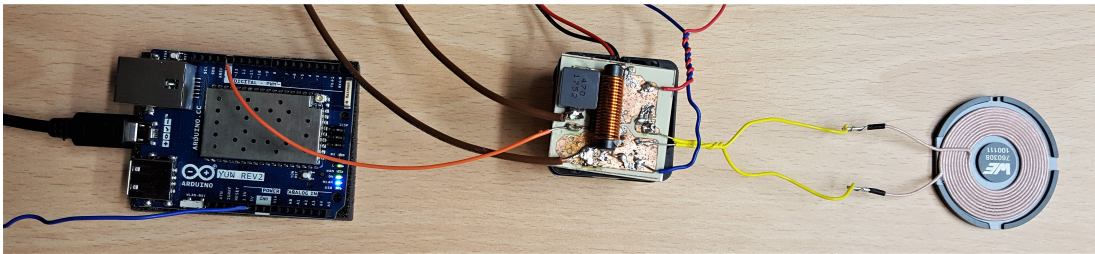
* Note: C_{oo} is the output capacitance given by the MOSFET datasheet for a given V_i

risk of overheating. The schematic and board layouts can be found in Appendix F, along with embedded code necessary to drive a switching signal at the required f_s and duty cycle D . The prototype transmitter system is shown in Figure 6.23. Voltages and currents were measured at different points along the board to confirm the theoretical model. Heat dissipation under different operating conditions was also measured using a thermal imaging camera. Figure 6.24 gives some key measurements, while a more detailed analysis of this implementation can be found in Appendix G.

In summary, the theoretical models and prototype boards agreed well, with some slight variations attributed to non-ideal as well as the use of cheaper low- Q components. With the models confirmed, the Class EF board design was refined to improve on its thermal performance and allow for extended use. This was achieved through a multilayer board with combination of ground planes and vias to facilitate air flow around components. A series of semi-populated multilayer boards were professionally made up, with each allowing for different components that effect the circuit characteristics to be quickly added as required by different system operating parameters. More details on the schematic and layout are found in Appenedix F, and Figure 6.25 below provides a 3D render as well as a photo of the fabricated board.

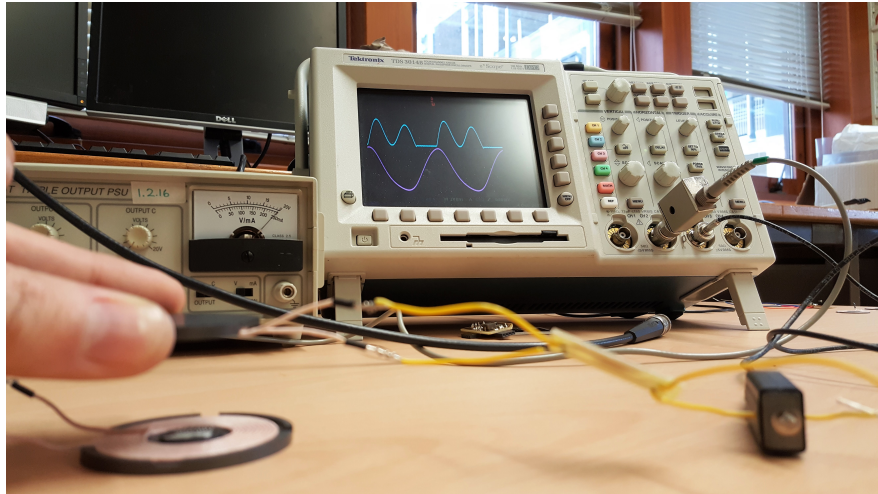


(a)

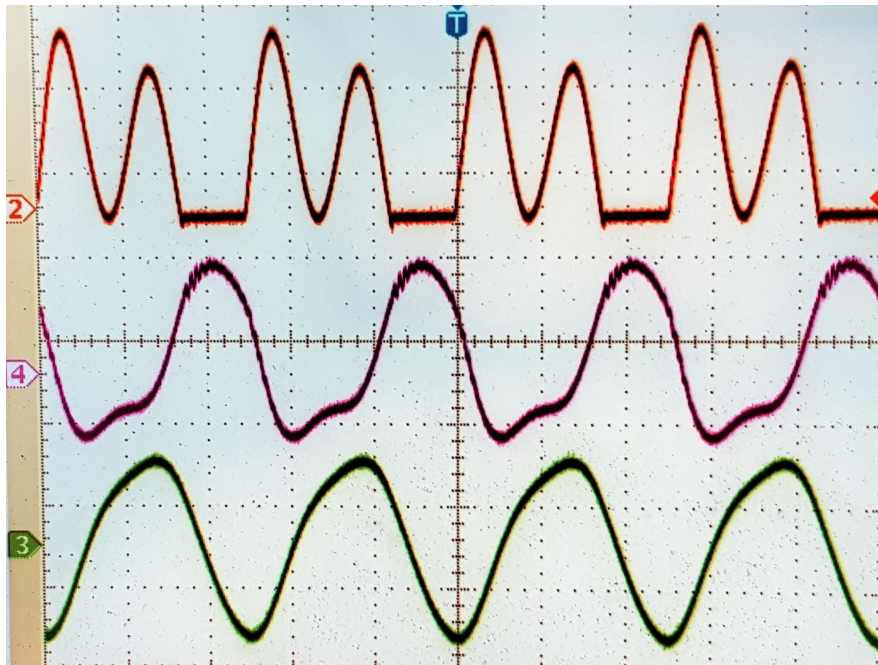


(b)

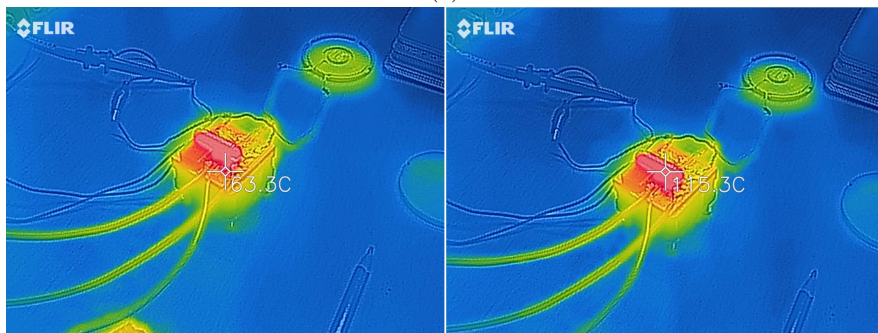
Figure 6.23: (a) Transmitter prototype, including DC power source and oscilloscope, and (b) top view of the signal generator (left), Class EF board (middle) and test transmitting coil L_3 (right).



(a)

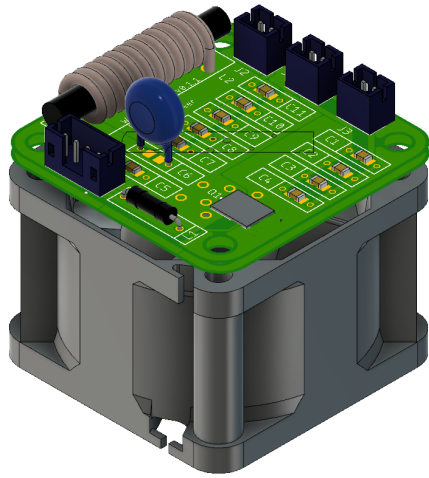


(b)

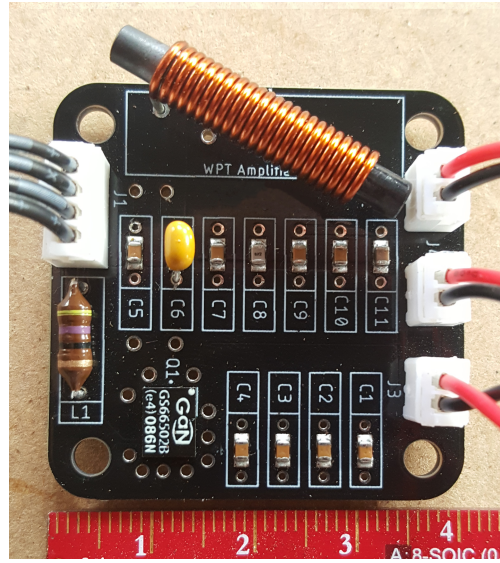


(c)

Figure 6.24: (a) Transmitting and receiving coils brought close to demonstrate tight coupling and associated (b) oscilloscope traces: voltage across MOSFET V_D (50V/div - red); voltage across $1 \Omega R_L$ (1V/div - magenta); current through $1 \Omega R_L$ (1A/div - green); and (c) thermal captures of the board after 1 hour operation with surface temperature reading of the MOSFET (left) and L_1 (right).



(a)



(b)

Figure 6.25: (a) 3D render and (b) photo of a fabricated Class EF board.

Chapter 7

Printed Resonant Structure Experiments and Results

Having established the expected behaviour for simulated resonator designs, this chapter reports on the observations of a select number of resonators under test.

7.1 Experiment set-up

In order to compare the high frequency characteristics simulated across a wide range, a vector network analyser (VNA) was sourced. Figure 7.1a shows the Rohde & Schwarz ZVB4 2-port VNA used throughout experiments which had a suitable frequency range of between 300kHz up to 4GHz. It also conveniently allowed for digital recordings to be saved and exported in industry standard formats simplifying analysis post-measurement.

There are several nuances in setting up and calibrating a VNA for accurate measurement of a standard device under test which will not be delved into here; however, it is important to note a key consideration which was specific to the needs of this work: during simulation, COMSOL's lumped port feature was used in order to drive the resonator structures. While documentation available is thorough, it never explicitly mentions that this particular feature calculates what's known as the differential impedance between the conductor terminals. For reference, a differential impedance is the ratio of the voltage to current, which in the real world, is measured

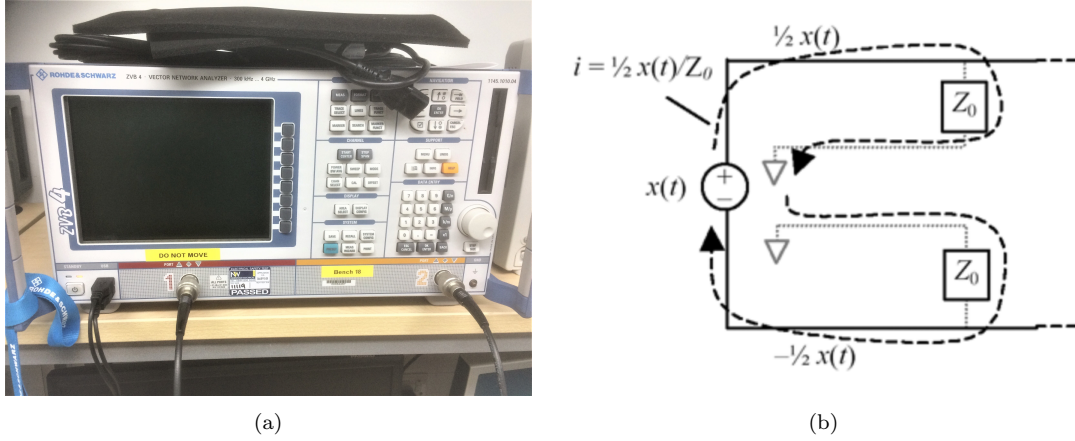


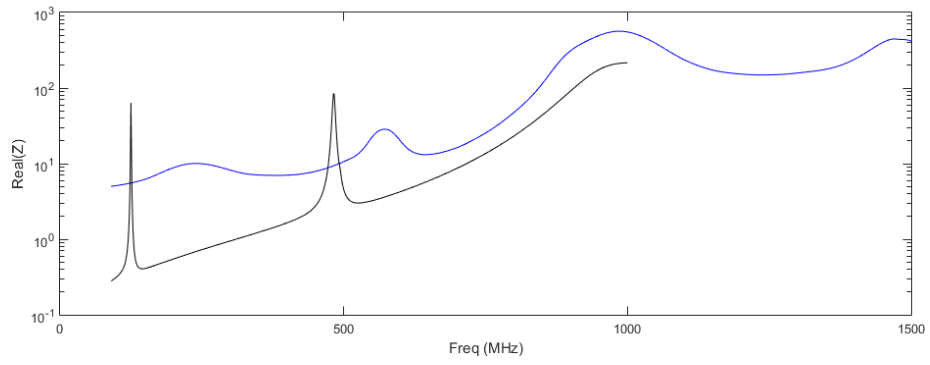
Figure 7.1: a) A Rohde & Schwarz ZVB4 2-port VNA used throughout experiments, and b) schematic for driving a pair of transmission lines in differential mode [230].

using a pair of transmission lines driven in differential mode (i.e. one positive signal with the other negative) as illustrated in Figure 7.1b. This, hence, required the sourced 2-port VNA to be set up to use both available ports concurrently in order to create the required excitation. Practically, this meant soldering together two SMA connectors so that their respective grounds were connected and thus, shorted. While crude, this functioned well for the purposes of comparing the physical resonator behaviour to the simulated one, under the condition that the probe lengths connecting the resonator were kept within $1/10^{\text{th}}$ the size of the maximum excitation wavelength.

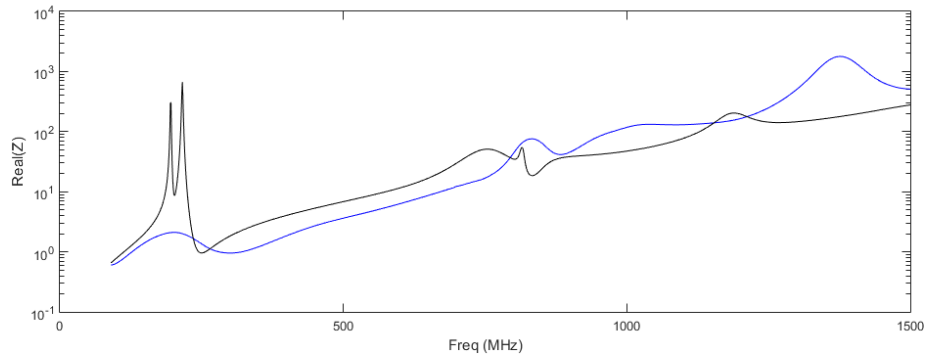
7.2 Observations of Singular Geometries

Several fabric applied resonators were tested initially in order to compare the simulated input impedance to the measured input impedance from the VNA. Figure 7.2 plots the real input impedance $\Re(Z_{in})$ for these selected resonators.

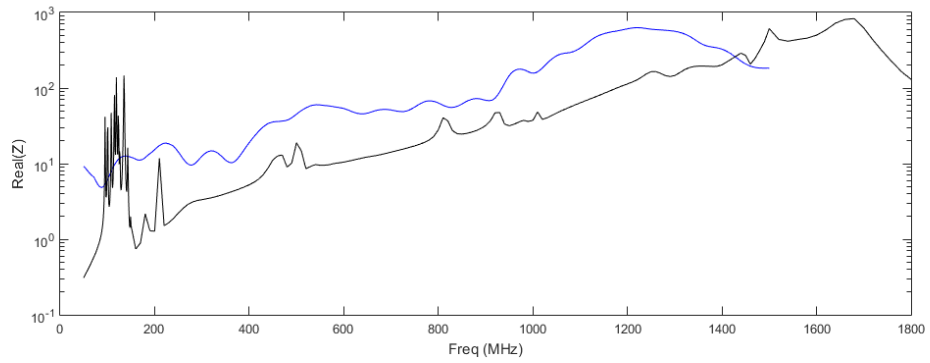
While there was a strong correlation between the theorised and measured input impedance, it was clear that the measured spectrum was shifted up and additionally showed a dampened SR mode amplitude when compared to the simulated impedance. It was initially theorised that this discrepancy may have been caused by the addition of the polyester fabric substrate; however, subsequent simulations showed that this was not the case. The next possibility was that the inks supplied and used for the construction of the resonators had different properties than were initially assumed during simulation.



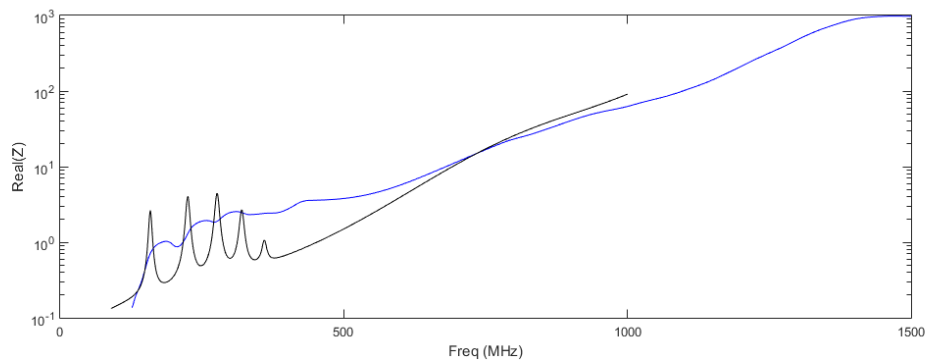
(a) $W(2 \times 2)$



(b) $W(3 \times 2)$



(c) $W(6 \times 6)$



(d) $O(4 \times 4)$

Figure 7.2: Plots of $\Re(Z_{in})$: differential measured (blue) vs differential simulation (black). Note, simulated spectrum in (b) was calculated using the newly calculated relative permeability ϵ of 2.73.

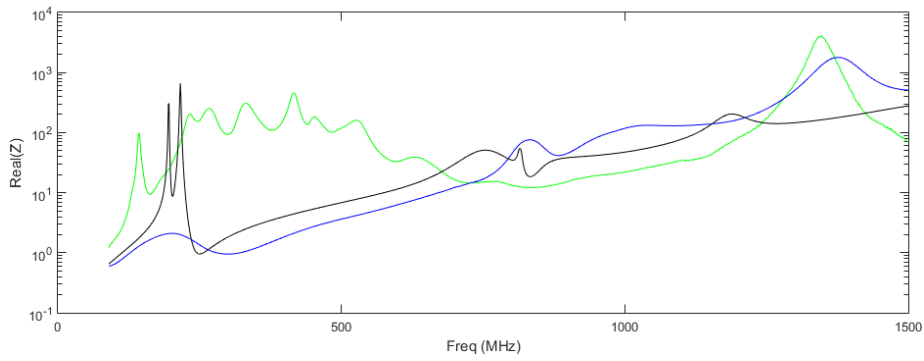
The spectral shift was substantially corrected when the relative permeability ϵ of the dielectric ink was set to 2.73 rather than the 3.9 simulated. The manufacturer had supplied the initial value of 3.9, and was already known to be a rough approximation given the difficulty in directly measuring this property, thus the need for an adjustment was expected. As shown in Figure 7.2b, even after this adjustment, a spectral shift was still present higher up the spectrum, indicating that the ϵ for this dielectric ink was, at least marginally, frequency dependent. For the SR range of interest, however, ϵ was assumed to be the 2.73 constant newly calculated.

The drop in the observed SR mode amplitude would most likely have been attributed to a decreased value of expected conductivity σ in the silver ink. However, direct measurement of the printed resonator layer properties by an external test-house showed that the ink's conductivity was in fact very consistent with the expected and subsequently simulated value. The only other reasonable cause for this apparent drop in σ was attributed to losses in the interface between the printed resonator and the VNA probes. This was highly probable given the difficulty in probing a fabric material with a solid wire, coupled in this case with a rough surface finish observed on the printed resonator. The losses were equivalent to a new effective σ of $3.2 \times 10^4 S/m$, a two orders of magnitude drop compared to the directly measured and simulated value.

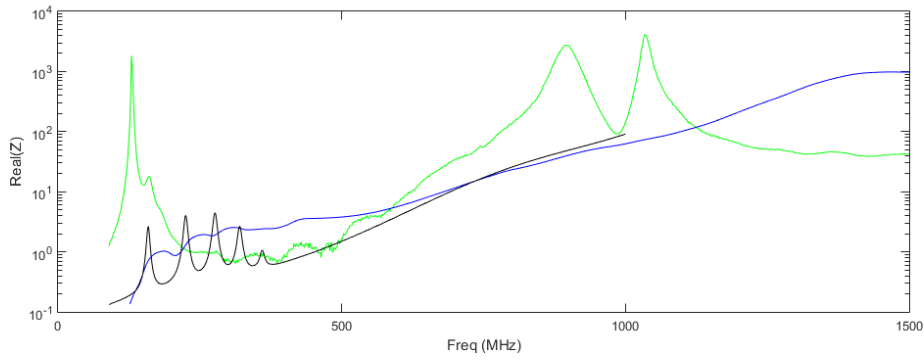
7.3 Observations of Coupled Resonator Structures

Having compared the individual resonator performance, power transfer between resonators was performed. Note that as the VNA sourced was only 2-port and not 4-port, hence creating a differential impedance port for two resonator measurements at the same time was not possible. This meant that the SR modes for WPT were not the same as those identified during simulation. To illustrate the degree of this difference, Figure 7.3 overlays the measured and simulated $\Re(Z_{in})$ for W(3×2) and O(4×4).

Note also that in order to achieve maximum power transfer and efficiency across a coupled system, the input impedance or the impedance *seen* at each VNA port must be equal to that VNA port impedance. The VNA ports had a characteristic impedance Z_o of 50 Ω , thus some additional circuitry between the port and resonator structure



(a) W(3×2)



(b) O(4×4)

Figure 7.3: Plots of $\Re(Z_{in})$: non-differential measured (green) vs differential measured (blue) vs differential simulation (black).

was needed in order to closely match them. There are various topologies which could have been implemented but for simplicity, an L-matching circuit topology was chosen. Figure 7.4 illustrates the L-matching circuit topology and Table 7.1 lists calculated values of inductance L and capacitance C needed to match the VNA port to specific SR modes under examination.

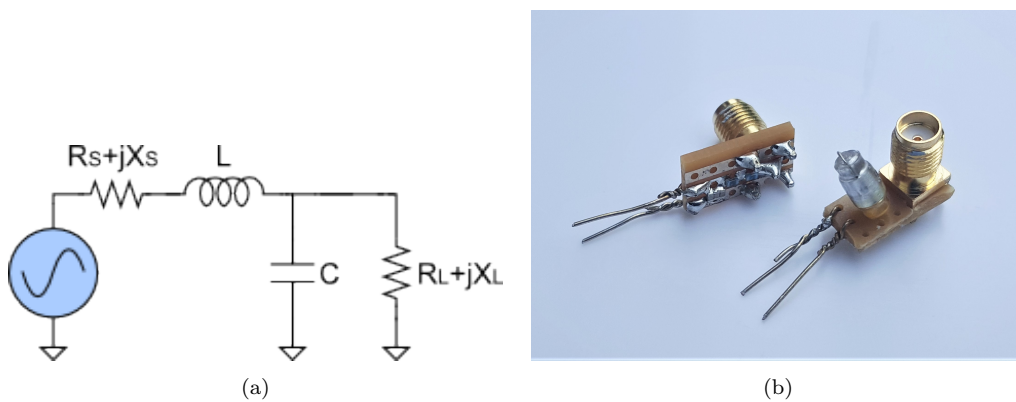


Figure 7.4: a) L-matching circuit schematic and b) example of two constructed SMA probe attachments.

Table 7.1: Component values calculated for desired matching networks

Design	Structure Size (mm)	Mode Frequency (MHz)	Mode R_L (Ω)	Mode X_L (Ω)	Calc. L (nH)	Calc. C (pF)
W(2×2)	93×93	572.2	28.54	-155.2	50.1	4.82
W(2×2)	93×93	985.4	565	-46.65	26.0	0.89
W(3×2)	116×76	149.2	35.23	-11.89	37.0	13.8
W(3×2)	116×76	281.8	50.44	7.66	9.55	6.84
W(3×2)	116×76	428.4	24.6	85.43	18.3	3.36
W(3×2)	116×76	529.9	42.69	111.7	44.9	2.87
W(3×2)	116×76	551.1	25.29	-119.5	41.7	5.71
O(4×4)	133×133	150.6	6.92	30.46	21.2	22.1

Figure 7.5 shows the WPT S-parameter plots for a selection of SR modes and Table 7.2 reports on the calculated transmission efficiency η based on these plots. As a matched system is assumed, equation (6.1.3) for η in terms of the S-parameters was simplified to,

$$\eta = \frac{|S_{21}|^2}{1 - |S_{11}|^2}$$

Note, the SR modes recorded during WPT were shifted down from those listed in Table 7.1 due to effects of overcoupling at the tested DS.

Table 7.2: Measured S-parameters and calculated power transfer efficiency η for coupled modes

Design	Structure Size (mm)	DS	Mode Frequency (MHz)	Mode S_{21}	Mode S_{11}	Power Transfer Efficiency η
W(3×2)	116×76	0.1	147.8	0.4632	0.3519	24.49%
W(3×2)	116×76	0.2	166.1	0.1227	0.5758	2.25%
W(3×2)	116×76	0.1	256.4	0.4395	0.3905	22.79%
W(3×2)	116×76	0.2	281.8	0.2570	0.4987	8.79%
W(3×2)	116×76	0.1	400.2	0.2408	0.4237	7.07%
W(3×2)	116×76	0.2	446.7	0.1137	0.3232	1.44%
W(3×2)	116×76	0.1	510.2	0.1900	0.2358	3.82%
W(3×2)	116×76	0.2	573.6	0.0969	0.1911	0.97%
O(4×4)	133×133	0.1	142.2	0.5072	0.4570	32.52%
O(4×4)	133×133	0.2	159.1	0.2011	0.7330	8.74%

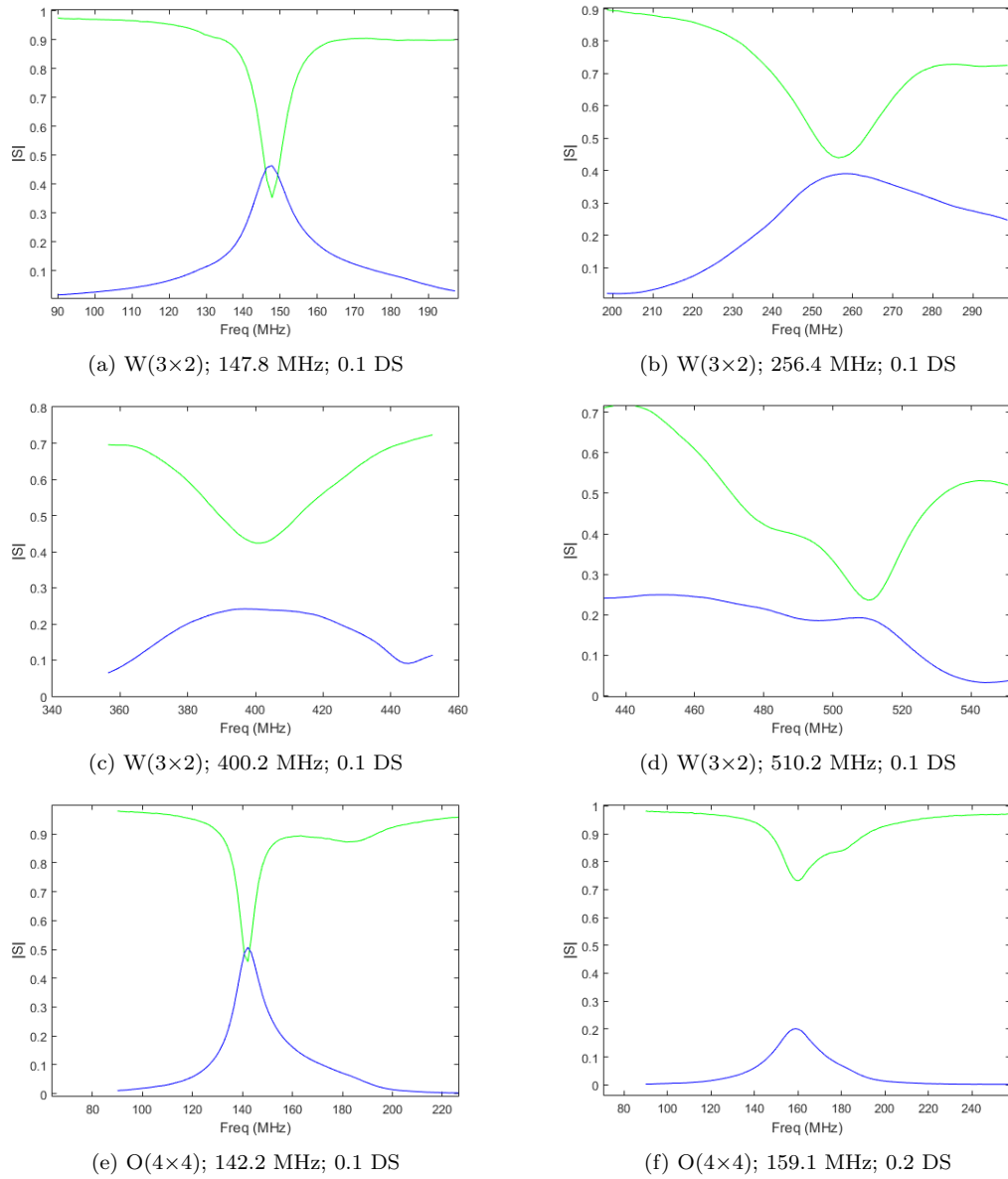


Figure 7.5: Plots of $|S_{11}|$ (green) and $|S_{21}|$ (blue) for a selection of coupled SR modes.

While not yielding as high a transfer efficiency as was initially simulated, these experiments have shown that the theorised resonant structures could be implemented in the real world with moderate performance. Any losses in efficiency could be attributed to a poor connection between the VNA probes and the resonant structure surface as previously discussed, as well as any imperfect matching via the matching network, both due to non-ideal components and the shift in SR mode due to proximity. Furthermore, the rapid drop in transfer efficiency with increasing separation distance could once more be attributed to the poor connection between probe and structure, as the lower

effective σ implies a much lower Q -factor; this being a key factor in maximising the effective range of WPT. Refining these parameters with appropriate design strategies would bring the calculated efficiencies much more in-line with the simulated results.

Of further note is the apparent presence of *antiphase* SR modes in the $W(3 \times 2)$ WPT case. With reference to Figure 7.3a), candidate SR modes indicated by $\Re(Z_{in})$ exist at approximately 149, 232, 281, 328, 428, 452 and 530 MHz. However, looking at the S_{21} plots shows that a peak only corresponds to odd-numbered SR modes (i.e. 149, 281, 428 and 530 MHz). Interestingly, the trough or lowest point between two peaks coincides with the even-numbered SR modes (i.e. 232, 328 and 452 MHz). There is in fact some mention in the literature of a similar observed behaviour during frequency splitting in classic helical coil WPT [75], in that the higher or *even* mode of the bifurcated frequency corresponds to the frequency at which the current in the transmission and receiving coils are in anti-phase or at opposite directions to one another, thus cancelling each other out. Considering the cyclical nature of phase and a presumed 90° phase shift in current per mode, it necessarily follows that every *even*-numbered mode could be considered an anti-phase mode. While a logical extension of WPT behaviour, this is still an important observation to note, as very rarely has prior work considered multi-modal coupled systems and even within those that do, this observed behaviour has yet to be reported. After observing the performance of these coupled resonator structures, a demo WPT system was subsequently implemented.

7.3.1 Implementation

The transmitter circuitry developed in the previous chapter performed exceedingly well up until a certain operating frequency defined by the voltage dependant value of the output capacitance attributed to the selected MOSFET $C_{oo}(V_{DS})$. For the class of MOSFET chosen, the value of C_{oo} is in the order of a few pF for $V_{DS} > 80$ V; however, will quickly increase to nearly 100 pF with V_{DS} below this value. Furthermore, the value of C_1 in the amplifier design would decrease dramatically with increasing operating frequency, meaning that unless high power operation is desired (and hence a new, more complex thermal management system to be designed), then the current amplifier design unfortunately could not be operated above ~ 20 MHz. Furthermore, even if

a more capable MOSFET was selected, the ATmega microprocessor on the current Arduino development board being used also has a maximum signal frequency that it can reliably generate. In this case, operating at < 48 MHz will allow for a high enough duty cycle select resolution for the selected D .

The test implementation instead used an off-the-shelf signal generator able to generate an AC signal between 35 MHz and 4 GHz at an output power of -1 dBm (or around 1mW). This was amplified with a signal generator which could maintain approximately 2.5 W output power P_i through a 50 Ω SMA port in the frequency range of interest. Note however, that during experimentation the real value of P_i entering into the Tx resonator structure was at best around half this value, primarily due to losses at the probe-resonator interface as was seen during testing with the VNA. This means that the overall transmission efficiency of the system drops significantly even before reaching the wireless link stage. This interface issue was further examined through the use of a thermal camera, and Figure 7.6 clearly illustrates how a majority of the power could not propagate into the resonator structure via the feed cable.

In terms of receiver side rectification, there were many possible designs based on the choice of application, but for simplicity, a 50 Ω resistive load matched to the resonator structure was employed and the corresponding output voltage V and current I were recorded using oscilloscope probes. The real or true power P_o could then be measured

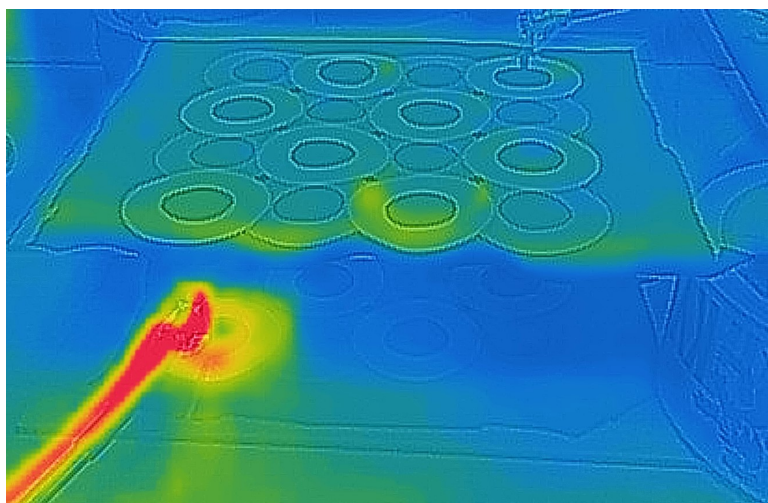
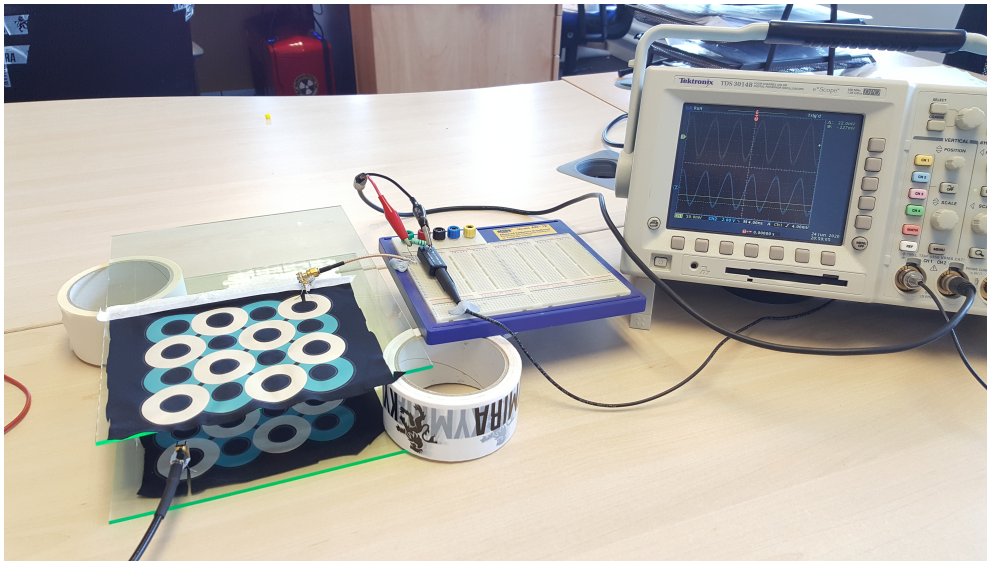


Figure 7.6: Thermal image capturing resistive heating across a WPT system, and demonstrating the vast majority of the power remaining within feed cable. Note, the colour spectral range was around 10-20°C with areas at the top of the range in red (28.5 C), and areas at the bottom range in blue (21.0 C).

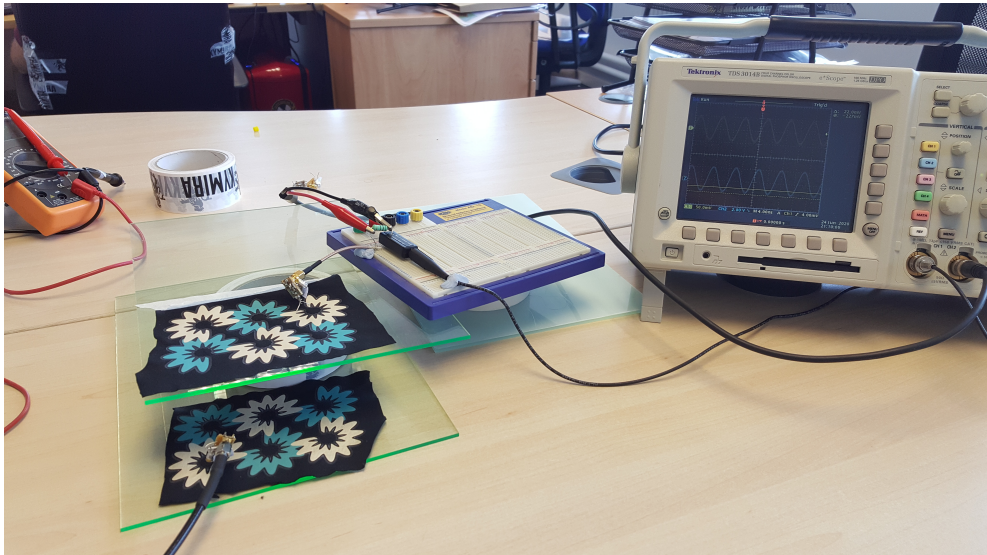
via equation (7.3.1).

$$P_o = V_{rms} I_{rms} \cos \phi \quad (7.3.1)$$

where V_{rms} and I_{rms} are the rms voltage and current values and ϕ is the impedance phase angle between the voltage and current waves. Figure 7.7 illustrates a pair of WPT implementations under test and Table 7.3 lists the calculated P_o from a selection of WPT test cases.



(a) O(4×4); 142.2 MHz; 0.28 DS



(b) W(3×2); 147.8 MHz; 0.38 DS

Figure 7.7: Example test implementations, showing the fabric printed resonators, transmitting power to a 50Ω load, plotting the received current and voltage on an oscilloscope.

Table 7.3: P_o from measured V_{rms} , I_{rms} and ϕ at a separation DS

Design	Structure Size (mm)	DS	Mode Freq. (MHz)	V_{rms} (mV)	I_{rms} (mA)	ϕ (deg)	P_o (mW)
O(4×4)	133×133	0.03	142.2	1,770	80.14	62.5	65.5
O(4×4)	133×133	0.28	142.2	2,120	106.07	8.5	222.52
W(3×2)	116×76	0.04	400.2	259.72	6.48	82.0	0.234
W(3×2)	116×76	0.38	400.2	88.38	3.54	0.0	0.31
W(3×2)	116×76	0.04	147.8	580.01	17.67	40.0	9.13
W(3×2)	116×76	0.38	147.8	1,410	33.94	6.0	36.66
W(3×2)	116×76	0.04	256.4	247.73	6.78	33.0	1.47
W(3×2)	116×76	0.04	510.2	8.83	0.47	58.0	0.002

The top six rows in Table 7.3 help to demonstrate the significant effect of resonator overcoupling, and thus how a shift or possibly even bifurcation of the resonant frequency could dramatically effect the WPT system’s efficiency. In the first row, the true power received at the load is just 30% that of the second row, even though the WPT test case in the first row is at a DS of just 0.03 and the second test case is at a DS of 0.28. The same is demonstrated between rows three and four, and five and six, where again the power received by the closer pair of resonators is significantly less than that received by the further separated set of resonators. ϕ is the key parameter to observe here, and minimising this parameter for a given DS by shifting the transmitting frequency leads to better transmission efficiency. The rest of the table illustrates test cases operated at the previously recorded SR modes and the power received. Again, overcoming the effects of overcoupling is key in maximising the transmission efficiency.

As these resonator structures are intended for use close to the end user’s skin, resistive heating was a concern. The resonator structures’ DC resistance was measured using an impedance analyser far away from any SR modes. Across all designs, the DC resistance fell between 160 m Ω and 1.1 Ω , hence, losses via resistive heating were expected to be suitably low. Nevertheless, the resonator’s temperature during operation was monitored via a thermal camera, and images captured are shown in Figure 7.8.

These images demonstrate how different resonator structures may cause a larger heating effect than others depending on the size and overlap area of their constituent elements. Moreover, they further illustrate how current flows within these structure,

and how, at different operating frequencies, different current loops emerge, forming a stationary pattern across the resonant structure.

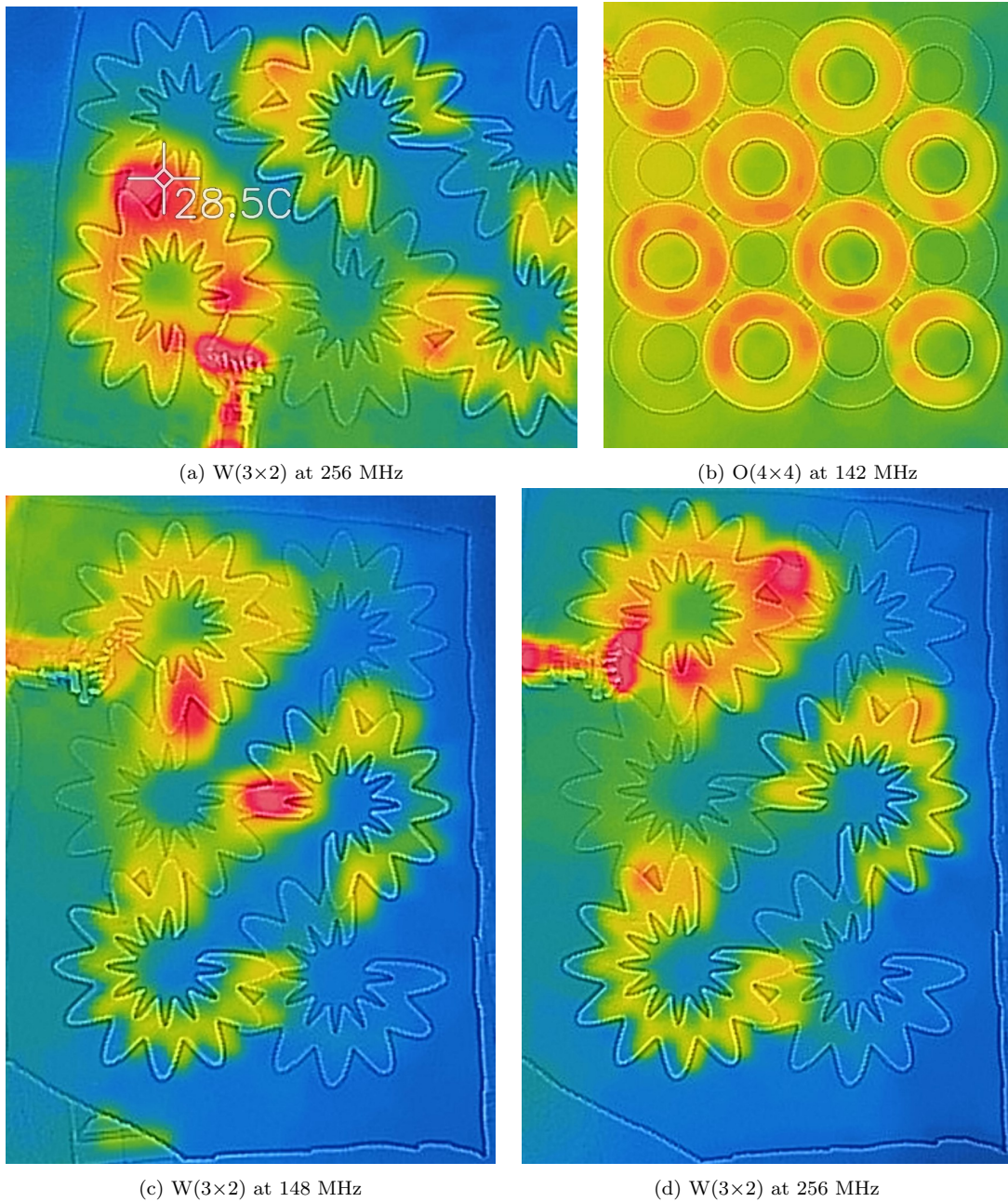


Figure 7.8: Thermal images capturing resistive heating from resonant structures, showing a) temperature increase after 300 seconds of operation on a W(3×2) design, b) distribution of current in a O(4×4) design, and confirmation of different current loops that form on a W(3×2) design at c) 148 MHz, and d) 256 MHz. Note, the colour spectral range shows areas at the top of the range in red (28.5 C), and areas at the bottom range in blue (21.0 C).

In summary, this chapter demonstrated the practical implementation of the proposed resonator structure. Observations with the VNA confirmed that the simulation and physical prototypes' characteristic behaviour correlated well, with any

variance discussed and attributed to connectivity issues between probe and the printed layers. This poor connectivity was further noted during testing with thermal imaging which further demonstrated that much of the power input is either lost or reflect back into the transmitter before reaching the wireless link stage.

Chapter 8

Future Work

This thesis presented a novel type of resonator for WPT with a specific focus on wearable applications. While a thorough analysis has been performed, there are still plenty of avenues along which this research could continue, even if the scope was to be limited to body worn applications:

1. Testing with ferrite loaded polymer layers: at ideation, the use of a ferrite loaded polymer was considered. As with traditional ferromagnetic cores, these would serve to confine and concentrate the magnetic fields, thus increasing resonator coupling efficiency as well as potentially shielding the wearer from potentially unsafe field leakage if higher power capture was required.

Several materials suppliers had been contacted, who were able to supply quite high- μ (>500) ferrite powders, with particle sizes of between 2 and 13 μm in order to be loaded into a polymer. Furthermore, methods were explored to economically impregnate ferrite powder into suitable polymers, both for the surface-level and yarn-level designs. For both cases, a low melting temperature polymer was identified which ensured suitability with the selected manufacturing processes. Polymers with specific particle loading ratios were briefly examined to ensure a material that maximised μ_{eff} , while at the same time maintaining durability, flexibility and elasticity as the application required. Unfortunately, there was no time to explore the effects of ferrite loaded polymer layers within the resonator design.

2. Going from textile swatches to full garments: the experiments discussed focused on identifying and understanding the behaviour of the resonator structure. Having made great strides in this, the next logical integration step would be to explore this behaviour when incorporating the resonator designs across the entire area of a garment.

In particular, this would allow an exploration of the behaviour as the resonator design begins to flex and bend around a curve (as would be expected with a torso garment), as well as when the resonator folds back on itself as expected along, for example, armpits. It is expected that this will have some effect to the frequency response, but to what degree is still unclear.

3. Exploring system optimisation with multiple coils: in moving from a 2- to a 4-coil architecture, the usual intuitions derived from standard WPT geometries break down, and thus further examination into design principles surrounding multi-coil WPT systems using these proposed resonant structures should take place in order to optimise transmission efficiency while maintaining the advantages garnered from this approach.

Moreover, testing with multiple receiver nodes on the garment could take place. It had been previously stated that the resonator design could act as the ultimate receiving element as in the case of a 2-coil system, but also as an intermediary resonator, serving only to potentially enhance system link efficiency and propagate useful power to other receiver coils. In this work, a single load coil was examined incorporated; however, in future works, it would be interesting to observe the effect of adding multiple load coils that could inductively couple to different areas across an entire resonator surface. This would better represent a real-world environment, whereby multiple and separated sensor nodes could be used within wearer biomonitring applications.

4. Examining resistive heating effects in the real world: while considered as part of this work, a more thorough investigation of the thermal effects of the thin resonator structures would be required before any use with living wearers was attempted. The goal in this proposed work would be to determine the level of

resistive heating experienced by the resonator structure at various power transfer levels. There would indubitably be a safe maximum power level that the worn resonator structure would be able to capture, and it is hypothesised that this very well may be less than the maximum power transfer level permissible under safe field explore guidelines.

5. Exploring broadband load-independent inverter designs: impedance matching in AC circuits is a crucial design task in order to deliver maximum power from a source to a receiving load. The current Class EF design demonstrated that impedance matching over a range of loads was possible, but given the multi-model nature of the resonator structure presented in this thesis, it would be pertinent to examine if this behaviour could be extended across a broad operating frequency range within the same design. Achieving this would enable an incredibly flexible transmitter-side design for future WPT applications beyond what has been presented here.

6. Experimenting with different element shapes as well as sizes and non-regular patterns: anyone looking into resonator geometry optimisation must proceed with caution, as this exercise could be viewed as a somewhat wasteful endeavour, given the vast amount of embodiments that could be conceived. Nevertheless, exploring different shaped and sized conductive elements within the same resonator design could enable new resonant modes to align better to some desired operating bands. For example, a particular design might be better suited for resonators wishing to strictly adhere to the discrete transmission frequency bands set by, say, the industrial, scientific and medical (ISM) radio bands, whose centre frequencies occupy the popular 6.78 MHz and 13.56 MHz allocations but also the 27.12 MHz, 40.68 MHz, 433.92 MHz and so on.

Furthermore, some exploration into how the system could cope with screen printing errors such as pin-hole or even layer misalignment. In both cases there might be some shorting between layers, the effort of which should be properly determined in order to set acceptance criteria in scaled manufacture.

7. Carry on with the yarn-level design: while initially discounted in this work due to

its complexity, there is particular merit to further exploring this type of resonator design principle. In particular, it brings about the creation of strongly inductive yarns that may in turn have usably low self-resonant frequencies. Furthermore, from a textile engineering perspective, working with different yarn resonator designs rather adds a new dimension to the garment design process, which could allow for better flexibility than a bounded surface structure added at the end of the garment making process.

8. Application testing in various environments: finally, all of the explored principles could benefit from a thorough investigation of their use and behaviour in real-world testing environments. As is often the case, many integration challenges only become known when attempting to incorporate or introduce an invention or system into its intended use environment. In this regard, testing these newly proposed resonator structures in specified environments for targeted applications would allow for the greatest opportunity for system refinement, leading to a higher chance of end-user adoption.

Chapter 9

Conclusions

This thesis has introduced an exciting new field within WPT - multi-model surface resonator structures. The stated aim of this work was to demonstrate a viable new approach to electronic resonator design. This has been achieved through rigorous examination of the proposed resonator structure. These thus forms the main contribution of this work: providing a new perspective to product developers in the employment of wireless charging, particularly for smart garment or wearable applications.

As this was a new exploration, this work predominantly focused on proving that the proposed approach was not only an interesting concept, but that the science to develop the thesis was sound and, more importantly, verifiable. Professional FEM simulation tools were used throughout in order to iterate development quickly, and these were themselves verified via known models from the literature. Doing so helped to establish confidence that the results generated from the new and unknown models could accurately represent implementations in the physical world. Of note in this regard, it was shown that the standard quasi-static approximation used across many WPT applications could just as easily be replaced with the more classical electromagnetic wave equations by employing powerful, yet commercially available software suites. Doing so helps move past the fuzzy notion of near- and far-field domains and allows for a conceptually smoother transition throughout the propagation medium without compromising on accuracy for the sake of simplification. This was an essential exercise, given that the proposed resonator structures do not neatly classify into standard

categories such as *coil* or *antenna*.

Indeed, the main exploration centred upon a surface-level implementation due to available resource; however, the principles explored could just as well extend to the yarn-level implementation explored in chapter 4, which might lead to even more possibilities for textile specific applications. Nevertheless, it has been shown that planar resonator structures, applied via printing and heat transfer to textiles, are a viable solution for garment-based WPT.

Different resonator designs were explored and select designs were demonstrated via simulation. Unlike classical coils, multiple and predictable modes for highly efficient power transfer have been shown to exist across a broad spectrum of possible operating frequencies. Choice resonator designs were constructed and tested with appropriate measurement equipment, firstly to verify the theoretical models, but also to confirm system functionality and practicability within the target application. The physical prototypes aligned quite well with the theoretical models, and while the final WPT performance fell short of the digital models, the root cause for this discrepancy is clearly understood and certainly solvable in follow-up work.

In retrospect, the original goal of achieving 4-coil equivalent mid-range WPT with such an innovative approach may have been overly ambitious, however, these planar resonators are theoretically capable of achieving a substantially more effective WPT system for the target application over the classical 2- and 3-coil systems. This was a first significant milestone and pursuing the elusive 4-coil equivalent mid-range WPT architecture could very much be accomplished through follow-up research projects.

Refinements and tuning of the resonator design process, both in simulation and in physical implementation, are of course still required, but nevertheless, the work accomplished through this PhD proves the viability of this unique approach and opens up a whole new dimension in the WPT system design space.

References

- [1] Statista, “Consumer Electronics Report 2020,” accessed 01.03.2021. [Online]. Available: <https://www.statista.com/study/55488/consumer-electronics-market-report/>
- [2] A. Kurs, “Power Transfer Through Strongly Coupled Resonances,” Thesis (S.M.), Massachusetts Institute of Technology, Dept. of Physics, 2007. [Online]. Available: <http://dspace.mit.edu/handle/1721.1/45429>
- [3] Magnet Academy, “Hans Christian Orsted,” accessed 03.12.2019. [Online]. Available: <https://nationalmaglab.org/education/magnet-academy/history-of-electricity-magnetism/pioneers/hans-christian-orsted>
- [4] H.C. Orsted, A. Wilson, K. Jalved, A.D. Jackson, O. Knudsen, “Selected Scientific Works of Hans Christian Orsted,” 2014.
- [5] A.K.T. Assis and J.P.M.C. Chaib, “Ampere’s Electrodynamics,” 2015.
- [6] IET Archives, “Archives Biographies: Michael Faraday,” accessed 03.12.2019. [Online]. Available: <https://www.theiet.org/publishing/library-archives/the-iet-archives/biographies/michael-faraday/>
- [7] —, “Archives Biographies: James Clerk Maxwell,” accessed 03.12.2019. [Online]. Available: <https://www.theiet.org/publishing/library-archives/the-iet-archives/biographies/james-clerk-maxwell/>
- [8] B.J. Hunt, “Maxwell, Measurement, and the Modes of Electromagnetic Theory,” pp. 303–339, 2015.
- [9] G. Stark, “Light,” accessed 03.12.2019. [Online]. Available: <https://www.britannica.com/science/light>
- [10] Anon, “Archives: Heinrich Rudolf Hertz,” accessed 03.12.2019. [Online]. Available: <https://web.archive.org/web/20090925102542/http://chem.ch.huji.ac.il/history/hertz.htm>
- [11] W. B. Carlson, “Tesla: Inventor of the Electrical Age,” 2015.
- [12] R. Lomas, “The Man Who Invented the Twentieth Century: Nikola Tesla, Forgotten Genius of Electricity,” 2013.
- [13] Z. Wang, X. Wei, and H. Dai, “Principle elaboration and system structure validation of wireless power transfer via strongly coupled magnetic resonances,” *2013 9th IEEE Vehicle Power and Propulsion Conference, IEEE VPPC 2013*, pp. 261–266, 2013.
- [14] A. P. Sample, D. A. Meyer, and J. R. Smith, “Analysis, Experimental Results, and Range Adaptation of Magnetically Coupled Resonators for Wireless Power Transfer,” *IEEE Transactions on Industrial Electronics*, vol. 58, no. 2, pp. 544–554, feb 2011. [Online]. Available: <http://ieeexplore.ieee.org/document/5437250/>
- [15] W. Brown, “Experiments in the transportation of energy by microwave beam,” in *IRE International Convention Record*, vol. 12. Institute of Electrical and Electronics Engineers, 1964, pp. 8–17. [Online]. Available: <http://ieeexplore.ieee.org/document/1147324/>

- [16] M. A. B. Abbasi, “Disruptive Beamforming Trends Improving Millimeter-Wave 5G,” accessed 01.03.2021. [Online]. Available: <https://uk5g.org/5g-updates/read-articles/disruptive-beamforming-trends-improving-millimeter/>
- [17] Q. Yuan, Q. Chen, L. Li, and K. Sawaya, “Numerical Analysis on Transmission Efficiency of Evanescent Resonant Coupling Wireless Power Transfer System,” *IEEE Transactions on Antennas and Propagation*, vol. 58, no. 5, pp. 1751–1758, may 2010. [Online]. Available: <http://ieeexplore.ieee.org/document/5422616/>
- [18] O. Keller, *Quantum Theory of Near-Field Electrodynamics*. Berlin, Heidelberg: Springer Berlin Heidelberg, 2011. [Online]. Available: http://link.springer.com/10.1007/978-3-642-17410-0_1
- [19] X. Lu, P. Wang, D. Niyato, D. Kim, and Z. Han, “Wireless Networks with RF Energy Harvesting: A Contemporary Survey,” *arXiv preprint*, vol. 17, no. c, pp. 1–33, 2014. [Online]. Available: <http://arxiv.org/abs/1406.6470>
- [20] A. Sample and J. Smith, “Experimental results with two wireless power transfer systems,” *2009 IEEE Radio and Wireless Symposium*, pp. 2009–2011, 2009.
- [21] X. Mou and H. Sun, “Wireless Power Transfer: Survey and Roadmap,” in *2015 IEEE 81st Vehicular Technology Conference (VTC Spring)*, vol. 2015, no. 646470. IEEE, may 2015, pp. 1–5. [Online]. Available: <http://ieeexplore.ieee.org/document/7146165>
- [22] A. Kurs, A. Karalis, R. Moffatt, J. D. Joannopoulos, P. Fisher, and M. Soljacic, “Wireless Power Transfer via Strongly Coupled Magnetic Resonances,” *Science*, vol. 317, no. 5834, pp. 83–86, jul 2007. [Online]. Available: <http://www.sciencemag.org/cgi/doi/10.1126/science.1143254>
- [23] S. Y. R. Hui, “Magnetic Resonance for Wireless Power Transfer,” *IEEE Power Electronics Magazine*, no. March, pp. 14–31, 2016.
- [24] T. Martin and N. Tesla, “The Inventions, Researches and Writings of Nikola Tesla - With Special Reference to His Work in Polyphase Currents and High Potential Lighting,” 1894.
- [25] S. Shimokawa, H. Kawano, K. Matsui, A. Uchida, and M. Taguchi, “A numerical study of power loss factors in resonant magnetic coupling,” *2011 IEEE MTT-S International Microwave Workshop Series on Innovative Wireless Power Transmission: Technologies, Systems, and Applications*, pp. 219–222, 2011. [Online]. Available: <http://ieeexplore.ieee.org/document/5877134>
- [26] T. Imura and Y. Hori, “Maximizing air gap and efficiency of magnetic resonant coupling for wireless power transfer using equivalent circuit and Neumann formula,” *IEEE Transactions on Industrial Electronics*, vol. 58, no. 10, pp. 4746–4752, 2011.
- [27] M. Shahmohammadi, M. Chabalko, and A. P. Sample, “High-Q, over-coupled tuning for near-field RFID systems,” *2016 IEEE International Conference on RFID (RFID)*, pp. 1–8, 2016. [Online]. Available: <http://ieeexplore.ieee.org/document/7488016>
- [28] X. Lu, P. Wang, D. Niyato, D. I. Kim, and Z. Han, “Wireless Charging Technologies: Fundamentals, Standards, and Network Applications,” *IEEE Communications Surveys & Tutorials*, vol. 18, no. 2, pp. 1413–1452, jan 2016. [Online]. Available: <http://ieeexplore.ieee.org/document/7327131>
- [29] C.-J. Chen, T.-H. Chu, C.-L. Lin, and Z.-C. Jou, “A Study of Loosely Coupled Coils for Wireless Power Transfer,” *IEEE Transactions on Circuits and Systems II: Express Briefs*, vol. 57, no. 7, pp. 536–540, jul 2010. [Online]. Available: <https://ieeexplore.ieee.org/document/5475182>
- [30] S. Li and C. C. Mi, “Wireless Power Transfer for Electric Vehicle Applications,” *IEEE Journal of Emerging and Selected Topics in Power Electronics*, vol. 3, no. 1, pp. 4–17, mar 2015. [Online]. Available: <http://ieeexplore.ieee.org/document/6804648/>

- [31] S. Roberts, "Conjugate-Image Impedances," *Proceedings of the IRE*, vol. 34, no. 4, pp. 198p–204p, apr 1946. [Online]. Available: <http://ieeexplore.ieee.org/document/1697051/>
- [32] S. Y. R. Hui, W. Zhong, and C. K. Lee, "A Critical Review of Recent Progress in Mid-Range Wireless Power Transfer," *IEEE Transactions on Power Electronics*, vol. 29, no. 9, pp. 4500–4511, sep 2014. [Online]. Available: <https://ieeexplore.ieee.org/document/6472081>
- [33] D. W. Knight, *The self-resonance and self-capacitance of solenoid coils: applicable theory, models and calculation methods*, 2016, no. May.
- [34] S. H. Lee and R. D. Lorenz, "Development and validation of model for 95%-efficiency 220-W wireless power transfer over a 30-cm air gap," *IEEE Transactions on Industry Applications*, vol. 47, no. 6, pp. 2495–2504, 2011.
- [35] L. Sandrolini, U. Reggiani, G. Pucetti, and Y. Neau, "Equivalent circuit characterization of resonant magnetic coupling for wireless transmission of electrical energy," *International Journal of Circuit Theory and Applications*, vol. 41, no. 7, pp. 753–771, jul 2013. [Online]. Available: <http://doi.wiley.com/10.1002/cta.1873>
- [36] T. Mizuno, T. Ueda, S. Yachi, R. Ohtomo, and Y. Goto, "Efficiency Dependence on Wire Type for Wireless Power Transfer of Magnetic Resonant Coupling," *15th International Conference on Electrical Machines and Systems (ICEMS)*, pp. 1–4, 2012.
- [37] T. Mizuno, S. Yachi, A. Kamiya, and D. Yamamoto, "Improvement in efficiency of wireless power transfer of magnetic resonant coupling using magnetoplated wire," *IEEE Transactions on Magnetics*, vol. 47, no. 10, pp. 4445–4448, 2011.
- [38] H. Wenshan, Y. Lingsong, L. Zhiwei, and Y. Hui, "Loss analysis and improvement of all parts of magnetic resonant wireless power transfer system," in *2015 Chinese Automation Congress (CAC)*. IEEE, nov 2015, pp. 2251–2256. [Online]. Available: <http://ieeexplore.ieee.org/document/7382878/>
- [39] C. Lee, W. Zhong, and S. Hui, "Recent progress in mid-range wireless power transfer," in *2012 IEEE Energy Conversion Congress and Exposition (ECCE)*. IEEE, sep 2012, pp. 3819–3824. [Online]. Available: <http://ieeexplore.ieee.org/document/6342288/>
- [40] Q. Yuan, Q. Chen, J. Li, and K. Sawaya, "Optimum load of WPT system analyzed by S-parameters," in *2012 6th European Conference on Antennas and Propagation (EUCAP)*, vol. 2, no. 4. IEEE, mar 2012, pp. 3604–3608. [Online]. Available: <http://ieeexplore.ieee.org/document/6206303/>
- [41] W. X. Zhong, C. K. Lee, and S. Y. R. Hui, "Wireless power domino-resonator systems with noncoaxial axes and circular structures," *IEEE Transactions on Power Electronics*, vol. 27, no. 11, pp. 4750–4762, 2012.
- [42] A. Sangswang, S. Nutwong, and S. Naetiladdanon, "Design of the wireless power transfer system with uncompensated secondary to increase power transfer capability," in *8th IET International Conference on Power Electronics, Machines and Drives (PEMD 2016)*. Institution of Engineering and Technology, 2016, pp. 1–5. [Online]. Available: <http://digital-library.theiet.org/content/conferences/10.1049/cp.2016.0291>
- [43] S. E. Miller, "Coupled Wave Theory and Waveguide Applications," *Bell System Technical Journal*, vol. 33, no. 3, pp. 661–719, 1954.
- [44] A. Karalis, J. D. Joannopoulos, and M. Soljačić, "Efficient wireless non-radiative mid-range energy transfer," *Annals of Physics*, vol. 323, no. 1, pp. 34–48, 2008.
- [45] H. A. Haus and W. Huang, "Coupled-Mode Theory," *Proceedings of the IEEE*, vol. 79, no. 10, pp. 1505–1518, 1991.
- [46] X. Wei, Z. Wang, and H. Dai, "A critical review of wireless power transfer via strongly coupled magnetic resonances," *Energies*, vol. 7, no. 7, pp. 4316–4341, 2014.

- [47] M. Kiani and M. Ghovanloo, "The circuit theory behind coupled-mode magnetic resonance-based wireless power transmission," *IEEE Transactions on Circuits and Systems I: Regular Papers*, vol. 59, no. 9, pp. 2065–2074, 2012.
- [48] S. D. Barman, A. W. Reza, N. Kumar, M. E. Karim, and A. B. Munir, "Wireless powering by magnetic resonant coupling: Recent trends in wireless power transfer system and its applications," *Renewable and Sustainable Energy Reviews*, vol. 51, pp. 1525–1552, nov 2015. [Online]. Available: <http://linkinghub.elsevier.com/retrieve/pii/S1364032115006784>
- [49] "S parameters or Scattering Parameters," accessed 12.04.2017. [Online]. Available: <http://www.rfwireless-world.com/Terminology/S-Parameters-Scattering-parameter.html>
- [50] T. S-parameters, "Scattering parameters," pp. 1–15, 2018.
- [51] "Network Analyzer basics," accessed 12.04.2017. [Online]. Available: <http://www.rfwireless-world.com/Terminology/SNA-Scalar-Network-Analyzer-vs-VNA-Vector-Network-Analyzer.html>
- [52] P. Belov, Mingzhao Song, I. Iorsh, and P. Kapitanova, "Application of High-Q dielectric resonators for wireless power transfer system," in *2015 SBMO/IEEE MTT-S International Microwave and Optoelectronics Conference (IMOC)*. IEEE, nov 2015, pp. 1–5. [Online]. Available: <http://ieeexplore.ieee.org/document/7369228>
- [53] H. Kim, C. Song, D.-H. Kim, D. H. Jung, I.-M. Kim, Y.-I. Kim, J. Kim, S. Ahn, and J. Kim, "Coil Design and Measurements of Automotive Magnetic Resonant Wireless Charging System for High-Efficiency and Low Magnetic Field Leakage," *IEEE Transactions on Microwave Theory and Techniques*, vol. 64, no. 2, pp. 1–18, 2016. [Online]. Available: <http://ieeexplore.ieee.org/document/7387785>
- [54] M. Schormans, V. Valente, and A. Demosthenous, "Frequency splitting analysis and compensation method for inductive wireless powering of implantable biosensors," *Sensors (Switzerland)*, vol. 16, no. 8, 2016.
- [55] X. Huang, L. Tan, W. Wang, Y. Zhou, and H. Qiang, "Resonant Frequency Splitting Analysis and Optimization of Wireless Power Transfer System," *PIERS Proceedings*, no. 1, pp. 684–688, 2012.
- [56] N. R., V. Juliet, S. Padmanaban, L. Mihet-Popa, and B. C., "Frequency Splitting Elimination and Cross-Coupling Rejection of Wireless Power Transfer to Multiple Dynamic Receivers," *Applied Sciences*, vol. 8, no. 2, p. 179, jan 2018. [Online]. Available: <http://www.mdpi.com/2076-3417/8/2/179>
- [57] Y. Zhang and Z. Zhao, "Frequency splitting analysis of two-coil resonant wireless power transfer," *IEEE Antennas and Wireless Propagation Letters*, vol. 13, no. 2, pp. 400–402, 2014.
- [58] N. Hoang and J. I. Agbinya, "Splitting Frequency Diversity in Wireless Power Transmission," *Power Electronics, IEEE Transactions on*, vol. 30, no. 11, pp. 6088–6096, 2015. [Online]. Available: <https://ieeexplore.ieee.org/document/7089278>
- [59] Y. Zhang, Z. Zhao, and K. Chen, "Frequency-splitting analysis of four-coil resonant wireless power transfer," *IEEE Transactions on Industry Applications*, vol. 50, no. 4, pp. 2436–2445, 2014.
- [60] W. Niu, W. Gu, J. Chu, and A. Shen, "Coupled-mode analysis of frequency splitting phenomena in CPT systems," *Electronics Letters*, vol. 48, no. 12, p. 723, 2012. [Online]. Available: <http://digital-library.theiet.org/content/journals/10.1049/el.2012.0953>
- [61] R. Huang, B. Zhang, D. Qiu, and Y. Zhang, "Frequency splitting phenomena of magnetic resonant coupling wireless power transfer," *IEEE Transactions on Magnetics*, vol. 50, no. 11, 2014.

- [62] N. Y. Kim, K. Y. Kim, and C.-W. Kim, "Automated frequency tracking system for efficient mid-range magnetic resonance wireless power transfer," *Microwave and Optical Technology Letters*, vol. 54, no. 6, pp. 1423–1426, jun 2012. [Online]. Available: <http://doi.wiley.com/10.1002/mop.26858>
- [63] C. Moorey, "Wireless Power Transfer Between Loops and Dipoles," Ph.D. dissertation, University of Reading, 2016.
- [64] W.-Q. Niu, J.-X. Chu, W. Gu, and A.-D. Shen, "Exact Analysis of Frequency Splitting Phenomena of Contactless Power Transfer Systems," *IEEE Transactions on Circuits and Systems*, vol. 60, no. 6, pp. 1670 – 1677, 2013.
- [65] Y.-L. Lyu, F.-Y. Meng, G.-H. Yang, B.-J. Che, Q. Wu, L. Sun, D. Erni, and J. L.-W. Li, "A Method of Using Nonidentical Resonant Coils for Frequency Splitting Elimination in Wireless Power Transfer," *IEEE Transactions on Power Electronics*, vol. 30, no. 11, pp. 6097–6107, nov 2015. [Online]. Available: <http://ieeexplore.ieee.org/document/7001689>
- [66] A. Triviño-Cabrera and J. Sánchez, "A Review on the Fundamentals and Practical Implementation Details of Strongly Coupled Magnetic Resonant Technology for Wireless Power Transfer," *Energies*, vol. 11, no. 10, p. 2844, oct 2018. [Online]. Available: <http://www.mdpi.com/1996-1073/11/10/2844>
- [67] J. Park, Y. Tak, Y. Kim, Y. Kim, and S. Nam, "Investigation of adaptive matching methods for near-field wireless power transfer," *IEEE Transactions on Antennas and Propagation*, vol. 59, no. 5, pp. 1769–1773, 2011.
- [68] D. Ahn, S. Kim, J. Moon, and I.-K. Cho, "Wireless Power Transfer With Automatic Feedback Control of Load Resistance Transformation," *IEEE Transactions on Power Electronics*, vol. 31, no. 11, pp. 7876–7886, nov 2016. [Online]. Available: <http://ieeexplore.ieee.org/document/7368178>
- [69] Y. L. Lv, F. Y. Meng, B. J. Che, Y.-H. Wu, Q. Wu, and L. Sun, "A novel method for frequency splitting suppression in wireless power transfer," in *Proceedings of 2014 3rd Asia-Pacific Conference on Antennas and Propagation*. IEEE, jul 2014, pp. 590–592. [Online]. Available: <http://ieeexplore.ieee.org/prox.lib.ncsu.edu/ielx7/6963206/6992393/06992563.pdf>
- [70] H. Hwang, J. Moon, B. Lee, C.-h. Jeong, and S.-w. Kim, "An analysis of magnetic resonance coupling effects on wireless power transfer by coil inductance and placement," *IEEE Transactions on Consumer Electronics*, vol. 60, no. 2, pp. 203–209, may 2014. [Online]. Available: <http://ieeexplore.ieee.org/document/6851995/>
- [71] V. Kindl, T. Kavalir, R. Pechanek, B. Skala, and J. Sobra, "Key construction aspects of resonant wireless low power transfer system," in *2014 ELEKTRO*, no. 5. IEEE, may 2014, pp. 303–306. [Online]. Available: <http://ieeexplore.ieee.org/document/6848907/>
- [72] T. Imura, "Study on maximum air-gap and efficiency of Magnetic Resonant Coupling for Wireless Power Transfer using Equivalent Circuit," in *2010 IEEE International Symposium on Industrial Electronics*. IEEE, jul 2010, pp. 3664–3669. [Online]. Available: <http://ieeexplore.ieee.org/document/5637357/>
- [73] M. Iordache, D. Niculae, L. I. Bobaru, and L. Mandache, "Circuit analysis of frequency splitting phenomena in wireless power transfer systems," in *2015 9th International Symposium on Advanced Topics in Electrical Engineering (ATEE)*. IEEE, may 2015, pp. 146–151. [Online]. Available: <http://ieeexplore.ieee.org/document/7133758/>
- [74] F. Mastri, A. Costanzo, and M. Mongiardo, "Coupling-Independent Wireless Power Transfer," *IEEE Microwave and Wireless Components Letters*, vol. 26, no. 3, pp. 222–224, mar 2016. [Online]. Available: <http://ieeexplore.ieee.org/document/7415979>
- [75] H. Hirayama, "Equivalent Circuit and Calculation of Its Parameters of Magnetic-Coupled-Resonant Wireless Power Transfer," in *Wireless Power Transfer - Principles and Engineering Explorations*. InTech, jan 2012, ch.

- Equivalent. [Online]. Available: <http://www.intechopen.com/books/wireless-power-transfer-principles-and-engineering-explorations/equivalent-circuit-and-calculation-of-its-parameters-of-magnetic-coupled-resonant-wireless-power-transfer>
- [76] A. Ong, J. P. K. Sampath, G. F. H. Beng, T. Yenkheng, D. M. Vilathgamuwa, and N. X. Bac, "Analysis of impedance matched circuit for wireless power transfer," *Proceedings, IECON 2014 - 40th Annual Conference of the IEEE Industrial Electronics Society*, pp. 2965–2970, 2015.
- [77] M. Kazmierkowski and A. Moradewicz, "Unplugged But Connected: Review of Contactless Energy Transfer Systems," *IEEE Industrial Electronics Magazine*, vol. 6, no. 4, pp. 47–55, dec 2012. [Online]. Available: <http://ieeexplore.ieee.org/document/6378529/>
- [78] M. P. Kazmierkowski, R. M. Miskiewicz, and A. J. Moradewicz, "Inductive coupled contactless energy transfer systems - a review," in *2015 Selected Problems of Electrical Engineering and Electronics (WZEE)*. IEEE, sep 2015, pp. 1–6. [Online]. Available: <http://ieeexplore.ieee.org/document/7394025/>
- [79] J. Kim, D. H. Kim, and Y. J. Park, "Analysis of Capacitive Impedance Matching Networks for Simultaneous Wireless Power Transfer to Multiple Devices," *IEEE Transactions on Industrial Electronics*, vol. 62, no. 5, pp. 2807–2813, 2015.
- [80] C.-s. Wang, G. a. Covic, and O. H. Stielau, "Power Transfer Capability and Bifurcation Phenomena of Loosely Coupled Inductive Power Transfer Systems," *IEEE Transactions on Industrial Electronics*, vol. 51, no. 1, pp. 148–157, 2004.
- [81] G. Monti, A. Costanzo, F. Mastri, and M. Mongiardo, "Optimal design of a wireless power transfer link using parallel and series resonators," *Wireless Power Transfer*, vol. 3, no. 02, pp. 105–116, sep 2016. [Online]. Available: http://www.journals.cambridge.org/abstract_S2052841816000075
- [82] J. Sallan, J. Villa, a. Llombart, and J. Sanz, "Optimal Design of ICPT Systems Applied to Electric Vehicle Battery Charge," *IEEE Transactions on Industrial Electronics*, vol. 56, no. 6, pp. 2140–2149, 2009. [Online]. Available: <https://ieeexplore.ieee.org/document/4787071>
- [83] J. L. Villa, J. Sallan, J. F. Sanz Osorio, and A. Llombart, "High-Misalignment Tolerant Compensation Topology For ICPT Systems," *IEEE Transactions on Industrial Electronics*, vol. 59, no. 2, pp. 945–951, feb 2012. [Online]. Available: <http://ieeexplore.ieee.org/document/5985526/>
- [84] L. Chen, S. Liu, Y. C. Zhou, and T. J. Cui, "An optimizable circuit structure for high-efficiency wireless power transfer," *IEEE Transactions on Industrial Electronics*, vol. 60, no. 1, pp. 339–349, 2013.
- [85] "Electronic Tutorials: Q," accessed 12.04.2017. [Online]. Available: <http://www.electronics-tutorials.com/basics/q.htm>
- [86] B. L. Cannon, J. F. Hoburg, D. D. Stancil, and S. C. Goldstein, "Magnetic Resonant Coupling As a Potential Means for Wireless Power Transfer to Multiple Small Receivers," *IEEE Transactions on Power Electronics*, vol. 24, no. 7, pp. 1819–1825, jul 2009. [Online]. Available: <http://ieeexplore.ieee.org/documents/5175611>
- [87] C. Park, S.-W. Lee, and C.-t. Rim, "5m-off-long-distance inductive power transfer system using optimum shaped dipole coils," in *Proceedings of The 7th International Power Electronics and Motion Control Conference*, vol. 2, no. 2010. IEEE, jun 2012, pp. 1137–1142. [Online]. Available: <http://ieeexplore.ieee.org/document/6258980>
- [88] International Commission on Non-Ionizing Radiation Protection, "Guidelines for limiting exposure to time-varying electric and magnetic fields (1 Hz to 100 kHz)." *Health physics*, vol. 99, no. 6, pp. 818–36, 2009. [Online]. Available: <http://www.ncbi.nlm.nih.gov/pubmed/21068601%5Cn>

- [89] S. Cheon, Y. H. Kim, S. Y. Kang, M. L. Lee, J. M. Lee, and T. Zyung, "Circuit-model-based analysis of a wireless energy-transfer system via coupled magnetic resonances," *IEEE Transactions on Industrial Electronics*, vol. 58, no. 7, pp. 2906–2914, 2011.
- [90] Q. Deng, J. Liu, D. Czarkowski, M. K. Kazimierczuk, M. Bojarski, H. Zhou, and W. Hu, "Frequency-Dependent Resistance of Litz-Wire Square Solenoid Coils and Quality Factor Optimization for Wireless Power Transfer," *IEEE Transactions on Industrial Electronics*, vol. 63, no. 5, pp. 2825–2837, may 2016. [Online]. Available: <http://ieeexplore.ieee.org/document/7383291>
- [91] J. McLean and R. Sutton, "The multipole nature of the extraneous field of a magnetic field wireless power transfer system," in *2016 IEEE International Symposium on Electromagnetic Compatibility (EMC)*. IEEE, jul 2016, pp. 582–587. [Online]. Available: <http://ieeexplore.ieee.org/document/7571713/>
- [92] J. Kim, D.-H. Kim, J. Choi, K.-H. Kim, and Y.-J. Park, "Free-Positioning Wireless Charging System for Small Electronic Devices Using a Bowl-Shaped Transmitting Coil," *IEEE Transactions on Microwave Theory and Techniques*, vol. 63, no. 3, pp. 791–800, mar 2015. [Online]. Available: <http://ieeexplore.ieee.org/document/7042363>
- [93] R. Melki and B. Moslem, "Optimizing the design parameters of a wireless power transfer system for maximizing power transfer efficiency: A simulation study," in *2015 Third International Conference on Technological Advances in Electrical, Electronics and Computer Engineering (TAECE)*. IEEE, apr 2015, pp. 278–282. [Online]. Available: <http://ieeexplore.ieee.org/document/7113640>
- [94] "Ansys Maxwell," accessed 12.04.2017. [Online]. Available: <http://www.ansys.com/products/electronics/ANSYS-Maxwell>
- [95] "COMSOL Multiphysics," accessed 12.04.2017. [Online]. Available: <https://www.comsol.com/>
- [96] W. Ding and X. Wang, "Magnetically coupled resonant using Mn-Zn ferrite for wireless power transfer," in *2014 15th International Conference on Electronic Packaging Technology*, no. 2. IEEE, may 2014, pp. 1561–1564. [Online]. Available: <http://ieeexplore.ieee.org/document/6922952/>
- [97] W. Ahn, S. Jung, W. Lee, S. Kim, J. Park, J. Shin, H. Kim, and K. Koo, "Design of coupled resonators for wireless power transfer to mobile devices using magnetic field shaping," in *2012 IEEE International Symposium on Electromagnetic Compatibility*. IEEE, aug 2012, pp. 772–776. [Online]. Available: <http://ieeexplore.ieee.org/document/6351667/>
- [98] K. Knaisch, M. Springmann, and P. Gratzfeld, "Comparison of coil topologies for inductive power transfer under the influence of ferrite and aluminum," in *2016 Eleventh International Conference on Ecological Vehicles and Renewable Energies (EVER)*. IEEE, apr 2016, pp. 1–9. [Online]. Available: <http://ieeexplore.ieee.org/document/7476339/>
- [99] J. Ma, X. Huang, J. Zhou, Y. Fang, J. Zhang, and Y. Gao, "Magnetic field design for optimal wireless power transfer to multiple receivers," *IET Power Electronics*, vol. 9, no. 9, pp. 1885–1893, jul 2016. [Online]. Available: <http://digital-library.theiet.org/content/journals/10.1049/iet-pel.2015.0915>
- [100] Y. H. Sohn, B. H. Choi, E. S. Lee, and C. T. Rim, "Comparisons of magnetic field shaping methods for ubiquitous wireless power transfer," in *2015 IEEE PELS Workshop on Emerging Technologies: Wireless Power (2015 WoW)*. IEEE, jun 2015, pp. 1–6. [Online]. Available: <http://ieeexplore.ieee.org/document/7132810/>
- [101] F. Ye, Q. Chen, and W. Chen, "Analysis and design of magnetic coupling structure in wireless power transmission system," in *2016 Asia-Pacific International Symposium on Electromagnetic Compatibility (APEMC)*. IEEE, may 2016, pp. 679–682. [Online]. Available: <http://ieeexplore.ieee.org/document/7522835/>

- [102] Y. Lim and J. Park, "A Novel Phase-Control-Based Energy Beamforming Techniques in Nonradiative Wireless Power Transfer," *IEEE Transactions on Power Electronics*, vol. 30, no. 11, pp. 6274–6287, nov 2015. [Online]. Available: <http://ieeexplore.ieee.org/document/6982203/>
- [103] G. Yang, M. R. V. Moghadam, and R. Zhang, "Magnetic beamforming for wireless power transfer," in *2016 IEEE International Conference on Acoustics, Speech and Signal Processing (ICASSP)*. IEEE, mar 2016, pp. 3936–3940. [Online]. Available: <http://ieeexplore.ieee.org/document/7472415/>
- [104] D. Huang, Y. Urzhumov, D. R. Smith, K. Hoo Teo, and J. Zhang, "Magnetic superlens-enhanced inductive coupling for wireless power transfer," *Journal of Applied Physics*, vol. 111, no. 6, pp. 1–20, 2012.
- [105] Y. Urzhumov and D. R. Smith, "Metamaterial-enhanced coupling between magnetic dipoles for efficient wireless power transfer," *Physical Review B*, vol. 83, no. 20, p. 205114, may 2011. [Online]. Available: <http://arxiv.org/abs/1102.2281>
- [106] J. C. Bose, "On the rotation of plane of polarization of electric waves by a twisted structure," *Proc. R. Soc.*, vol. 63, pp. 146–152, 1898.
- [107] V. G. Veselago, "The Electrodynamics of Substances with Simultaneously Negative Values of Epsilon and Mu," *Soviet Physics Uspekhi*, vol. 10, p. 509, 1968.
- [108] N. Engheta and R. W. Ziolkowski, "A Positive Future for Double-Negative Metamaterials," vol. 53, no. 4, pp. 1535–1556, 2005.
- [109] D. R. Smith, W. J. Padilla, D. C. Vier, and S. Schultz, "Composite Medium with Simultaneously Negative Permeability and Permittivity," *Phys. Rev. Lett.*, vol. 84, pp. 4184–4187, 2000.
- [110] D. R. Smith and N. Kroll, "Negative Refractive Index in Left-Handed Materials," *Physical Review Letters*, vol. 85, no. 3, pp. 2933–2936, 2000.
- [111] R. A. Shelby, D. R. Smith, and S. Schultz, "Experimental Verification of a Negative Index of Refraction," *Phys. Rev. Lett.*, vol. 84, no. April, pp. 4184–4187, 2001.
- [112] V. Rawat and S. Kale, "Metamaterials for Energy-Harvesting Applications : A Review," *Nanotech Insights*, vol. 6, no. 2, pp. 2–8, 2015.
- [113] N. I. Landy, S. Sajuyigbe, J. J. Mock, D. R. Smith, and W. J. Padilla, "Perfect metamaterial absorber," *Physical Review Letters*, vol. 100, no. 20, pp. 1–4, 2008.
- [114] C. J. Stevens, "Some consequences of the properties of metamaterials for wireless power transfer," *2015 9th International Congress on Advanced Electromagnetic Materials in Microwaves and Optics (METAMATERIALS)*, no. September, pp. 295–297, 2015. [Online]. Available: <http://ieeexplore.ieee.org/document/7342607>
- [115] M. R. Alshareef and O. M. Ramahi, "Electrically small resonators for energy harvesting in the infrared regime," *Journal of Applied Physics*, vol. 114, no. 22, 2013.
- [116] M. E. Badawe and O. M. Ramahi, "Efficient Metasurface Rectenna for Electromagnetic Wireless Power Transfer and Energy Harvesting," *Progress In Electromagnetics Research*, vol. x, no. January, pp. 1–6, 2018. [Online]. Available: <http://www.jpier.org/PIER/pier161/04.18011003.pdf>
- [117] X. Duan, X. Chen, and L. Zhou, "A metamaterial electromagnetic energy rectifying surface with high harvesting efficiency," *AIP Advances*, vol. 6, no. 12, 2016.
- [118] —, "Design of a novel rectenna array based on metamaterials with embedded diodes for low power harvesting," *2016 IEEE Conference on Antenna Measurements and Applications, CAMA 2016*, pp. 1–3, 2017.
- [119] C. Fowler, "A Metamaterial - inspired Approach to RF Energy Harvesting," *Arxiv*, vol. 1705, no. 07718, pp. 1–11, 2017.

- [120] D. R. Smith, J. B. Pendry, and M. C. K. Wiltshire, "Metamaterials and Negative Refractive Index," vol. 305, no. August, pp. 788–793, 2004.
- [121] Y. Dong, W. Li, X. Yang, C. Yao, and H. Tang, "Design Of Unit Cell for Metamaterials Applied In A Wireless Power Transfer System," no. 1, pp. 143–147, 2017.
- [122] S. Nishimura, J. D. Almeida, C. Vollaie, and C. Sartori, "Enhancing the inductive coupling and efficiency of wireless power transmission system by using metamaterials Enhancing the inductive coupling and efficiency of wireless power transmission system by using metamaterials," no. December 2015, pp. 121–125, 2014.
- [123] B. Wang and K. H. Teo, "Metamaterials for wireless power transfer," *IEEE International Workshop on Antenna Technology*, no. 1, pp. 161–164, 2012.
- [124] B. Wang, T. Nishino, and K. H. Teo, "Wireless power transmission efficiency enhancement with metamaterials," *2010 IEEE International Conference on Wireless Information Technology and Systems*, no. 1, pp. 1–4, 2010.
- [125] B. Wang, W. Yerazunis, and K. H. Teo, "Wireless power transfer: Metamaterials and array of coupled resonators," *Proceedings of the IEEE*, vol. 101, no. 6, pp. 1359–1368, 2013.
- [126] Y. Cho, S. Lee, S. Jeong, H. Kim, C. Song, K. Yoon, J. Song, S. Kong, Y. Yun, and J. Kim, "Hybrid metamaterial with zero and negative permeability to enhance efficiency in wireless power transfer system," *2016 IEEE Wireless Power Transfer Conference, WPTC 2016*, pp. 3–5, 2016.
- [127] T. Asano, K. Itoh, S. Matsumoto, T. Kiyoshi, H. Wada, and G. Kido, "Enhanced concentration of the magnetic flux in a superconducting cylinder," *IEEE Transactions on Applied Superconductivity*, vol. 15, no. 2 PART III, pp. 3157–3160, 2005.
- [128] C. Navau, J. Prat-Camps, and A. Sanchez, "Magnetic energy harvesting and concentration at a distance by transformation optics," *Physical Review Letters*, vol. 109, no. 26, pp. 1–5, 2012.
- [129] A. Díaz-Rubio, J. Carbonell, and J. Sánchez-Dehesa, "Wireless energy transfer between anisotropic metamaterials shells," *Annals of Physics*, vol. 345, pp. 55–62, jun 2014. [Online]. Available: <http://linkinghub.elsevier.com/retrieve/pii/S0003491614000608>
- [130] M. J. Chabalko, J. Besnoff, and D. S. Ricketts, "Magnetic Field Enhancement in Wireless Power With Metamaterials and Magnetic Resonant Couplers," *IEEE Antennas and Wireless Propagation Letters*, vol. 15, no. c, pp. 452–455, 2016. [Online]. Available: <http://ieeexplore.ieee.org/document/7145412>
- [131] A. Ranaweera, T. Duong, and J.-W. Lee, "Investigation on threshold distance for efficiency enhanced wireless power transfer using bulk metamaterial," *2014 Asia-Pacific Microwave Conference Proceedings, APMC 2014*, pp. 5–7, 2014.
- [132] D. Ahn, M. Kiani, and M. Ghovanloo, "Enhanced Wireless Power Transmission Using Strong Paramagnetic Response," *IEEE Transactions on Magnetism*, vol. 50, no. 3, pp. 96–103, mar 2014. [Online]. Available: <http://ieeexplore.ieee.org/document/6623165>
- [133] M. Kiani, Uei-Ming Jow, and M. Ghovanloo, "Design and Optimization of a 3-Coil Inductive Link for Efficient Wireless Power Transmission," *IEEE Transactions on Biomedical Circuits and Systems*, vol. 5, no. 6, pp. 579–591, dec 2011. [Online]. Available: <http://ieeexplore.ieee.org/document/5951804>
- [134] W. X. Zhong, C. Zhang, X. Liu, and S. Y. R. Hui, "A methodology for making a three-coil wireless power transfer system more energy efficient than a two-coil counterpart for extended transfer distance," *IEEE Transactions on Power Electronics*, vol. 30, no. 2, pp. 933–942, 2015.

- [135] Jian Zhang, Xinmei Yuan, and Chuang Wang, "A study of three-coil magnetically coupled resonators for wireless power transfer," in *2015 IEEE International Wireless Symposium (IWS 2015)*. IEEE, mar 2015, pp. 1–4. [Online]. Available: <http://ieeexplore.ieee.org/document/7164536>
- [136] Z.-h. Ye, Y. Sun, X. Dai, C.-s. Tang, Z.-h. Wang, and Y.-g. Su, "Energy Efficiency Analysis of U-coil Wireless Power Transfer System," *IEEE Transactions on Power Electronics*, vol. 31, no. 7, pp. 1–1, 2015. [Online]. Available: <http://ieeexplore.ieee.org/document/7283620/>
- [137] J. T. Boys, "Inductive power transfer across an extended gap," Patent WO/1998/050 993, Nov 12, 1998.
- [138] X. Shi, C. Qi, and S. Ye, "Frequency effects of coil locations on wireless power transfer via magnetic resonance coupling," in *2015 Asia-Pacific Microwave Conference (APMC)*. IEEE, dec 2015, pp. 1–3. [Online]. Available: <http://ieeexplore.ieee.org/document/7411732>
- [139] X. Shi, C. Qi, M. Qu, S. Ye, and G. Wang, "A study on effects of coil locations in wireless power transfer," in *2015 IEEE MTT-S International Conference on Numerical Electromagnetic and Multiphysics Modeling and Optimization (NEMO)*. IEEE, aug 2015, pp. 1–3. [Online]. Available: <http://ieeexplore.ieee.org/document/7414996>
- [140] Z. Dang and A. Qahouq, "Range and misalignment tolerance comparisons between two-coil and four-coil wireless power transfer systems," in *2015 IEEE Applied Power Electronics Conference and Exposition (APEC)*. IEEE, mar 2015, pp. 1234–1240. [Online]. Available: <http://ieeexplore.ieee.org/document/7104505/>
- [141] Z. Yan, Y. Li, C. Zhang, and Q. Yang, "Influence Factors Analysis and Improvement Method on Efficiency of Wireless Power Transfer Via," *Ieee Transactions on Magnetics*, vol. 50, no. 4, pp. 1–4, 2014.
- [142] Z. N. Low, R. A. Chinga, R. Tseng, and J. Lin, "Design and test of a high-power high-efficiency loosely coupled planar wireless power transfer system," *IEEE Transactions on Industrial Electronics*, vol. 56, no. 5, pp. 1801–1812, 2009.
- [143] F. Jolani, Z. Chen, and Y. Yu, "Enhanced planar wireless power transfer using strongly coupled magnetic resonance," *Electronics Letters*, vol. 51, no. 2, pp. 173–175, jan 2015. [Online]. Available: <http://digital-library.theiet.org/content/journals/10.1049/el.2014.4104>
- [144] D. G. Nottiani and F. Leccese, "A simple method for calculating lumped parameters of planar spiral coil for wireless energy transfer," in *2012 11th International Conference on Environment and Electrical Engineering*, no. February 2016. IEEE, may 2012, pp. 869–872. [Online]. Available: <http://ieeexplore.ieee.org/document/6221498/>
- [145] P. J. Gonzalez, K. A. Quintana, and S. V. Georgakopoulos, "Misalignment sensitivity and human body effects on wearable conformal SCMR system," in *2016 International Workshop on Antenna Technology (iWAT)*. IEEE, feb 2016, pp. 89–91. [Online]. Available: <http://ieeexplore.ieee.org/document/7434810/>
- [146] B. Nukala, J. Tsay, D. Lie, J. Lopez, and T. Q. Nguyen, "Efficient near-field inductive wireless power transfer for miniature implanted devices using strongly coupled magnetic resonance at 5.8 GHz," in *2016 Texas Symposium on Wireless and Microwave Circuits and Systems (WMCS)*. IEEE, mar 2016, pp. 1–4. [Online]. Available: <http://ieeexplore.ieee.org/document/7577481/>
- [147] Peng Yang, Linxi Dong, Yonghai Jing, Y. Yang, Xiang Su, and Y. Cheng, "A study of wireless power transfer for implantable devices by using wearable devices," in *2015 IEEE 16th International Conference on Communication Technology (ICCT)*. IEEE, oct 2015, pp. 626–629. [Online]. Available: <http://ieeexplore.ieee.org/document/7399915>

- [148] F. Jolani, Y.-q. Yu, and Z. David Chen, "Electromagnetic modeling and optimization of magnetic resonant coupling wireless power transfer using coil array," in *2015 IEEE MTT-S International Conference on Numerical Electromagnetic and Multiphysics Modeling and Optimization (NEMO)*, vol. 1. IEEE, aug 2015, pp. 1–3. [Online]. Available: <http://ieeexplore.ieee.org/document/7415044>
- [149] F. Zhang, S. A. Hackworth, W. Fu, and M. Sun, "The relay effect on wireless power transfer using witrlicity," *Digests of the 2010 14th Biennial IEEE Conference on Electromagnetic Field Computation, CEFC 2010*, vol. 317, p. 7062, 2010.
- [150] X. Liu and G. Wang, "A Novel Wireless Power Transfer System with Double Intermediate Resonant Coils," *IEEE Transactions on Industrial Electronics*, vol. 0046, no. c, pp. 1–1, 2015. [Online]. Available: <http://ieeexplore.ieee.org/document/7362019>
- [151] Y. Zhang, T. Lu, Z. Zhao, K. Chen, F. He, and L. Yuan, "Wireless Power Transfer to Multiple Loads Over Various Distances Using Relay Resonators," *IEEE Microwave and Wireless Components Letters*, vol. 25, no. 5, pp. 337–339, may 2015. [Online]. Available: <http://ieeexplore.ieee.org/document/7061967/>
- [152] D. Wang, Y. Zhu, H. Guo, X. Zhu, T. Mo, and Q. Huang, "Enabling Multi-Angle Wireless Power Transmission via Magnetic Resonant Coupling," in *7th International Conference on Computing and Convergence Technology (ICCT)*, 2012, pp. 1395–1400.
- [153] C. Zhang, D. Lin, and S. Y. Hui, "Basic Control Principles of Omni-Directional Wireless Power Transfer," *IEEE Transactions on Power Electronics*, vol. 8993, no. c, pp. 1–1, 2015. [Online]. Available: <http://ieeexplore.ieee.org/document/7270317>
- [154] W. M. Ng, C. Zhang, D. Lin, and S. Y. R. Hui, "Two- and three-dimensional omnidirectional wireless power transfer," *IEEE Transactions on Power Electronics*, vol. 29, no. 9, pp. 4470–4474, 2014.
- [155] D. Daerhan, H. Hu, and S. V. Georgakopoulos, "Misalignment study of two Strongly Coupled Magnetic Resonance systems," in *2015 IEEE 16th Annual Wireless and Microwave Technology Conference (WAMICON)*. IEEE, apr 2015, pp. 1–3. [Online]. Available: <http://ieeexplore.ieee.org/document/7120412/>
- [156] Z. Dang, Y. Cao, and J. A. Abu Qahouq, "Reconfigurable Magnetic Resonance-Coupled Wireless Power Transfer System," *IEEE Transactions on Power Electronics*, vol. 30, no. 11, pp. 6057–6069, 2015. [Online]. Available: <http://ieeexplore.ieee.org/document/7084654>
- [157] H. Mao, B. Yang, Z. Li, and S. Song, "Controlled-resonance power architecture enables efficient flexible wireless power transfer," in *2016 IEEE Wireless Power Transfer Conference (WPTC)*. IEEE, may 2016, pp. 1–4. [Online]. Available: <http://ieeexplore.ieee.org/document/7498856/>
- [158] D. Stone, R. Zhao, and D. Gladwin, "Maximum efficiency point tracking for resonant wireless power transfer," in *8th IET International Conference on Power Electronics, Machines and Drives (PEMD 2016)*. Institution of Engineering and Technology, 2016, pp. 1–5. [Online]. Available: <http://digital-library.theiet.org/content/conferences/10.1049/cp.2016.0279>
- [159] R. Zhang and C. K. Ho, "MIMO broadcasting for simultaneous wireless information and power transfer," *IEEE Transactions on Wireless Communications*, vol. 12, no. 5, pp. 1989–2001, 2013.
- [160] P. Perez-Nicoli, A. Rodriguez-Esteva, and F. Silveira, "Bidirectional Analysis and Design of RFID Using an Additional Resonant Coil to Enhance Read Range," *IEEE Transactions on Microwave Theory and Techniques*, vol. 64, no. 7, pp. 2357–2367, jul 2016. [Online]. Available: <http://ieeexplore.ieee.org/document/7492195/>

- [161] A. Pacini, F. Mastri, R. Trevisan, A. Costanzo, and D. Masotti, "Theoretical and experimental characterization of moving wireless power transfer systems," in *2016 10th European Conference on Antennas and Propagation (EuCAP)*. IEEE, apr 2016, pp. 1–4. [Online]. Available: <http://ieeexplore.ieee.org/document/7481913/>
- [162] H. Ku and P. Kong, "Efficiency optimising scheme for wireless power transfer system with two transmitters," *Electronics Letters*, vol. 52, no. 4, pp. 310–312, feb 2016. [Online]. Available: <http://digital-library.theiet.org/content/journals/10.1049/el.2015.3736>
- [163] M. R. Vedady Moghadam and R. Zhang, "Multiuser charging control in wireless power transfer via magnetic resonant coupling," *ICASSP, IEEE International Conference on Acoustics, Speech and Signal Processing - Proceedings*, vol. 2015-Augus, no. 1, pp. 3182–3186, 2015.
- [164] A. Yoshida, E. Nishiyama, and I. Toyoda, "Selective Wireless Power Transfer Using Two Transmission Coils Sandwiching Reception Coils," in *2015 International Symposium on Antennas and Propagation (ISAP)*, 2015, pp. 1–3.
- [165] Y.-j. Kim, D. Ha, W. J. Chappell, and P. P. Irazoqui, "Selective Wireless Power Transfer for Smart Power Distribution in a Miniature-Sized Multiple-Receiver System," *IEEE Transactions on Industrial Electronics*, vol. 63, no. 3, pp. 1853–1862, mar 2016. [Online]. Available: <http://ieeexplore.ieee.org/document/7302578/>
- [166] G. Monti, W. Che, Q. Wang, M. Dionigi, M. Mongiardo, R. Perfetti, and Y. Chang, "Wireless power transfer between one transmitter and two receivers: optimal analytical solution," *Wireless Power Transfer*, vol. 3, no. 01, pp. 63–73, mar 2016. [Online]. Available: http://www.journals.cambridge.org/abstract_S2052841816000038
- [167] G. Di Capua, N. Femia, G. Petrone, G. Lisi, D. Du, and R. Subramonian, "Power and efficiency analysis of high-frequency Wireless Power Transfer Systems," *International Journal of Electrical Power & Energy Systems*, vol. 84, pp. 124–134, jan 2017. [Online]. Available: <http://linkinghub.elsevier.com/retrieve/pii/S014206151630062X>
- [168] G. Di Capua, N. Femia, and G. Lisi, "Impact of losses and mismatches on power and efficiency of Wireless Power Transfer Systems with controlled secondary-side rectifier," *Integration, the VLSI Journal*, vol. 55, pp. 384–392, sep 2016. [Online]. Available: <http://linkinghub.elsevier.com/retrieve/pii/S0167926016300086>
- [169] S.-y. Hong, H.-s. Kim, J.-k. Jeong, and K.-b. Kim, "Implementation of 10 [W] Level Wireless Power Transfer System with 6 . 78 MHz Class-D Inverter," vol. 2, pp. 1–7, 2015.
- [170] Y. Akuzawa, K. Tsuji, H. Matsumori, Y. Ito, T. Ezoe, and K. Sakai, "A 95% efficient inverter with 300-W power output for 6.78-MHz magnetic resonant wireless power transfer system," in *2015 IEEE MTT-S International Microwave Symposium*. IEEE, may 2015, pp. 1–3. [Online]. Available: <http://ieeexplore.ieee.org/document/7166894/>
- [171] M. R. Basar, M. Y. Ahmad, J. Cho, and F. Ibrahim, "Stable and High-Efficiency Wireless Power Transfer System for Robotic Capsule Using a Modified Helmholtz Coil," *IEEE Transactions on Industrial Electronics*, vol. 64, no. 2, pp. 1113–1122, feb 2017. [Online]. Available: <http://ieeexplore.ieee.org/document/7579164/>
- [172] Z. Wang, X. Wang, and B. Zhang, "A magnetic coupled resonance WPT system design method of double-end impedance converter networks with Class-E amplifier," in *IECON 2015 - 41st Annual Conference of the IEEE Industrial Electronics Society*, no. 1. IEEE, nov 2015, pp. 003 093–003 098. [Online]. Available: <http://ieeexplore.ieee.org/document/7392575>
- [173] "Press release: Off road trials for electric highways technology," accessed 12.04.2017. [Online]. Available: <https://www.gov.uk/government/news/off-road-trials-for-electric-highways-technology>
- [174] "Witricity," accessed 12.04.2017. [Online]. Available: <http://witricity.com/>

- [175] “Wireless Power Consortium: members list,” accessed 12.04.2017. [Online]. Available: <https://www.wirelesspowerconsortium.com/member-list/>
- [176] “Samsung, Qualcomm start up Alliance for Wireless Power to take on Qi,” accessed 12.04.2017. [Online]. Available: <https://www.engadget.com/2012/05/08/samsung-qualcomm-start-alliance-for-wireless-power/>
- [177] “Airfuel Certified Products list,” accessed 12.04.2017. [Online]. Available: <http://www.airfuel.org/certified-products/certified-products>
- [178] F. Carobolante, “Qualcomm-Resonant Wireless Power Transfer Technology & Integration Roadmap,” *Cicc*, 2015.
- [179] J. Perzow, “Measuring wireless charging efficiency in real world,” in *presented at WPC Trade Conference*, 2015.
- [180] “Pike Research Group,” accessed 12.04.2017. [Online]. Available: <http://www.pikeresearch.com/>
- [181] “Market Research Reports,” accessed 12.04.2017. [Online]. Available: <http://www.marketsandmarkets.com/>
- [182] “About the International Commission on Non-Ionizing Radiation Protection,” accessed 12.04.2017. [Online]. Available: <http://www.icnirp.org/>
- [183] International Commission on Non-Ionizing Radiation Protection, “ICNIRP Guidelines for Limiting Exposure To Time-Varying Electric, Magnetic and Electromagnetic fields,” *Health Physics*, vol. 74, pp. 494–522, 1998.
- [184] T. Campi, S. Cruciani, V. De Santis, and M. Feliziani, “EMF Safety and Thermal Aspects in a Pacemaker Equipped With a Wireless Power Transfer System Working at Low Frequency,” *IEEE Transactions on Microwave Theory and Techniques*, vol. 64, no. 2, pp. 1–8, 2016. [Online]. Available: <http://ieeexplore.ieee.org/document/7386710/>
- [185] M. Kesler, “Highly Resonant Wireless Power Transfer: Safe, Efficient, and over Distance,” Tech. Rep., 2013. [Online]. Available: <http://www.witricity.com/pdfs/highly-resonant-power-transfer-kesler-witricity-2013.pdf>
- [186] H. Hirayama, T. Amano, N. Kikuma, and K. Sakakibara, “Undesired emission and biological effect of open-end and short-end antennas for coupled-resonant wireless power transfer,” in *2013 Asia-Pacific Symposium on Electromagnetic Compatibility (APEMC)*, vol. 1. IEEE, may 2013, pp. 1–4. [Online]. Available: <http://ieeexplore.ieee.org/document/7360618/>
- [187] Y. Zhang, T. Yoshikawa, and I. Awai, “Analysis of Electric and Magnetic Coupling Components for Spiral Resonators Used in Wireless Power Transfer,” *Asia-Pacific Microwave Conference Proceedings*, pp. 1366–1368, 2014.
- [188] W. K. Christ, E. G. Hahn, K. Honegge, M. Zefferer, E. Neufeld, W. Rascher, R. Janka, W. Bautz, J. Chen, B. Kiefer, P. Schmitt, H. P. Hollenbach, J. Shen, M. Oberle, D. Szczerba, A. Kam, J.W. Guag and N. Kuster, “The Virtual Family Project: Development of Anatomical Whole-Body Models of Two Adults and Two Children,” *Phys. Med. Biol.*, vol. 55, pp. 23–38, 2010.
- [189] P. Hasgall, E. Neufeld, M. C. Gosselin, A. Klingenbock and N. Kuster., “IT’IS database for thermal and electromagnetic parameters of biological tissues,” accessed 12.04.2017. [Online]. Available: <http://www.itis.ethz.ch/database>
- [190] K. Agarwal and Y. X. Guo, “Interaction of electromagnetic waves with humans in wearable and biomedical implant antennas,” *2015 Asia-Pacific International Symposium on Electromagnetic Compatibility, APEMC 2015*, pp. 154–157, 2015.
- [191] a. Hirata, S. Tsuchida, and I. Laakso, “Variability of SAR in different human models due to wireless power transfer with magnetic resonance,” *Electromagnetic Compatibility (EMC EUROPE), 2013 International Symposium on*, pp. 89–92, 2013.

- [192] O. Jonah and S. V. Georgakopoulos, "Specific Absorption Rate (SAR) distribution in human tissue with magnetic resonance," *Proceedings of the 2012 IEEE International Symposium on Antennas and Propagation*, pp. 1–2, 2012. [Online]. Available: <http://ieeexplore.ieee.org/document/6349034>
- [193] H. Hu and S. V. Georgakopoulos, "Wireless powering of biomedical implants by Conformal Strongly Coupled Magnetic Resonators," in *2015 IEEE International Symposium on Antennas and Propagation & USNC/URSI National Radio Science Meeting*, vol. 2015-Octob. IEEE, jul 2015, pp. 1207–1208. [Online]. Available: <http://ieeexplore.ieee.org/document/7304992>
- [194] —, "Wireless power transfer in human tissue via Conformal Strongly Coupled Magnetic Resonance," in *2015 IEEE Wireless Power Transfer Conference (WPTC)*, vol. 61, no. 3. IEEE, may 2015, pp. 1–4. [Online]. Available: <http://ieeexplore.ieee.org/document/7140150/>
- [195] M. Ferreira, C. Oliveira, F. Cardoso, and L. M. Correia, "SAR assessment of google glasses at cellular wireless frequency bands," in *2016 10th European Conference on Antennas and Propagation (EuCAP)*. IEEE, apr 2016, pp. 1–4. [Online]. Available: <http://ieeexplore.ieee.org/document/7481301/>
- [196] A. J. Swerdlow, M. Feychting, A. C. Green, L. Kheifets, and D. Savitz, "ICNIRP Sci Review on Mobile Phones, Brain Tumours and The Interphone Study: Where Are We Now?" *Environ Health Perspect* 119(11):1534-1538; 2011, 2011.
- [197] Army Staff, "The Energy Circuit: A roundup of projects and efforts to power change in Army energy," accessed 16.10.2019. [Online]. Available: <https://asc.army.mil/web/access-log-the-energy-circuit/>
- [198] Anon, "Energous: Wirelss Charging 2.0," accessed 16.10.2019. [Online]. Available: <https://www.energous.com/>
- [199] H. Hickery, "Wireless power could cut cord for patients with implanted heart pumps'," accessed 16.10.2019. [Online]. Available: <https://www.washington.edu/news/2011/07/12/wireless-power-could-cut-cord-for-patients-with-implanted-heart-pumps/>
- [200] S. Bhardwaj, "The Future of Wireless Charging," accessed 16.10.2019. [Online]. Available: <https://www.geekinsider.com/the-future-of-wireless-charging/>
- [201] D. Zhu, N. J. Grabham, L. Clare, B. H. Stark, and S. P. Beeby, "Inductive power transfer in e-textile applications: Reducing the effects of coil misalignment," *2015 IEEE Wireless Power Transfer Conference, WPTC 2015*, vol. 1, pp. 0–3, 2015.
- [202] N. J. Grabham, Y. Li, L. R. Clare, B. H. Stark, and S. P. Beeby, "Fabrication Techniques for Manufacturing Flexible Coils on Textiles for Inductive Power Transfer," *IEEE Sensors Journal*, vol. 02, no. c, pp. 1–1, 2018. [Online]. Available: <http://ieeexplore.ieee.org/document/8265161/>
- [203] I. Ortego-Isasa, K. P. Benli, F. Casado, J. I. Sancho, and D. Valderas, "Topology Analysis of Wireless Power Transfer Systems Manufactured Via Inkjet Printing Technology," *IEEE Transactions on Industrial Electronics*, vol. 64, no. 10, pp. 7749–7757, 2017.
- [204] C. R. Sullivan and L. Beghou, "Design methodology for a high-Q self-resonant coil for medical and wireless-power applications," *2013 IEEE 14th Workshop on Control and Modeling for Power Electronics, COMPEL 2013*, 2013.
- [205] Q. Li and Y. C. Liang, "An Inductive Power Transfer System with a High-Q Resonant Tank for Mobile Device Charging," *IEEE Transactions on Power Electronics*, vol. 30, no. 11, pp. 6203–6212, 2015.
- [206] A. L. Stein, P. A. Kyaw, and C. R. Sullivan, "High-Q self-resonant structure for wireless power transfer," *Conference Proceedings - IEEE Applied Power Electronics Conference and Exposition - APEC*, pp. 3723–3729, 2017.

- [207] A. L. Stein, P. A. Kyaw, J. Feldman-Stein, and C. R. Sullivan, "Thin self-resonant structures with a high-Q for wireless power transfer," *Conference Proceedings - IEEE Applied Power Electronics Conference and Exposition - APEC*, vol. 2018-March, pp. 1044–1051, 2018.
- [208] A. L. Stein, P. A. Kyaw, and C. R. Sullivan, "Wireless Power Transfer Utilizing a High-Q Self-Resonant Structure," *IEEE Transactions on Power Electronics*, vol. 8993, no. c, pp. 1–14, 2018.
- [209] R. W. Pryor, *Multiphysics Modeling using COMSOL*. Sudbury, Massachusetts: Jones and Bartlett Publishers, 2005.
- [210] E. Ekmekçi and G. Turhan-Sayan, "Investigation of effective permittivity and permeability for a novel V-shaped metamaterial using simulated S-parameters," *5th International Conference on Electrical and Electronics Engineering*, 2007.
- [211] Z. Hong, C. Zhao, X. Luo, Z. Huang, H. Zhu, and S. Zhu, "Effective permeability measurement of μ -negative metamaterials using an inductance method," *22nd Microoptics Conference, MOC 2017*, vol. 2017-Novem, no. 1, pp. 202–203, 2017.
- [212] C. Y. Liou, C. J. Kuo, S. S. Lin, and S. G. Mao, "Printed spiral metamaterial resonators for wireless powering system with proximal metal plates," *2015 IEEE International Symposium on Radio-Frequency Integration Technology, RFIT 2015 - Proceedings*, vol. 2, no. c, pp. 70–72, 2016.
- [213] T. Batra, E. Schaltz, and S. Ahn, "Effect of ferrite addition above the base ferrite on the coupling factor of wireless power transfer for vehicle applications," *Journal of Applied Physics*, vol. 117, no. 17, pp. 1–5, 2015.
- [214] S. C. Tang, S. Y. R. Hui, and H. S. H. Chung, "Evaluation of the shielding effects on printed-circuit-board transformers using ferrite plates and copper sheets," *IEEE Transactions on Power Electronics*, vol. 17, no. 6, pp. 1080–1088, 2002.
- [215] B. Tushar and S. Erik, "Magnetic emissions reduction by varying secondary side capacitor for ferrite geometry based series-parallel topology wireless power transfer to vehicles," *PCIM Europe Conference Proceedings*, pp. 1392–1400, 2014.
- [216] C. Stergiou and V. Zaspalis, "Impact of ferrite shield properties on the low-power Inductive Power Transfer," *IEEE Transactions on Magnetics*, vol. 02, no. c, pp. 1–1, 2016. [Online]. Available: <http://ieeexplore.ieee.org/lpdocs/epic03/wrapper.htm?arnumber=7422785>
- [217] X. Shi, C. Qi, M. Qu, S. Ye, G. Wang, L. Sun, and Z. Yu, "Effects of coil shapes on wireless power transfer via magnetic resonance coupling," *Journal of Electromagnetic Waves and Applications*, vol. 28, no. 11, pp. 1316–1324, jul 2014. [Online]. Available: <https://www.tandfonline.com/doi/full/10.1080/09205071.2014.919879>
- [218] N. Sokal and A. Sokal, "Class E - A new class of high-efficiency tuned single-ended switching power amplifiers," *IEEE Journal of Solid-State Circuits*, vol. 10, no. 3, pp. 168–176, 1975.
- [219] S. Keeping, "A Review of Zero-Voltage Switching and its Importance to Voltage Regulation," 2014. [Online]. Available: <https://www.digikey.com/en/articles/techzone/2014/aug/a-review-of-zero-voltage-switching-and-its-importance-to-voltage-regulation>
- [220] M. K. Kazimierczuk and J. Jwik, "Resonant dc/dc Converter with Class-E Inverter and Class-E Rectifier," *IEEE Transactions on Industrial Electronics*, vol. 36, no. 4, pp. 468–478, 1989.
- [221] S. Kee, I. Aoki, A. Hajimiri, and D. Rutledge, "The class-E/F family of ZVS switching amplifiers," *IEEE Transactions on Microwave Theory and Techniques*, vol. 51, no. 6, pp. 1677–1690, jun 2003. [Online]. Available: <http://ieeexplore.ieee.org/document/1201800/>

- [222] S. Aldhafer, D. C. Yates, and P. D. Mitcheson, "Design and Development of a Class EF2 Inverter and Rectifier for Multimegahertz Wireless Power Transfer Systems," *IEEE Transactions on Power Electronics*, vol. 31, no. 12, pp. 8138–8150, dec 2016. [Online]. Available: <http://ieeexplore.ieee.org/document/7445230/>
- [223] S. Aldhafer, P. D. Mitcheson, and D. C. Yates, "Load-independent Class EF inverters for inductive wireless power transfer," in *2016 IEEE Wireless Power Transfer Conference (WPTC)*, no. 1. IEEE, may 2016, pp. 1–4. [Online]. Available: <http://ieeexplore.ieee.org/document/7498864/>
- [224] S. Aldhafer, P. D. Mitcheson, J. M. Arteaga, G. Kkelis, and D. C. Yates, "Light-Weight Wireless Power Transfer for Mid-Air Charging of Drones," *2017 11th European Conference on Antennas and Propagation (EuCAP)*, pp. 336–340, 2017.
- [225] S. Aldhafer, D. C. Yates, and P. D. Mitcheson, "Load-Independent Class E/EF Inverters and Rectifiers for MHz-Switching Applications," *IEEE Transactions on Power Electronics*, vol. 33, no. 10, pp. 8270–8287, oct 2018.
- [226] R. Zulinski and K. Grady, "Load-independent class E power inverters. I. Theoretical development," *IEEE Transactions on Circuits and Systems*, vol. 37, no. 8, pp. 1010–1018, 1990. [Online]. Available: <http://ieeexplore.ieee.org/document/56074/>
- [227] R. Zulinski, J. Mandojana, and K. Herman, "The infeasibility of self-regulating constant-current-fed class E power inverters," *IEEE Transactions on Circuits and Systems*, vol. 37, no. 4, pp. 558–561, apr 1990. [Online]. Available: <http://ieeexplore.ieee.org/document/52762/>
- [228] R. Zulinski, K. Herman, and J. Mandojana, "The infeasibility of constant output power in a constant-current-fed class-E power inverter," *IEEE Transactions on Industrial Electronics*, vol. 38, no. 1, pp. 81–82, apr 1991. [Online]. Available: <http://ieeexplore.ieee.org/document/103490/>
- [229] L. Roslaniec, A. S. Jurkov, A. Al Bastami, and D. J. Perreault, "Design of single-switch inverters for variable resistance/load modulation operation," *IEEE Transactions on Power Electronics*, vol. 30, no. 6, pp. 3200–3214, 2015.
- [230] H. Johnson, *High-Speed Signal Propagation[c] Advanced Black Magic*, 2005.
- [231] S. Aldhafer, D. C. Yates, and P. D. Mitcheson, "Modeling and Analysis of Class EF and Class E/F Inverters with Series-Tuned Resonant Networks," *IEEE Transactions on Power Electronics*, vol. 31, no. 5, pp. 3415–3430, 2016.

Appendices

A Mathematical Derivations for Class E Inverter

Consider the following circuit for analysis:

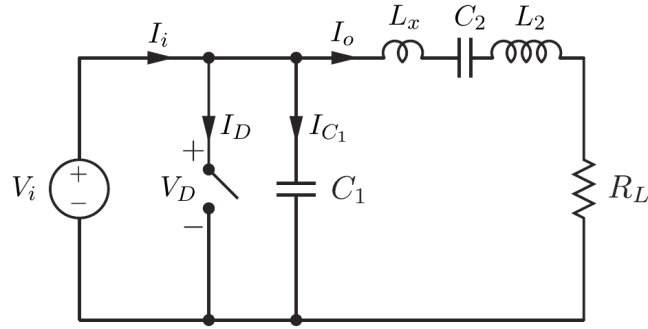


Figure A.1: A Class E inverter circuit

under ideal operating and design conditions, the output current I_o can be defined by

$$I_o(\omega t) = I_m \sin(\omega t + \phi) \quad (\text{A.1})$$

where I_m is the amplitude of the output current wave, ωt is the period of the signal between 0 and 2π , and ϕ is the phase shift with respect to the switch's open-close cycle.

For $0 \leq \omega t < \pi$, the switch is closed and conducting,

$\therefore V_D(\omega t) = 0$, $I_{C_1}(\omega t) = 0$ and the drain current $I_D(\omega t)$ is simply the sum of I_i and $I_o(\omega t)$,

$$\therefore I_D(\omega t) = I_i + I_m \sin(\omega t + \phi) \quad (\text{A.2})$$

For $\pi \leq \omega t < 2\pi$ the switch is open and $I_D(\omega t) = 0$. Therefore, current begins to flow into C_1 which is defined by

$$I_{C_1}(\omega t) = I_i + I_m \sin(\omega t + \phi) \quad (\text{A.3})$$

This causes a voltage to form across C_1 in time, which equals the switch voltage $V_D(\omega t)$,

$$V_D(\omega t) = \frac{1}{\omega C_1} \int_{\pi}^{\omega t} I_{C_1}(\omega t) d\omega t + V_D(\pi) \quad (\text{A.4})$$

Under the assumption of ZVS, $V_D(\pi) = 0$. Integrating with respect to ωt ,

$$\begin{aligned} V_D(\omega t) &= \frac{1}{\omega C_1} \int_{\pi}^{\omega t} I_i + I_m \sin(\omega t + \phi) d\omega t \\ &= \frac{1}{\omega C_1} \left[I_i \omega t - I_m \cos(\omega t + \phi) \right]_{\pi}^{\omega t} \\ &= \frac{1}{\omega C_1} \left(I_i \omega t - I_i \pi - I_m \cos(\omega t + \phi) + I_m \cos(\pi + \phi) \right) \end{aligned}$$

and using $\cos(A + B) = \cos A \cos B - \sin A \sin B$,

$$V_D(\omega t) = \frac{1}{\omega C_1} \left(I_i(\omega t - \pi) - I_m(\cos(\omega t + \phi) + \cos \phi) \right) \quad (\text{A.5})$$

I_m can now be found from the ZVS condition when $\omega t = 2\pi$,

$$V_D(2\pi) = \frac{1}{\omega C_1} \left(I_i(2\pi - \pi) - I_m(\cos(2\pi + \phi) + \cos \phi) \right)$$

again using $\cos(A + B) = \cos A \cos B - \sin A \sin B$,

$$0 = \frac{1}{\omega C_1} \left(I_i \pi - I_m(\cos \phi + \cos \phi) \right)$$

$$0 = I_i \pi - I_m 2 \cos \phi$$

$$\therefore I_m = \frac{I_i \pi}{2 \cos \phi} \quad (\text{A.6})$$

The phase shift ϕ can now be found by substituting A.6 into A.5 and applying the ZDVS condition when $\omega t = 2\pi$,

$$\begin{aligned}
V_D(\omega t) &= \frac{1}{\omega C_1} \left(I_i(\omega t - \pi) - \frac{I_i \pi}{2 \cos \phi} (\cos(\omega t + \phi) + \cos \phi) \right) \\
&= \frac{1}{\omega C_1} \left(I_i(\omega t - \pi) - \frac{I_i \pi}{2 \cos \phi} \cos(\omega t + \phi) + \frac{I_i \pi}{2} \right) \\
&= \frac{I_i}{\omega C_1} \left(\omega t - \pi - \frac{\pi}{2 \cos \phi} \cos(\omega t + \phi) + \frac{\pi}{2} \right) \\
&= \frac{I_i}{\omega C_1} \left(\omega t - \frac{3\pi}{2} - \frac{\pi}{2 \cos \phi} \cos(\omega t + \phi) \right) \\
\therefore \frac{dV_D(\omega t)}{d\omega t} &= \frac{I_i}{\omega C_1} \left(1 + \frac{\pi}{2 \cos \phi} \sin(\omega t + \phi) \right) \\
\left. \frac{dV_D(\omega t)}{d\omega t} \right|_{\omega t=2\pi} &= 0 \text{ for ZDVS} \\
0 &= \frac{I_i}{\omega C_1} \left(1 + \frac{\pi}{2 \cos \phi} \sin(2\pi + \phi) \right) \\
&\text{and using } \sin(A + B) = \sin A \cos B + \cos A \sin B, \\
0 &= \frac{I_i}{\omega C_1} \left(1 + \frac{\pi}{2 \cos \phi} \sin \phi \right) \\
0 &= 1 + \frac{\pi \sin \phi}{2 \cos \phi} \\
\therefore \tan \phi &= -\frac{2}{\pi}, \quad \phi \approx 0.5669 \text{ rad} \tag{A.7}
\end{aligned}$$

Substituting A.7 into A.6,

$$\begin{aligned}
I_m &= \frac{I_i \pi}{2 \cos(\tan^{-1}(-2/\pi))} \\
&= \frac{I_i \pi \sqrt{\pi^2 + 4}}{2 \pi} \\
\therefore I_m &= \frac{\sqrt{\pi^2 + 4}}{2} I_i, \quad I_m \approx 1.8621 I_i \tag{A.8}
\end{aligned}$$

Additionally, I_i can be determined in terms of the input voltage V_i . This DC voltage is the average of the switch's drain voltage over the whole period ωt , given by

$$V_i = \frac{1}{2\pi} \int_0^{2\pi} V_D(\omega t) d\omega t \tag{A.9}$$

It was previously determined that

$$V_D(\omega t) = \begin{cases} 0 & \text{for } 0 \leq \omega t < \pi \\ \frac{I_i}{\omega C_1} \left(\omega t - \frac{3\pi}{2} - \frac{\pi}{2 \cos \phi} \cos(\omega t + \phi) \right) & \text{for } \pi \leq \omega t < 2\pi \end{cases}$$

$$\begin{aligned} \therefore V_i &= \frac{1}{2\pi} \int_{\pi}^{2\pi} \frac{I_i}{\omega C_1} \left(\omega t - \frac{3\pi}{2} - \frac{\pi}{2 \cos \phi} \cos(\omega t + \phi) \right) d\omega t \\ &= \frac{I_i}{2\pi \omega C_1} \left[\frac{\omega t^2}{2} - \frac{3\pi \omega t}{2} - \frac{\pi}{2 \cos \phi} \sin(\omega t + \phi) \right]_{\pi}^{2\pi} \end{aligned}$$

and using $\sin(A + B) = \sin A \cos B + \cos A \sin B$,

$$\begin{aligned} &= \frac{I_i}{2\pi \omega C_1} \left[\frac{\omega t^2}{2} - \frac{3\pi \omega t}{2} - \frac{\pi \sin \omega t \cos \phi}{2 \cos \phi} - \frac{\pi \cos \omega t \sin \phi}{2 \cos \phi} \right]_{\pi}^{2\pi} \\ &= \frac{I_i}{2\pi \omega C_1} \left[\frac{\omega t^2}{2} - \frac{3\pi \omega t}{2} - \frac{\pi \sin \omega t}{2} + \cos \omega t \right]_{\pi}^{2\pi} \\ &= \frac{I_i}{2\pi \omega C_1} \left(-\frac{2\pi^2}{2} + 1 + \frac{2\pi^2}{2} + 1 \right) \\ &= \frac{2I_i}{2\pi \omega C_1} \end{aligned}$$

$$\therefore I_i = \pi \omega C_1 V_i \quad (\text{A.10})$$

Substituting A.10 into A.8 gives,

$$I_m = \frac{\sqrt{\pi^2 + 4}}{2} \pi \omega C_1 V_i \quad (\text{A.11})$$

Normalising the equations for I_D , I_{C_1} , I_o and V_D with respect to I_i and V_i gives the characteristic current and voltage waveforms over ωt for the Class E Inverter design,

$$\frac{I_D(\omega t)}{I_i} = \begin{cases} 1 + \frac{\sqrt{\pi^2+4}}{2} \sin(\omega t + \phi) & \text{for } 0 \leq \omega t < \pi \\ 0 & \text{for } \pi \leq \omega t < 2\pi \end{cases}$$

$$\frac{I_{C_1}(\omega t)}{I_i} = \begin{cases} 0 & \text{for } 0 \leq \omega t < \pi \\ 1 + \frac{\sqrt{\pi^2+4}}{2} \sin(\omega t + \phi) & \text{for } \pi \leq \omega t < 2\pi \end{cases}$$

$$\frac{I_o(\omega t)}{I_i} = \frac{\sqrt{\pi^2+4}}{2} \sin(\omega t + \phi)$$

$$\frac{V_D(\omega t)}{V_i} = \begin{cases} 0 & \text{for } 0 \leq \omega t < \pi \\ \pi \left(\omega t - \frac{3\pi}{2} - \frac{\pi}{2} \cos \omega t - \sin \omega t \right) & \text{for } \pi \leq \omega t < 2\pi \end{cases}$$

The component values of C_1 , C_2 , L_2 , L_x and R_L for this optimum switching need to be determined. The values for C_2 and L_2 can simply be chosen such that, at resonance (i.e. f_s), the voltage across the them will be zero. Assuming, ideal switching, where all the input power is delivered to the load,

$$P_i = P_o = \frac{1}{2} I_m^2 R_L$$

$$\therefore V_i I_i = \frac{1}{2} I_m^2 R_L$$

$$\frac{V_i}{I_i} = R_i = \frac{1}{2} \left(\frac{I_m}{I_i} \right)^2 R_L$$

using A.8, $\frac{V_i}{I_i} = R_i = \frac{\pi^2 + 4}{8} R_L$

where R_i is the input impedance of the inverter. From A.10,

$$\frac{V_i}{I_i} = \frac{1}{\pi \omega C_1}$$

$$\therefore \frac{\pi^2 + 4}{8} R_L = \frac{1}{\pi \omega C_1}$$

$$\therefore C_1 = \frac{8}{\pi(\pi^2 + 4)\omega R_L} \approx \frac{0.1836}{\omega R_L}$$

To find L_x , the output voltage V_o will need to be determined. During operation at f_s , L_2 and C_2 will act as a short circuit. Therefore, using $V = IR$, the voltages across the series connected

R_L and L_x are given by

$$V_{R_L} = I_m R_L \sin(\omega t + \phi)$$

and

$$V_{L_x} = L_x \frac{d}{dt} \left[I_m \sin(\omega t + \phi) \right]$$

$$\begin{aligned} \therefore V_o &= V_{R_L} + V_{L_x} \\ &= I_m R_L \sin(\omega t + \phi) + I_m \omega L_x \cos(\omega t + \phi) \end{aligned}$$

Hence V_o can be viewed as a Fourier Trigonometric Series of the form

$$\frac{a_o}{2} + \sum_{k=1}^{\infty} (a_k \cos kx + b_k \sin kx)$$

where

$$a_k = \frac{1}{\pi} \int_0^{2\pi} f(x) \cos kx \, dx$$

$$b_k = \frac{1}{\pi} \int_0^{2\pi} f(x) \sin kx \, dx$$

where k are the integer multiples of the fundamental frequency given by f_s . V_o is equal to $V_D(\omega t)$, thus

$$a_k = I_m \omega L_x = \frac{1}{\pi} \int_0^{2\pi} V_D(\omega t) \cos(k\omega t + \phi) \, d\omega t$$

$$b_k = I_m R_L = \frac{1}{\pi} \int_0^{2\pi} V_D(\omega t) \sin(k\omega t + \phi) \, d\omega t$$

and due to the L_2C_2 resonant tank, V_o will be only be equal to the fundamental component of V_D , therefore $k = 1$. The voltage across L_x will be given by

$$\begin{aligned}
V_{L_x} &= \frac{1}{\pi} \int_{\pi}^{2\pi} V_i \pi \left(\omega t - \frac{3\pi}{2} - \frac{\pi}{2} \cos \omega t - \sin \omega t \right) \cos(\omega t + \phi) d\omega t \\
&= \frac{V_i}{4\sqrt{\pi^2 + 4}} \left[\pi^2 \omega t + 4\omega t - 4\pi \sin \omega t + 6\pi^2 \sin \omega t - 8 \sin \omega t \right. \\
&\quad \left. - 2 \sin 2\omega t - 2\pi \cos 2\omega t + \left(8(\omega t - 2\pi) + \pi^2 \sin \omega t \right) \cos \omega t \right]_{\pi}^{2\pi} \\
&= \frac{\pi(\pi^2 - 4)}{4\sqrt{\pi^2 + 4}} V_i \\
\omega L_x &= \frac{V_{L_x}}{I_m} = \frac{\frac{\pi(\pi^2 - 4)}{4\sqrt{\pi^2 + 4}} V_i}{\frac{\pi^2 + 4}{2} \pi \omega C_1} = \frac{\pi^2 - 4}{2(\pi^2 + 4)\omega C_1} \\
\therefore L_x &= \frac{\pi^2 - 4}{2(\pi^2 + 4)\omega^2 C_1} \approx \frac{0.2116}{\omega^2 C_1}
\end{aligned}$$

B Mathematical Derivations for Class EF Inverter

Consider the following circuit for analysis:

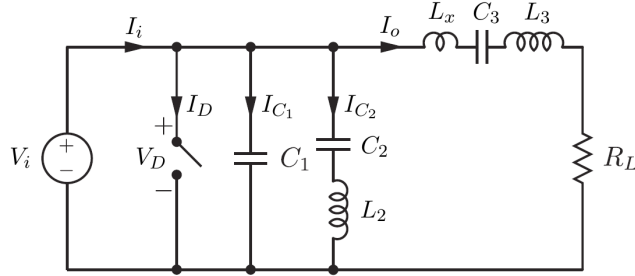


Figure B.1: A Class EF inverter circuit

The output current I_o will once again be sinusoidal due through $L_3 C_3$,

$$I_o(\omega t) = I_m \sin(\omega t + \phi) \quad (\text{B.1})$$

where I_m is the amplitude of the output current wave, ωt is the period of the signal between 0 and 2π , and ϕ is the phase shift with respect to the switch's open-close cycle.

For $0 \leq \omega t < 2\pi D$, the switch is closed and conducting.

$\therefore V_D(\omega t) = 0$, hence $V_{L_2 C_2} = 0$. Since the voltage across $L_2 C_2$ is zero, this resonant network

will become a source free, undamped system. From the constitute relations,

$$V_{L_2C_2} = 0 = \omega L_2 \frac{dI_{C_2}(\omega t)}{d\omega t} + \frac{1}{\omega C} \int_0^{2\pi D} I_{C_2}(\omega t) d\omega t$$

Normalising with respect to I_i and differentiating with respect to ωt gives a second order differential equation of the following form,

$$0 = \frac{d^2 \frac{I_{C_2}(\omega t)}{I_i}}{d\omega t^2} + \frac{1}{\omega^2 L_2 C_2} \frac{I_{C_2}(\omega t)}{I_i}$$

with the following general solution,

$$\frac{I_{C_2}(\omega t)}{I_i} = A_1 \cos(q_1 \omega t) + B_1 \sin(q_1 \omega t) \quad (\text{B.2})$$

where A_1 and B_1 are coefficients to be determined from the initial boundary conditions and $q_1 = \frac{1}{\omega \sqrt{L_2 C_2}}$. Furthermore, $I_{C_1}(\omega t) = 0$, therefore the drain current $I_D(\omega t)$ is simply the sum of I_i , $I_{C_2}(\omega t)$ and $I_o(\omega t)$.

$$\therefore \frac{I_D(\omega t)}{I_i} = 1 - A_1 \cos(q_1 \omega t) - B_1 \sin(q_1 \omega t) - \frac{I_m}{I_i} \sin(\omega t + \phi) \quad (\text{B.3})$$

For $2\pi D \leq \omega t < 2\pi$, the switch is open and $I_D(\omega t) = 0$. Current through L_2C_2 is now

$$\begin{aligned} I_{C_2}(\omega t) &= I_i - I_o - I_{C_1}(\omega t) \\ &= I_i - I_m \sin(\omega t + \phi) - \omega C_1 \frac{dV_D(\omega t)}{d\omega t} \end{aligned} \quad (\text{B.4})$$

Likewise,

$$\begin{aligned} V_D(\omega t) &= V_{L_2C_2} + V_{C_2}(2\pi D) \\ &= \omega L_2 \frac{dI_{C_2}(\omega t)}{d\omega t} + \frac{1}{\omega C_2} \int_{2\pi D}^{2\pi} I_{C_2}(\omega t) + V_{C_2}(2\pi D) \\ \therefore \frac{dV_{C_2}(2\pi D)}{d\omega t} &= \omega L_2 \frac{d^2 I_{C_2}(\omega t)}{d\omega t^2} + \frac{1}{\omega C_2} I_{C_2}(\omega t) \end{aligned}$$

Substituting into B.4

$$\begin{aligned}
I_{C_2}(\omega t) &= I_i - I_m \sin(\omega t + \phi) - \omega^2 L_2 C_1 \frac{d^2 I_{C_2}(\omega t)}{d\omega t^2} - \frac{C_1}{C_2} I_{C_2}(\omega t) \\
\therefore I_i - I_m \sin(\omega t + \phi) &= \omega^2 L_2 C_1 \frac{d^2 I_{C_2}(\omega t)}{d\omega t^2} + \left(1 + \frac{C_1}{C_2}\right) I_{C_2}(\omega t) \\
\frac{I_i - I_m \sin(\omega t + \phi)}{\omega^2 L_2 C_1} &= \frac{d^2 I_{C_2}(\omega t)}{d\omega t^2} + \left(\frac{C_2 + C_1}{\omega^2 L_2 C_1 C_2}\right) I_{C_2}(\omega t)
\end{aligned}$$

which is a second order differential equation with a forced response. The solution may be expressed as

$$I_{C_2}(\omega t) = I_{C_2}(\omega t)_\eta + I_{C_2}(\omega t)_\rho$$

where $I_{C_2}(\omega t)_\eta$ is the complementary solution, being that of an undamped oscillator similar to B.2 and $I_{C_2}(\omega t)_\rho$ is known as the particular solution, which when coupled with $I_{C_2}(\omega t)_\eta$, gives the general solution sought for the second order differential equation. Finding $I_{C_2}(\omega t)_\rho$ is non-trivial and would normally require the application of *Methods of Undetermined coefficients* or *Variation of Parameters* method. For this type of forces response, it has been shown [231] that the general solution when normalised with respect to I_i is

$$\frac{I_{C_2}(\omega t)}{I_i} = A_2 \cos(q_2 \omega t) + B_2 \sin(q_2 \omega t) - \frac{q_2^2 \rho}{q_2^2 - 1} \sin(\omega t + \phi) + \frac{1}{k + 1} \quad (\text{B.5})$$

where

$$k = \frac{C_1}{C_2} \quad ; \quad q_2 = \sqrt{\frac{C_1 + C_2}{L_2 C_1 C_2}} = q_1 \sqrt{\frac{k + 1}{k}} \quad ; \quad \rho = \frac{C_2}{C_1 + C_2} \frac{I_m}{I_i} \quad (\text{B.6})$$

and A_2 and B_2 as with B.2 are coefficients to be determined from the initial boundary conditions. A_1, A_2, B_1, B_2 are four unknowns that can be determined simultaneously from the continuity equations of voltage and current for linear circuits at the switch opening and closing points; i.e. voltage across a capacitor and current through an inductor can not change instantaneously and hence are continuous in time.

$$\therefore I_{C_2}(2\pi D^-) = I_{C_2}(2\pi D^+) \quad \text{and} \quad I_{C_2}(0) = I_{C_2}(2\pi) \quad \text{where}$$

$$\begin{aligned}
I_{C_2}(\omega t) \Big|_{0 \leq \omega t < 2\pi D} &= A_1 \cos(q_1 \omega t) + B_1 \sin(q_1 \omega t) \\
I_{C_2}(\omega t) \Big|_{2\pi D \leq \omega t < 2\pi} &= A_2 \cos(q_2 \omega t) + B_2 \sin(q_2 \omega t) - \frac{q_2^2 \rho}{q_2^2 - 1} \sin(\omega t + \phi) + \frac{1}{k + 1}
\end{aligned}$$

Likewise

$$\left. \frac{dI_{C_2}(\omega t)}{d\omega t} \right|_{\omega t=2\pi D^+} = \left. \frac{dI_{C_2}(\omega t)}{d\omega t} \right|_{\omega t=2\pi D^-} \quad \text{and} \quad \left. \frac{dI_{C_2}(\omega t)}{d\omega t} \right|_{\omega t=0} = \left. \frac{dI_{C_2}(\omega t)}{d\omega t} \right|_{\omega t=2\pi}$$

$$\therefore \left. \frac{dI_{C_2}(\omega t)}{d\omega t} \right|_{0 \leq \omega t < 2\pi D} = -A_1 q_1 \sin(q_1 \omega t) + B_1 q_1 \cos(q_1 \omega t)$$

and

$$\left. \frac{dI_{C_2}(\omega t)}{d\omega t} \right|_{2\pi D \leq \omega t < 2\pi} = -A_2 q_2 \sin(q_2 \omega t) + B_2 q_2 \cos(q_2 \omega t) - \frac{q_2^2 \rho}{q_2^2 - 1} \cos(\omega t + \phi)$$

Solving for $I_{C_2}(0) = I_{C_2}(2\pi)$

$$A_1 = A_2 \cos(2\pi q_2) + B_2 \sin(2\pi q_2) - \frac{q_2^2 \rho}{q_2^2 - 1} \sin \phi + \frac{1}{k+1} \quad (\text{B.7})$$

Solving for $\left. \frac{dI_{C_2}(\omega t)}{d\omega t} \right|_{\omega t=0} = \left. \frac{dI_{C_2}(\omega t)}{d\omega t} \right|_{\omega t=2\pi}$

$$B_1 = -A_2 \frac{q_2}{q_1} \sin(2\pi q_2) + B_2 \frac{q_2}{q_1} \cos(2\pi q_2) - \frac{q_2^2 \rho}{q_1 (q_2^2 - 1)} \cos \phi \quad (\text{B.8})$$

Solving for $I_{C_2}(2\pi D^-) = I_{C_2}(2\pi D^+)$

$$\begin{aligned} & A_1 \cos(2\pi D q_1) + B_1 \sin(2\pi D q_1) \\ &= A_2 \cos(2\pi D q_2) + B_2 \sin(2\pi D q_2) - \frac{q_2^2 \rho}{q_2^2 - 1} \sin(2\pi D + \phi) + \frac{1}{k+1} \end{aligned} \quad (\text{B.9})$$

and solving for $\left. \frac{dI_{C_2}(\omega t)}{d\omega t} \right|_{\omega t=2\pi D^+} = \left. \frac{dI_{C_2}(\omega t)}{d\omega t} \right|_{\omega t=2\pi D^-}$

$$\begin{aligned} & A_1 q_1 \sin(2\pi D q_1) - B_1 q_1 \cos(2\pi D q_1) \\ &= A_2 q_2 \sin(2\pi D q_2) - B_2 q_2 \cos(2\pi D q_2) + \frac{q_2^2 \rho}{q_2^2 - 1} \cos(2\pi D + \phi) \end{aligned} \quad (\text{B.10})$$

These equations can now be solved to give an analytical solution for A_1 , A_2 , B_1 , B_2 . The other two unknowns in this analysis are ϕ and ρ . To determine their values the conditions of ZVS and ZDVS will be applied to the open-close transition of the switch, i.e at $\omega t = 2\pi$.

$$V_D(\omega t) = \frac{1}{\omega C_1} \int_{2\pi D}^{\omega t} I_{C_1}(\omega t) d\omega t$$

where $I_{C_1}(\omega t) = I_i - I_o - I_{C_2}(\omega t)$

$$= I_i - I_m \sin(\omega t + \phi) - I_i \left[A_2 \cos(q_2 \omega t) + B_2 \sin(q_2 \omega t) - \frac{q_2^2 \rho}{q_2^2 - 1} \sin(\omega t + \phi) + \frac{1}{k+1} \right]$$

$$\begin{aligned} \therefore V_D(\omega t) &= \frac{I_i}{\omega C_1} \int_{2\pi D}^{\omega t} 1 - \frac{I_m}{I_i} \sin(\omega t + \phi) - A_2 \cos(q_2 \omega t) - B_2 \sin(q_2 \omega t) \\ &\quad + \frac{q_2^2 \rho}{q_2^2 - 1} \sin(\omega t + \phi) - \frac{1}{k+1} d\omega t \\ &= \frac{I_i}{\omega C_1} \left[\omega t + \frac{I_m}{I_i} \cos(\omega t + \phi) - \frac{A_2}{q_2} \sin(q_2 \omega t) + \frac{B_2}{q_2} \cos(q_2 \omega t) \right. \\ &\quad \left. - \frac{q_2^2 \rho}{q_2^2 - 1} \cos(\omega t + \phi) - \frac{\omega t}{k+1} \right]_{2\pi D}^{\omega t} \end{aligned}$$

$$\begin{aligned} \text{and } \rho &= \frac{C_2}{C_1 + C_2} \frac{I_m}{I_i} \\ &= \frac{1}{\frac{C_1}{C_2} + 1} \frac{I_m}{I_i} \\ &= \frac{1}{k+1} \frac{I_m}{I_i} \\ \frac{I_m}{I_i} &= \rho(k+1) \end{aligned} \tag{B.11}$$

$$\begin{aligned} \therefore V_D(\omega t) &= \frac{I_i}{\omega C_1} \left(\frac{k(\omega t - 2\pi D)}{k+1} + \rho(\cos(2\pi D + \phi) - \cos(\omega t + \phi)) \left(\frac{q_2^2}{q_2^2 - 1} - (k+1) \right) \right. \\ &\quad \left. + \frac{A_2}{q_2} (\sin(2\pi D q_2) - \sin(q_2 \omega t)) + \frac{B_2}{q_2} (\cos(q_2 \omega t) - \cos(2\pi D q_2)) \right) \end{aligned}$$

From ZVS, $V_D(2\pi) = 0$, therefore,

$$\begin{aligned} 0 &= 2\pi \frac{k}{k+1} (1 - D) + \rho(\cos(2\pi D + \phi) - \cos \phi) \left(\frac{q_2^2}{q_2^2 - 1} - (k+1) \right) \\ &\quad + \frac{A_2}{q_2} (\sin(2\pi D q_2) - \sin(2\pi q_2)) + \frac{B_2}{q_2} (\cos(2\pi q_2) - \cos(2\pi D q_2)) \end{aligned} \tag{B.12}$$

and from ZDVS, $\left. \frac{dV_D(\omega t)}{d\omega t} \right|_{\omega t=2\pi} = 0$, therefore

$$\begin{aligned}
\frac{dV_D(\omega t)}{d\omega t} &= \frac{I_{C_1}(\omega t)}{\omega C_1} \\
\therefore 0 &= I_{C_1}(2\pi) \\
&= 1 - \frac{I_m}{I_i} \sin(2\pi + \phi) - A_2 \cos(2\pi q_2) - B_2 \sin(2\pi q_2) \\
&\quad + \frac{q_2^2 \rho}{q_2^2 - 1} \sin(2\pi + \phi) - \frac{1}{k+1} \\
&= 1 - \rho(k+1) \sin \phi - A_2 \cos(2\pi q_2) - B_2 \sin(2\pi q_2) \\
&\quad + \frac{q_2^2 \rho}{q_2^2 - 1} \sin \phi - \frac{1}{k+1} \\
\therefore 0 &= \frac{k}{k+1} + \rho \sin \phi \left(\frac{q_2^2}{q_2^2 - 1} - (k+1) \right) - A_2 \cos(2\pi q_2) - B_2 \sin(2\pi q_2) \quad (\text{B.13})
\end{aligned}$$

As previously demonstrated I_i can be given in terms of the input voltage V_i . As before, this is the average of the switch's drain voltage over the whole period of ωt ,

$$\begin{aligned}
V_i &= \frac{1}{2\pi} \int_0^{2\pi} V_D(\omega t) d\omega t \\
\therefore &= \frac{I_i}{2\pi\omega C_1} \int_0^{2\pi} \int_{2\pi D}^{2\pi} \frac{I_{C_1}(\omega t)}{I_i} d\omega t d\omega t
\end{aligned}$$

Normalising $V_D(\omega t)$ with respect to V_i ,

$$\frac{V_D(\omega t)}{V_i} = 2\pi \frac{\alpha}{\beta}$$

where,

$$\begin{aligned}
\alpha &= \frac{k(\omega t - 2\pi D)}{k+1} + \rho(\cos(2\pi D + \phi) - \cos(\omega t + \phi)) \left(\frac{q_2^2}{q_2^2 - 1} - (k+1) \right) \\
&\quad + \frac{A_2}{q_2} (\sin(2\pi D q_2) - \sin(q_2 \omega t)) + \frac{B_2}{q_2} (\cos(q_2 \omega t) - \cos(2\pi D q_2))
\end{aligned}$$

and

$$\beta = \int_0^{2\pi} \int_{2\pi D}^{2\pi} \frac{I_{C_1}(\omega t)}{I_i} d\omega t d\omega t$$

In summary, the waveforms for this Class EF inverter design are given by

$$\frac{I_D(\omega t)}{I_i} = \begin{cases} 1 - A_1 \cos(q_1 \omega t) - B_1 \sin(q_1 \omega t) - \rho(k+1) \sin(\omega t + \phi) & \text{for } 0 \leq \omega t < 2\pi D \\ 0 & \text{for } 2\pi D \leq \omega t < 2\pi \end{cases}$$

$$\frac{I_o(\omega t)}{I_i} = \rho(k+1) \sin(\omega t + \phi)$$

$$\frac{V_D(\omega t)}{V_i} = \begin{cases} 0 & \text{for } 0 \leq \omega t < 2\pi D \\ 2\pi \frac{\alpha}{\beta} & \text{for } 2\pi D \leq \omega t < 2\pi \end{cases}$$

and for a given k , q_1 and D , equations B.7 - B.13 can be solved numerically to give values for A_1 , A_2 , B_1 , B_2 , ρ and ϕ .

Finally, the component values of the circuit would need to be determined to realise this inverter operation. C_1 , C_2 and L_2 can easily be calculated based on the desired values of q_1 and k . Likewise, the values of C_3 and L_3 are chosen in order to resonate with the switching frequency f_s . This leaves R_L and L_x , which as previously shown, can be found by determining the relationship between the input impedance R_i and R_L , and by finding the voltage across L_x and using $V = IR$. The DC input current I_i will be the average of the current through the switch over the period $0 \leq \omega t < 2\pi$,

$$\begin{aligned} \therefore I_i &= \frac{1}{2\pi} \int_0^{2\pi} I_D(\omega t) d\omega t \\ 1 &= \frac{1}{2\pi} \int_0^{2\pi} \frac{I_D(\omega t)}{I_i} d\omega t \\ &= \frac{1}{2\pi} \int_0^{2\pi D} 1 - A_1 \cos(q_1 \omega t) - B_1 \sin(q_1 \omega t) - \frac{I_m}{I_i} \sin(\omega t + \phi) d\omega t \\ &= \frac{1}{2\pi} \left[\omega t + \frac{1}{q_1} \left(B_1 \cos(q_1 \omega t) - A_1 \sin(q_1 \omega t) \right) + \frac{I_m}{I_i} \cos(\omega t + \phi) \right]_0^{2\pi D} \\ \frac{I_m}{I_i} &= \frac{2\pi(1-D) + \frac{A_1}{q_1} \sin(2\pi D q_1) + \frac{2B_1}{q_1} \sin^2(\pi D q_1)}{\cos(2\pi D + \phi) - \cos \phi} \end{aligned}$$

Once again, assuming ideal switching where all the input power is delivered to R_L ,

$$\begin{aligned}
P_i &= P_o = \frac{1}{2} I_m^2 R_L \\
\therefore V_i I_i &= \frac{1}{2} I_m^2 R_L \\
\frac{V_i}{I_i} &= R_i = \frac{1}{2} \left(\frac{I_m}{I_i} \right)^2 R_L \\
&= \frac{1}{2} \left(\frac{2\pi(1-D) + \frac{A_1}{q_1} \sin(2\pi D q_1) + \frac{2B_1}{q_1} \sin^2(\pi D q_1)}{\cos(2\pi D + \phi) - \cos \phi} \right)^2 R_L
\end{aligned}$$

Likewise,

$$\begin{aligned}
\frac{V_i}{I_i} &= \frac{1}{2\pi\omega C_1} \beta \tag{B.14} \\
\text{where } \beta &= \int_0^{2\pi} \int_{2\pi D}^{2\pi} \frac{I_{C_1}(\omega t)}{I_i} d\omega t d\omega t \\
\therefore \frac{1}{2\pi\omega C_1} \beta &= \frac{1}{2} \left(\frac{2\pi(1-D) + \frac{A_1}{q_1} \sin(2\pi D q_1) + \frac{2B_1}{q_1} \sin^2(\pi D q_1)}{\cos(2\pi D + \phi) - \cos \phi} \right)^2 R_L \\
C_1 &= \frac{\beta}{\pi\omega R_L} \left(\frac{\cos(2\pi D + \phi) - \cos \phi}{2\pi(1-D) + \frac{A_1}{q_1} \sin(2\pi D q_1) + \frac{2B_1}{q_1} \sin^2(\pi D q_1)} \right)^2
\end{aligned}$$

From Fourier Trigonometric Series, the voltage across L_x is

$$\begin{aligned}
V_{L_x} &= \frac{1}{\pi} \int_0^{2\pi} V_D(\omega t) \cos(\omega t + \phi) d\omega t \tag{B.15} \\
\omega L_x &= \frac{V_{L_x}}{I_m} \text{ and } V_D(\omega t) = \alpha \frac{I_i}{\omega C_1} \\
\therefore L_x &= \frac{\int_{2\pi D}^{2\pi} \alpha \cos(\omega t + \phi) d\omega t}{\pi\omega^2 C_1} \frac{\cos(2\pi D + \phi) - \cos \phi}{2\pi(1-D) + \frac{A_1}{q_1} \sin(2\pi D q_1) + \frac{2B_1}{q_1} \sin^2(\pi D q_1)} \\
\text{where } \alpha &= \frac{k(\omega t - 2\pi D)}{k+1} + \rho(\cos(2\pi D + \phi) - \cos(\omega t + \phi)) \left(\frac{q_2^2}{q_2^2 - 1} - (k+1) \right) \\
&\quad + \frac{A_2}{q_2} (\sin(2\pi D q_2) - \sin(q_2 \omega t)) + \frac{B_2}{q_2} (\cos(q_2 \omega t) - \cos(2\pi D q_2))
\end{aligned}$$

C MATLAB code for Class E and Class EF Waveforms

Class E plot and component code

```
1 res = 1000;
2 phi = atan(-2/pi);
3 Im = sqrt(pi^2 + 4)/2;
4 wta = 0:pi/res:2*pi;
5 wto = pi:pi/res:2*pi;
6 wtf = 0:pi/res:pi;
7
8 ID = 1 + Im*sin(wtf + phi);
9 IC = 1 + Im*sin(wto + phi);
10 Io = Im*sin(wta + phi);
11 VD = pi*(wto - (3*pi/2) - (pi/2)*cos(wto) - sin(wto));
12
13 IDp = [ID(1:size(ID,2)-1), zeros(1,res+1)];
14 VDp = [zeros(1,res), VD];
15 ICp = [zeros(1,res), IC];
16
17 [IDm, IDmid] = max(IDp, [], 2);
18 [VDm, VDmid] = max(VDp, [], 2);
19 [IoM, ~] = max(Io, [], 2);
20 [Iom, ~] = min(Io, [], 2);
21 [ICM, ~] = max(ICp, [], 2);
22 [ICm, ~] = min(ICp, [], 2);
23
24 figure;
25 subplot(2,2,1:2);
26 plot([0,wta(IDmid)], [IDm IDm], 'LineStyle', '--', 'Color', 'k', 'LineWidth', 0.5)
    ; hold on
27 plot([0,wta(VDmid)], [VDm VDm], 'LineStyle', '--', 'Color', 'k', 'LineWidth', 0.5)
    ; hold on
28 plot(wta, IDp, 'LineWidth', 1, 'Color', [0 0.4470 0.7410]); hold on
29 plot(wta, VDp, 'LineWidth', 1, 'Color', 'r'); hold on
30 set(gca, 'xtick', [0 pi/2 pi 3*pi/2 2*pi]);
31 tick = {'0'; '\pi/2'; '\pi'; '3\pi/2'; '2\pi'};
32 set(gca, 'xticklabel', tick);
33 set(gca, 'ytick', [0 IDm VDm]);
34 grid on
35 grid minor
36
37 subplot(2,2,3); plot(wta, ICp, 'LineWidth', 1);
38 set(gca, 'xtick', [0 pi/2 pi 3*pi/2 2*pi]);
39 tick = {'0'; '\pi/2'; '\pi'; '3\pi/2'; '2\pi'};
40 set(gca, 'xticklabel', tick);
41 set(gca, 'ytick', [round(ICm,2) 0 round(ICM,2)]);
42 grid on
43 grid minor
44
45 subplot(2,2,4);
46 plot(wta, Io, 'LineWidth', 1, 'Color', [0 0.4470 0.7410]);
47 set(gca, 'xtick', [0 pi/2 pi 3*pi/2 2*pi]);
48 tick = {'0'; '\pi/2'; '\pi'; '3\pi/2'; '2\pi'};
49 set(gca, 'xticklabel', tick);
50 set(gca, 'ytick', [round(Iom,2) 0 round(IoM,2)]);
51 grid on
52 grid minor

1 function [ C1, C2, Lx] = ClassE_50(RL, L2, f)
2
3 w = 2*pi*f;
4 C1 = 8/(sqrt(pi^2 + 4)*pi*RL*w);
5 Lx = (pi^2 - 4) / (2*(pi^2 + 4)*(w^2)*C1);
6 C2 = 1/((w^2)*L2);
```

Class EF plot and component code

```

1 D = 0.3750; k = 0.867; q1 = 2;
2 cons = [D k q1]; % Setting constants to pass to function EFeqns
3 Fun = @(x) EFeqns(x, cons); % Function of dummy variable x
4 x = fsolve(Fun,[0 0 0 0 0 0]);
5
6 A1 = x(1); B1 = x(2); A2 = x(3); B2 = x(4); phi = x(5); p = x(6);
7
8 % Creating Voltage and Current waveforms
9
10 q2 = q1*sqrt((k+1)/k);
11 syms wt
12
13 alphas = (k*(wt - 2*pi*D))/(k+1) + p*(cos(2*pi*D + phi) - cos(wt + phi))*((q2^2)/(
    q2^2-1)-(k+1)) + (A2/q2)*(sin(2*pi*D*q2) - sin(wt*q2)) + (B2/q2)*(cos(wt*q2) -
    cos(2*pi*D*q2)) ;
14 betas = int(alphas, wt, 2*pi*D, 2*pi);
15
16 res = 1000;
17 wta = 0:pi/res:2*pi;
18 wto = 2*pi*D:pi/res:2*pi;
19 wtf = 0:pi/res:2*pi*D;
20
21 alpha = (k*(wto - 2*pi*D))/(k+1) + p*(cos(2*pi*D + phi) - cos(wto + phi))*((q2^2)
    /(q2^2-1)-(k+1)) + (A2/q2)*(sin(2*pi*D*q2) - sin(wto*q2)) + (B2/q2)*(cos(wto*
    q2) - cos(2*pi*D*q2)) ;
22 beta = double(betas);
23
24 ID = 1 - A1*cos(q1*wtf) - B1*sin(q1*wtf) - p*(k+1)*sin(wtf+phi); % Normalised
    current through the switch
25 VD = 2*pi*(alpha/beta); % Normalised voltage across the switch
26 Io = p*(k+1)*sin(wta + phi); % Normalised output current
27 IC2_1 = A1*cos(q1*wtf) + B1*sin(q1*wtf); % Normalised current through the harmonic
    LC network when switch is closed
28 IC2_2 = A2*cos(q2*wto) + B2*sin(q2*wto) - ((p*q2^2)/(q2^2-1))*sin(wto+phi) + 1/(k
    +1); % Normalised current through the harmonic LC network when switch is open
29
30 IDp = [ID(1:size(ID,2)-1), zeros(1,size(wto,2))]; % Normalised current waveform
    through switch
31 VDP = [zeros(1,size(wtf,2)-1), VD]; % Normalised voltage waveform across switch
32 IC2p = [IC2_1(1:size(IC2_1,2)-1), IC2_2]; % Normalised current waveform through LC
    network
33
34 figure;
35 subplot(2,2,[1 3]);
36 plot(wta, IDp, 'LineWidth', 1, 'Color', [0 0.4470 0.7410]); hold on
37 plot(wta, VDP, 'LineWidth', 1, 'Color', 'r'); hold on
38 set(gca, 'xtick', [0 pi/2 pi 3*pi/2 2*pi]);
39 tick = {'0'; '\pi/2'; '\pi'; '3\pi/2'; '2\pi'};
40 set(gca, 'xticklabel', tick);
41 grid on
42 grid minor
43
44 subplot(2,2,2);
45 plot(wtf(1:size(wtf,2)-1), IC2_1(1:size(IC2_1,2)-1), 'LineWidth', 1, 'Color', [1
    17 181] ./ 255); hold on
46 plot(wto, IC2_2, 'LineWidth', 1, 'Color', [251 111 66] ./ 255 ); hold on
47 set(gca, 'xtick', [0 pi/2 pi 3*pi/2 2*pi]);
48 tick = {'0'; '\pi/2'; '\pi'; '3\pi/2'; '2\pi'};
49 set(gca, 'xticklabel', tick);
50 grid on
51 grid minor
52
53 subplot(2,2,4);
54 plot(wta, Io, 'LineWidth', 1, 'Color', [0 0.4470 0.7410]); hold on
55 set(gca, 'xtick', [0 pi/2 pi 3*pi/2 2*pi]);
56 tick = {'0'; '\pi/2'; '\pi'; '3\pi/2'; '2\pi'};
57 set(gca, 'xticklabel', tick);
58 grid on

```

```

59 grid minor
60
61 % Calculating values for C1 Lx C2 L2
62 RL = 5; fs = 6780000; w = 2*pi*fs; % Set parameters according to design
    preferences
63
64 C1 = beta/(pi*w*RL)*((cos(2*pi*D + phi) - cos(phi))/(2*pi*(1-D) + (A1/q1)*sin(2*pi
    *D*q1) + (2*B1/q1)*(sin(pi*D*q1))^2))^2;
65 Lx = (double(int((alphas*cos(wt+phi)), wt, 2*pi*D, 2*pi)))*(cos(2*pi*D + phi) -
    cos(phi))/(pi*w^2*C1)*(2*pi*(1-D) + (A1/q1)*sin(2*pi*D*q1) + (2*B1/q1)*(sin(
    pi*D*q1))^2));
66 C2 = C1/k;
67 L2 = 1/((q1*w)^2)*C2);

1 function F = EFeqns(x, cons)
2 % x(1) = A1
3 % x(2) = B1
4 % x(3) = A2
5 % x(4) = B2
6 % x(5) = phi
7 % x(6) = p
8
9 D = cons(1);
10 k = cons(2);
11 q1 = cons(3);
12 q2 = q1*sqrt((k+1)/k);
13
14 % Equations made equal to 0
15 F(1) = x(3)*cos(q2*2*pi) + x(4)*sin(q2*2*pi) - ((q2^2*x(6))/(q2^2-1))*sin(x(5)) +
    1/(k+1) - x(1);
16 F(2) = -x(3)*q2*sin(q2*2*pi) + x(4)*q2*cos(q2*2*pi) - ((q2^2*x(6))/(q2^2 - 1))*cos
    (x(5)) - x(2)*q1;
17 F(3) = x(3)*cos(q2*2*pi*D) + x(4)*sin(q2*2*pi*D) - ((q2^2*x(6))/(q2^2-1))*sin(2*pi
    *D + x(5)) + 1/(k+1) - x(1)*cos(q1*2*pi*D) - x(2)*sin(q1*2*pi*D);
18 F(4) = x(3)*q2*sin(q2*2*pi*D) - x(4)*q2*cos(q2*2*pi*D) + ((q2^2*x(6))/(q2^2 - 1))*
    cos(2*pi*D + x(5)) - x(1)*q1*sin(q1*2*pi*D) + x(2)*q1*cos(q1*2*pi*D);
19 F(5) = (2*pi*k)/(k+1)*(1-D) + x(6)*(cos(2*pi*D + x(5)) - cos(x(5)))*((q2^2)/(q2
    ^2-1) - (k+1)) + (x(3)/q2)*(sin(2*pi*D*q2) - sin(2*pi*q2)) + (x(4)/q2)*(cos(2*
    pi*q2) - cos(2*pi*D*q2));
20 F(6) = k/(k+1) + x(6)*sin(x(5))*((q2^2)/(q2^2-1)-(k+1)) - x(3)*cos(2*pi*q2) - x(4)
    *sin(2*pi*q2);

```

D Analytical derivations and MATLAB code for a varying load in a standard Class EF inverter

With changing values of R_L the assumption of ZVS would no longer hold, hence, a new set of simultaneous equations are needed to numerically calculate values of A_1 , A_2 , B_1 , B_2 , ρ and ϕ dependent on R_L at each instance under investigation. Similar to the Fourier analysis conducted in Appendices A and B, V_o can be given by,

$$\frac{a_o}{2} + \sum_{k=1}^{\infty} (a_k \cos kx + b_k \sin kx)$$

where,

$$a_k = \frac{1}{\pi} \int_0^{2\pi} f(x) \cos kx \, dx$$

$$b_k = \frac{1}{\pi} \int_0^{2\pi} f(x) \sin kx \, dx$$

where k is the integer multiples of the fundamental frequency f_s . V_o is also equal to $V_D(\omega t)$, and thus

$$a_k = I_m \omega L_x = \frac{1}{\pi} \int_0^{2\pi} V_D(\omega t) \cos(\omega t + \phi) \, d\omega t$$

$$b_k = I_m R_L = \frac{1}{\pi} \int_0^{2\pi} V_D(\omega t) \sin(\omega t + \phi) \, d\omega t$$

for the fundamental component of $V_D(\omega t)$. Hence, multiplying by I_i and substituting in equation (B.11), the above becomes

$$\rho(k+1) \omega L_x = \frac{I_i}{\pi} \int_0^{2\pi} V_D(\omega t) \cos(\omega t + \phi) \, d\omega t$$

$$\rho(k+1) R_L = \frac{I_i}{\pi} \int_0^{2\pi} V_D(\omega t) \sin(\omega t + \phi) \, d\omega t$$

$$\therefore \rho(k+1) \omega L_x = \frac{1}{\omega C_1 \pi} \int_0^{2\pi} \alpha \cos(\omega t + \phi) \, d\omega t$$

$$\rho(k+1) R_L = \frac{1}{\omega C_1 \pi} \int_0^{2\pi} \alpha \sin(\omega t + \phi) \, d\omega t$$

Furthermore, the second harmonic component of V_D (i.e. when $k=1$), will be zero due to the LC resonant circuit, resulting in the following equations,

$$0 = \int_0^{2\pi} \alpha \cos(2\omega t + \phi) \, d\omega t$$

$$0 = \int_0^{2\pi} \alpha \sin(2\omega t + \phi) \, d\omega t$$

Hence, these four new equations can be combined with either of the previous ones determined from the continuity equations of voltage and current for linear circuits at the switch opening and closing points, to form a new set of six simultaneous equations with six unknowns. The MATLAB code used to solve these equations and generate the associated plots for different values of R_L is found below.

```
1 % Measuring the effect on Load Variation for Ropt, 0.75*Ropt, 1.25*Ropt
2 % with fixed values of D, K, RL - if you want to change these values you
```

```

3 % also need to change the vRLeqns script to emulate more EFeqns
4
5 % Using parameters with known results
6 D = 0.3750; k = 0.867; q1 = 2; RL = 1;
7 guess=[0,0,0,0,0,0];
8
9 %% Ropt
10
11 % Solving equations to measure effect on Load Variation
12 Fun = @(x) vRLeqns(x, RL); % Function of dummy variable x
13 x = fsolve(Fun, guess); % Solving for unknowns
14
15 A1 = x(1); B1 = x(2); A2 = x(3); B2 = x(4); phi = x(5); p = x(6);
16
17 % Creating Voltage and Current waveforms using optimum RL
18
19 syms wt
20 q2 = q1*sqrt((k+1)/k);
21
22 res = 1000;
23 wta = 0:pi/res:2*pi;
24 wto = 2*pi*D:pi/res:2*pi;
25 wtf = 0:pi/res:2*pi*D;
26
27 syms wt
28 betas = (k*(wt - 2*pi*D))/(k+1) + p*(cos(2*pi*D + phi) - cos(wt + phi))*((q2^2)/
    (q2^2-1)-(k+1)) + (A2/q2)*(sin(2*pi*D*q2) - sin(wt*q2)) + (B2/q2)*(cos(wt*q2) -
    cos(2*pi*D*q2)) ;
29 alphas = int(betas, wt, 2*pi*D, 2*pi);
30 alpha = double(alphas);
31
32 beta = (k*(wto - 2*pi*D))/(k+1) + p*(cos(2*pi*D + phi) - cos(wto + phi))*((q2^2)/
    (q2^2-1)-(k+1)) + (A2/q2)*(sin(2*pi*D*q2) - sin(wto*q2)) + (B2/q2)*(cos(wto*q2)
    - cos(2*pi*D*q2)) ;
33
34 ID = 1 - A1*cos(q1*wtf) - B1*sin(q1*wtf) - p*(k+1)*sin(wtf+phi); % Normalised
    current through the switch
35 VD = 2*pi*(beta/alpha); % Normalised voltage across the switch
36 Io = p*(k+1)*sin(wta + phi); % Normalised output current
37
38 IDp = [ID(1:size(ID,2)-1), zeros(1,size(wto,2))]; % Normalised current waveform
    through switch
39 VDP = [zeros(1,size(wtf,2)-1), VD]; % Normalised voltage waveform across switch
40
41 figure(1);
42 subplot(1,3,1);
43 plot(wta, VDP, 'LineWidth', 1, 'Color', 'k'); hold on
44 set(gca, 'xtick', [0 pi/2 pi 3*pi/2 2*pi]);
45 tick = {'0'; '\pi/2'; '\pi'; '3\pi/2'; '2\pi'};
46 set(gca, 'xticklabel', tick);
47
48 subplot(1,3,2);
49 plot(wta, IDp, 'LineWidth', 1, 'Color', 'k'); hold on
50 set(gca, 'xtick', [0 pi/2 pi 3*pi/2 2*pi]);
51 tick = {'0'; '\pi/2'; '\pi'; '3\pi/2'; '2\pi'};
52 set(gca, 'xticklabel', tick);
53
54 subplot(1,3,3);
55 plot(wta, Io, 'LineWidth', 1, 'Color', 'k'); hold on
56 set(gca, 'xtick', [0 pi/2 pi 3*pi/2 2*pi]);
57 tick = {'0'; '\pi/2'; '\pi'; '3\pi/2'; '2\pi'};
58 set(gca, 'xticklabel', tick);
59
60 IC2_1 = A1*cos(q1*wtf) + B1*sin(q1*wtf); % Normalised current through the harmonic
    LC network when switch is closed
61 IC2_2 = A2*cos(q2*wto) + B2*sin(q2*wto) - ((p*q2^2)/(q2^2-1))*sin(wto+phi) + 1/(k
    +1); % Normalised current through the harmonic LC network when switch is open
62 IC2p = [IC2_1(1:size(IC2_1,2)-1), IC2_2]; % Normalised current waveform through LC
    network
63

```

```

64 figure(2);
65 subplot(2,2,[1 3]);
66 plot(wta, IDp, 'LineWidth', 1, 'Color', 'k'); hold on
67 plot(wta, VDp, 'LineWidth', 1, 'Color', 'r'); hold on
68 set(gca, 'xtick', [0 pi/2 pi 3*pi/2 2*pi]);
69 tick = {'0'; '\pi/2'; '\pi'; '3\pi/2'; '2\pi'};
70 set(gca, 'xticklabel', tick);
71
72 subplot(2,2,2);
73 plot(wtf(1:size(wtf,2)-1), IC2_1(1:size(IC2_1,2)-1), 'LineWidth', 1, 'Color', 'k')
    ; hold on
74 plot(wto, IC2_2, 'LineWidth', 1, 'Color', [0 0.4470 0.7410]); hold on
75 set(gca, 'xtick', [0 pi/2 pi 3*pi/2 2*pi]);
76 tick = {'0'; '\pi/2'; '\pi'; '3\pi/2'; '2\pi'};
77 set(gca, 'xticklabel', tick);
78
79 subplot(2,2,4);
80 plot(wta, Io, 'LineWidth', 1, 'Color', 'k'); hold on
81 set(gca, 'xtick', [0 pi/2 pi 3*pi/2 2*pi]);
82 tick = {'0'; '\pi/2'; '\pi'; '3\pi/2'; '2\pi'};
83 set(gca, 'xticklabel', tick);
84
85
86 %% Ropt*0.75
87
88 % Solving equations to measure effect on Load Variation
89 Fun = @(x) vRLeqns(x, RL*0.75); % Function of dummy variable x
90 x = fsolve(Fun, guess); % Solving for unknowns
91
92 A1 = x(1); B1 = x(2); A2 = x(3); B2 = x(4); phi = x(5); p = x(6);
93
94 % Creating Voltage and Current waveforms using optimum RL - should be the
95 % same as running regular ClassEF procedure
96
97 syms wt
98 q2 = q1*sqrt((k+1)/k);
99
100 res = 1000;
101 wta = 0:pi/res:2*pi;
102 wto = 2*pi*D:pi/res:2*pi;
103 wtf = 0:pi/res:2*pi*D;
104
105 syms wt
106 betas = (k*(wt - 2*pi*D))/(k+1) + p*(cos(2*pi*D + phi) - cos(wt + phi))*((q2^2)/(
    q2^2-1)-(k+1)) + (A2/q2)*(sin(2*pi*D*q2) - sin(wt*q2)) + (B2/q2)*(cos(wt*q2) -
    cos(2*pi*D*q2)) ;
107 alphas = int(betas, wt, 2*pi*D, 2*pi);
108 alpha = double(alphas);
109
110 beta = (k*(wto - 2*pi*D))/(k+1) + p*(cos(2*pi*D + phi) - cos(wto + phi))*((q2^2)/(
    q2^2-1)-(k+1)) + (A2/q2)*(sin(2*pi*D*q2) - sin(wto*q2)) + (B2/q2)*(cos(wto*q2)
    - cos(2*pi*D*q2)) ;
111
112 ID = 1 - A1*cos(q1*wtf) - B1*sin(q1*wtf) - p*(k+1)*sin(wtf+phi); % Normalised
    current through the switch
113 VD = 2*pi*(beta/alpha); % Normalised voltage across the switch
114 Io = p*(k+1)*sin(wta + phi); % Normalised output current
115
116 IDp = [ID(1:size(ID,2)-1), zeros(1, size(wto,2))]; % Normalised current waveform
    through switch
117 VDp = [zeros(1, size(wtf,2)-1), VD]; % Normalised voltage waveform across switch
118
119 figure(1);
120 subplot(1,3,1);
121 plot(wta, VDp, 'LineWidth', 1, 'Color', [0 0.4470 0.7410]); hold on
122 set(gca, 'xtick', [0 pi/2 pi 3*pi/2 2*pi]);
123 tick = {'0'; '\pi/2'; '\pi'; '3\pi/2'; '2\pi'};
124 set(gca, 'xticklabel', tick);
125
126 subplot(1,3,2);

```

```

127 plot(wta, IDp, 'LineWidth', 1, 'Color', [0 0.4470 0.7410]); hold on
128 set(gca, 'xtick', [0 pi/2 pi 3*pi/2 2*pi]);
129 tick = {'0'; '\pi/2'; '\pi'; '3\pi/2'; '2\pi'};
130 set(gca, 'xticklabel', tick);
131
132 subplot(1,3,3);
133 plot(wta, Io, 'LineWidth', 1, 'Color', [0 0.4470 0.7410]); hold on
134 set(gca, 'xtick', [0 pi/2 pi 3*pi/2 2*pi]);
135 tick = {'0'; '\pi/2'; '\pi'; '3\pi/2'; '2\pi'};
136 set(gca, 'xticklabel', tick);
137
138 IC2_1 = A1*cos(q1*wtf) + B1*sin(q1*wtf); % Normalised current through the harmonic
    LC network when switch is closed
139 IC2_2 = A2*cos(q2*wto) + B2*sin(q2*wto) - ((p*q2^2)/(q2^2-1))*sin(wto+phi) + 1/(k
    +1); % Normalised current through the harmonic LC network when switch is open
140 IC2p = [IC2_1(1:size(IC2_1,2)-1), IC2_2]; % Normalised current waveform through LC
    network
141
142 figure(2);
143 subplot(2,2,[1 3]);
144 plot(wta, IDp, 'LineWidth', 1, 'Color', [0 0.4470 0.7410]); hold on
145 plot(wta, VDP, 'LineWidth', 1, 'Color', 'r'); hold on
146 set(gca, 'xtick', [0 pi/2 pi 3*pi/2 2*pi]);
147 tick = {'0'; '\pi/2'; '\pi'; '3\pi/2'; '2\pi'};
148 set(gca, 'xticklabel', tick);
149
150 subplot(2,2,2);
151 plot(wtf(1:size(wtf,2)-1), IC2_1(1:size(IC2_1,2)-1), 'LineWidth', 1, 'Color', [1
    17 181] ./ 255); hold on
152 plot(wto, IC2_2, 'LineWidth', 1, 'Color', [0 0.4470 0.7410]); hold on
153 set(gca, 'xtick', [0 pi/2 pi 3*pi/2 2*pi]);
154 tick = {'0'; '\pi/2'; '\pi'; '3\pi/2'; '2\pi'};
155 set(gca, 'xticklabel', tick);
156
157 subplot(2,2,4);
158 plot(wta, Io, 'LineWidth', 1, 'Color', [0 0.4470 0.7410]); hold on
159 set(gca, 'xtick', [0 pi/2 pi 3*pi/2 2*pi]);
160 tick = {'0'; '\pi/2'; '\pi'; '3\pi/2'; '2\pi'};
161 set(gca, 'xticklabel', tick);
162
163
164 %% Ropt*1.25
165
166 % Solving equations to measure effect on Load Variation
167 Fun = @(x) vRLeqns(x, RL*1.25); % Function of dummy variable x
168 x = fsolve(Fun, guess); % Solving for unknowns
169
170 A1 = x(1); B1 = x(2); A2 = x(3); B2 = x(4); phi = x(5); p = x(6);
171
172 % Creating Voltage and Current waveforms using optimum RL - should be the
173 % same as running regular ClassEF procedure
174
175 syms wt
176 q2 = q1*sqrt((k+1)/k);
177
178 res = 1000;
179 wta = 0:pi/res:2*pi;
180 wto = 2*pi*D:pi/res:2*pi;
181 wtf = 0:pi/res:2*pi*D;
182
183 syms wt
184 betas = (k*(wt - 2*pi*D))/(k+1) + p*(cos(2*pi*D + phi) - cos(wt + phi))*((q2^2)/(
    q2^2-1)-(k+1)) + (A2/q2)*(sin(2*pi*D*q2) - sin(wt*q2)) + (B2/q2)*(cos(wt*q2) -
    cos(2*pi*D*q2));
185 alphas = int(betas, wt, 2*pi*D, 2*pi);
186 alpha = double(alphas);
187
188 beta = (k*(wto - 2*pi*D))/(k+1) + p*(cos(2*pi*D + phi) - cos(wto + phi))*((q2^2)/(
    q2^2-1)-(k+1)) + (A2/q2)*(sin(2*pi*D*q2) - sin(wto*q2)) + (B2/q2)*(cos(wto*q2)
    - cos(2*pi*D*q2));

```

```

189
190 ID = 1 - A1*cos(q1*wtf) - B1*sin(q1*wtf) - p*(k+1)*sin(wtf+phi); % Normalised
    current through the switch
191 VD = 2*pi*(beta/alpha); % Normalised voltage across the switch
192 Io = p*(k+1)*sin(wta + phi); % Normalised output current
193
194 IDp = [ID(1:size(ID,2)-1), zeros(1, size(wto,2))]; % Normalised current waveform
    through switch
195 VDp = [zeros(1, size(wtf,2)-1), VD]; % Normalised voltage waveform across switch
196
197 figure(1);
198 subplot(1,3,1);
199 plot(wta, VDp, 'LineWidth', 1, 'Color', [251 111 66] ./ 255); hold on
200 set(gca, 'xtick', [0 pi/2 pi 3*pi/2 2*pi]);
201 tick = {'0'; '\pi/2'; '\pi'; '3\pi/2'; '2\pi'};
202 set(gca, 'xticklabel', tick);
203 grid on
204 grid minor
205
206 subplot(1,3,2);
207 plot(wta, IDp, 'LineWidth', 1, 'Color', [251 111 66] ./ 255); hold on
208 set(gca, 'xtick', [0 pi/2 pi 3*pi/2 2*pi]);
209 tick = {'0'; '\pi/2'; '\pi'; '3\pi/2'; '2\pi'};
210 set(gca, 'xticklabel', tick);
211 grid on
212 grid minor
213
214 subplot(1,3,3);
215 plot(wta, Io, 'LineWidth', 1, 'Color', [251 111 66] ./ 255); hold on
216 set(gca, 'xtick', [0 pi/2 pi 3*pi/2 2*pi]);
217 tick = {'0'; '\pi/2'; '\pi'; '3\pi/2'; '2\pi'};
218 set(gca, 'xticklabel', tick);
219 grid on
220 grid minor
221
222 IC2_1 = A1*cos(q1*wtf) + B1*sin(q1*wtf); % Normalised current through the harmonic
    LC network when switch is closed
223 IC2_2 = A2*cos(q2*wto) + B2*sin(q2*wto) - ((p*q2^2)/(q2^2-1))*sin(wto+phi) + 1/(k
    +1); % Normalised current through the harmonic LC network when switch is open
224 IC2p = [IC2_1(1:size(IC2_1,2)-1), IC2_2]; % Normalised current waveform through LC
    network
225
226 figure(2);
227 subplot(2,2,[1 3]);
228 plot(wta, IDp, 'LineWidth', 1, 'Color', [251 111 66] ./ 255); hold on
229 plot(wta, VDp, 'LineWidth', 1, 'Color', 'r'); hold on
230 set(gca, 'xtick', [0 pi/2 pi 3*pi/2 2*pi]);
231 tick = {'0'; '\pi/2'; '\pi'; '3\pi/2'; '2\pi'};
232 set(gca, 'xticklabel', tick);
233 grid on
234 grid minor
235
236 subplot(2,2,2);
237 plot(wtf(1:size(wtf,2)-1), IC2_1(1:size(IC2_1,2)-1), 'LineWidth', 1, 'Color', [1
    17 181] ./ 255); hold on
238 plot(wto, IC2_2, 'LineWidth', 1, 'Color', [251 111 66] ./ 255 ); hold on
239 set(gca, 'xtick', [0 pi/2 pi 3*pi/2 2*pi]);
240 tick = {'0'; '\pi/2'; '\pi'; '3\pi/2'; '2\pi'};
241 set(gca, 'xticklabel', tick);
242 grid on
243 grid minor
244
245 subplot(2,2,4);
246 plot(wta, Io, 'LineWidth', 1, 'Color', [251 111 66] ./ 255); hold on
247 set(gca, 'xtick', [0 pi/2 pi 3*pi/2 2*pi]);
248 tick = {'0'; '\pi/2'; '\pi'; '3\pi/2'; '2\pi'};
249 set(gca, 'xticklabel', tick);
250 grid on
251 grid minor

```

```

1 function F = vRLeqns3(x, RL)
2 %guess=[-1,-1,-1,-1,2.5,0,0.8];
3
4 % x(1) = A1
5 % x(2) = B1
6 % x(3) = A2
7 % x(4) = B2
8 % x(5) = phi
9 % x(6) = p
10 % RL=1; %0.75, %1.25
11 q1=2; D=0.375; k=0.867;
12 q2 = q1*sqrt((k+1)/k);
13 %RL=1;
14 %w=1;
15 wC1=131.8374e-003; wLx= 2.0339;
16 %
17 % D = cons(1);
18 % k = cons(2);
19 % q1 = cons(3);
20 % fs = cons(4);
21 % RL = cons(5);
22 % Lx = cons(6);
23 % C1 = cons(7);
24 % q2 = q1*sqrt((k+1)/k);
25 % w = 2*pi*fs;
26
27
28 F(1) = x(3)*cos(q2*2*pi*D) + x(4)*sin(q2*2*pi*D) - ((q2^2*x(6))/(q2^2-1))*sin(2*pi
    *D + x(5)) + 1/(k+1) - x(1)*cos(q1*2*pi*D) - x(2)*sin(q1*2*pi*D);
29 F(2) = x(3)*cos(q2*2*pi) + x(4)*sin(q2*2*pi) - ((q2^2*x(6))/(q2^2-1))*sin(x(5)) +
    1/(k+1) - x(1);
30
31 % getting alpha, where is VDS = (Iin/wC1)*(alpha)
32 syms wt
33 alpha = (k*(wt - 2*pi*D))/(k+1) + x(6)*(cos(2*pi*D + x(5)) - cos(wt + x(5)))*((q2
    ^2)/(q2^2-1)-(k+1)) + (x(3)/q2)*(sin(2*pi*D*q2) - sin(wt*q2)) + (x(4)/q2)*(cos
    (wt*q2) - cos(2*pi*D*q2)) ;
34
35 F(3) = (1/(pi*wC1))*int(alpha*sin(wt+x(5)), wt, 2*pi*D, 2*pi) - x(6)*(k+1)*RL;
36 F(4) = (1/(pi*wC1))*int(alpha*cos(wt+x(5)), wt, 2*pi*D, 2*pi) - x(6)*(k+1)*wLx;
37 F(5) = int(alpha*sin(2*wt+x(5)), wt, 2*pi*D, 2*pi);
38 F(6) = int(alpha*cos(2*wt+x(5)), wt, 2*pi*D, 2*pi);

```

E Mathematical Derivation and MATLAB code for a Constant Output Current Class EF Inverter

Following on from the analysis presented in Appendix B, the voltage across the load resistor can be written as,

$$V_{R_L} = I_m R_L = \frac{1}{\pi} \int_0^{2\pi} V_D(\omega t) \sin(\omega t + \phi) d\omega t \quad (\text{E.1})$$

and, assuming no losses,

$$\begin{aligned}
 P_i &= P_o = \frac{1}{2} I_m^2 R_L \\
 \therefore V_i I_i &= \frac{1}{2} I_m^2 R_L \\
 \frac{V_i}{I_i} &= \frac{1}{2} \left(\frac{I_m}{I_i} \right)^2 R_L \\
 \therefore R_L &= \frac{2V_i}{I_i \left(\frac{I_m}{I_i} \right)^2}
 \end{aligned}$$

Now, substituting this relationship for R_L into equation E.1 and dividing by V_i gives,

$$\begin{aligned}
 \frac{I_m}{V_i} \frac{2V_i}{I_i \left(\frac{I_m}{I_i} \right)^2} &= \frac{2}{\beta} \int_{2\pi D}^{2\pi} \alpha \sin(\omega t + \phi) d\omega t \\
 \frac{I_m}{I_i} &= \frac{1}{\beta} \int_{2\pi D}^{2\pi} \alpha \sin(\omega t + \phi) d\omega t
 \end{aligned}$$

and substituting equation B.11 gives

$$\frac{1}{(k+1)} = \frac{\rho}{\beta} \int_{2\pi D}^{2\pi} \alpha \sin(\omega t + \phi) d\omega t$$

For constant current operation, various parameters in the above equation would need to remain constant as ρ changes, or put another way,

$$\frac{d}{d\rho} \left(\frac{\rho}{\beta} \int_{2\pi D}^{2\pi} \alpha \sin(\omega t + \phi) d\omega t \right) = 0$$

and using this condition as well as equations B.7 to B and B.13, will give a new set of simultaneous equations which can be solved in order to generate the desired waveforms from the following equations;

$$X_c \frac{I_D(\omega t)}{V_i} = \begin{cases} \frac{2\pi}{\beta} \left(1 - A_1 \cos(q_1 \omega t) - B_1 \sin(q_1 \omega t) - \rho(k+1) \sin(\omega t + \phi) \right) & \text{for } 0 \leq \omega t < 2\pi D \\ 0 & \text{for } 2\pi D \leq \omega t < 2\pi \end{cases}$$

$$X_c \frac{I_o(\omega t)}{V_i} = \frac{2\pi \rho(k+1)}{\beta} \sin(\omega t + \phi)$$

$$\frac{V_D(\omega t)}{V_i} = \begin{cases} 0 & \text{for } 0 \leq \omega t < 2\pi D \\ 2\pi \frac{\alpha}{\beta} & \text{for } 2\pi D \leq \omega t < 2\pi \end{cases}$$

Furthermore, using B.14 and B.15, the component values for C_1 and L_x can also be found with respect to a set upper bound value for R_L , which are given by,

$$C_1 = \frac{\beta}{\pi \rho^2 (k+1)^2 \omega R_L}$$

$$L_x = \frac{\int_{2\pi D}^{2\pi} \alpha \sin(\omega t + \phi) d\omega t}{\pi \omega^2 C_1 \rho (k+1)}$$

The MATLAB code used to solve these equations and plot waveforms for different values of ρ are found below.

```

1  % Measuring the effect on Load Variation for varying p
2
3  % Using parameters with known results
4  D = 0.3; k = 1.3296; q1 = 1.67; fs = 6780000; w = 2*pi*fs; RL = 1;q2 = q1*sqrt((k
      +1)/k);
5
6  %% first set with p = 3
7  p = 3;
8
9  %Limiting upper and lower bounds to what we should be expecting
10 x0 = [3 -4 5 5 2];
11 lb = [3 -4 5 5 2];
12 ub = [4 3 6 6 3];
13
14 cons = [D k q1 q2 p]; % Setting constants to pass to function
15 Fun = @(x) newLIEqns(x, cons); % Function of dummy variable x
16 options = optimoptions('lsqnonlin', 'Display','off', 'TolFun', 1e-12, 'TolX', 1e
      -6);
17 x = lsqnonlin(Fun,x0,lb,ub,options); %run lsqnonlin which is essentially fsolve,
      with ub and lb
18
19 A1 = x(1); B1 = x(2); A2 = x(3); B2 = x(4); phi = x(5);
20
21 res = 1000;
22 wta = 0:pi/res:2*pi;
23 wto = 2*pi*D:pi/res:2*pi;
24 wtf = 0:pi/res:2*pi*D;
25
26 syms wt
27 betas = (k*(wt - 2*pi*D))/(k+1) + p*(cos(2*pi*D + phi) - cos(wt + phi))*((q2^2)/(
      q2^2-1)-(k+1)) + (A2/q2)*(sin(2*pi*D*q2) - sin(wt*q2)) + (B2/q2)*(cos(wt*q2) -
      cos(2*pi*D*q2)) ;
28 alphas = int(betas, wt, 2*pi*D, 2*pi);
29 alpha = double(alphas);
30
31 beta = (k*(wto - 2*pi*D))/(k+1) + p*(cos(2*pi*D + phi) - cos(wto + phi))*((q2^2)/(
      q2^2-1)-(k+1)) + (A2/q2)*(sin(2*pi*D*q2) - sin(wto*q2)) + (B2/q2)*(cos(wto*q2)
      - cos(2*pi*D*q2)) ;
32
33 ID = (2*pi/alpha)*(1 - A1*cos(q1*wtf) - B1*sin(q1*wtf) - p*(k+1)*sin(wtf+phi)); %
      Normalised current through the switch with factor (Xc.ID)/Vi
34 VD = 2*pi*(beta/alpha); % Normalised voltage across the switch
35 Io = (2*pi/alpha)*(p*(k+1)*sin(wta + phi)); % Normalised output current
36
37 IDp = [ID(1:size(ID,2)-1), zeros(1,size(wto,2))]; % Normalised current waveform
      through switch
38 VDP = [zeros(1,size(wtf,2)-1),VD]; % Normalised voltage waveform across switch
39
40 figure(1);
41 subplot(1,3,1);
42 plot(wta, VDP, 'LineWidth', 1, 'Color', 'k'); hold on
43 set(gca, 'xtick', [0 pi/2 pi 3*pi/2 2*pi]);

```

```

44 tick = {'0'; '\pi/2'; '\pi'; '3\pi/2'; '2\pi'};
45 set(gca, 'xticklabel', tick);
46 grid on
47 grid minor
48
49 subplot(1,3,2);
50 plot(wta, IDp, 'LineWidth', 1, 'Color', 'k'); hold on
51 set(gca, 'xtick', [0 pi/2 pi 3*pi/2 2*pi]);
52 tick = {'0'; '\pi/2'; '\pi'; '3\pi/2'; '2\pi'};
53 set(gca, 'xticklabel', tick);
54 grid on
55 grid minor
56
57 subplot(1,3,3);
58 plot(wta, Io, 'LineWidth', 1, 'Color', 'k'); hold on
59 set(gca, 'xtick', [0 pi/2 pi 3*pi/2 2*pi]);
60 tick = {'0'; '\pi/2'; '\pi'; '3\pi/2'; '2\pi'};
61 set(gca, 'xticklabel', tick);
62 grid on
63 grid minor
64
65 IC2_1 = A1*cos(q1*wtf) + B1*sin(q1*wtf); % Normalised current through the harmonic
    LC network when switch is closed
66 IC2_2 = A2*cos(q2*wto) + B2*sin(q2*wto) - ((p*q2^2)/(q2^2-1))*sin(wto+phi) + 1/(k
    +1); % Normalised current through the harmonic LC network when switch is open
67 IC2p = [IC2_1(1:size(IC2_1,2)-1), IC2_2]; % Normalised current waveform through LC
    network
68
69 figure(2);
70 subplot(2,2,[1 3]);
71 plot(wta, IDp, 'LineWidth', 1, 'Color', 'k'); hold on
72 plot(wta, VDP, 'LineWidth', 1, 'Color', 'r'); hold on
73 set(gca, 'xtick', [0 pi/2 pi 3*pi/2 2*pi]);
74 tick = {'0'; '\pi/2'; '\pi'; '3\pi/2'; '2\pi'};
75 set(gca, 'xticklabel', tick);
76 grid on
77 grid minor
78
79 subplot(2,2,2);
80 plot(wtf(1:size(wtf,2)-1), IC2_1(1:size(IC2_1,2)-1), 'LineWidth', 1, 'Color', 'k')
    ; hold on
81 plot(wto, IC2_2, 'LineWidth', 1, 'Color', [0 0.4470 0.7410]); hold on
82 set(gca, 'xtick', [0 pi/2 pi 3*pi/2 2*pi]);
83 tick = {'0'; '\pi/2'; '\pi'; '3\pi/2'; '2\pi'};
84 set(gca, 'xticklabel', tick);
85 grid on
86 grid minor
87
88 subplot(2,2,4);
89 plot(wta, Io, 'LineWidth', 1, 'Color', 'k'); hold on
90 set(gca, 'xtick', [0 pi/2 pi 3*pi/2 2*pi]);
91 tick = {'0'; '\pi/2'; '\pi'; '3\pi/2'; '2\pi'};
92 set(gca, 'xticklabel', tick);
93 grid on
94 grid minor
95
96 %% With p= 1.5
97 p=1.5;
98
99 %Limiting upper and lower bounds to what we should be expecting
100 x0 = [2 -4 4 2 2];
101 lb = [1 -5 3 1 2];
102 ub = [3 -3 4 3 3];
103
104 cons = [D k q1 q2 p]; % Setting constants to pass to function
105 Fun = @(x) newLIEqns(x, cons); % Function of dummy variable x
106 options = optimoptions('lsqnonlin', 'Display','off', 'TolFun', 1e-12, 'TolX', 1e
    -6);
107 x = lsqnonlin(Fun,x0,lb,ub,options); %run lsqnonlin which is essentially fsolve,
    with ub and lb

```

```

108
109 A1 = x(1); B1 = x(2); A2 = x(3); B2 = x(4); phi = x(5);
110
111 res = 1000;
112 wta = 0:pi/res:2*pi;
113 wto = 2*pi*D:pi/res:2*pi;
114 wtf = 0:pi/res:2*pi*D;
115
116 syms wt
117 betas = (k*(wt - 2*pi*D))/(k+1) + p*(cos(2*pi*D + phi) - cos(wt + phi))*((q2^2)/(
    q2^2-1)-(k+1)) + (A2/q2)*(sin(2*pi*D*q2) - sin(wt*q2)) + (B2/q2)*(cos(wt*q2) -
    cos(2*pi*D*q2)) ;
118 alphas = int(betas, wt, 2*pi*D, 2*pi);
119 alpha = double(alphas);
120
121 beta = (k*(wto - 2*pi*D))/(k+1) + p*(cos(2*pi*D + phi) - cos(wto + phi))*((q2^2)/(
    q2^2-1)-(k+1)) + (A2/q2)*(sin(2*pi*D*q2) - sin(wto*q2)) + (B2/q2)*(cos(wto*q2)
    - cos(2*pi*D*q2)) ;
122
123 ID = (2*pi/alpha)*(1 - A1*cos(q1*wtf) - B1*sin(q1*wtf) - p*(k+1)*sin(wtf+phi)); %
    Normalised current through the switch with factor (Xc.ID)/Vi
124 VD = 2*pi*(beta/alpha); % Normalised voltage across the switch
125 Io = (2*pi/alpha)*(p*(k+1)*sin(wta + phi)); % Normalised output current
126
127 IDp = [ID(1:size(ID,2)-1), zeros(1,size(wto,2))]; % Normalised current waveform
    through switch
128 VDP = [zeros(1,size(wtf,2)-1), VD]; % Normalised voltage waveform across switch
129
130 figure(1);
131 subplot(1,3,1);
132 plot(wta, VDP, 'LineWidth', 1, 'Color', [0 0.4470 0.7410]); hold on
133 set(gca, 'xtick', [0 pi/2 pi 3*pi/2 2*pi]);
134 tick = {'0'; '\pi/2'; '\pi'; '3\pi/2'; '2\pi'};
135 set(gca, 'xticklabel', tick);
136 grid on
137 grid minor
138
139 subplot(1,3,2);
140 plot(wta, IDp, 'LineWidth', 1, 'Color', [0 0.4470 0.7410]); hold on
141 set(gca, 'xtick', [0 pi/2 pi 3*pi/2 2*pi]);
142 tick = {'0'; '\pi/2'; '\pi'; '3\pi/2'; '2\pi'};
143 set(gca, 'xticklabel', tick);
144 grid on
145 grid minor
146
147 subplot(1,3,3);
148 plot(wta, Io, 'LineWidth', 1, 'Color', [0 0.4470 0.7410]); hold on
149 set(gca, 'xtick', [0 pi/2 pi 3*pi/2 2*pi]);
150 tick = {'0'; '\pi/2'; '\pi'; '3\pi/2'; '2\pi'};
151 set(gca, 'xticklabel', tick);
152 grid on
153 grid minor
154
155 IC2_1 = A1*cos(q1*wtf) + B1*sin(q1*wtf); % Normalised current through the harmonic
    LC network when switch is closed
156 IC2_2 = A2*cos(q2*wto) + B2*sin(q2*wto) - ((p*q2^2)/(q2^2-1))*sin(wto+phi) + 1/(k
    +1); % Normalised current through the harmonic LC network when switch is open
157 IC2p = [IC2_1(1:size(IC2_1,2)-1), IC2_2]; % Normalised current waveform through LC
    network
158
159 figure(2);
160 subplot(2,2,[1 3]);
161 plot(wta, IDp, 'LineWidth', 1, 'Color', [0 0.4470 0.7410]); hold on
162 plot(wta, VDP, 'LineWidth', 1, 'Color', 'r'); hold on
163 set(gca, 'xtick', [0 pi/2 pi 3*pi/2 2*pi]);
164 tick = {'0'; '\pi/2'; '\pi'; '3\pi/2'; '2\pi'};
165 set(gca, 'xticklabel', tick);
166 grid on
167 grid minor
168

```

```

169 subplot(2,2,2);
170 plot(wtf(1:size(wtf,2)-1), IC2_1(1:size(IC2_1,2)-1), 'LineWidth', 1, 'Color', [1
    17 181] ./ 255); hold on
171 plot(wto, IC2_2, 'LineWidth', 1, 'Color', [0 0.4470 0.7410]); hold on
172 set(gca, 'xtick', [0 pi/2 pi 3*pi/2 2*pi]);
173 tick = {'0'; '\pi/2'; '\pi'; '3\pi/2'; '2\pi'};
174 set(gca, 'xticklabel', tick);
175 grid on
176 grid minor
177
178 subplot(2,2,4);
179 plot(wta, Io, 'LineWidth', 1, 'Color', [0 0.4470 0.7410]); hold on
180 set(gca, 'xtick', [0 pi/2 pi 3*pi/2 2*pi]);
181 tick = {'0'; '\pi/2'; '\pi'; '3\pi/2'; '2\pi'};
182 set(gca, 'xticklabel', tick);
183 grid on
184 grid minor
185
186 %% With p = 5
187 p=5;
188
189 %Limiting upper and lower bounds to what we should be expecting
190 x0 = [5 -4 6 10 2];
191 lb = [1 -5 6 9 2];
192 ub = [6 -3 7 10 3];
193
194 cons = [D k q1 q2 p]; % Setting constants to pass to function
195 Fun = @(x) newLIEqns(x, cons); % Function of dummy variable x
196 options = optimoptions('lsqnonlin', 'Display','off', 'TolFun', 1e-12, 'TolX', 1e
    -6);
197 x = lsqnonlin(Fun,x0,lb,ub,options); %run lsqnonlin which is essentially fsolve,
    with ub and lb
198
199 A1 = x(1); B1 = x(2); A2 = x(3); B2 = x(4); phi = x(5);
200
201 res = 1000;
202 wta = 0:pi/res:2*pi;
203 wto = 2*pi*D:pi/res:2*pi;
204 wtf = 0:pi/res:2*pi*D;
205
206 syms wt
207 betas = (k*(wt - 2*pi*D))/(k+1) + p*(cos(2*pi*D + phi) - cos(wt + phi))*((q2^2)/(
    q2^2-1)-(k+1)) + (A2/q2)*(sin(2*pi*D*q2) - sin(wt*q2)) + (B2/q2)*(cos(wt*q2) -
    cos(2*pi*D*q2)) ;
208 alphas = int(betas, wt, 2*pi*D, 2*pi);
209 alpha = double(alphas);
210
211 beta = (k*(wto - 2*pi*D))/(k+1) + p*(cos(2*pi*D + phi) - cos(wto + phi))*((q2^2)/(
    q2^2-1)-(k+1)) + (A2/q2)*(sin(2*pi*D*q2) - sin(wto*q2)) + (B2/q2)*(cos(wto*q2)
    - cos(2*pi*D*q2)) ;
212
213 ID = (2*pi/alpha)*(1 - A1*cos(q1*wtf) - B1*sin(q1*wtf) - p*(k+1)*sin(wtf+phi)); %
    Normalised current through the switch with factor (Xc.ID)/Vi
214 VD = 2*pi*(beta/alpha); % Normalised voltage across the switch
215 Io = (2*pi/alpha)*(p*(k+1)*sin(wta + phi)); % Normalised output current
216
217 IDp = [ID(1:size(ID,2)-1), zeros(1,size(wto,2))]; % Normalised current waveform
    through switch
218 VDP = [zeros(1,size(wtf,2)-1), VD]; % Normalised voltage waveform across switch
219
220 figure(1);
221 subplot(1,3,1);
222 plot(wta, VDP, 'LineWidth', 1, 'Color', [251 111 66] ./ 255); hold on
223 set(gca, 'xtick', [0 pi/2 pi 3*pi/2 2*pi]);
224 tick = {'0'; '\pi/2'; '\pi'; '3\pi/2'; '2\pi'};
225 set(gca, 'xticklabel', tick);
226 grid on
227 grid minor
228
229 subplot(1,3,2);

```

```

230 plot(wta, IDp, 'LineWidth', 1, 'Color', [251 111 66] ./ 255); hold on
231 set(gca, 'xtick', [0 pi/2 pi 3*pi/2 2*pi]);
232 tick = {'0'; '\pi/2'; '\pi'; '3\pi/2'; '2\pi'};
233 set(gca, 'xticklabel', tick);
234 grid on
235 grid minor
236
237 subplot(1,3,3);
238 plot(wta, Io, 'LineWidth', 1, 'Color', [251 111 66] ./ 255); hold on
239 set(gca, 'xtick', [0 pi/2 pi 3*pi/2 2*pi]);
240 tick = {'0'; '\pi/2'; '\pi'; '3\pi/2'; '2\pi'};
241 set(gca, 'xticklabel', tick);
242 grid on
243 grid minor
244
245 IC2_1 = A1*cos(q1*wtf) + B1*sin(q1*wtf); % Normalised current through the harmonic
      LC network when switch is closed
246 IC2_2 = A2*cos(q2*wto) + B2*sin(q2*wto) - ((p*q2^2)/(q2^2-1))*sin(wto+phi) + 1/(k
      +1); % Normalised current through the harmonic LC network when switch is open
247 IC2p = [IC2_1(1:size(IC2_1,2)-1), IC2_2]; % Normalised current waveform through LC
      network
248
249 figure(2);
250 subplot(2,2,[1 3]);
251 plot(wta, IDp, 'LineWidth', 1, 'Color', [251 111 66] ./ 255); hold on
252 plot(wta, VDP, 'LineWidth', 1, 'Color', 'r'); hold on
253 set(gca, 'xtick', [0 pi/2 pi 3*pi/2 2*pi]);
254 tick = {'0'; '\pi/2'; '\pi'; '3\pi/2'; '2\pi'};
255 set(gca, 'xticklabel', tick);
256 grid on
257 grid minor
258
259 subplot(2,2,2);
260 plot(wtf(1:size(wtf,2)-1), IC2_1(1:size(IC2_1,2)-1), 'LineWidth', 1, 'Color', [1
      17 181] ./ 255); hold on
261 plot(wto, IC2_2, 'LineWidth', 1, 'Color', [251 111 66] ./ 255); hold on
262 set(gca, 'xtick', [0 pi/2 pi 3*pi/2 2*pi]);
263 tick = {'0'; '\pi/2'; '\pi'; '3\pi/2'; '2\pi'};
264 set(gca, 'xticklabel', tick);
265 grid on
266 grid minor
267
268 subplot(2,2,4);
269 plot(wta, Io, 'LineWidth', 1, 'Color', [251 111 66] ./ 255); hold on
270 set(gca, 'xtick', [0 pi/2 pi 3*pi/2 2*pi]);
271 tick = {'0'; '\pi/2'; '\pi'; '3\pi/2'; '2\pi'};
272 set(gca, 'xticklabel', tick);
273 grid on
274 grid minor

1 function F = newLIEqns(x, cons)
2 % x(1) = A1
3 % x(2) = B1
4 % x(3) = A2
5 % x(4) = B2
6 % x(5) = phi
7
8 D = cons(1);
9 k = cons(2);
10 q1 = cons(3);
11 q2 = cons(4);
12 p = cons(5);
13
14 F(1) = x(3)*cos(q2*2*pi) + x(4)*sin(q2*2*pi) - ((q2^2*p)/(q2^2-1))*sin(x(5)) + 1/(
      k+1) - x(1);
15 F(2) = -x(3)*q2*sin(q2*2*pi) + x(4)*q2*cos(q2*2*pi) - ((q2^2*p)/(q2^2 - 1))*cos(x
      (5)) - x(2)*q1;
16 F(3) = x(3)*cos(q2*2*pi*D) + x(4)*sin(q2*2*pi*D) - ((q2^2*p)/(q2^2-1))*sin(2*pi*D
      + x(5)) + 1/(k+1) - x(1)*cos(q1*2*pi*D) - x(2)*sin(q1*2*pi*D);
17 F(4) = (2*pi*k)/(k+1)*(1-D) + p*(cos(2*pi*D + x(5)) - cos(x(5)))*((q2^2)/(q2^2-1))

```

```

- (k+1) + (x(3)/q2)*(sin(2*pi*D*q2) - sin(2*pi*q2)) + (x(4)/q2)*(cos(2*pi*q2)
- cos(2*pi*D*q2));
18
19 syms wt p phi A2 B2 q2 k
20 alpha = (k*(wt - 2*pi*D))/(k+1) + p*(cos(2*pi*D + phi) - cos(wt + phi))*((q^2)/(
q^2-1)-(k+1)) + (A2/q2)*(sin(2*pi*D*q2) - sin(wt*q2)) + (B2/q2)*(cos(wt*q2) -
cos(2*pi*D*q2));
21 beta = int(alpha, wt, 2*pi*D, 2*pi);
22 ppsi = p*int(alpha*sin(wt + phi), wt, 2*pi*D, 2*pi);
23 eqn = diff(ppsi/beta, p);
24
25 F(5) = subs(eqn, [A2 B2 phi p k q2], [x(3) x(4) x(5) cons(5) cons(2) cons(4)]);

```

F Schematic, Layout and Embedded Code for Class EF boards

The schematic and board layout for the initial prototype board is shown below, along with an unpopulated aluminium etched board.

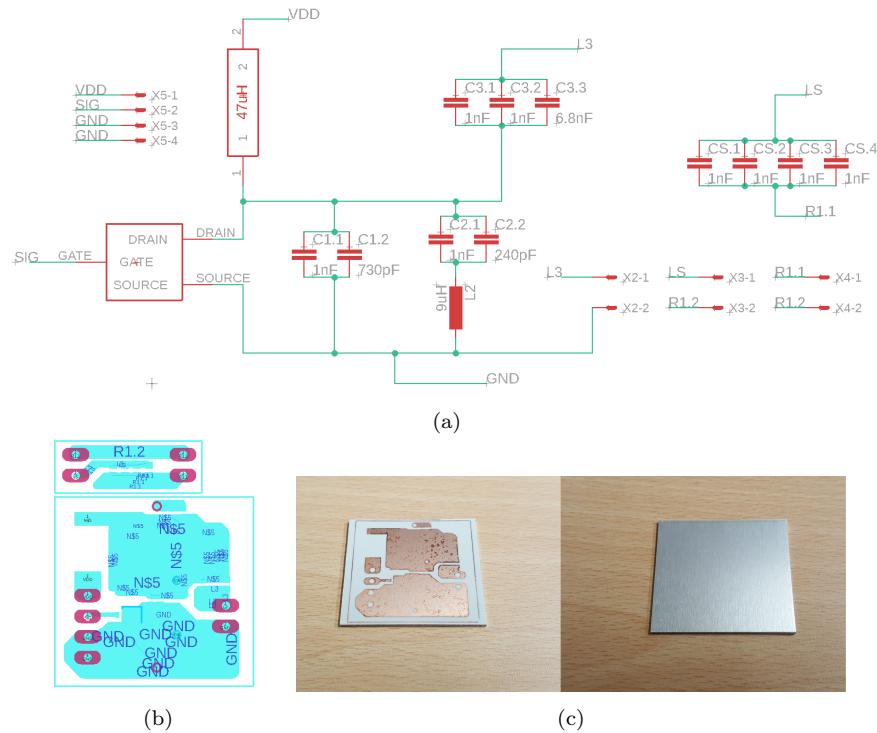


Figure F.1: (a) Schematic of the Class EF Inverter and receiving side circuitry, (b) Board layout, and (c) Etched layout on a single layer Aluminium Board

The schematic and board layout for the externally constructed and populated boards is shown below.

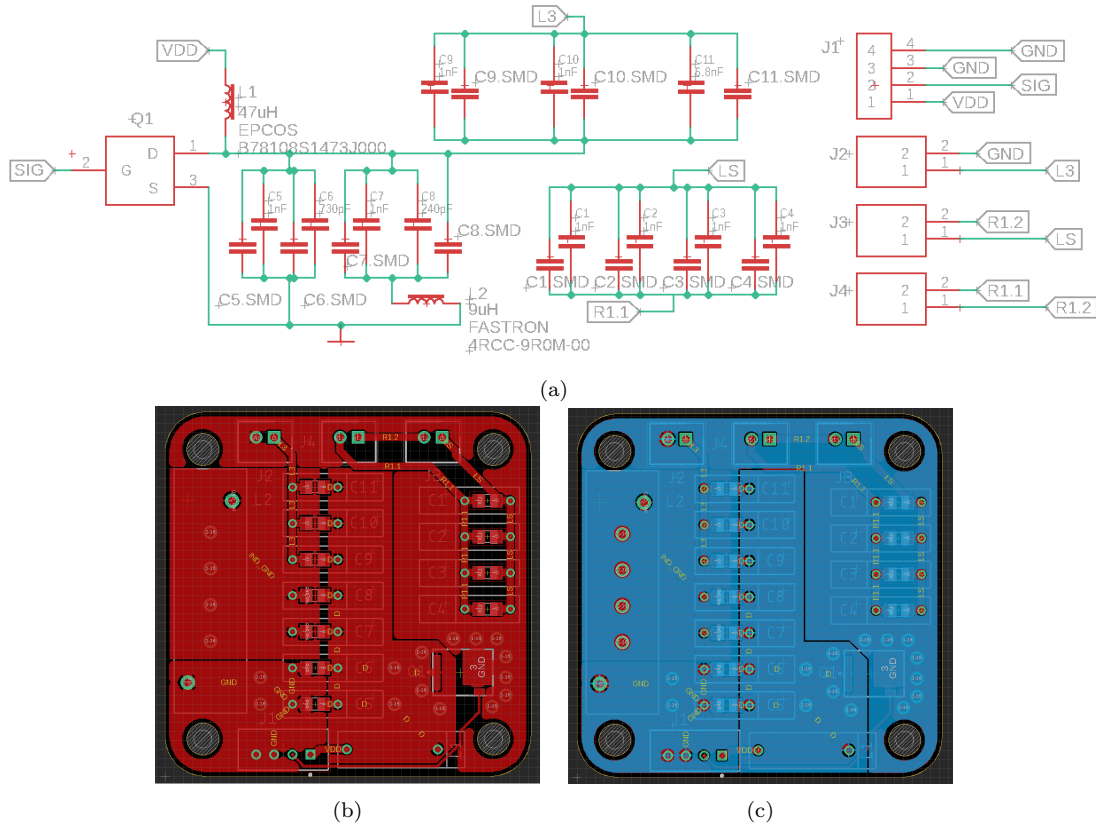


Figure F.2: (a) Schematic of the Class EF Inverter and receiving side circuitry, (b) Board layout highlighting the Top Layer, and (c) Board layout highlighting the Bottom Layer.

This ATmega32U4 is the main microprocessor chip on the Arduino Yún which was used to generate a fast switching signal with a desired duty cycle. This chip is able to achieve quite high frequency switching on its PWM pins (up to 96MHz) but at the cost of duty cycle resolution. For a 1MHz signal, the duty cycle resolution was adequate, and the code to implement this design is given below.

```

1 #include <avr/io.h>
2
3 void setup() {
4
5   pinMode(13,OUTPUT); //Output Pin for OC4A
6
7   PLLFRQ |= (1 << PLLTM0); // Pass the 48 MHz PLL clock straight
   through to the Timer4 Prescale module
8   TCCR4A = (1 << COM4A1) | (1 << PWM4A); // Set the PWM output to OC4A
9   TCCR4D = (1 << WGM40); // Set the timer up for Phase and
   Frequency correct PWM mode.
10  TCCR4E = (1 << ENHC4); // Activate Enhanced PWM mode
11
12  float period = 2; // Set Period; micro-seconds
13  float onTime = 0.6; // Set onTime; micro-seconds
14  unsigned int top; // Holds the register-equivalent period value
15  unsigned int match; // Holds the register-equivalent on time value
16
17  top = (unsigned int)(48 * period/2); // Set the period for Timer4
18  match = (unsigned int)(48 * onTime); // Set the on-time for the PWM

```

```

19
20 // Assign the calculated values to the correct registers
21 TC4H = (top >> 8); // Set the high 3 bits of the timer period
22 OCR4C = (unsigned char)top; // Set the lower 8 bytes of the timer period
23
24 TC4H = (match >> 8); // Set the high 3 bytes of the timer on-time
25 OCR4A = (unsigned char)match; // Set the lower 8 bytes of the timer on-time
26
27 TCCR4B &= ~(B00001111); // Clear the existing prescaler bits
28 TCCR4B |= 1; // Set the new prescaler value (1:1)
29 }
30
31 void loop() {}

```

G Analysis and Supplementary Figures of a Constant Output Current Class EF Inverter Implementation

Once the ClassEF inverter was constructed, it was examined to ensure that the performance was as expected. A Power source was supplied by a standard bench power supply which was capable of delivering the $\sim 30\text{V}$ needed for V_i . A Tektronix TDS 3014B four channel oscilloscope, capable of up to 100 MHz signal capture, was used in order to view the signals probed. Due to the expected fast signal changes, a low capacitance voltage probe was required in order to capture a good signal. An HP 10432A Probe was used which had a rated capacitance of just 7.5pF. Furthermore, a Tektronic CT-2 current transformer with P6041 Probe was also used in order to capture the current signal and display it on the oscilloscope. This was chosen as it had a very high sensitivity (1mA/mV), good frequency response (1.2 kHz - 200 MHz) and adequate operating range (up to 2.5A RMS). Finally, a FLIR One Gen 2 thermal imaging camera smartphone attachment was used to view the thermal performance of the board. This had a rated resolution of 0.1°C and surface temperature capture range of -20 to 150°C . The circuit was initially checked to ensure that it was stable as expected with no load on the output. A driving signal with an on-period duty cycle D of 30% was used to drive the MOSFET for 30 minutes, both with and without the 12 VDC PC cooling fan. The results are shown in Figure G.1.

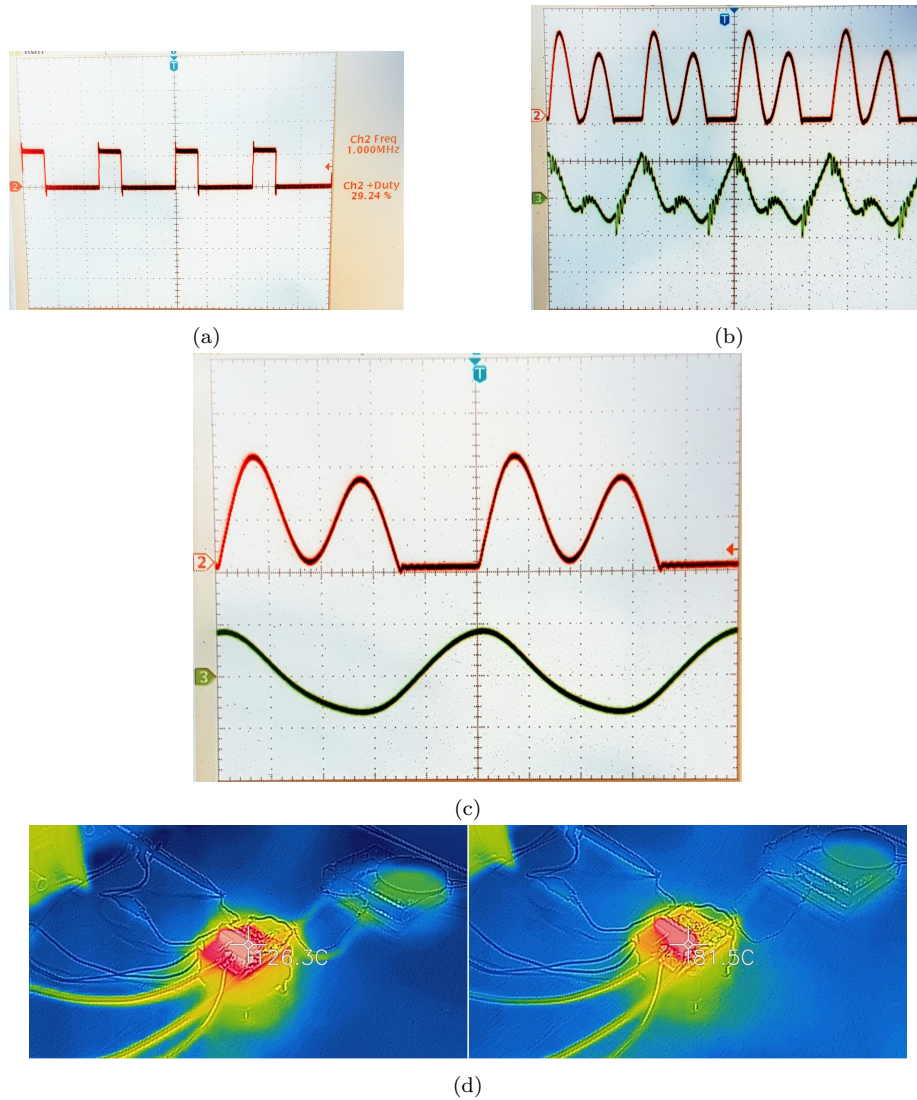


Figure G.1: Oscilloscope traces at no load R_L for (a) the drive signal from Arduino at 1 Mhz f_s and 30% D (5V/div); (b) the voltage across the MOSFET V_D (50V/div - red) and the input current I_i (0.2V/div - green); (c) a close-up of the voltage across the MOSFET V_D (50V/div - red) and the Output current I_o (1A/div - green); and (d) thermal images of Class EF circuit board after 30 minutes operation without the cooling fan (left) and with the cooling fan (right).

The measured voltages and currents are within the expected range, and the heat dissipation warranted the use of an aluminium board and cooling fan. A closed-loop resonant receiver with a negligible resistive load was brought close to the transmitting coil to observe the behaviour of the circuit. Figure G.2 illustrates how the voltage waveform across the MOSFET changed as the resonant receiver approached.

Of note is that when the coils were in very close proximity, the transmitting circuit lost its ZVS characteristic, and was operating suboptimally. It is noted that this may have been do to the large cross-coupling effect between the two coils, changing the

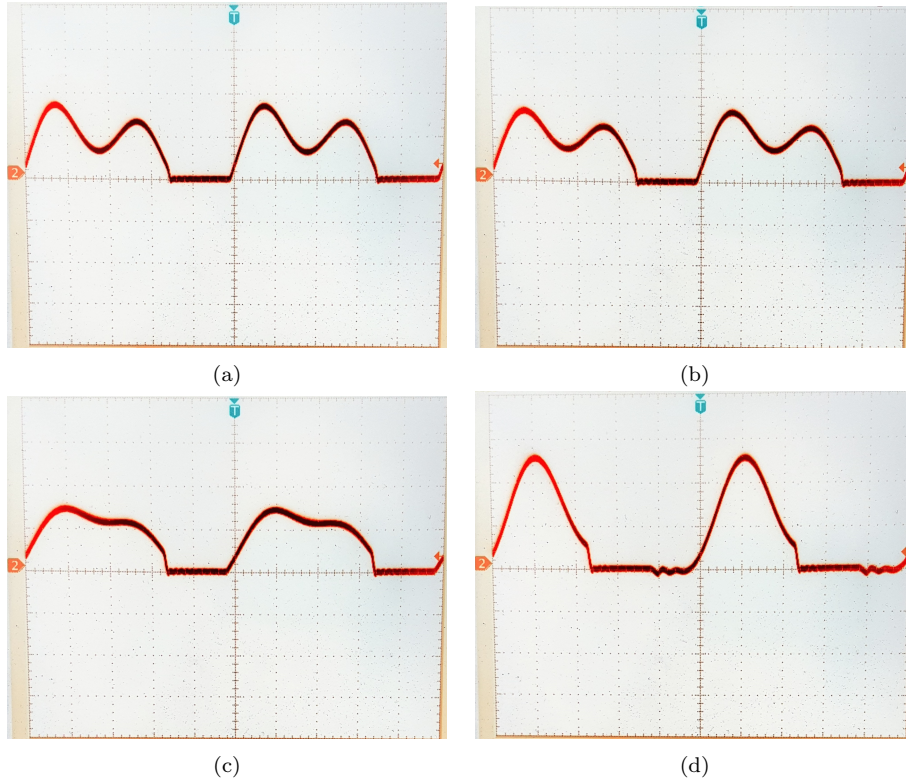


Figure G.2: Oscilloscope traces of the the voltage across the MOSFET V_D (50V/div) as a resonant receiver approaches the transmitting coil L_3 from (a) 6cm through to (d) a few mm.

effective reactances in the transmitting circuit. Loaded receivers were then applied at varying distances, each with different receiving resistances, and thus different values of R_L at similar coil separations. Figure G.3 shows the output waveforms at these instances. Finally, Figure G.4 show WPT using an LED on the receiving circuit to illustrate received power with different coil separation distances.

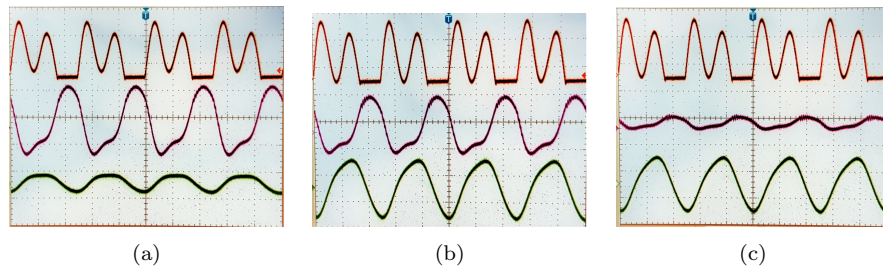
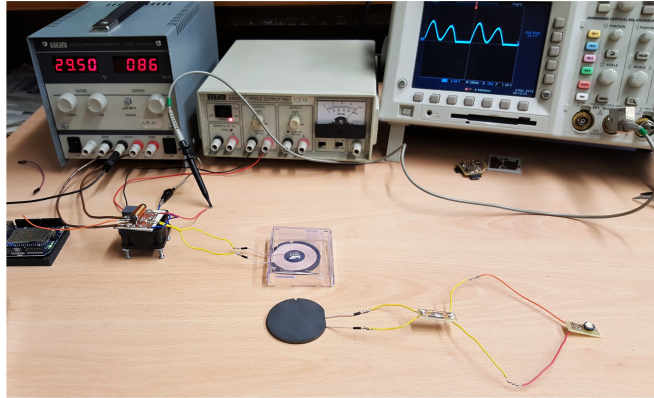
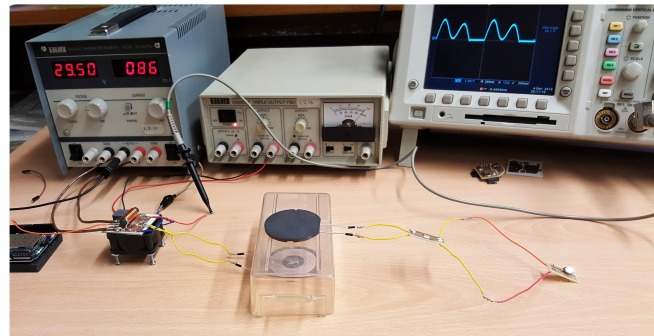


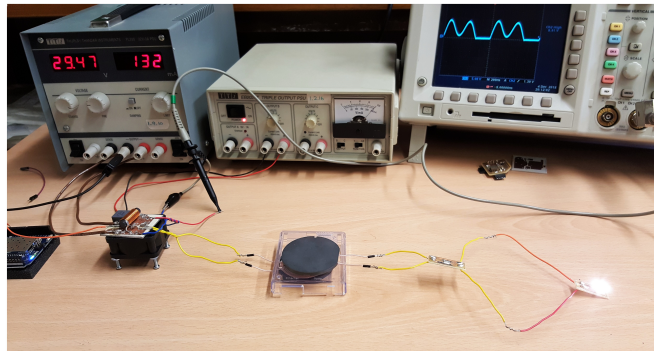
Figure G.3: Oscilloscope traces of the voltage across the MOSFET V_D (50V/div - red); voltage across the load R_L (1V/div - magenta) and current through the load R_L (1A/div - green) when the Load on the receiver is (a) 8.2Ω (b) 1Ω (c) 0.1Ω , separated by the same distance away from the transmitting coil L_3 .



(a)



(b)



(c)

Figure G.4: Bench top images of the WPT system, illustrating power transfer through a high-power LED when (a) no power is transmitted, (b) some power is transmitted to dim the LED and (c) sufficient power is transferred to fully switch on the LED.